RATIONAL DESIGN OF COLLOIDAL NOBLE METALLIC NANOCATALYSTS AND
DEVELOPMENT OF A MICROFLUIDIC PLATFORM FOR FUNDAMENTAL
ASSESSMENT OF CATALYTIC ACTIVITY

By

RUI LIN

A DISSERTATION

Submitted to
Michigan State University
in partial fulfillment of the requirements
for the degree of

Chemical Engineering-Doctor of Philosophy

2013

ABSTRACT

RATIONAL DESIGN OF COLLOIDAL NOBLE METALLIC NANOCATALYSTS AND
DEVELOPMENT OF A MICROFLUIDIC REACTOR PLATFORM FOR FUNDAMENTAL
ASSESSMENT OF CATALYTIC ACTIVITY

By

RUI LIN

Multiphase catalytic hydrogenations play a significant role in converting bio-derived
materials to commodity chemicals and liquid fuels. It is desirable to conduct the reaction
efficiently, economically and in an environmentally-friendly manner to achieve the goals of
green chemistry. However, mass transfer limitations and harsh reaction conditions often interfere
with the assessment of intrinsic catalyst performance, and induce undesired side reactions. To
provide a partial solution to this problem, we have combined colloid science, nanotechnology,
and microfluidics to construct a reaction platform that operates under mild reaction conditions,
enables rapid and accurate catalyst assessment, and minimizes or significantly reduces mass
transfer limitations.

In the first part of this dissertation, we report on the rational design of colloidal noble
metallic nanocatalysts, to take advantage of their high surface-area-to-volume ratios and the
resulting enhanced surface reactivity. We have used thermal decomposition to synthesize
uniform stable noble metallic (palladium, platinum and ruthenium) nanoparticles (NPs) less than
10 nm in diameter. The synthesis procedure was further enhanced by polyol reduction, to
improve the yield and efficiency of the process. Characterization by electron microscopy and
elemental analysis confirmed the uniform morphology and composition of the NPs.

In the second part of this dissertation, we developed continuous flow microreactor systems
with metal NPs immobilized on the reactor walls, for fast catalyst screening and performance

assessment under minimized mass transfer limitations. The first-generation microreactor was a polydimethylsiloxane (PDMS) microfluidic system fabricated by soft lithography, with NPs synthesized by thermal decomposition and immobilized *in-situ*. The effectiveness of immobilization in the microfluidic reactors was confirmed by hydrogenation of 6-bromo-1-hexene at room temperature and one atmosphere of hydrogen pressure. The turnover frequencies (TOF) measured in the microreactor were hundreds of times larger than those measured under identical reaction conditions in batch reactors. To improve catalyst stability and system compatibility, we developed second-generation microreactors using glass capillaries with NPs immobilized on the walls, and used the hydrogenation of cinnamaldehyde to assess catalyst activity and selectivity under different reaction conditions. We also investigated the effects of size and composition on catalyst performance.

In summary, the combination of well-defined nanocatalysts and microfluidics significantly enhance the diffusion of hydrogen to catalytic sites, thus eliminating mass transfer limitations and enabling evaluation of intrinsic catalytic activity. The system provides a convenient platform for high throughput screening of catalysts, and for conducting mechanistic studies of reaction kinetics.

To my beloved parents Mr. Lin Yu and Mrs. Li Yaoyu

献给我亲爱的父母林宇先生和李耀瑜女士

ACKNOWLEDGEMENTS

This dissertation could not have been completed without the guidance and help of my advisor, Professor Robert Ofoli. He has provided me with invaluable academic independence yet made sure I stayed on the right track. I want to thank him for his scientific insight, unconditional support, valuable advice and warm encouragement along the way. I am grateful for the opportunity to have worked with Professor Ofoli in the past several years. I thank him for being such a great advisor and mentor.

I want to thank my committee members Professor James Jackson, Professor Dennis Miller, Professor Sherine Obare and Professor Merlin Bruening. The discussions with all of them have always been productive and helpful. Professor Jackson, Professor Miller and Professor Obare have kept a close relationship with our research group and provided many brilliant ideas, insightful suggestions and accessibility to their laboratories, without which the dissertation would not have been completed. I am indebted to all the help from the members of those research groups (especially Ruel Freemantle and Dr. Lars Peereboom) in experimental set-up and equipment trouble-shooting. Professor Bruening helped build an academic foundation for my surface chemistry background from his advanced analytical chemistry course. I want to express my special appreciation to all of them.

I want to express my thanks to my group members Xianfeng Ma and Hao Yuan. Xianfeng, with whom I have had numerous enlightening discussions and closely worked with in the past five years, has always been an inspiring example for me in his passion for research, intelligence and hard work. Previous group members Dr. Greiner and Dr. Castro-Forero taught me soft lithography protocols and gave me a lot of advice in the transition from college to graduate

TABLE OF CONTENTS

LIST OF TABLES

LIST OF FIGURES

KEY TO SYMBOLS AND ABBREVIATIONS

A   cross-sectional area of capillary

A_G cross-sectional area of capillary occupied by gas or vapor

A_L cross-sectional area of capillary occupied by liquid

V   volume of capillary

v_G gas volume flow rate

v_L liquid volume flow rate;

ρ_G gas density

ρ_L liquid density

ε liquid hold-up fraction;

τ liquid residence time in capillary/microfluidics channels

x   ratio of gas mass flow rate to total mass flow rate

χ Lockhart-Martinelli-Chisholm parameter

Φ_L Lockhart-Martinelli parameter

APTMS   (3-Aminopropyl)trimethoxysilane

atm   atmospheric pressure

BET   Brunauer-Emmett-Teller

C   carbon

CAL   trans-cinnamaldehyde

COL   cinnamyl alcohol

DI   deionized

EDC   *N*-(3-Dimethylaminopropyl)-N$^{\text{'}}$-ethylcarbodiimide hydrochloride

EDS	energy dispersive X-ray spectroscopy
FT-IR	Fourier transform infrared spectroscopy
GC	gas chromatography
GC-MS	gas chromatography mass spectroscopy
HCAL	hydrocinnamaldehyde
HCl	hydrochloric acid
HCOL	hydrocinnamyl alcohol
HPLC	high-performance liquid chromatography
HRTEM	high-resolution transmission electron microscopy
ICP-AES	ionic coupled plasma atomic emission spectroscopy
I.D.	internal diameter
IPA	isopropyl alcohol
MW	molecular weight
nDS	n-dodecyl sulfide
NHS	N-Hydroxysuccinimide
NPs	nanoparticles
O.D.	outside diameter
Pd	palladium
Pt	platinum
PVP	poly-N-vinyl-2-pyrrolidone
PDMS	polydimethylsiloxane
rpm	revolutions per minute
Ru	ruthenium

S   sulfur

SAD   selected area diffraction

SEM   scanning electron microscopy

TOF   turnover frequency

XANES   x-ray absorption near edge spectroscopy

XPS   x-ray photoelectron spectroscopy

XRD   powder x-ray diffraction

UV-Vis   ultraviolet/visible light spectroscopy

CHAPTER 1 INTRODUCTION AND BACKGROUND

1.1 Multiphase hydrogenation in the biorefinery

The global chemical industry, which relies on fossil fuels, faces several challenges: excessive greenhouse gas emission, imbalance between limited resources and soaring demand, and potential energy security issues. It is a pressing challenge to find economical and sustainable alternative resources to replace fossil fuels, which are expected to be depleted in about 150 years. Biomass, with abundant production and relatively easy access, is one of the potential alternative resources [1, 2]. The integrated processes to convert biomass to fuels, power, and chemicals are defined as the biorefinery [3]. To become one of the future replacements or a current competitive alternative to the petroleum refinery, the biorefinery must be comparable in terms of efficiency, profitability and sustainability [3]. However, core chemical differences between biomass and fossil fuels require unique processing technologies in the biorefinery. Biomass (primarily carbohydrates) is generally polar, nonvolatile, and sensitive to acid and heat. Fossil fuels (primarily hydrocarbons) are typically non-polar, volatile, and thermally stable [4]. Instead of the high temperature and high pressure vapor phase reactions used in petroleum refining, conversions in the biorefinery are normally conducted in the liquid phase under moderate reaction conditions to prevent undesirable side reactions [4, 5].

Similar to the petroleum refinery, catalytic conversions of raw materials to value-added products are critical. Catalysis in the petroleum refinery focuses on adding desired functionalities to substrates, while emphasis shifts to defunctionalization (e.g., deoxygenation) in the biorefinery [4]. As a result, the key to a successful biorefinery is a series of highly effective catalysts for the various conversions required. There are two major steps in the biorefinery: a) conversions from biomass to a number of platform products (e.g., organic acids) via industrial-scale biological processes; and b) upgrading of platform products to a wide range of commodity

chemicals via catalytic conversions (e.g., hydrogenation, hydrolysis, condensation, and polymerization). This research project is focused on the latter issue.

Important building blocks such as organic acids and α, ß-unsaturated carbonyls from biomass fermentation can be converted to a number of valuable chemicals used in food, medicine and cosmetics [6]. One of the major routes is multiphase catalytic hydrogenation, in which the liquid substrate reacts with molecular hydrogen in the presence of solid catalysts. These gas-liquid-solid hydrogenations are typically performed in flow reactors such as triple bed reactors, slurry bubble columns or packed bed reactors [7]. Precious metals have been shown to be effective for gas-liquid-solid hydrogenations, and reactions have been studied at different temperatures, pressures, catalyst loading and substrate concentrations [8-10]. However, a number of scientific and technological barriers are yet to be overcome to improve the efficiency of catalytic multiphase hydrogenation.

First, it is desirable to rationally design efficient catalysts for gas-liquid-solid hydrogenations under mild reaction conditions. Ideally, catalysts with targeted activity and selectivity would be controlled by carefully tuning their physical and chemical properties. Platinum group metals have proven to be excellent hydrogenation catalysts for their unique electronic properties, chemical tolerance and high heat resistance. However, reserves of platinum group metals are scarce, so it is critical to achieve satisfactory product yields and selectivity with the minimum amount of catalysts. Another major challenge for multiphase hydrogenation is mass transfer limitation, resulting from the extremely low hydrogen solubility in organic and aqueous solvents, and the slow substrate diffusion to catalyst surfaces [11]. High temperatures and pressures are usually applied to enhance the interactions among the substrate, hydrogen, and solid catalyst. However, under these circumstances, the substrates are prone to

undergo side reactions due to their unstable chemical properties. Furthermore, mass transfer limitations affect the accuracy of measurements to assess intrinsic catalyst activity and reaction kinetics, which are the keys to a better understanding of mechanisms and optimization of the reactions. To address these issues, we have combined nanotechnology and microfluidics technology to develop novel catalysts and reactor systems for multiphase hydrogenation. The system incorporates nanocatalysts with high surface activity into microfluidic reactors, to minimize or negate mass transfer limitations.

1.2 Noble metal nanocrystals for gas-liquid-solid hydrogenations

Surface chemistry plays a vital role in catalytic reactions. Metal NPs have a much higher surface-area-to-volume ratios than their bulk counterparts. Assuming atoms are closely-packed spheres, approximately 11% of the total atoms in a 3-nm Pd particle are on the surface, compared to only 0.03% on a 1-µm particle. As a result, more accessible catalytic sites and better atom economy are achieved as catalysts get smaller. In addition, the unique electronic and geometric properties of typical nanoscale particles allow more efficient catalyst-reactant interaction and higher turnover frequencies under milder reaction conditions [12-14]. Noble metal nanocrystals with well-defined morphology and structures are thus excellent systems to study the correlation between material properties and catalytic performance. The information is critical in the rational design and optimization of catalytic systems.

Several examples have been reported in the literature on the effect of catalyst morphology (size and shape), composition and structure on catalyst selectivity and activity. Bhattacharjee et al. reported synthesis of Pd NPs of various sizes embedded in polyelectrolyte films for the catalytic hydrogenation of unsaturated alcohols. They observed a 20-fold higher selectivity with 2.2-nm Pd NPs in comparison to 3.4-nm Pd NPs[15]. Plomp demonstrated that the surface

properties of the carbon nanofiber support changed the adsorption mode for different sizes of Pt

(1.8-3.4 nm) and Ru (2.2-3.5 nm) NPs used for cinnamaldehyde hydrogenation. They observed

that the largest particles had the highest   selectivity towards cinnamyl alcohol before oxygen

removal from the carbon nanofiber support, and just the opposite after oxygen removal [16].

Tsung et al. synthesized sub-10 nm Pt NPs of various shapes and sizes, observed a higher

selectivity to n-butylamine for Pt nanocubes compared to nanopolyhedra, and attributed the

result to enhanced ring-opening ability of the Pt nanocubes [17]. Sang et al. studied the size

effects of Ru NPs (2.1-6.0 nm) on CO oxidation, and found that the 6.0-nm Ru NPs were 16

times more active than the 2.1-nm Ru NPs. This study demonstrated that smaller particles did not

always produce higher catalytic activity. They attributed the higher oxidation activity of larger

Ru NPs to more stable adsorption layers of catalytically active RuO_2 on the larger metallic Ru

NP surface. By contrast, the RuO_2 layers on the smaller Ru NP surface were less stable, and

were quickly transformed into inactive oxide phases, resulting in lower oxidation activity[18].

Research groups at Northwestern University and Argonne National Laboratory synthesized Pt-

Ru bimetallic NPs (4.5 nm) by atomic layer deposition and demonstrated enhanced activity for

methanol decomposition compared to a simple mixture of Pt and Ru single metallic NPs at

similar loading [19]. Most recently, Wu et al. synthesized $Pd_{50}Ru_{50}$ NPs with three distinct

structures for formic acid fuel cells applications, and reported superior performance over

commercial Pd on carbon[20].

1.3 Liquid-phase synthesis and characterization of noble metallic NPs

Advances in colloid chemistry and nanotechnology have enabled the development of

effective liquid-phase synthesis methods for metal nanocrystals [17, 21-26]. A number of

reaction parameters are adjusted systematically to control particle nucleation and growth rates, leading to desired sizes, shapes, crystal structures or compositions of the nanocrystals. Our collaborators, Dr. Obare and her group, have used thio-ethers as stabilizing ligands to prepare uniform platinum group colloidal NPs via thermal decomposition for catalytic and environmental applications [27, 28]. The sulfur atoms in the stabilizer coordinate with the metal atoms while the long carbon chains provide steric hindrance to avoid particle aggregation. Decomposition temperatures, solvents, stabilizing ligand to metal precursor ratios, ligand types and reaction time can be adjusted to finely control the size and shape of the NPs.

Another common liquid-phase method widely used to synthesize size- and shape-controlled Pd, Pt, Ru, Rh, Au, Ag NPs and bimetallic NPs is polyol (alkyl alcohols) reduction [10, 17, 19, 20, 24-26, 29-34]. PVP, a water-soluble linear polymer with hydroxyl end groups, has served as a steric stabilizer or capping agent to protect the colloidal particles from agglomeration, and also as a very mild reducer for metal salt precursors [33, 34]. Reducing alcohol types, metal precursor types, ratio of metal precursor to PVP, molecular weight of PVP, reduction temperature and solvents are among the primary reaction parameters used to control particle morphology and composition.

Information on the morphology and composition of colloidal metal nanocrystals is generally obtained by HRTEM integrated with EDS. The shape and size are captured in the HRTEM digital images, and metal particle size distribution can be computed by the mass average of particle diameters of a sufficient number of NPs. The elemental composition of the particle is determined by EDS. The bulk particle composition can be analyzed by ICP-AES in the liquid phase. This method is used to determine the yield of NPs from metal precursors. The SAD in HRTEM reveals particle crystal fringes, and the measurement of the ring size and lattice fringes

can be used to determine the type of crystal facets of the particles. Another method to measure particle size and size distribution in a suspension is DLS, which gives the hydrodynamic diameter of the metal core and stabilizing ligands. As a result, the values are less accurate if the particle size is under 5 nm. For nanocrystals, the particle diameter can also be estimated by XRD, using the Scherrer equation. The measured values should match the diameter obtained from HRTEM measurements reasonably well for nanocrystals. However, when the particle size decreases below 5 nm, the diffraction peaks broaden, making it much more difficult to estimate the particle size. The crystal structures of the solid NPs can be determined precisely by XRD. Interaction between metal atoms and stabilizers can be characterized by FT-IR. During the synthesis process, the color change of the reaction mixture can be monitored by UV-Vis to determine when the reaction is complete. Since the main focus of this dissertation is on colloidal metal/bimetallic nanocrystals with emphasis on their morphology and composition, the combination of HRTEM and EDS is the primary characterization tool.

1.4 Microfluidic reactors in multiphase catalytic hydrogenation

1.4.1 Advantages of using microfluidic reactors in catalysis

In order to accurately assess catalyst performance, it is critical to design a chemical reactor with the following desirable characteristics: robust incorporation of catalysts, efficient mass and heat transfer, low fabrication cost and operational convenience and safety. Batch reactors are still the main-stream tool to assess catalytic NPs in hydrogenation reactions. However, continuous microfluidic reactors have been used as a complementary tool to minimize mass transfer limitations and reduce the time required for evaluation of nanocatalysts under moderate reaction conditions.

7

Microreactors, defined as reactors with at least one inner dimension under 1 mm, have

received increasing attention in the past twenty years in the area of organic synthesis [35] [10,

36-43]. Microreactors have unique characteristics due to their size. The most important feature is

the high surface-area-to-volume ratio in the typical range of 10, 000 to 50, 000 $m^2 m^{-3}$, compared

to about 100 $m^2 m^{-3}$ for conventional reactors which seldom reach 1, 000 $m^2 m^{-3}$ [10, 35, 37-39,

44]. Compared to conventional batch reactors, microreactors allow much higher interfacial

contact between different phases in heterogeneous catalytic reactions, resulting in mass transfer

coefficients two or three orders of magnitude higher[35, 44-46]. Heat transfer efficiency in

microreactors is also significantly higher than in conventional reactors, allowing for easier

temperature control, suppression of side reactions, and improvement of reaction selectivity and

product yield [35, 37-41]. Mass transport is considerably better, due to the short molecular

diffusion distances and short mixing times. The enhanced mass transfer is especially valuable in

ensuring the acquisition of intrinsic kinetic data for modeling reactions [35, 37-41]. Flows in

microreactors are mostly laminar, dominated by surface and interfacial forces, and allow precise

control of flow rates and flow patterns [35, 37-41]. Furthermore, the small reaction volumes

enable easy control of reaction parameters such as temperature, pressure, residence time, and

quantity of reactants. They also ensure inherent safety of operation, especially for explosive and

toxic reactions [35, 37-41].

1.4.2 Fabrication of microfluidic reactors

Several materials can be used to fabricate microfluidic reactors, including silica, stainless

steel and polymers [40-43, 47]. Microfluidic channels can be either cylindrical or rectangular.

Traditional lithography methods apply MEMS technology to etch channels on silica and glass

substrates [48-51]. Microfluidic reactors fabricated from silica can withstand high temperatures and pressures, and are chemically resistant and mechanically strong [17, 52, 53]. However, the fabrication process demands a clean-room environment and is highly labor-intensive and costly. Capillary and separation columns are another type of microfluidic reactors which are simple, commercially available and allow flexible packaging of catalysts [49, 54-63]. Soft lithography (specifically rapid prototyping and replica molding) uses an elastomeric material to transfer patterns. It is an inexpensive and rapid process compared to conventional photolithography [64, 65]. Transparent PDMS is the most widely-used elastomer to fabricate microfluidic devices for its easy conformity and good durability, low interfacial energy, gas permeability, thermal and electrical insulation properties, chemical inertness, and low cost [66-68]. PDMS can be oxidized by exposure to plasma, then brought into contact with glass to form an irreversible bond [66-68]. Limitations of PDMS include its incompatibility with non-polar organic solvents, instability under high temperature and pressure, and defects and deformations due to its soft properties [66-68]. For hydrogenations under mild reaction conditions, PDMS microfluidic and glass capillary microreactors are suitable systems.

1.4.3 Catalyst immobilization in microfluidic reactors

In order to meet the guidelines for green chemistry, immobilization of catalysts in microfluidic reactors is highly desirable for easy catalyst recycling and reuse. The most straightforward way is to pack catalyst particles to form micro packed-bed reactors [45, 46, 69]. This process is now used most commonly in commercial catalyst screening, especially for pre-developed catalysts used in conventional reactions. However, this type of micro packed-bed reactor faces two major challenges as a result of random catalyst packaging: flow mal-distribution and broad RTD. One solution is structured packed-bed microreactors with more

9

orderly flow distribution and narrower RTD. The structured packed-bed is usually composed of ceramic or zeolite fibrous/foams/tissues/filters materials [45, 70-73]. However, high pressure drop still remains an issue, be it randomly- or orderly-packed microreactors, especially with small catalyst particles.

To address the above issues, catalytic-wall microfluidic reactors have been developed [45, 46]. Catalysts can be anchored to the reactor wall surfaces through physical, chemical or electrical interactions. Metal catalysts can be immobilized onto the walls by sputter coating [40, 74, 75], impregnation [76], sol-gel methods [54, 55, 57, 59, 77, 78], or wet-washing coating [45, 46]. An ideal catalytic wall microreactor for multiphase hydrogenation will have uniform catalyst particles evenly anchored on the surface of the walls. The liquid substrate and gas mixture in different flow regimes then interact with the catalysts for maximum mass and heat transfer efficiency. The flow regimes observed inside microchannels include bubble flow, slug flow, churn flow and annular flow, and can be measured experimentally or modeled theoretically [79, 80].

1.4.4 Examples of catalytic wall microfluidic reactors for multiphase reactions

In the last decade, several research groups have carried out multiphase reaction in catalytic wall microfluidic reactors, and demonstrated the high efficiency of the systems. Kobayashi and his group developed etched glass microreactors with polymer encapsulated Pd catalysts, and achieved fast hydrogenation of double- and triple-carbon bonds [44]. The system was also used with super-critical CO_2 as a solvent for improved catalyst performance [44]. Trapp and colleagues used a fused silica capillary column coated with a copolymer film with embedded Pd NPs for hydrogenation of a list of ring compounds, to efficiently screen a library of catalysts

10

prepared under different conditions [62, 81]. The major challenge for encapsulated metal catalysts was the limited accessibility of substrate to catalyst surfaces.

Most recently, mesoporous support layers with embedded metal catalysts coated on the wall of the microreactors have been developed [57, 59, 77, 82] . This method allows good control of catalyst loading, larger surface area and easy catalyst regeneration. For example, nitrobenzene hydrogenation to aniline was successfully conducted in a glass capillary coated with mesoporous silica embedded with Pt NPs [83]. A fused silica capillary coated with gamma-aluminum film impregnated with Pd was used for hydrogenation reactions in a continuous segment flow system [36]. The Schouten group has published a number of papers on using titanium-coated fused silica capillary embedded with Pt, Pd or Au NPs for selective hydrogenation of α, ß-unsaturated aldehydes and ketones [57, 59, 77, 82]. However, diffusion limitations in the small pores of the support hindered the accurate measurement of intrinsic reaction kinetics. Supports with larger pores such as carbon nanofibers loaded with Ni were grown inside a rectangular micro-channel to greatly increase the surface area and prevent surface diffusion limitations [84].

1.5 Outline of this dissertation

This dissertation summarizes attempts to combine nanotechnology and microfluidics to develop efficient catalysts and reactor systems for multiphase hydrogenation of biorenewable materials. Following the introduction and background in this chapter, Chapter 2 focuses on catalyst design and preparation, and details the synthesis and characterization of well-defined noble metallic NPs. Chapters 3 and 4 describe the development of two different microreactor systems with immobilized nanocatalysts and their use for catalyst assessment in model hydrogenations. Chapter 5 summarizes the primary results of the entire work and briefly discusses suggested future research directions.

REFERENCES

12

REFERENCES

1.   Kamm, B. and M. Kamm, *Biorefinery - Systems.* Chemical and Biochemical Engineering Quarterly, 2004. **18**(1): p. 1-6.

2.   Kamm, B. and M. Kamm, *Principles of biorefineries.* Applied Microbiology and Biotechnology, 2004. **64**(2): p. 137-145.

3.   Fernando, S., et al., *Biorefineries: Current status, challenges, and future direction.* Energy & Fuels, 2006. **20**(4): p. 1727-1737.

4.   Lynd, L.R., C.E. Wyman, and T.U. Gerngross, *Biocommodity engineering.* Biotechnology Progress, 1999. **15**(5): p. 777-793.

5.   Ragauskas, A.J., et al., *The path forward for biofuels and biomaterials.* Science, 2006. **311**(5760): p. 484-489.

6.   Varadarajan, S. and D.J. Miller, *Catalytic upgrading of fermentation-derived organic acids.* Biotechnology Progress, 1999. **15**(5): p. 845-854.

7.   Duduković, M.P., F. Larachi, and P.L. Mills, *Multiphase catalytic reactors: a perspective on current knowledge and future trends.* Catalysis Reviews: Science and Engineering, 2002. **44**(1): p. 123-246.

8.   Chen, Y.Q., D.J. Miller, and J.E. Jackson, *Kinetics of aqueous-phase hydrogenation of organic acids and their mixtures over carbon supported ruthenium catalyst.* Industrial & Engineering Chemistry Research, 2007. **46**(10): p. 3334-3340.

9.   Jere, F.T., J.E. Jackson, and D.J. Miller, *Kinetics of the aqueous-phase hydrogenation of L-alanine to L-alaninol.* Industrial & Engineering Chemistry Research, 2004. **43**(13): p. 3297-3303.

10.   Fletcher, P.D.I., et al., *Micro reactors: principles and applications in organic synthesis.* Tetrahedron, 2002. **58**(24): p. 4735-4757.

11.   Pazmino, J.H., et al., *Metallic Pt as active sites for the Water-Gas Shift reaction on alkali-promoted supported catalysts.* Journal of Catalysis, 2012. **286**: p. 279-286.

12.   Bonnemann, H. and R.M. Richards, *Nanoscopic metal particles - Synthetic methods and potential applications.* European Journal of Inorganic Chemistry, 2001(10): p. 2455-2480.

13.   Thomas, J.M., et al., *High-performance nanocatalysts for single-step hydrogenations.* Accounts of Chemical Research, 2003. **36**(1): p. 20-30.

14.   Raimondi, F., et al., *Nanoparticles in energy technology: Examples from electrochemistry and catalysis.* Angewandte Chemie-International Edition, 2005. **44**(15): p. 2190-2209.

15.   Bhattacharjee, S., D.M. Dotzauer, and M.L. Bruening, *Selectivity as a function of nanoparticle size in the catalytic hydrogenation of unsaturated alcohols.* Journal of the American Chemical Society 2009. **131**: p. 3601-3610.

16.   Plomp, A.J., et al., *Particle size effects for carbon nanofiber supported platinum and ruthenium catalysts for the selective hydrogenation of cinnamaldehyde.* Applied Catalysis A: General, 2008. **351**: p. 9-15.

17.   Tsung, C.-K., et al., *Sub-10 nm Platinum Nanocrystals with size and shape control: Catalytic study for ethylene and pyrrole hydrogenation.* Journal of the American Chemical Society, 2009. **131**: p. 5816-5822.

18.   Sang, H.J., et al., *Size effect of Ruthenium nanoparticles in catalytic carbon monoxide oxidation.* Nano Letters, 2010. **10**: p. 2709-2713.

19.   Christensen, S.T., et al., *Supported Ru-Pt bimetallic nanoparticle catalysts prepared by atomic layer deposition.* Nano Letters, 2010. **10**: p. 3047-3051.

20.   Wu, D., et al., *Mixed-phase PdRu bimetallic structures with high activity and stability for formic acid electrooxidation.* Physcal Chemistry Chemical Physics, 2012. **14**: p. 8051-8057.

21.   Kobayashi, J., Y. Mori, and S. Kobayashi, *Multiphase organic synthesis in microchannel reactors.* Chemistry-an Asian Journal, 2006. **1**(1-2): p. 22-35.

14

22.   Narayanan, R., *Recent Advances in Noble Metal Nanocatalysts for Suzuki and Heck Cross-Coupling Reactions.* Molecules, 2010. **15**(4): p. 2124-2138.

23.   Cheong, S.S., J.D. Watt, and R.D. Tilley, *Shape control of platinum and palladium nanoparticles for catalysis.* Nanoscale, 2010. **2**(10): p. 2045-2053.

24.   Semagina, N. and L. Kiwi-Minsker, *Recent Advances in the Liquid-Phase Synthesis of Metal Nanostructures with Controlled Shape and Size for Catalysis.* Catalysis Reviews-Science and Engineering, 2009. **51**(2): p. 147-217.

25.   Narayanan, R. and M.A. El-Sayed, *Catalysis with transition metal nanoparticles in colloidal solution: Nanoparticle shape dependence and stability.* Journal of Physical Chemistry B, 2005. **109**(26): p. 12663-12676.

26.   Astruc, D., F. Lu, and J.R. Aranzaes, *Nanoparticles as recyclable catalysts: The frontier between homogeneous and heterogeneous catalysis.* Angewandte Chemie-International Edition, 2005. **44**(48): p. 7852-7872.

27.   Ganesan, M., R.G. Freemantle, and S.O. Obare, *Monodisperse thioether-stabilized palladium nanoparticles: Synthesis, characterization, and reactivity.* Chemistry of Materials, 2007. **19**(14): p. 3464-3471.

28.   Freemantle, R.G., *Synthesis and characterization of monodisperse metallic nanoparticles and their catalytic activity*. 2009, Western Michigan University: Kalamazoo. p. 196.

29.   Lim, B., et al., *Shape-Controlled Synthesis of Pd Nanocrystals in Aqueous Solutions.* Advanced Functional Materials, 2009. **19**(2): p. 189-200.

30.   Grass, M.E., et al., *Colloidally Synthesized Monodisperse Rh Nanoparticles Supported on SBA-15 for Size- and Pretreatment-Dependent Studies of CO Oxidation.* Journal of Physical Chemistry C, 2009. **113**(20): p. 8616-8623.

31.   Xiong, Y.J. and Y.N. Xia, *Shape-controlled synthesis of metal nanostructures: The case of palladium.* Advanced Materials, 2007. **19**(20): p. 3385-3391.

32.   Borodko, Y., et al., *Charge-transfer interaction of poly(vinylpyrrolidone) with platinum and rhodium nanoparticles.* Journal of Physical Chemistry C, 2007. **111**(17): p. 6288-6295.

33.   Xiong, Y.J., et al., *Poly(vinyl pyrrolidone): A dual functional reductant and stabilizer for the facile synthesis of noble metal nanoplates in aqueous solutions.* Langmuir, 2006. **22**(20): p. 8563-8570.

34.   Washio, I., et al., *Reduction by the end groups of poly(vinyl pyrrolidone): A new and versatile route to the kinetically controlled synthesis of Ag triangular nanoplates.* Advanced Materials, 2006. **18**(13): p. 1745-+.

35.   Jahnisch, K., et al., *Chemistry in microstructured reactors.* Angewandte Chemie-International Edition, 2004. **43**(4): p. 406-446.

36.   Bakker, J.J.W., et al., *Heterogeneously Catalyzed Continuous-Flow Hydrogenation Using Segmented Flow in Capillary Columns.* ChemCatChem, 2011. **3**(7): p. 1155-1157.

37.   Hessel, V. and H. Lowe, *Organic synthesis with microstructured reactors.* Chemical Engineering & Technology, 2005. **28**(3): p. 267-284.

38.   Watts, P. and S.J. Haswell, *The application of micro reactors for organic synthesis.* Chemical Society Reviews, 2005. **34**(3): p. 235-246.

39.   Geyer, K., J.D.C. Codee, and P.H. Seeberger, *Microreactors as tools for synthetic chemists - The chemists' round-bottomed flask of the 21st century?* Chemistry-a European Journal, 2006. **12**(33): p. 8434-8442.

40.   Watts, P. and C. Wiles, *Recent advances in synthetic micro reaction technology.* Chemical Communications, 2007(5): p. 443-467.

41.   Mason, B.P., et al., *Greener approaches to organic synthesis using microreactor technology.* Chemical Reviews, 2007. **107**(6): p. 2300-2318.

42.   Yoshida, J.I., A. Nagaki, and T. Yamada, *Flash chemistry: Fast chemical synthesis by using microreactors.* Chemistry-a European Journal, 2008. **14**(25): p. 7450-7459.

43.   Fukuyama, T., et al., *Adventures in inner space: Microflow systems for practical organic synthesis.* Synlett, 2008(2): p. 151-163.

44.   Kobayashi, J., M. Yuichiro, and S. Kobayashi, *Hydrogenation reactions using scCO2 as a solvent in microchannel reactors.* Chemical Communications, 2005: p. 2567-2568.

45.   Yuranov, I., A. Renken, and L. Kiwi-Minsker, *Zeolite/sintered metal fibers composites as effective structured catalysts.* Applied Catalysis A: General, 2005. **281**: p. 55-60.

46.   Klemm, E., et al., *Microstructured reactors in heterogeneous catalysis.* Chemical Engineering & Technology, 2007. **30**(12): p. 1615-1621.

47.   Wiles, C. and P. Watts, *Continuous flow reactors, a tool for the modern synthetic chemist.* European Journal of Organic Chemistry, 2008(10): p. 1655-1671.

48.   Henriksen, T.R., et al., *Highly sensitive silicon microreactor for catalyst testing.* Review of Scientific Instruments, 2009. **80**(12).

49.   Trachsel, F., et al., *Solid catalyzed hydrogenation in a Si/glass microreactor using supercritical CO2 as the reaction solvent.* Journal of Supercritical Fluids, 2009. **48**(2): p. 146-153.

50.   Kusakabe, K., et al., *Fabrication of parallel microchannel reactors for use in catalyst testing.* Journal of Chemical Engineering of Japan, 2002. **35**(9): p. 914-917.

51.   L'Hostis, E., et al., *Microreactor and electrochemical detectors fabricated using Si and EPON SU-8.* Sensors and Actuators B-Chemical, 2000. **64**(1-3): p. 156-162.

52.   Nagy, K.D. and K.F. Jensen, *Catalytic processes in small scale flow reactors Status and opportunities.* Chimica Oggi-Chemistry Today, 2011. **29**(4): p. 18-21.

53.   McMullen, J.P. and K.F. Jensen, *Rapid Determination of Reaction Kinetics with an Automated Microfluidic System.* Organic Process Research & Development, 2011. **15**(2): p. 398-407.

54.   Javaid, R., et al., *Fabrication of microtubular reactors coated with thin catalytic layer (M=Pd, Pd-Cu, Pt, Rh, Au).* Catalysis Communications, 2010. **11**(14): p. 1160-1164.

55.   Hornung, C.H., et al., *A Palladium Wall Coated Microcapillary Reactor for Use in Continuous Flow Transfer Hydrogenation.* Advanced Synthesis & Catalysis, 2010. **352**(10): p. 1736-1745.

56.   Weber, S.K., S. Bremer, and O. Trapp, *Integration of reaction and separation in a micro-capillary column reactor-Palladium nanoparticle catalyzed C-C bond forming reactions.* Chemical Engineering Science, 2010. **65**(7): p. 2410-2416.

57.   Muraza, O., et al., *Selectivity control in hydrogenation reactions by nanoconfinement of polymetallic nanoparticles in mesoporous thin films.* Applied Catalysis a-General, 2009. **368**(1-2): p. 87-96.

58.   Rebrov, E.V., et al., *Selective Hydrogenation of 2-Methyl-3-butyne-2-ol in a Wall-Coated Capillary Microreactor with a Pd25Zn75/TiO2 Catalyst.* Organic Process Research & Development, 2009. **13**(5): p. 991-998.

59.   Rebrov, E.V., et al., *Capillary microreactors wall-coated with mesoporous titania thin film catalyst supports.* Lab on a Chip, 2009. **9**(4): p. 503-506.

60.   Bussard, A.G., et al., *Hydrogenation of alpha-methylstyrene in a piston-oscillating monolith reactor.* Industrial & Engineering Chemistry Research, 2008. **47**(14): p. 4623-4631.

61.   Ueno, M., et al., *Development of microchannel reactors using polysilane-supported palladium catalytic systems in capillaries.* Chemical Communications, 2008(14): p. 1647-1649.

62.   Trapp, O., et al., *High-throughput kinetic study of hydrogenation over palladium nanoparticles: Combination of reaction and analysis.* Chemistry-a European Journal, 2008. **14**(15): p. 4657-4666.

63.   Tsoligkas, A.N., et al., *Kinetic and selectivity studies of gas-liquid reaction under Taylor flow in a circular capillary.* Catalysis Today, 2007. **128**(1-2): p. 36-46.

64.   McCreedy, T., *Rapid prototyping of glass and PDMS microstructures for micro total analytical systems and micro chemical reactors by microfabrication in the general laboratory.* Analytica Chimica Acta, 2001. **427**(1): p. 39-43.

18

65.   McDonald, J.C., et al., *Fabrication of microfluidic systems in poly(dimethylsiloxane).* Electrophoresis, 2000. **21**(1): p. 27-40.

66.   Whitesides, G.M. and A.D. Stroock, *Flexible methods for microfluidics.* Physics Today, 2001. **54**(6): p. 42-48.

67.   McDonald, J.C. and G.M. Whitesides, *Poly(dimethylsiloxane) as a material for fabricating microfluidic devices.* Accounts of Chemical Research, 2002. **35**(7): p. 491-499.

68.   Xia, Y.N., D. Qin, and Y.D. Yin, *Surface patterning and its application in wetting/dewetting studies.* Current Opinion in Colloid & Interface Science, 2001. **6**(1): p. 54-64.

69.   Losey, M.W., M.A. Schmidt, and K.F. Jensen, *Microfabricated multiphase packed-bed reactors: Characterization of mass transfer and reactions.* Industrial & Engineering Chemistry Research, 2001. **40**(12): p. 2555-2562.

70.   Moritz, T., et al., *Modular Micro Reaction System Including Ceramic Components.* International Journal of Applied Ceramic Technology, 2005. **2**(6): p. 521-528.

71.   Richardson, J.T., D. Remue, and J.K. Hung, *Properties of ceramic foam catalyst supports: mass and heat transfer.* Applied Catalysis a-General, 2003. **250**: p. 319-329.

72.   Kiwi-Minsker, L., et al., *Supported glass fibers catalysts for novel multi-phase reactor design.* Chemical Engineering Science, 1999. **54**: p. 4785-4790.

73.   Yuranov, I., L. Kiwi-Minsker, and A. Renken, *Structured combustion catalysts based on sintered metal fibre filters.* Applied Catalysis b-Environmental, 2003. **43**: p. 217-227.

74.   Nassar, R., et al., *Modeling of cyclohexene hydrogenation and dehydrogenation reactions in a continuous-flow microreactor.* Catalysis Today, 2007. **120**(1): p. 121-124.

75.   Besser, R.S., X. Ouyang, and H. Surangalikar, *Hydrocarbon hydrogenation and dehydrogenation reactions in microfabricated catalytic reactors.* Chemical Engineering Science, 2003. **58**(1): p. 19-26.

76.   Abdallah, R., et al., *Gas-liquid and gas-liquid-solid catalysis in a mesh microreactor.* Chemical Communications, 2004(4): p. 372-373.

77.   Rebrov, E.V., et al., *Gold supported on mesoporous titania thin films for application in microstructured reactors in low-temperature water-gas shift reaction.* Catalysis Today, 2008. **138**(3-4): p. 210-215.

78.   Rebrov, E.V., et al., *Thin catalytic coatings on microreactor walls A way to make industrial processes more efficient.* Chimica Oggi-Chemistry Today, 2009. **27**(4): p. 4-7.

79.   Haeberle, S. and R. Zengerle, *Microfluidic platforms for lab-on-a-chip applications.* Lab on a Chip, 2007. **7**(9): p. 1094-1110.

80.   Gunther, A. and K.F. Jensen, *Multiphase microfluidics: from flow characteristics to chemical and materials synthesis.* Lab on a Chip, 2006. **6**(12): p. 1487-1503.

81.   Trapp, O., et al., *High-throughput screening of catalysts by combining reaction and analysis.* Angewandte Chemie-International Edition, 2007. **46**(38): p. 7307-7310.

82.   Rebrov, E.V., et al., *Selective Hydrogenation of 2-Methyl-3-butyne-2-ol in a Wall-Coated Capillary Microreactor with a Pd(25)Zn(75)/TiO(2) Catalyst.* Organic Process Research & Development, 2009. **13**(5): p. 991-998.

83.   Kataoka, S., et al., *Microreactor containing platinum nanoparticles for nitrobenzene hydrogenation.* Applied Catalysis A: General, 2012. **427-428**: p. 119-124.

84.   de Loos, S.R.A., et al., *Heterogeneous catalysis in a microchannel using a layer of carbon nanofibers on the channel wall.* Chemical Engineering Journal, 2012. **179**: p. 242-252.

CHAPTER 2

RATIONAL DESIGN OF COLLOIDAL NOBLE METALLIC NANOPARTICLES FOR

CATALYTIC APPLICATIONS: SYNTHESIS AND CHARACTERIZATION

2.1 Abstract

We report on the synthesis of colloidal noble metallic NPs by thermal decomposition and polyol reduction, and their characterization by various techniques. In the first protocol, zero-charge metal precursors were decomposed by heating in the presence of stabilizing ligands to form thio-ether stabilized NPs. In the second protocol, a mixture of metal precursors and the polymeric capping agent PVP was reduced by 1,4-butanediol to form hydrophilic PVP-stabilized NPs. The as-synthesized sub-10 nm NPs were uniform in morphology and stable, as confirmed by HRTEM characterization. The composition of the NPs was confirmed by EDS, and the fraction of metal precursors converted to NPs was measured by ICP-AES. The thermal decomposition protocol allowed flexible functionalization of particle surfaces. However, the yield was relatively low and the reaction conditions were harsh and time-consuming. By contrast, polyol reduction achieved a high yield of NPs under milder reaction conditions, and in a shorter reaction time.

2.2 Introduction

Heterogeneous catalysis is the key to the development of commodity and fine chemicals, and drugs from biorenewable raw materials [1, 2]. Precise control of metal dispersion and distribution of active sites on catalyst surfaces is highly desirable in catalytic applications. The knowledge obtained from a well-defined catalyst system is critical to the molecular understanding of catalysis and rational catalyst design for reactions of industrial significance [3]. Ideal heterogeneous catalyst systems should meet the four criteria of green chemistry, which are efficiency, stability, sustainability and recyclability (ESSR) [4].

The use of transition-metal colloidal NPs in catalysis has enabled superior efficiency in terms of activity, selectivity and stability in heterogeneous catalytic systems that operate under green chemistry principles [2, 5, 6]. Compared to their bulk counterparts, transition metal NPs have much higher surface-area-to-volume ratios, and a much larger fraction of their catalytically active sites on the particle surfaces [5-7]. This is especially important because it ensures the optimal use of noble metals with low total reserves on earth. In addition, the drastic changes in electronic properties resulting from atomic confinement in NPs affects the binding energy of reactive intermediates to catalyst surfaces and thus determines the catalytic routes in the reactions [8]. The better atom economy and unique electronic properties of metal NPs have enabled numerous examples of efficient catalytic applications with high selectivity and high conversion rates under mild reaction conditions [3, 4, 9-11]. The stability of metal NPs is crucial for many industrial applications because industrial catalysis demands catalyst robustness under a wide range of reaction conditions. By carefully selecting stabilizers and solvents, one can tune the interaction between stabilizer functional groups and metal surfaces, thus preventing aggregation of NPs and consequent loss of activity. In addition, colloidal metal NPs can be

immobilized on various solid supports to allow catalyst recyclability and easy separation from reaction products. The surface chemistry of the metal NPs can be finely adjusted to enable particle isolation, re-dispersion and reuse.

Transition-metal colloidal NPs are clusters containing from a few tens to several thousand metal atoms, stabilized by ligands, surfactants, or polymers to prevent particle agglomeration in aqueous or organic media [11]. Noble metals (Pd, Pt and Ru) are typical catalysts with excellent hydrogenation ability. Recent advances in colloid chemistry have established a number of solution-based synthesis protocols for noble metallic and bimetallic NPs, and enabled a level of control over particle morphology and composition which was almost impossible to achieve with classical heterogeneous catalyst preparation methods [4, 5, 12-15]. The control over the size, shape, composition and crystal structures of metal NPs is of fundamental significance for structure-sensitive catalytic reactions, and enables the correlation between material properties and catalytic performance [7, 16-19] .

In this chapter, we focused on the strategic synthesis of colloidal noble metallic NPs. We adapted and compared two common methods, thermal decomposition and polyol reduction. The goals of this chapter were to optimize the synthesis procedures, and to understand how the reaction parameters can be adjusted to better control particle morphology and composition for enhanced catalytic applications.

2.3 Materials and characterization techniques

2.3.1 Materials

D-biotin (99%), *n*-dodecyl sulfide (93%), toluene (anhydrous, 99.8%), methanol (reagent grade, 99.9%), isopropanol (HPLC grade, 99.9%), APTMS, PVP (MW: 55K), *n*DS and acetone (ACS reagent, ≥99.5%) were purchased from Sigma-Aldrich (St.Louis, MO). Palladium acetate

$[Pd_3(OAc)_6]$ (99+%), ruthenium acetylacetonate $[Ru(acac)_3]$ (99%) and platinum

acetylacetonate $[Pt(acac)_2]$(98%) were purchased from Strem Chemicals (Newburyport, MA).

Phenyl ether (99%) and 1,4-butanediol (99%) were purchased from Alfa Aesar (Ward Hill, MA).

High purity argon gas (99.99%) was purchased from Airgas (Lansing, MI). All chemicals were

used without further purification. Copper grids with 3-nm carbon film coating for TEM analysis

were purchased from Ted Pella, Inc. (Redding, CA).

2.3.2 HRTEM, STEM and EDS characterization

One drop of each colloidal nanoparticle solution (1 µL) was drop-cast on a 3-nm carbon film

coated copper grid. The grids were first dried in vacuum desiccators at room temperature

overnight and then at $80^{\circ}C$ for about 12 h before being placed in the sample holder of a JEOL

2200FS TEM (Tokyo, Japan). HRTEM images were acquired with a field emission gun operated

at 200 kV. The microscope was fitted with an ultra-high-resolution (UHR) pole piece with a

point resolution of 0.19 nm and high angle dark field STEM resolution of 0.13 nm. The images

were collected with a Gatan Multiscan camera at a resolution of 1024×1024. The average

particle size was determined by measuring the diameters of at least 100 randomly selected

images of particles and calculating the mass average diameter. The composition of NPs were

determined by EDS (Oxford Instrument, UK) equipped with the TEM instrument. Elemental

point analysis, line scan, and mapping under STEM mode were conducted for both dark field and

bright field images.

2.3.3 ICP-AES measurements

The metal content of each sample was determined by ICP-AES (Vista Pro, Varian, Cary,

NC) analysis. For each characterization, 0.5 mL of the colloid was transferred into a screw–

capped centrifuge tube and the solvent was removed by vaporization. Then 2.0 mL of aqua regia (a mixture of 1 volume of HNO_3 and 3 volumes of HCl) was added to the tube. [Caution: we should note that aqua regia is extremely corrosive, and requires appropriate protective gear.] The mixture was heated to 80°C and maintained at this temperature for 3 h, followed by centrifugation (4000 RPM, 6 min) to remove trace insoluble materials. The supernatant obtained was diluted with DI water and analyzed by ICP-AES. Each element was calibrated with standard solutions at various salt concentrations (0.08, 0.4, 2, 10 and 50 ppm) to construct a calibration curve. The calibration curves were then used to calculate the concentration of each sample, using the average of two instrument measurements. The yield of the synthesis procedure (fraction of the metal precursor in the NPs) was calculated from the ICP-AES results.

2.3.4 XRD

XRD data were collected on a Scintag XDS Model 2000 diffractometer (Scintag, Inc., Sunnyvale, CA). For XRD measurements, the NP sample was dried, mixed with 325 mesh Si powder, and placed on a Si wafer sample holder.

2.4 Synthesis and characterization of Pd, Pt and Ru NPs by thermal decomposition

2.4.1 Rationale

The synthesis of platinum group metal NPs (Pd, Pt and Ru) has received great attention because of their superior catalytic efficiency in hydrogenation and carbon-carbon coupling reactions [4, 20-24]. Among these, protocols for the synthesis of monodisperse Ru NPs are the least developed, because it is a major challenge to prepare uniform and monodisperse transition metal nanocrystals in the 1 to 10 nm diameter range. Thus, the development and adaptation of reliable and reproducible liquid-phase synthesis methods for well-defined Pd, Pt and Ru NPs is of great importance.

The thermal decomposition of zero-valent metal precursors in the presence of stabilizing ligands has been shown to be effective for formation of noble metallic NPs with uniform morphology [25-27]. One can adjust decomposition temperatures, reaction time, solvents, types of metal precursors and stabilizers, and stabilizer to metal precursor ratios to control the size and shape of the NPs [25-27]. The symmetric structure of nDS makes it a good candidate for use as a stabilizing ligand, because the sulfur atom in the molecule coordinates well with metal surface atoms, while the 12-carbon chain prevents aggregation of the NPs through steric interactions. D-biotin is similarly suitable for particle stabilization because its soft donor sulfur atom coordinates well with metal surfaces while the long carbon chain guards against aggregation of the NPs,. In addition, the carboxylic acid functional groups in D-biotin allows further surface modification of the metal NPs. APTMS, whose primary amino groups can coordinate with metal surface atoms , also provides the necessary steric hindrance with its three-carbon chain to prevent particle aggregation [28] . Sometimes, metal NPs need to be re-dispersed in a different solvent after synthesis to enable catalytic activity, and this can be achieved by exchange of stabilizing ligands [28]. In this study, we first used Pd NPs to explore the effects of different types of ligands on particle morphology, and to find an optimal ligand. We then used the thermal decomposition protocol with the optimal ligands to synthesize uniform Pt and Ru NPs under 5 nm.

2.4.2 Synthesis of biotinylated Pd NPs

To synthesize biotinylated Pd NPs, palladium acetate (0.03 g, 0.0445 mmol) and D-biotin (0.1089 g, 0.445 mmol) were dissolved in 80 mL of methanol, and placed in a 150 mL round bottom flask. The resulting yellow solution was degassed, heated to 70°C and held at this temperature for 24 h in a nitrogen-saturated atmosphere. The color of the solution turned from

27

yellow to dark brown after 24 h of heating, indicating the formation of Pd NPs. The solvent was removed under vacuum, and the resulting residue was washed twice with acetone (25 mL) and then centrifuged. The purified biotinylated Pd NPs were re-dispersed in methanol [29].

To synthesize *n*DS-stabilized Pd NPs, palladium acetate (0.20 g, 0.30 mmol) and *n*DS (1.12 g, 3.0 mmol) were added to 50 mL of toluene[30]. The mixture was degassed for 15 min, heated to 95°C and held at that temperature for 3 h under an argon atmosphere. The color of the solution turned from orange to black. The solvent was removed under vacuum, and the resulting residue was washed twice with ethanol (25 mL) and then dissolved in toluene. APTMS-stabilized Pd NPs were synthesized by adding APTMS (0.52 mL, 3 mmol) to the *n*DS-Pd NP solution, and stirring the mixture for 24 h to complete the ligand exchange process [29, 31].

To synthesize *n*DS-stabilized Pt NPs, platinum acetylacetonate (0.12 g, 0.30 mmol) and *n*-dodecyl sulfide (0.56 g, 1.5 mmol) were added to 50 mL of phenyl ether. The mixture was degassed for 15 min at 50$^{\mathbf{o}}$C, heated to 180$^{\mathbf{o}}$C, and held at this temperature for 1 h under an argon atmosphere. The solvent was removed under vacuum, and the resulting residue was washed twice with acetone and re-dissolved in toluene.

To synthesize *n*DS-stabilized Ru NPs, ruthenium acetylacetonate (0.031 g, 0.0782 mmol) and *n*DS (0.2922 g, 0.782 mmol) were added to 50 mL of toluene. The mixture was gently heated at 50$^{\mathbf{o}}$C to ensure complete dissolution of the metal precursor, followed by 15 min of degassing. It was then heated to 110$^{\mathbf{o}}$C under an argon atmosphere, and held at this temperature for 24 h with continued stirring. The solvent was removed under vacuum, and the resulting residue was washed twice with acetone and re-dispersed in toluene. Table 2.1 gives a summary

of the synthesis parameters, and Figure 2.1 shows a cartoon of a typical experimental set-up for

NP synthesis.

Table 2.1. Experimental parameters for synthesis of noble metallic NPs by thermal decomposition.

NPs	Stabilizing ligand	Precursor	Ratio of ligand to precursor	T($^\circ$C)	Time(h)	Solvent
Pd	nDS	$Pd_3(OAc)_6$	10:1	95	3	Toluene
Pt	nDS	$Pt(acac)_2$	5:1	180	1	Phenol ether
Ru	nDS	$Ru(acac)_3$	10:1	110	24	Toluene
Pd	D-biotin	$Pd_3(OAc)_6$	10:1	70	24	Methanol
Pd	APTMS	$Pd_3(OAc)_6$	10:1	25	24	Methanol
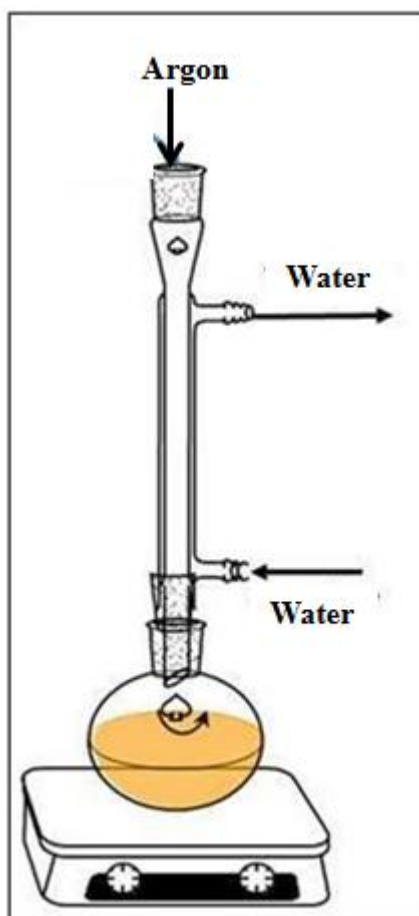
Figure 2.1. Experimental set-up for synthesis of NPs. The round bottom Schlenk flask is cooled by running water to induce reflux, and heated under a nitrogen or argon atmosphere. The flask is

Figure 2.1 (cont'd)
heated in an oil bath whose temperature is monitored by a thermometer, under continuous magnetic stirring. For interpretation of the references to color in this and all other figures, the reader is referred to the electronic version of this dissertation.

2.4.3 Characterization results and discussion

2.4.3.1 ICP-AES measurements

ICP-AES results show that approximately 30% of the metal precursors were converted to NPs by the end of the reaction, indicating inefficient use of costly chemicals. Sulfur was also detected because it is part of the stabilizing ligand. Since sulfur has been known to poison catalysts [32], this suggests that removal of the ligand would be necessary for successful catalytic applications.

2.4.3.2 HRTEM and EDS characterization of biotinylated and APTMS-stabilized Pd NPs

The synthesis of biotinylated Pd NPs has not been reported previously. We have shown that thio-ethers are excellent ligands to stabilize Pd NPs and control their size and uniformity [30]. Since biotin also contains a thio-ether moiety, it also serves as a potential stabilizing ligand for Pd NPs. Figures 2.2(a) and (b) show the HRTEM images at different magnifications of biotinylated Pd NPs obtained directly from the reaction flask without a size selection process. One can observe the crystal structures of Pd NPs at the higher magnifications (see red arrow in Figure 2.2b). The histogram in Figure 2.2(c) shows that the particles have a narrow size distribution and an average particle diameter of 3.3 ± 0.5 nm. The EDS spectrum confirms that the sample contains Pd (Figure 2.2d).

The nDS-Pd NPs were synthesized using a procedure similar to what was used for biotinylated Pd NPs. Due to the ease of solubility of nDS in toluene, toluene was used as the solvent in this procedure instead of methanol. Also, because of the higher boiling point of

toluene relative to methanol, the reaction was carried out at $95^{o}C$, and thus required a shorter reaction time relative to the biotin-stabilized procedure described earlier. The particles obtained from the reaction were 3.2 ± 0.6 nm in diameter, with a relatively narrow size distribution (Figure 2.3(a)).

The nDS-stabilized Pd NPs were mixed with APTMS to allow partial functionalization of the amino groups on the Pd NP surfaces. A small degree of aggregation was detected after the Pd NPs were functionalized with APTMS (Figure 2.3 (b)). The electron diffraction image of the biotin- and APTMS-stabilized Pd NPs each exhibit three diffuse rings which can be assigned to the (111), (200) and(220) reflections of a face-centered cubic (fcc) Pd crystal facets (Figure 2.4).

All three stabilizing ligands are shown to facilitate the formation of monodisperse and uniform Pd NPs under 5 nm. The end functional groups of the stabilizing ligands enable further modification of the particle surfaces. Of the three, nDS-stabilized Pd NPs have the best stability (no obvious agglomeration after six months). Also, the synthesis procedure using nDS was the least time-consuming. Thus, nDS was chosen as the optimal stabilizing ligand for Pd NPs, and this method was used for the synthesis of Pt and Ru NPs.
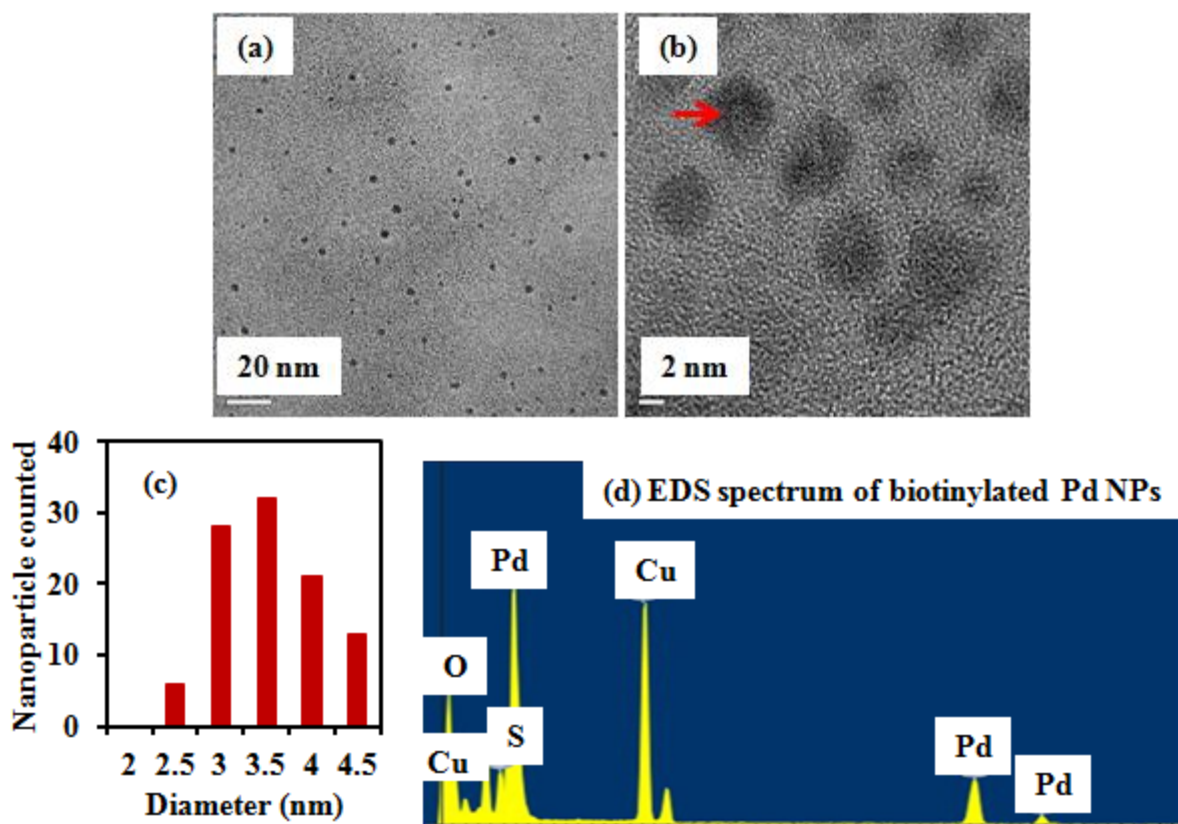
Figure 2.2. HRTEM images of biotinylated Pd NPs at a magnification of (a) 100 K (scale bar = 20 nm) and (b) 600 K (scale bar = 2 nm); (c) histogram of biotinylated Pd NPs, showing an average particle size of 3.3 ± 0.5 nm; (d) EDS spectrum of biotinylated Pd NPs.
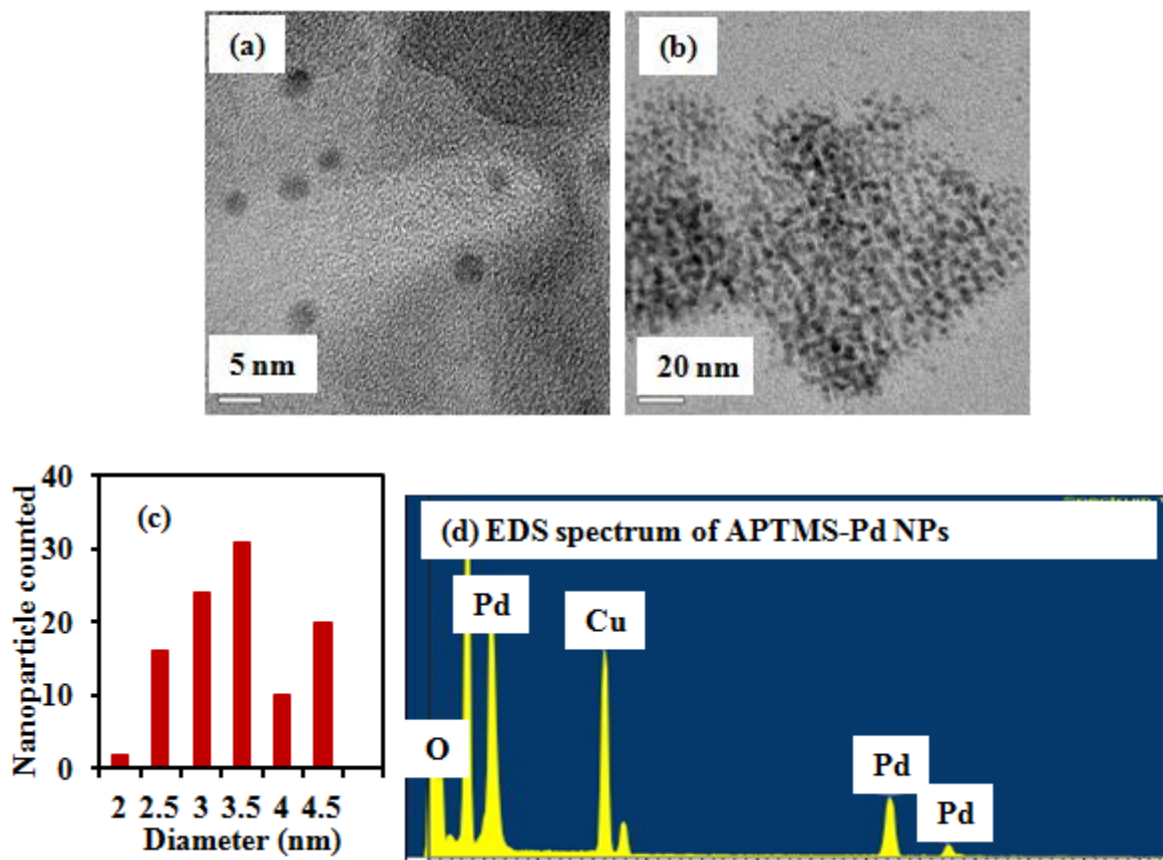
Figure 2.3. (a) HRTEM image of APTMS-Pd NPs at a magnification of (a) 400 K (scale bar = 5 nm) and (b) 100 K (scale bar = 20 nm); (c) histogram of APTMS-Pd NPs, showing an average particle size of 3.2 ± 0.6 nm; (d) EDS spectrum of APTMS-Pd NPs.
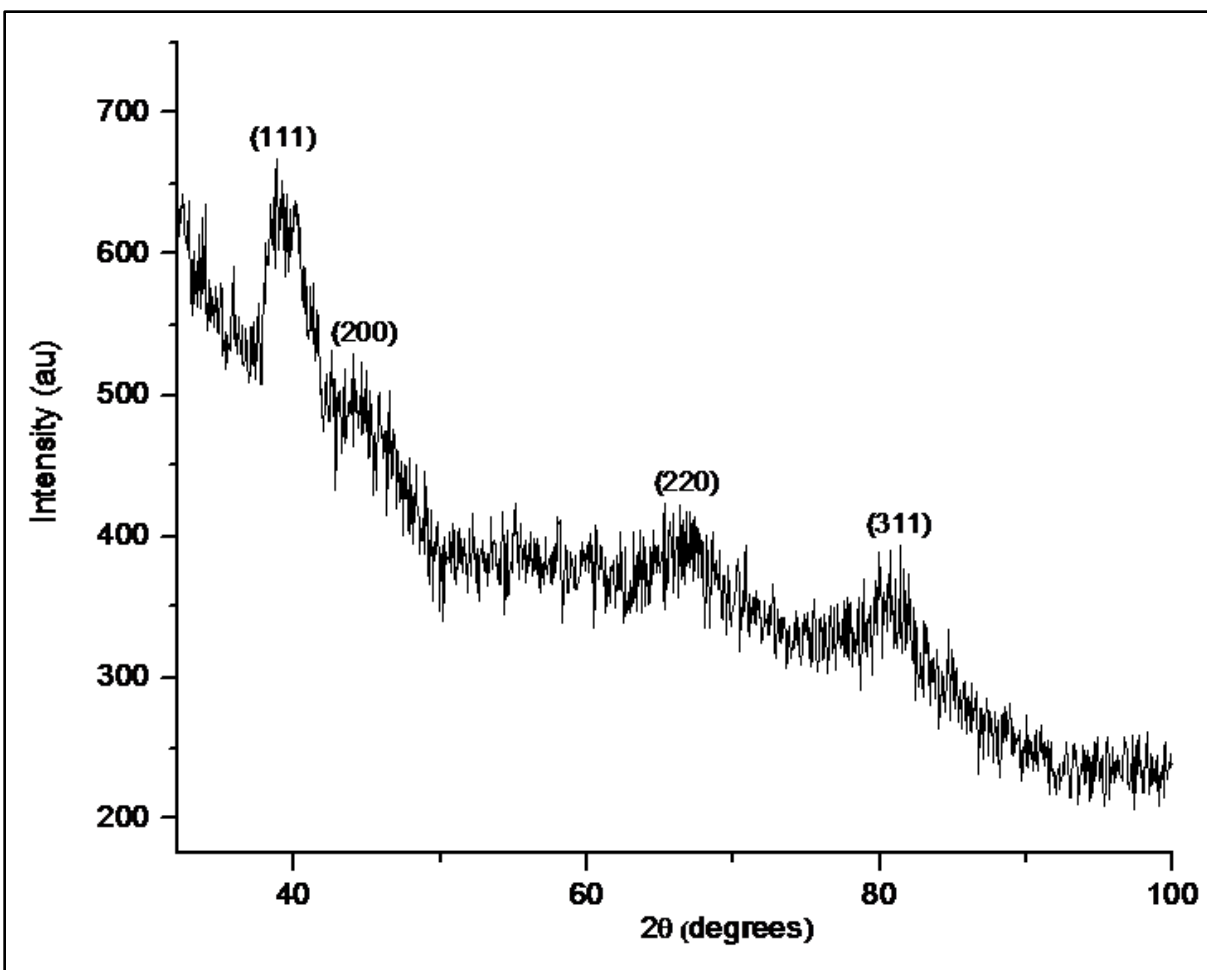
Figure 2.4. Powder XRD pattern of Pd NPs, with three diffuse rings assigned to the (111), (200) and (220) facets, respectively.

2.4.3.3 Synthesis of Pt and Ru NPs stabilized by *n*DS

The ligand *n*DS is effective in stabilizing Pd, Pt and Ru NPs during synthesis, leading to particles with uniform morphology and narrow size distribution. Toluene was the most appropriate solvent for synthesis of Pd and Ru NPs, due to the high solubility of *n*DS in toluene. However, Pt precursors have a much higher decomposition temperature than those of Pd and Ru precursors. Thus, phenyl ether was chosen as the solvent for synthesis of Pt because of its higher boiling point (259°C vs. 111°C for toluene). This temperature caused the oil bath to boil, so we switched to a sand bath. Both Pd and Pt NPs were obtained within 5 h of reaction. By contrast, the Ru precursor did not fully decompose until 24 h after the reaction was initiated, demonstrating the difficulty of synthesizing Ru NPs. HRTEM images show that the *n*DS-stabilized NPs are stable, uniform and monodisperse (Figure 2.5 (a)-(f)).The inner-lattice distance for *n*DS-Ru NPs is 2.1 Å, in agreement with other reports in the literature [33, 34]. The average diameter of the spherical Pd, Pt and Ru nanoparticles were 3.0 ± 0.3 nm, 3.3 ± 0.7 nm and 3.5± 0.4 nm, respectively. EDS spectra confirm the existence of Pd, Pt, Ru and S elements in the NPs (Figures 2.5(g)-(i)).
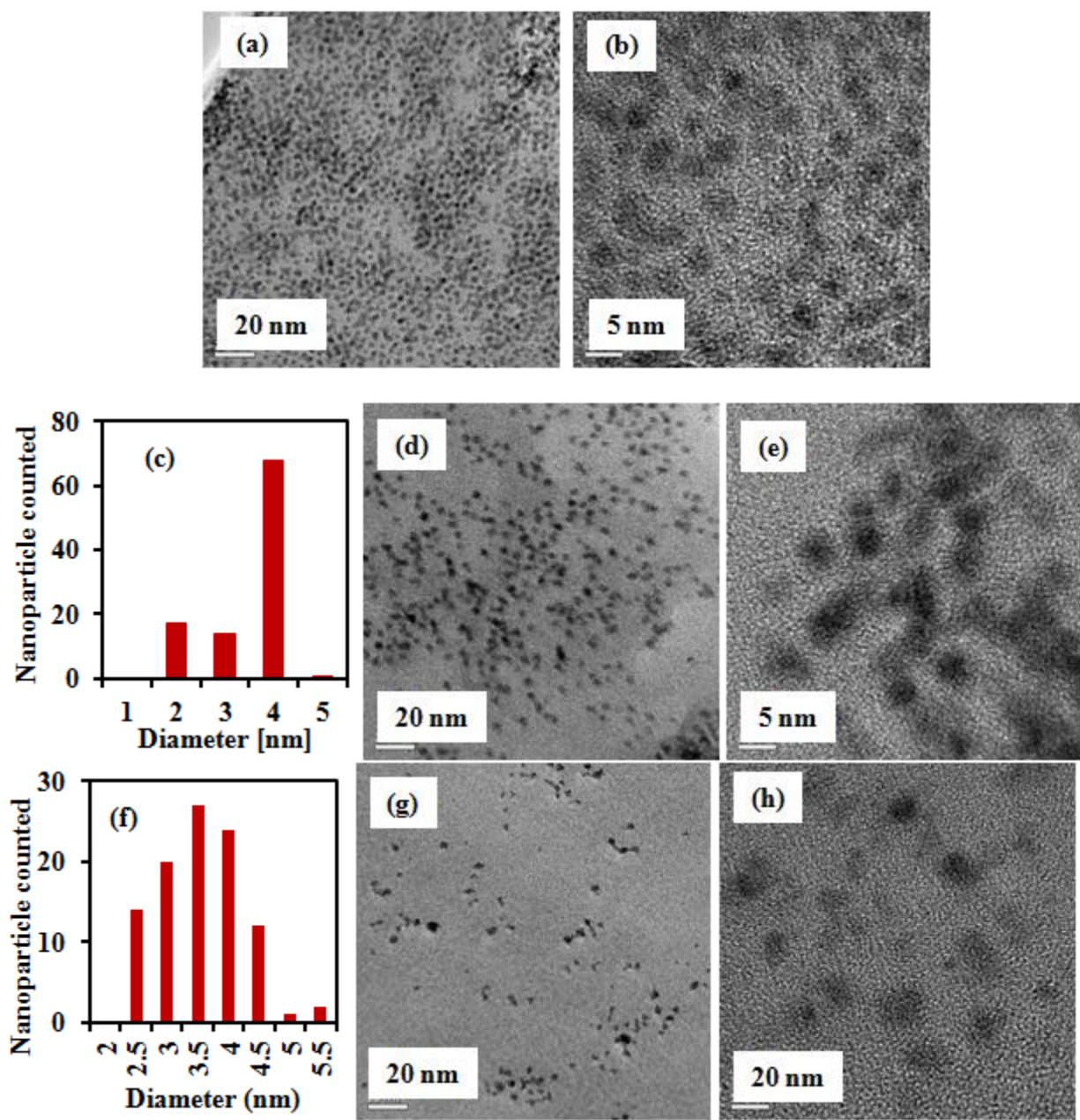
Figure 2.5. (a and b) HRTEM images of *n*DS-Pd NPs at magnifications of 100 K and 400 K (scale bars of 20 nm and 5 nm, respectively); (c) histogram of *n*DS-Pd NPs, showing an average particle size of 3.0 ± 0.3 nm; (d and e) HRTEM images of *n*DS-Pt NPs at magnifications of 100 K and 400 K (scale bars of 20 nm and 5 nm, respectively); (f) histogram of *n*DS-Pt NPs, showing an average particle size of 3.3 ± 0.7 nm; (g and h) HRTEM images of *n*DS-Ru NPs at magnifications of 100 K and 400 K (scales bars of 20 nm and 5 nm, respectively); (i) histogram of *n*DS-Ru NPs, showing an average particle size of 3.5 ± 0.4 nm; (j-l) EDS spectra of *n*DS-Pd, *n*DS-Pt and *n*DS-Ru NPs, showing characteristic elements of Pd, Pt, Ru and S, respectively.

Figure 2.5 (cont'd)
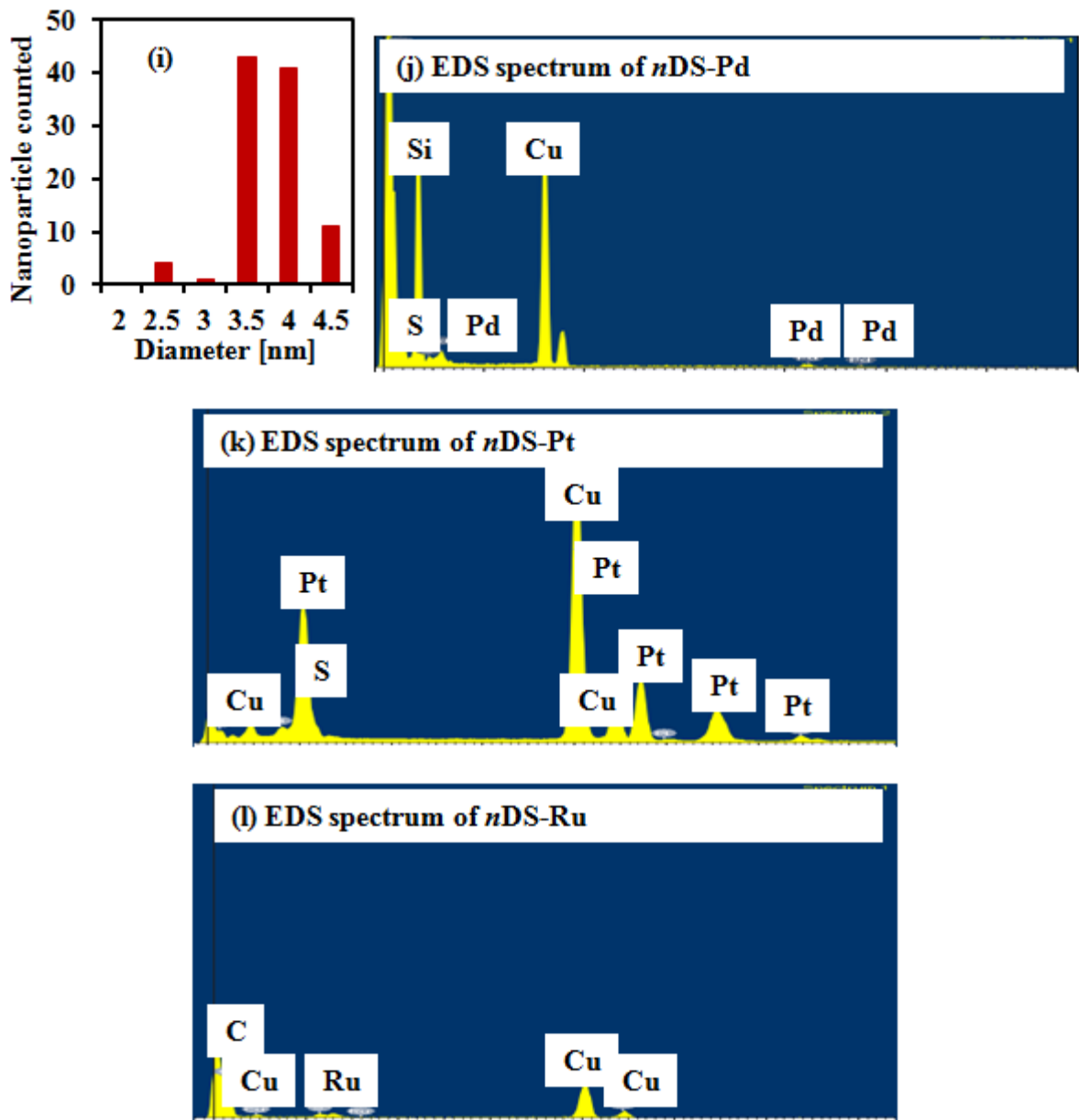
2.5 Synthesis and characterization of Pd and Ru NPs stabilized by PVP

2.5.1 Rationale

Thermal decomposition has been used to successfully synthesize uniform and stable noble

metal NPs in organic media [28]. However, this method can be improved in terms of metal

precursor yield. It is also desirable to synthesize transition metal NPs under milder reaction

conditions, and in more environmentally-friendly media. Polyol reduction, using water-soluble linear polymers such as PVP, has proven to be an effective method to synthesize size- and shape-tunable Pd, Pt and Ru NPs soluble in the aqueous phase [4, 23, 35, 36]. Reduction temperature, reducing agents, precursor types, ratio of stabilizing agent to precursor, and type of stabilizing agent are all important and adjustable parameters that can be used to control the morphology and structure of the metallic NPs. Previous examples include synthesis of PVP-stabilized Pd nanospheres, Pt nanocubes, and Pd and Pt nanowires and nanorods [4, 33, 37-42]. Metallic NPs with different morphologies and crystal structures have been used in structure-sensitive catalytic reactions such as hydrogenation of multiple carbon-carbon double bonds and Heck reactions to control reaction selectivity and product distribution [43-47].

Typically, PVP serves as a protective agent surrounding metal NPs to prevent particle aggregation. The carbonyl groups of the PVP molecule coordinate to the surface metal atoms. Part of the main PVP chain is also physically adsorbed on the metal surface. Modification of the functional groups enables catalyst immobilization and promotion of the catalytic activity of the metallic NPs [36]. It is necessary to activate the particle surface by removing the PVP stabilizers to expose the surface active sites. In this section, we have adapted polyol reduction protocols to synthesize PVP-stabilized Pd and Ru NPs with controlled size and shape.

2.5.2 Synthesis

PVP-stabilized Pd NPs were synthesized by a polyol reduction method based on a published protocol [21]. In a typical synthesis, 0.0603 g of palladium acetate and 0.222 g of PVP were dissolved in 10 mL of 1,4- butanediol in a 50 mL round bottom Schlenk flask. The mixture was heated from room temperature to 90°C under magnetic stirring to completely dissolve the salt, followed by 15 min of evacuation and introduction of argon into the system. The temperature

38

was then raised to 120°C, and maintained for 3 h. After 2 h, 0.1 mL of the reaction mixture was withdrawn periodically using a long needle syringe and mixed with 1.25 mL of acetone in a centrifuge tube. After centrifugation for 5 min, the color of the supernatant was used to determine the degree of completion of the reaction. The supernatant became colorless after 3 h of reaction, an indication that the reaction was complete. The Pd NPs were then washed with acetone and re-dispersed in 20 mL of methanol.

The PVP-stabilized Ru NPs were synthesized by a polyol reduction method based on previous reports [4, 23, 33, 40, 42, 48, 49]. In a typical synthesis, 0.079 g ruthenium acetylacetonate and 0.222 g PVP were dissolved in 20 mL of 1,4-butanediol in a 50 mL round bottom Schlenk flask. The solution was heated from room temperature to 130°C under magnetic stirring, and the excess air was removed at this temperature after 10 min of evacuation. Argon was then introduced, and the solution was heated to 180°C and maintained at that temperature for 1.5 h. After the mixture was cooled down to room temperature, acetone was poured into the solution to form a cloudy black suspension. This suspension was centrifuged at 5000 RPM for 6 min. The precipitated Ru NPs were collected, washed once with acetone, and re-dispersed in 20 mL of methanol.

2.5.3 Characterization of catalytic NPs

2.5.3.1 ICP-AES results

ICP-AES analysis shows that about 90% of the metal precursors were converted to NPs during the reaction, indicating a much more efficient usage of the costly starting materials, in comparison to the thermal decomposition method.

2.5.3.2 HRTEM and EDS characterization results and discussion

The HRTEM images (Figures 2.6 (a)-(d)) show that the as-synthesized PVP Ru NPs were mostly spherical, uniform in size, and monodisperse, with an average particle diameter of 3.5 ± 0.5 nm. The inner-lattice distance is about 2.1 Å, but part of the crystal lattice could not be observed in the HRTEM images because the PVP stabilizer surrounds the particles. This observation suggests a need to remove the stabilizer prior to using the NPs to conduct hydrogenation reactions. The atoms in the Ru nanospheres are hexagonal-closed-packed (*hcp*), and contain mostly (101) crystal facets on the surfaces.

PVP-stabilized Pd NPs have the shapes of nanospheres and nanotetrahedrons, with an average particle size of 14.1 ± 2.7 nm (Figures 2.7 (a)-(c)). The atoms in the Pd nanospheres and nanotetrahedrons show face-centered cubical (*fcc*) crystal structures with their surfaces bound by a mix of (111) and (100) facets. The good dispersion of PVP-stabilized Pd and Ru NPs demonstrates that the bulky PVP molecules surrounding the metal center atoms provide an effective steric barrier to close contact among the metal particles [37, 38].
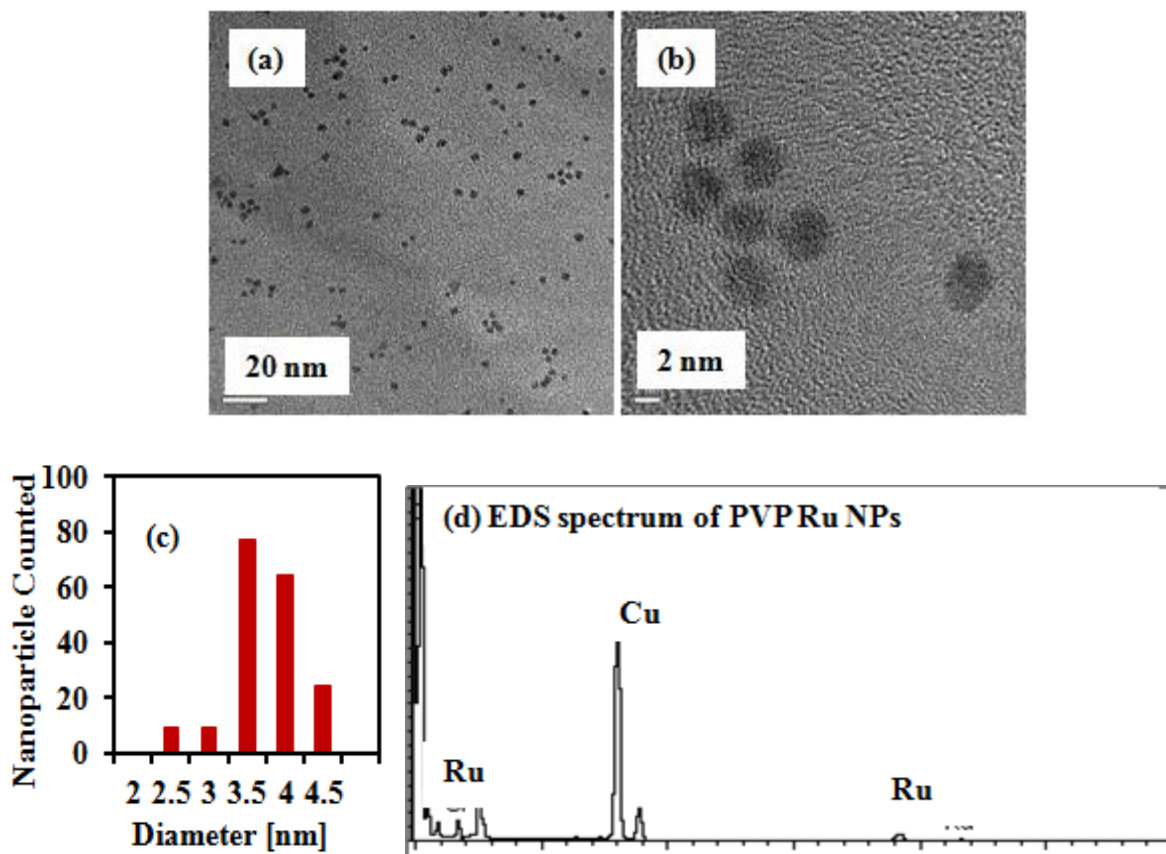
Figure 2.6. (a) and (b) HRTEM images of PVP-Ru NPs at magnifications of 100K and 600K, respectively (scale bars of 20 nm and 2 nm); (c) histogram of PVP-Ru NPs, showing an average size of 3.5 ± 0.5 nm; (d) EDS spectrum of PVP-Ru NPs, confirming the existence of Ru.
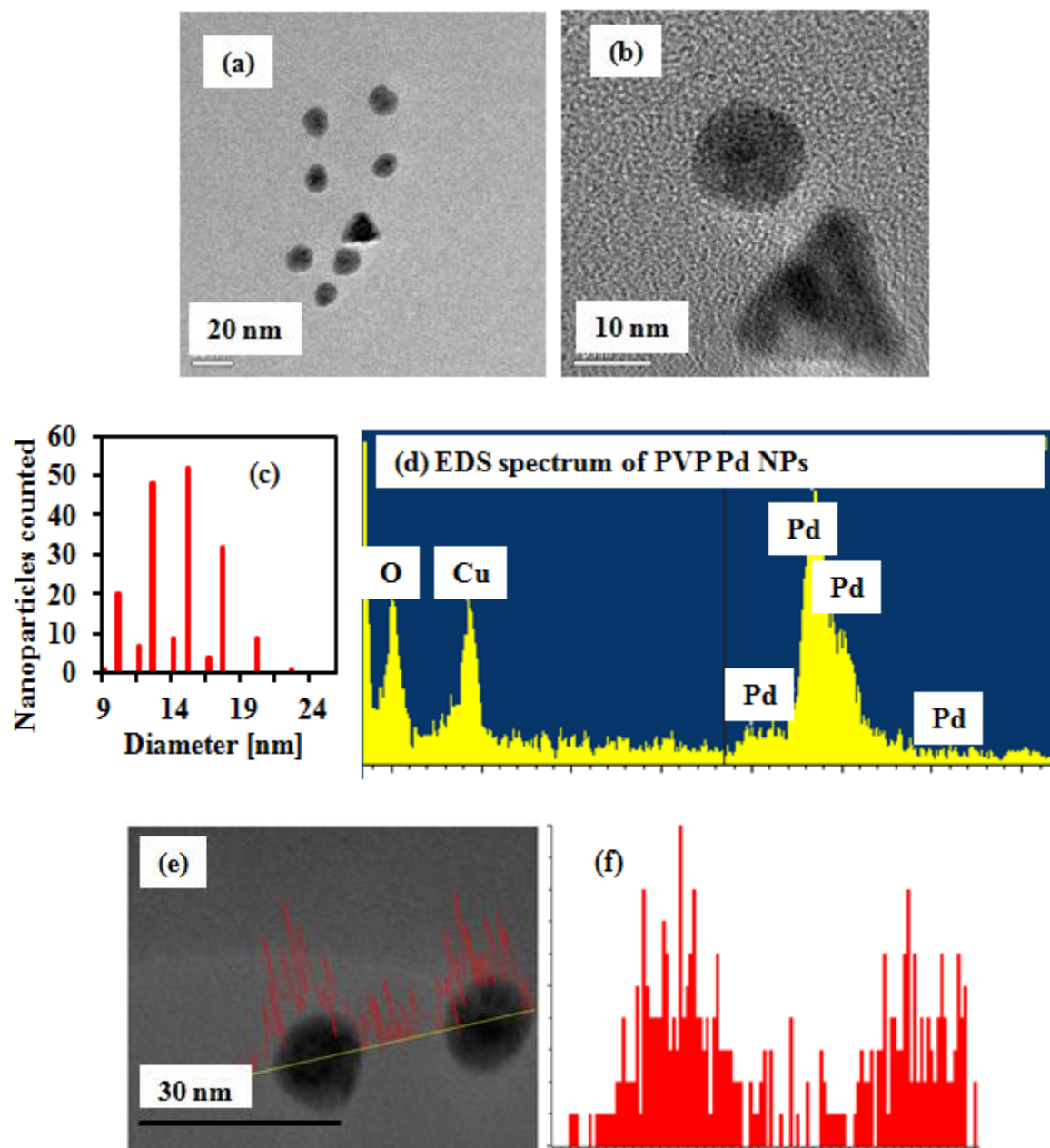
Figure 2.7. (a) and (b) HRTEM images of PVP-Pd at a magnification of 100K and 200K (scale bars of 20 nm and 10 nm, respectively); (c) histogram of PVP-Pd, showing an average particle size of 14.1 ± 2.7 nm; (d) EDS spectrum of PVP-Pd confirming Pd content; (e) STEM image at a magnification of 3.0 M, coupled with an elemental line scan (scale bar 30 nm); (f) Pd elemental line scan, with the x-axis representing the line distance drawn in the STEM image, and the y-axis representing the detection signal strength.

2.6 Characterization results of size-tunable Ru and bimetallic NPs stabilized by PVP

    Xianfeng Ma, a member of our group, has modified an existing protocol [48, 50, 51]to develop polyol reduction protocols to prepare size-tunable Ru NPs over a broad range of sizes (3.5 -120.0 nm) and Pd-Ru bimetallic NPs with various fractions of the two metals [52]. Reduction temperature, precursor type, PVP molecular weight, metal salt to stabilizer ratio, among other parameters, were systematically adjusted to control the morphology and composition of the NPs. By varying the molar ratios of Ru(II) and Ru(III) precursors, the size and size distribution of the PVP-stabilized NPs could be controlled. The molar ratios of the Pd and Ru precursors also allowed the control of the morphology of the bimetallic NPs. In this work, two samples of Ru NPs with different diameters (labeled as Ru2 and Ru3, prepared at different molar ratios of the two Ru precursors) and one sample of bimetallic NPs (labeled PdRu, Pd:Ru molar ratio = 1:1) were chosen to study the effects of size and composition in the microfluidic reactors (see Chapter 4). To aid the interpretation of the microreactor results, the characterization results for morphology and composition of these samples are presented in this section, even though the syntheses were not part of this work.

    Ru2 NPs show a wide distribution of particle sizes (Figure 2.8 (a), (c)), with a bimodal distribution of sizes in the 25-30 nm and 85-90 nm ranges. The particle surface is rough, with needle-like shapes at the edge (Figure 2.8 (b)), indicating the need for surface activation to expose the nanocrystals for catalyst applications. EDS spectrum confirmed the existence of Ru in the particles. Ru3 NPs also have a rough surface, with a much larger diameter than Ru2 and most of the particle sizes falling in the range of 120 to 170 nm (Figure 2.9 (a) –(c)). Elemental line scan coupled with STEM confirmed that the particles are Ru (Figure 2.9 (d)-(e)).

Pd-Ru bimetallic NPs show a similar morphology to pure Pd NPs, with an average size of 14.2 ± 2.9 nm (Figure 2.10), and lattice fringes clearly observable in the images. EDS line scan, mapping and point analysis spectra confirmed the homogeneous distribution of both Pd and Ru elements, confirming the bimetallic alloy structure (Figure 2.11). The alloy structures observed are similar to those of Pt-Ru bimetallic alloy NPs reported in the literature [20]. More advanced characterization techniques such as XANES can be used to observe the localized distribution of both elements for future studies. However, our current characterization techniques are sufficient to provide strong evidence that the Pd-Ru NPs are alloys rather than core-shell or heterogeneous structures.
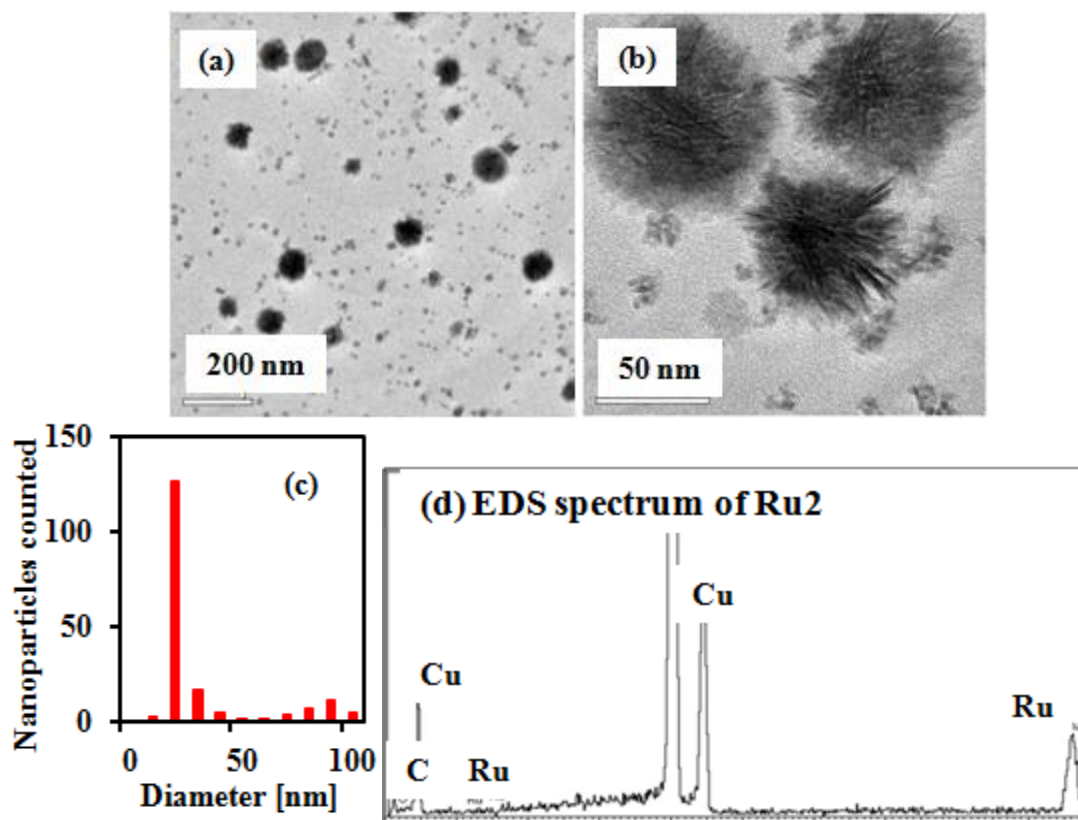
Figure 2.8. HRTEM images of Ru2 NPs (a) at a magnification of 15 K (scale bar of 200 nm) and (b) at a magnification of 100 K (scale bar of 50 nm); (c) histogram of Ru2 with an average particle size of 27 ± 24 nm, showing a bimodal distribution (with one centered at 25 nm, the other at 95 nm); (d) EDS spectrum of Ru2, confirming the existence of Ru element in the particles.
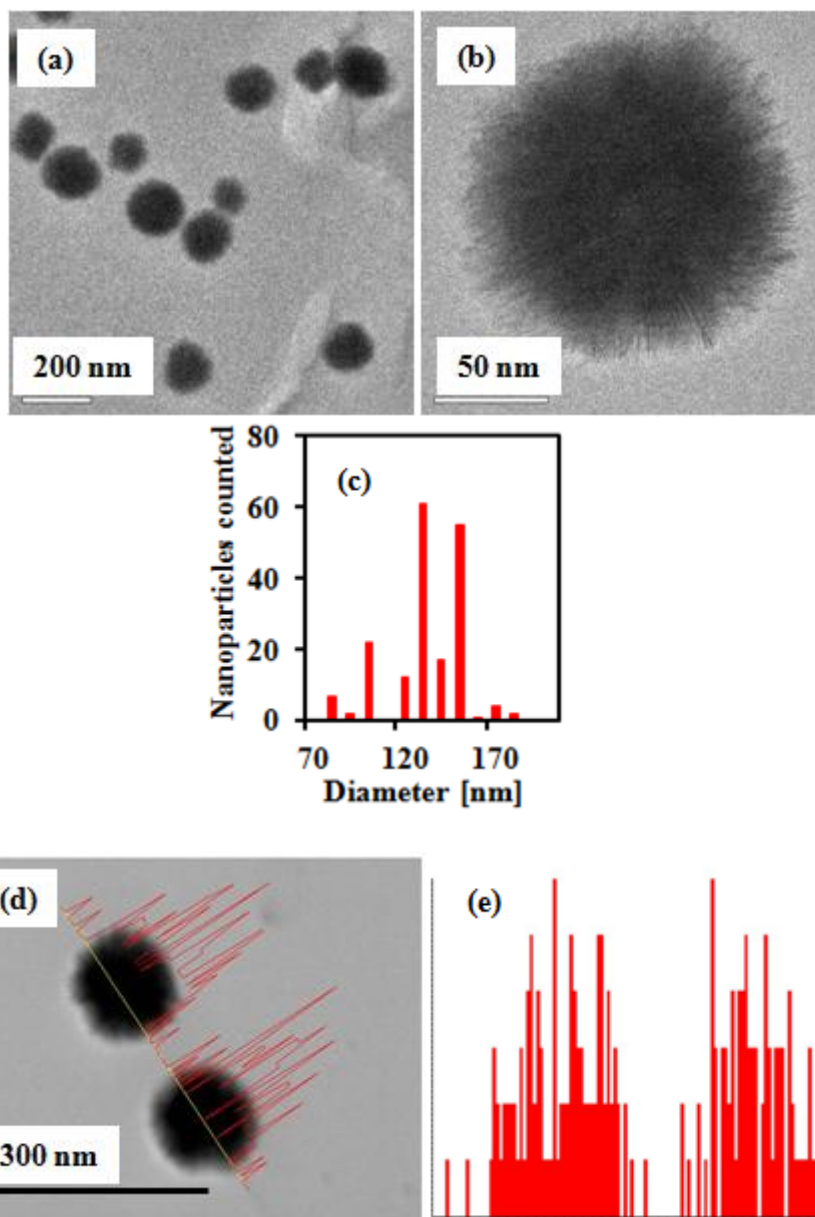
Figure 2.9. HRTEM images of Ru3 (a) at a magnification of 15 K (scale bar of 200 nm) and (b) at a magnification of 100 K (scale bar of 50 nm); (c) histogram of Ru3, showing an average particle size of 129 ± 21 nm; (d) STEM image with line scan profile of Ru3 at a magnification of 30 K (scale bar of 300 nm); (e) elemental line scan spectrum of Ru3, with the x-axis representing the line distance drawn in the STEM image, and the y-axis representing the detection signal strength.
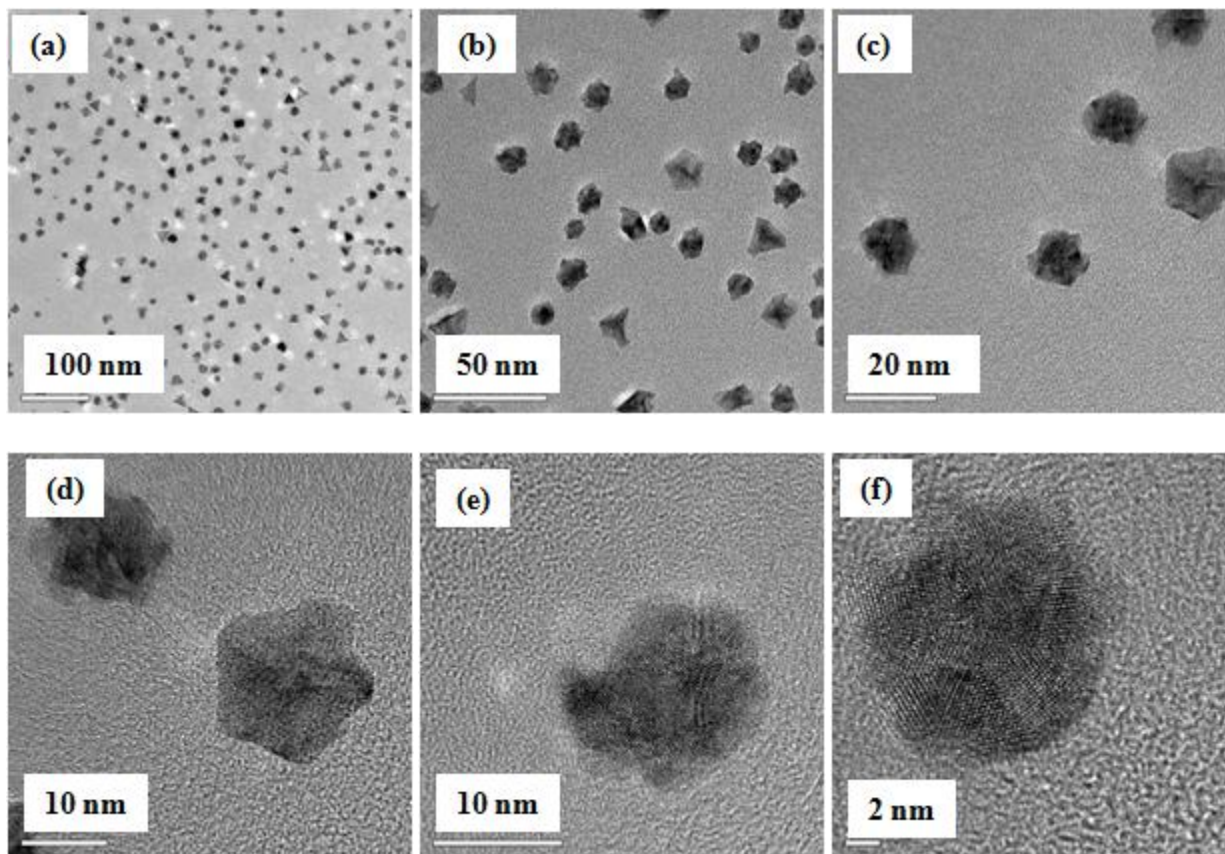
Figure 2.10. HRTEM images of Pd-Ru bimetallic NPs at different magnifications: (a) 30 K (scale bar of 100 nm); (b) 100 K (scale bar of 50 nm; (c) 200 K(scale bar of 20 nm); (d) 400 K (scale bar of 10 nm); (e) 600 K (scale bar of 10 nm); and (f) – (h) 800 K (scale bar of 2 nm); the particles are spherical, tetrahedron and pentahedron; (i) histogram of Pd-Ru NPs, with an average particle size of 14.2 ± 2.9 nm.

Figure 2.10 (cont'd)
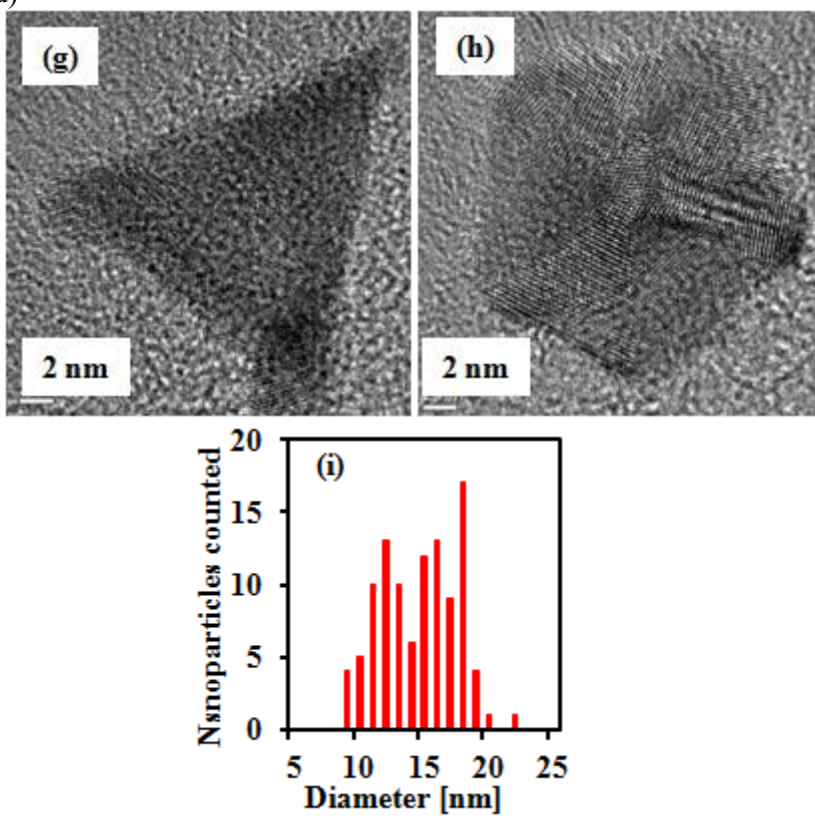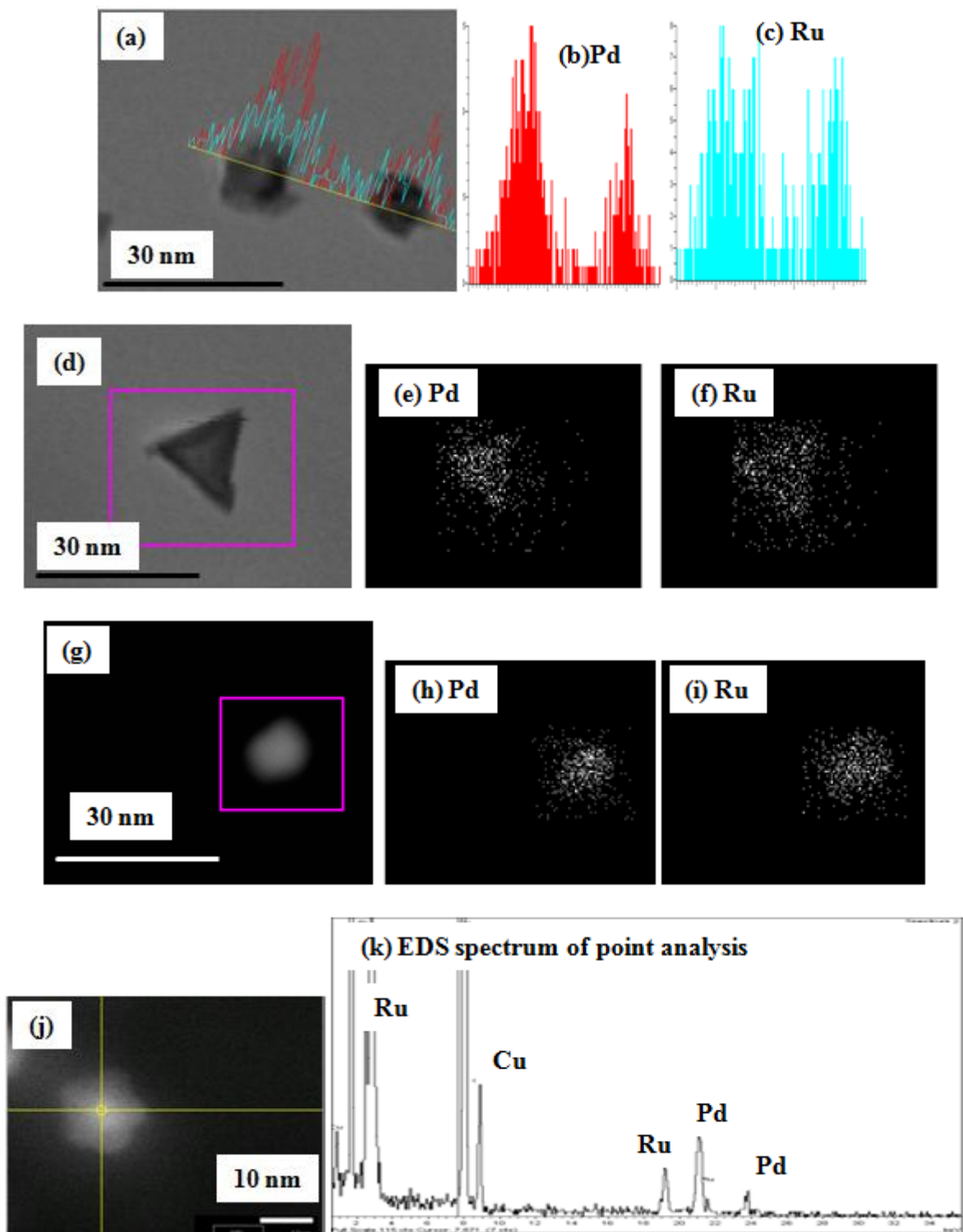
Figure 2.11. STEM images coupled with EDS analysis for Pd-Ru NPs: (a) STEM image at a magnification of 3.0M (scale bar of 30 nm); (b) and (c) elemental line scan spectra of Pd and Ru, where the x-axis represents the length of the yellow line in image (a) and y-axis represents the

Figure 2.11 (cont'd)
elemental signal strength at different locations along the line; (d) STEM image at a magnification
of 3.0 M (scale bar of 30 nm); (e) and (f) elemental mapping of Pd and Ru, respectively, for the
tetrahedron particle in image (d); (g) dark field STEM image at a magnification of 3.0 M (scale
bar of 30 nm); (h) and (i) elemental mapping of Pd and Ru, respectively, for the spherical
particle in image (g); (j) dark field STEM image at a magnification of 3.0 M (scale bar of 10
nm); (k) EDS spectrum of point analysis for image (j), showing characteristic peaks of both Pd
and Ru.

2.7 Summary

In this chapter, noble metallic NPs (Pd, Pt and Ru) were successfully synthesized by thermal

decomposition, using effective stabilizing ligands such as thio-ethers. The as-synthesized sub-10

nm NPs had controlled morphology, uniformity and single crystallinity. In addition, the

functional groups on the ligand enabled further modification of particle surfaces. However, the

metal NPs stabilized by thio-ethers were only soluble in organic solvents due to the hydrophobic

nature of the ligand, and the yield was relatively low. Polyol reduction was used to synthesize

water-soluble Pd and Ru NPs stabilized by the linear polymer PVP. The yield of NPs improved

by a factor of three, allowing more efficient use of the expensive metal precursors. The NPs

stabilized by PVP demonstrated controlled morphology and monodispersity.

The characterization results for selected samples of size-tunable PVP-stabilized Ru NPs

demonstrated that the type of metal precursor has the greatest influence on particle morphology.

The PVP stabilized Pd-Ru (at a one to one molar ratio) bimetallic NPs had similar morphology to

pure Pd NPs. Both elements were homogeneously distributed throughout the particles to form

bimetallic alloy structures.

By using a colloid chemistry approach and advanced electron microscopic techniques,

syntheses and characterization of well-controlled noble metallic NPs were achieved. This work

has laid a foundation for future research in heterogeneous catalysis, in terms of catalyst

immobilization and catalyst assessment. The ability to correlate catalytic properties to characteristic material properties of well-defined metal NPs is an important strength. The knowledge obtained has the potential to further the fundamental understanding of heterogeneous catalysis at the molecular level, and to advance the rational design of catalysts for practical applications.

REFERENCES

REFERENCES

1. Alonso, D.M., J.Q. Bond, and J.A. Dumesic, *Catalytic conversion of biomass to biofuels.* Green Chemistry, 2010. **12**(9): p. 1493-1513.

2. Gabriele Centi, R.A.v.S., *Catalysis for Renewables: From Feedstock to Energy Production.* Wiley-VCH, 2007.

3. Raimondi, F., et al., *Nanoparticles in energy technology: Examples from electrochemistry and catalysis.* Angewandte Chemie-International Edition, 2005. **44**(15): p. 2190-2209.

4. Tsung, C.-K., et al., *Sub-10 nm Platinum Nanocrystals with size and shape control: Catalytic study for ethylene and pyrrole hydrogenation.* Journal of the American Chemical Society, 2009. **131**: p. 5816-5822.

5. Zahmakiran, M. and S. Ozkar, *Metal nanoparticles in liquid phase catalysis; from recent advances to future goals.* Nanoscale, 2011. **3**(9): p. 3462-3481.

6. Semagina, N. and L. Kiwi-Minsker, *Recent Advances in the Liquid-Phase Synthesis of Metal Nanostructures with Controlled Shape and Size for Catalysis.* Catalysis Reviews-Science and Engineering, 2009. **51**(2): p. 147-217.

7. Zhou, X., et al., *Ru nanoparticles stabilized by poly(N-vinyl-2-pyrrolidone) grafted onto silica: Very active and stable catalysts for hydrogenation of aromatics.* Journal of Molecular Catalysis A: Chemical, 2009. **306**: p. 143-148.

8. Kalidindi, S.B. and B.R. Jagirdar, *Nanocatalysis and propects of green chemistry.* ChemSusChem, 2012. **5**: p. 65-75.

9. Bonnemann, H. and R.M. Richards, *Nanoscopic metal particles - Synthetic methods and potential applications.* European Journal of Inorganic Chemistry, 2001(10): p. 2455-2480.

10. Thomas, J.M., et al., *High-performance nanocatalysts for single-step hydrogenations.* Accounts of Chemical Research, 2003. **36**(1): p. 20-30.

11.   Pachón, L.D. and G. Rothenberg, *Transition-metal nanoparticles: synthesis, stability and the leaching issue.* Applied Organometallic Chemistry, 2008. **22**(6): p. 288-299.

12.   Jin, R., *The impacts of nanotechnology on catalysis by precious metal nanoparticles.* Nanotechnology Reviews, 2012. **1**(1): p. 31-56.

13.   Zhang, J., et al., *Synthesis of Metallic Nanoparticles Using Electrogenerated Reduced Forms of alpha-SiW(12)O(40) (4-) as Both Reductants and Stabilizing Agents.* Chemistry of Materials, 2011. **23**(21): p. 4688-4693.

14.   Yuan, X., et al., *Synthesis of Highly Fluorescent Metal (Ag, Au, Pt, and Cu) Nanoclusters by Electrostatically Induced Reversible Phase Transfer.* Acs Nano, 2011. **5**(11): p. 8800-8808.

15.   Wang, D.S. and Y.D. Li, *Bimetallic Nanocrystals: Liquid-Phase Synthesis and Catalytic Applications.* Advanced Materials, 2011. **23**(9): p. 1044-1060.

16.   Sonstrom, P. and M. Baumer, *Supported colloidal nanoparticles in heterogeneous gas phase catalysis: on the way to tailored catalysts.* Physical Chemistry Chemical Physics, 2011. **13**(43): p. 19270-19284.

17.   Bakker, J.J.W., et al., *Heterogeneously Catalyzed Continuous-Flow Hydrogenation Using Segmented Flow in Capillary Columns.* ChemCatChem, 2011. **3**(7): p. 1155-1157.

18.   Norskov, J.K., et al., *Density functional theory in surface chemistry and catalysis.* Proceedings of the National Academy of Sciences of the United States of America, 2011. **108**(3): p. 937-943.

19.   Somorjai, G.A., F. Tao, and J.Y. Park, *The nanoscience revolution: Merging of colloid science, catalysis and nanoelectronics.* Topics in Catalysis, 2008. **47**(1-2): p. 1-14.

20.   Wang, D.S., P. Zhao, and Y.D. Li, *General preparation for Pt-based alloy nanoporous nanoparticles as potential nanocatalysts.* Scientific Reports, 2011. **1**.

21.   Fang, M., N. Machalaba, and R.A. Sanchez-Delgado, *Hydrogenation of arenes and N-heteroaromatic compounds over ruthenium nanoparticles on poly(4-vinylpyridine): a versatile catalyst operating by a substrate-dependent dual site mechanism.* Dalton Transactions, 2011. **40**(40): p. 10621-10632.

22.   Albiter, M.A., R. Morales, and F. Zaera, *Dendrimer-based synthesis of Pt catalysts for hydrocarbon conversion.* Applied Catalysis a-General, 2011. **391**(1-2): p. 386-393.

23.   Sang, H.J., et al., *Size effect of Ruthenium nanoparticles in catalytic carbon monoxide oxidation.* Nano Letters, 2010. **10**: p. 2709-2713.

24.   Luque, R. and J.H. Clark, *Water-tolerant Ru-Starbon (R) materials for the hydrogenation of organic acids in aqueous ethanol.* Catalysis Communications, 2010. **11**(10): p. 928-931.

25.   Pelzert, K., et al., *New Ru nanoparticles stabilized by organosilane fragments.* Chemistry of Materials, 2004. **16**(24): p. 4937-4941.

26.   Pelzer, K., et al., *Organometallic synthesis of size-controlled polycrystalline ruthenium nanoparticles in the presence of alcohols.* Advanced Functional Materials, 2003. **13**(2): p. 118-126.

27.   Jansat, S., et al., *Synthesis, characterization and catalytic reactivity of ruthenium nanoparticles stabilized by chiral N-donor ligands.* New Journal of Chemistry, 2006. **30**(1): p. 115-122.

28.   Freemantle, R.G., *Synthesis and characterization of monodisperse metallic nanoparticles and their catalytic activity*. 2009, Western Michigan University: Kalamazoo. p. 196.

29.   Lin, R., et al., *In-situ immobilization of palladium nanoparticles in microfluidic reactors and assessment of their catalytic reactivity.* 2010.

30.   Ganesan, M., R.G. Freemantle, and S.O. Obare, *Monodisperse thioether-stabilized palladium nanoparticles: Synthesis, characterization, and reactivity.* Chemistry of Materials, 2007. **19**(14): p. 3464-3471.

31.   Lin, R., et al., *Facile hydrogenation of carbon-carbon double bonds using catalytic noble nanoparticles immobilized in microfluidic reactors.* Catalysis Communications, 2012. **18**: p. 168-175.

32.   Besson, M. and P. Gallezot, *Deactivation of metal catalysts in liquid phase organic reactions.* Catalysis Today, 2003. **81**: p. 547-559.

33.	Brayner, R., G. Viau, and F. Bozon-Verduraz, *Liquid-phase hydrogenation of hexadienes on metallic colloidal nanoparticles immobilized on support via coordination capture by bifunctional organic molecules.* Journal of Molecular Catalysis A: Chemical, 2002. **182-183**: p. 227-238.

34.	Brink, M.V., et al., *Alkylamine stabilized ruthenium nanocrystals: Faceting and branching.* Journal of Physical Chemistry C, 2008. **112**(32): p. 12122-12126.

35.	Zawadzki, M. and J. Okal, *Synthesis and structure characterization of Ru nanoparticles stabilized by PVP or gamma-Al2O3.* Materials Research Bulletin, 2008. **43**(11): p. 3111-3121.

36.	Kataoka, S., et al., *Characterization of mesoporous catalyst supports on microreactor walls.* Applied Catalysis a-General, 2008. **342**(1-2): p. 107-112.

37.	Borodko, Y., et al., *Probing the interaction of poly(vinylpyrrolidone) with platinum nanocrystals by UV-Raman and FTIR.* Journal of Physical Chemistry B, 2006. **110**(46): p. 23052-23059.

38.	Borodko, Y., et al., *Spectroscopic Study of the Thermal Degradation of PVP-Capped Rh and Pt Nanoparticles in H(2) and O(2) Environments.* Journal of Physical Chemistry C, 2010. **114**(2): p. 1117-1126.

39.	Castellana, E.T., et al., *Direct writing of metal nanoparticle films inside sealed microfluidic channels.* Analytical Chemistry, 2006. **78**(1): p. 107-112.

40.	Jurgens, B., et al., *Colloidally Prepared Nanoparticles for the Synthesis of Structurally Well-Defined and Highly Active Heterogeneous Catalysts.* Angewandte Chemie-International Edition, 2008. **47**(46): p. 8946-8949.

41.	Shekhar, M., et al., *Counting Au Catalytic Sites for the Water-Gas Shift Reaction.* Journal of Catalysis, 2012. **293**: p. 94-102.

42.	Su, F.B., et al., *Thermally reduced ruthenium nanoparticles as a highly active heterogeneous catalyst for hydrogenation of monoaromatics.* Journal of the American Chemical Society, 2007. **129**(46): p. 14213-14223.

43.	Christopher, P. and S. Linic, *Shape- and Size-Specific Chemistry of Ag Nanostructures in Catalytic Ethylene Epoxidation.* Chemcatchem, 2010. **2**(1): p. 78-83.

44.   He, B.L., et al., *Synthesis of solvent-stabilized colloidal nanoparticles of platinum, rhodium, and ruthenium by microwave-polyol process.* Journal of Nanoscience and Nanotechnology, 2005. **5**(2): p. 266-270.

45.   Jun, Y.W., et al., *Symmetry-controlled colloidal nanocrystals: Nonhydrolytic chemical synthesis and shape determining parameters.* Journal of Physical Chemistry B, 2005. **109**(31): p. 14795-14806.

46.   Katarzyna Morawa Eblagon, T.V.-S., K.M. Kerry Yu, Anibal J. Ramirez-Cuesta, Shik Chi Tsang, *Size-controlled preparation of ruthenium nanoparticles using polyaromatic amine-containing compounds as hydrogenation nanocatalyst precursors.* International Journal of Nanoparticles, 2010. **3**(2): p. 104-122.

47.   Pan, C., et al., *A new synthetic method toward bimetallic ruthenium platinum nanoparticles; composition induced structural changes.* Journal of Physical Chemistry B, 1999. **103**(46): p. 10098-10101.

48.   Zhang, Y.W., et al., *One-step polyol synthesis and langmuir-blodgett monolayer formation of size-tunable monodisperse rhodium nanocrystals with catalytically active (111) surface structures.* Journal of Physical Chemistry C, 2007. **111**(33): p. 12243-12253.

49.   Joo, S.H., et al., *Size Effect of Ruthenium Nanoparticles in Catalytic Carbon Monoxide Oxidation.* Nano Letters, 2010. **10**(7): p. 2709-2713.

50.   Chen, Y., K.Y. Liew, and J.L. Li, *Size-controlled synthesis of Ru nanoparticles by ethylene glycol reduction.* Materials Letters, 2008. **62**(6-7): p. 1018-1021.

51.   Somorjai, G.A., H. Frei, and J.Y. Park, *Advancing the Frontiers in Nanocatalysis, Biointerfaces, and Renewable Energy Conversion by Innovations of Surface Techniques.* Journal of the American Chemical Society, 2009. **131**(46): p. 16589-16605.

52.   Ma, X., *Ruthenium-based Model Catalysts for Liquid Phase Hydrogenation of Bio-derived Organic Acids and Aldehydes*, in *Department of Chemical Engineering & Materials Science*. 2013, Michigan State University: East Lansing.

CHAPTER 3 *IN-SITU* IMMOBILIZATION OF NOBLE METALLIC NANOPARTICLES IN

MICROFLUIDIC REACTORS AND ASSESSMENT OF THEIR CATALYTIC ACTIVITY[1]

3.1 Abstract

We report on the immobilization of Pd NPs in microfluidic reactors fabricated from PDMS (all acronyms and variables are defined at the beginning of this dissertation). The Pd NPs were stabilized with D-biotin or APTMS to promote immobilization on the walls of the microfluidic reactors. Biotinylated Pd NPs were immobilized on APTMS-modified PDMS and glass surfaces through formation of covalent amide bonds between activated biotin and surface amino groups. By contrast, APTMS-stabilized Pd NPs were immobilized directly onto PDMS and glass surfaces rich in hydroxyl groups. FT-IR and XPS results showed successful attachment of both types of Pd NPs on glass and PDMS.

After establishing the protocol, both types of Pd NPs were immobilized *in-situ* in sealed PDMS microfluidic reactors after similar surface modification. The effectiveness of immobilization in the microfluidic reactors was evaluated by hydrogenation of 6-bromo-1-hexene at room temperature and one atmosphere of hydrogen pressure. An average first-run conversion of 85% and selectivity of 100% were achieved in 2 min of residence time. Control experiments showed that no hydrogenation occurred in the absence of the nanocatalysts. We developed two methods to introduce catalysts into the system and assessed the effects of substrate concentration on reactant conversions. Intrinsic turnover frequencies were calculated and compared to the values obtained under similar reaction conditions in a batch reactor system. The immobilized Pd NPs proved to be robustly attached to the reactor surfaces, with no detectable leaching during the reactions.

Similarly, we immobilized *n*DS stabilized Pd, Pt and Ru NPs *in situ* in the APTMS-modified PDMS microfluidic reactors. XPS characterization confirmed successful immobilization of the NPs on reactor surfaces. ICP-AES data did not detect any leaching NPs in

the reactor within its detection limit (80 ppb). The system was used to measure the intrinsic catalytic activity and TOF of the three nanocatalysts. The TOF of reactions run with immobilized nanocatalysts in the microfluidic reactor were hundreds of times larger than what was measured in batch reactors under identical reaction conditions. Effects of substrate concentrations and liquid flow rates on conversions were investigated using the same model reaction (hydrogenation of 6-bromo-1-hexene). SEM characterization on the reactor surfaces revealed that particle aggregation may have played a major role in catalyst deactivation during catalyst recycling studies.

In summary, the combination of well-defined nanocatalysts and microfluidics significantly enhances hydrogen diffusion to catalytic sites, thus minimizing mass transfer limitations and enabling evaluation of the intrinsic catalytic activity. The system provides a convenient platform for high throughput screening of catalysts, and for conducting mechanistic studies of reaction kinetics.

3.2 Introduction

Tri-phasic hydrogenation with solid catalysts, molecular hydrogen, and liquid substrates plays an important role in many academic and industrial laboratories. However, mass transfer between the gas, liquid and solid phases can often be inefficient, making it difficult to get sufficient hydrogen to catalytic sites for the required reactions. As a result, tri-phasic hydrogenation is usually carried out under high temperature and high hydrogen pressure over long periods of time. Such harsh reaction conditions and long reaction times can lead to problems that include undesirable side reactions, lack of operational safety and high energy consumption [1, 2]. It can also hinder assessment of the intrinsic reaction kinetics. An effective solution to these problems is to combine catalytic NPs (which are well-characterized and provide significantly enhanced surface areas) with microfluidics (which reduces the diffusion length for hydrogen transport). The resulting improvement in multiphase mass transfer enables high yield and selectivity under mild reaction conditions, in an efficient and environmentally friendlier manner.

Noble metallic NPs under 10 nm in diameter have proven to be highly effective catalysts relative to their bulk counterparts, due to their high surface-area-to-volume ratios and atom economy [3-5]. An important requirement for any effective catalyst is to provide uniform catalytic sites, and the use of NPs that are uniform in morphology fulfills this important need. NPs with well-controlled particle sizes and narrow size distributions also have a high percentage of their catalytically active atoms on the surface, which greatly enhances reactivities. Stabilizing ligands are required to prevent particle agglomeration, to maintain catalytic activity. In the previous chapter, nDS, D-biotin and APTMS were shown to be effective stabilizing ligands for synthesizing uniform Pd, Pt and Ru NPs in the 2-5 nm size range [6].

Microfluidic reactors are devices that have a series of channels with at least one dimension in the sub millimeter range etched on a planar substrate made from metals, polymers or oxides, and other materials [7]. Their small dimensions and flow characteristics provide several advantages for chemical reactions. The most important is a high surface-area-to-volume ratio 10 to 500 times larger than that in conventional reactors [8-12]. In addition, microfluidic reactors allow flexible flow regimes, short diffusion distances, efficient heat and mass transfer, shorter reaction times, operational safety and ease of scale-up [8-12]. There has been increased use of microfluidic reactors over the last decade for catalyst assessment in multiphase reactions, because they provide a flexible platform for mechanistic studies of catalyst activity, while enabling precise control of fluid flow, fast delivery of reagents to catalyst sites, and economy of materials [1, 13, 14]. Once assembled, microfluidic reactors enable efficient probe of a number of parameters, including assessment of the effect of substrate concentration, catalyst loading, reaction temperature, and pressure on catalyst performance[1, 13, 14].

Microfluidic systems fabricated from PDMS have been used widely in biomedical research because of their biocompatibility, easy and inexpensive assembly, versatility of surface functionalization, and high hydrogen permeability compared to those constructed from silicon, glass or stainless steel. As a result of these attributes, they have been drawing increasing attention in synthetic chemistry and catalysis[15-23]. In spite of their low tolerance for temperature ($T_g \sim 125^{\circ}$C) and tendency to swell in non-polar organic solvents, PDMS microfluidic reactors provide excellent systems for hydrogenation in aqueous or polar organic media under mild reaction conditions[24].

Immobilization of catalysts in microfluidic reactors is necessary to facilitate catalyst recovery and recycling. Catalysts can be filled into microfluidic reactors to form micro packed-bed reactors [25]. To reduce randomness of catalyst packing and high pressure drops in micro packed-bed reactors, microfluidic reactors with catalytically active walls have been developed [13]. Catalysts can be anchored to the walls through physical, chemical or electrical interactions between the wall surface and particles. A metal catalyst can be incorporated into microfluidic reactors by sputter coating [22, 26, 27] or impregnation [28]. For example, Kobayashi and his group developed glass microfluidic reactors with immobilized Pd catalysts and conducted the reduction of double- and triple- bonds with complete conversion in minutes [29, 30]. Trapp and colleagues used a capillary reactor coated with a polymer film with embedded Pd NPs to efficiently screen a library of catalysts for hydrogenation of a list of ring compounds [31, 32].

We believe the integration of nano-scale metallic catalysts with microfluidic reactors provides an important tool for assessing chemical reactions and maintaining precise control of the reaction parameters. In this chapter, we demonstrate that metallic NPs can be successfully immobilized *in-situ* in sealed microfluidic reactors by covalently and robustly bonding them to glass and PDMS surfaces. To the best of our knowledge, this is the first example of *in-situ* immobilization of metallic NPs in a sealed microfluidic reactor. We used the hydrogenation of 6-bromo-1-hexene at room temperature and a hydrogen pressure of 1 atm as a model reaction to assess the catalytic microfluidic system. This reaction produces 1-bromohexane under mild reaction conditions, with the bromide atom not affected during the reaction. The reaction product is widely used in the manufacture of pharmaceuticals and organic chemicals. In addition, the concentrations of the reactant and product mixture can be readily determined by gas chromatography (GC), thus enabling quantitative analysis.

The objectives of this chapter were to: a) design and fabricate a PDMS microfluidic reactor for multiphase hydrogenation reactions, b) devise a protocol for *in-situ* immobilization of the NPs in pre-assembled sealed microfluidic reactors, c) assess the effectiveness of the immobilization scheme using a model reaction, d) measure the intrinsic TOF of the NPs, study effects of different reaction conditions on reactant conversions, and e) assess effectiveness of catalyst recycling and study the causes of catalyst deactivation.

3.3 Experimental

3.3.1 Materials

APTMS, NHS, EDC, 6-bromo-1-hexene (95%), n-heptane (≥99%, GC grade) and acetone (ACS reagent, ≥99.5%) were purchased from Sigma-Aldrich (St.Louis, MO). High purity hydrogen gas (99.99995%) was purchased from Airgas Great Lakes (Lansing, MI). All chemicals were used without further purification.

For fabrication of PDMS microfluidic reactors, Sylgard® 184 silicone elastomer curing agent was obtained from Dow Corning Corporation (Midland, MI). Silicon wafers with one side polished were purchased from Wafer World, Inc. (West Palm Beach, FL). Silicon wafers polished on one side and coated with a 500 Å aluminum layer were purchased from NOVA Wafers (Carrollton, TX). The SU-8 2000 series photoresist kit was obtained from MicroChem Corporation (Newton, MA).

3.3.2 Fabrication and characterization of PDMS microfluidic reactors

The fabrication of microfluidic channels in PDMS followed the widely used soft lithography method of Whitesides and coworkers [33, 34]. The detailed fabrication procedure is described below and shown in Figure 3.1. The channel pattern was designed by Adobe Illustrator and printed on a dark background high-resolution transparency (Infinity Graphics, Okemos, MI) on

which only the pattern is transparent (Figure 3.2). The Y-shaped inlets provide individual entries for reactants and hydrogen. The channel width and length are 500 µm and 30 cm, respectively. The height of the microfluidic channel was controlled by the type of photoresist used, spinning time, spinning speed and post-baking time.

In a typical fabrication, 4 mL of SU-8 2050 photoresist was deposited on a thoroughly-cleaned silicon wafer (diameter of 100 mm). The substrate was spun at 500 RPM for 10 s at an acceleration of 100 RPM/s, then at 1700 RPM for 30 s at an acceleration of 300 RPM/sec. The substrate with the thin layer of spin-coated photoresist was soft-baked on a hot plate at 65°C for 5 min, then at 95°C for 15 min. The spin-coated substrate was then covered by the transparency containing the designed pattern, and placed under high frequency UV light for 2 min, followed by post-baking on a hot plate at 65°C for 5 min, and at 95°C for 10 min. The pattern could be observed on the spin-coated substrate after post baking. The photoresist under the transparent pattern was hardened by UV light, while the photoresist beneath the dark background was washed away by a developer solution, leaving a positive pattern on the silicon wafer. The substrate with the pattern was finally rinsed with isopropanol and dried with nitrogen. A mixture of PDMS precursor and cross-linker (10:1 weight ratio) was poured onto the silicon wafer with the positive master in a clean petri dish, degassed for 30 min in a vacuum desiccator, and cured in an oven at 70°C for at least 2 h to form a PDMS block containing the negative pattern. The PDMS block was peeled off the silicon wafer and cleaned with scotch tape to make it dust free. A piece of microscope slide was carefully cleaned by sonication in isopropanol and dried with nitrogen. The PDMS blocks with the negative pattern on top and the glass slide were placed in a

plasma cleaner (Harric Plasma, Ithaca, NY) for 1.5 min of oxygen plasma treatment to create

hydroxyl groups on the surfaces. The PDMS block with the negative pattern and the glass slide

were brought into contact immediately after plasma treatment to create an irreversible bond for

the sealed microfluidic reactor.

For characterization of the as-prepared PDMS microfluidic channels, a piece of PDMS

block with negative pattern was carefully cut into smaller pieces and mounted top-wise and

cross-section-wise on a SEM sample holder. The samples were treated with osmium for 10 s to

make the surface conductive for analysis by scanning electron microscopy (SEM). All SEM

images were taken at an acceleration voltage of 15 kV and emission current of 20 µA, with a

working distance of 4.5 mm.
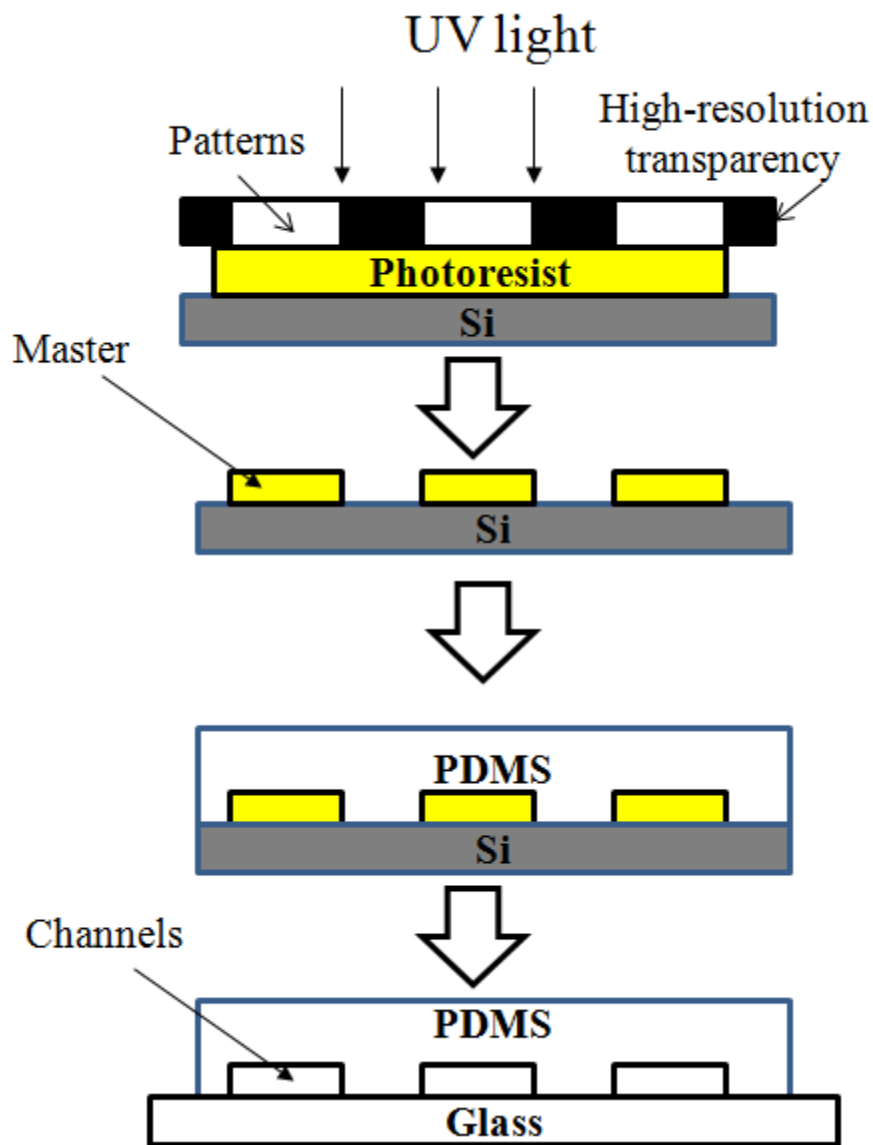
Figure 3.1. Schematics of PDMS microfluidic reactor fabrication using soft lithography. The procedure involves pattern transfer from a computer design to a silicon wafer, then to the PDMS block, followed by irreversible bonding of the PDMS block to a microscope slide to obtain a sealed microfluidic reactor.
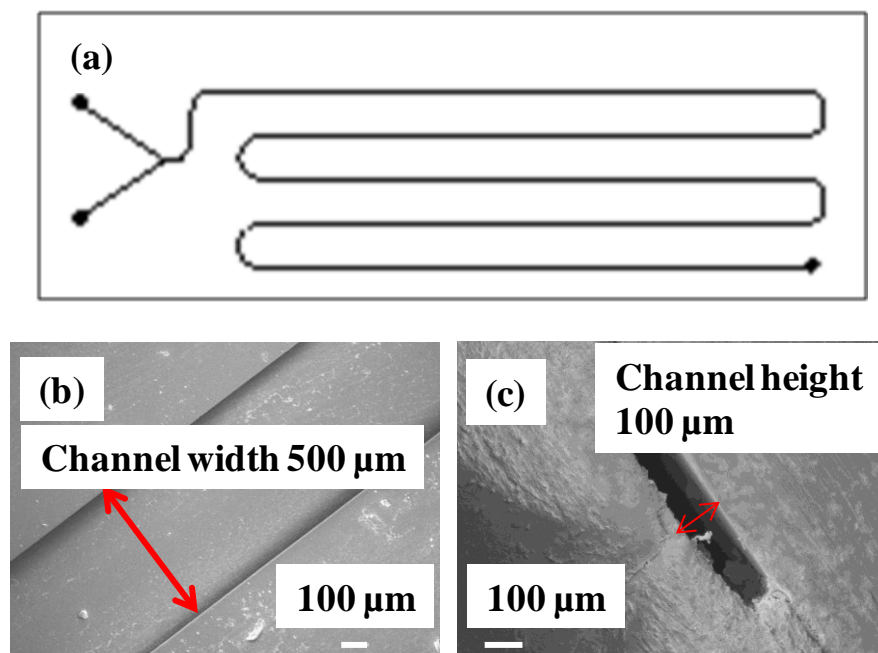
Figure 3.2. (a) Schematics of a serpentine microfluidic channel with a Y-shaped inlet to enable simultaneous influx of hydrogen and reactants through separate entrances. The reactor volume can be controlled by the number of loops that constitute the channel. (b) SEM image of the channel at a magnification of 85 (top view), showing a channel width of 500 μm. (c) SEM image of the channel (cross sectional view) at a magnification of 120, showing a channel height of 100 μm.

3.3.3 Substrate functionalization and immobilization of NPs

All the surface functionalization procedures were first carried out on a number of glass, PDMS and aluminum-coated substrates (1×1 cm). All substrates were thoroughly cleaned with isopropanol and deionized water and dried with nitrogen, followed by 10 min of oxygen plasma treatment to install hydroxyl groups. APTMS (2% in anhydrous methanol) was then deposited onto the hydroxyl-rich surfaces, and loose materials were washed away to achieve a robust film of primary amine groups. The aminosilanized surfaces were then cured at 60°C to induce further cross-linking [35]. To immobilize biotinylated Pd NPs, the aminosilanized substrates were immersed in a solution of biotinylated Pd NPs activated by NHS and EDC, allowing the

formation of covalent amide bonds between the carboxylic groups of the biotinylated Pd NPs and the amine groups on the surfaces [36, 37], as shown in Figure 3.3. APTMS-Pd NPs were immobilized by immersing the oxygen plasma-treated surfaces into APTMS-Pd solutions overnight, then curing at 60°C for 1 h. Immobilization of *nDS*-stabilized Pd, Pt and Ru NPs was achieved by sequential immersion of aminosilanized surfaces into Pd, Pt or Ru NPs solutions for several hours, followed by curing in an oven at 70°C (Figure 3.4).
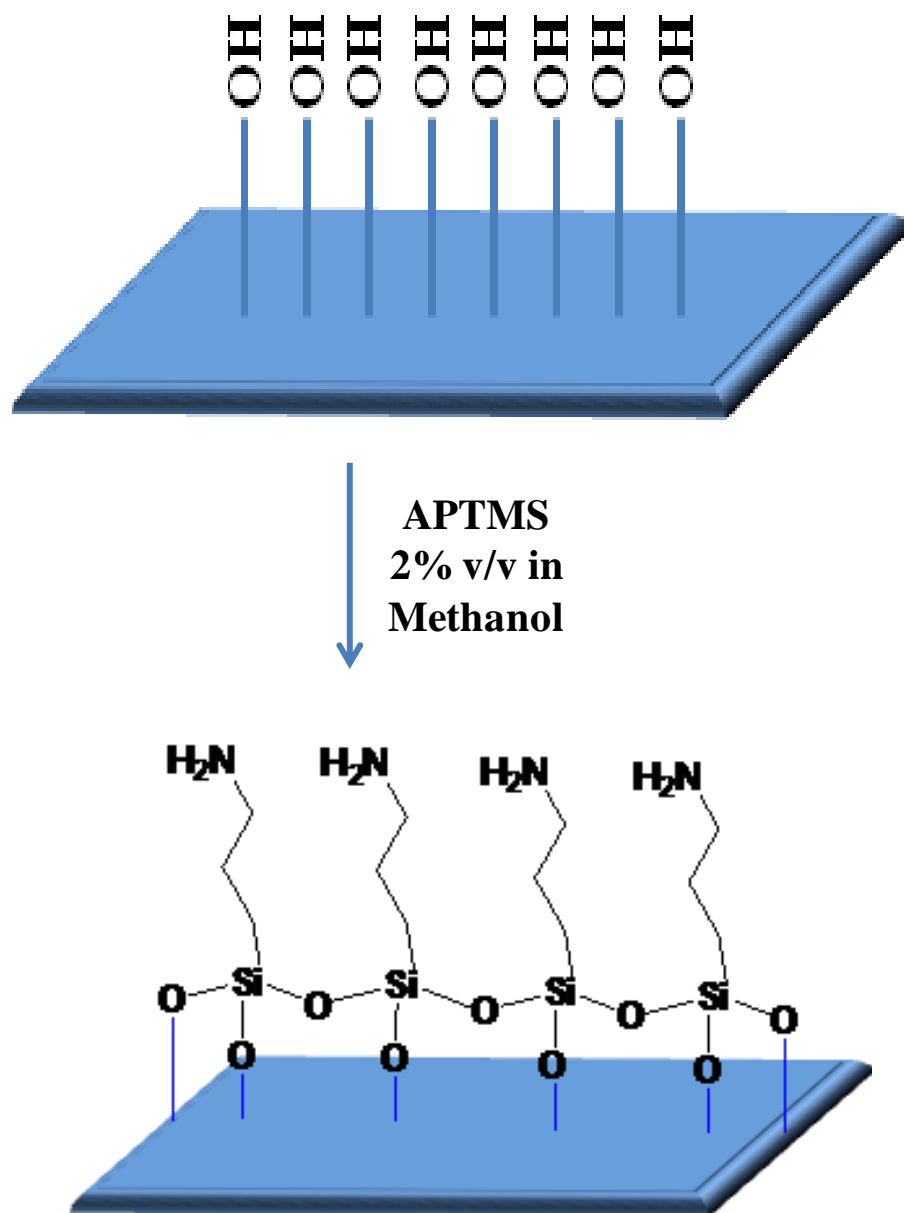
Figure 3.3. Scheme for immobilization of biotinylated Pd NPs on substrates. Oxygen plasma treatment leads to deposition of hydroxyl (OH) groups on the surface. The subsequent attachment of APTMS to the OH groups provides the amine groups required to immobilize the NPs.

Figure 3.3 (cont'd)

**Biotinylated
Pd NPs**
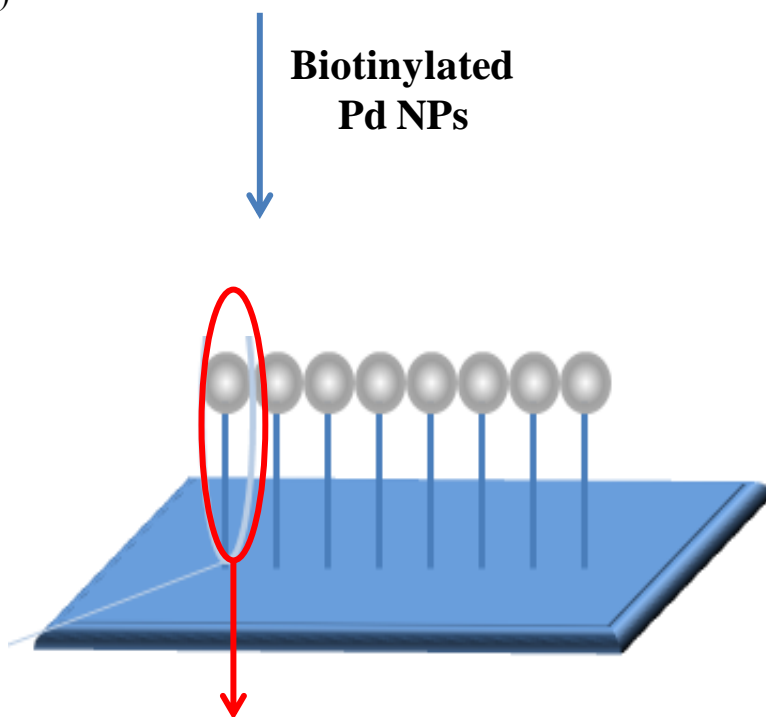
Figure 3.3 (cont'd)
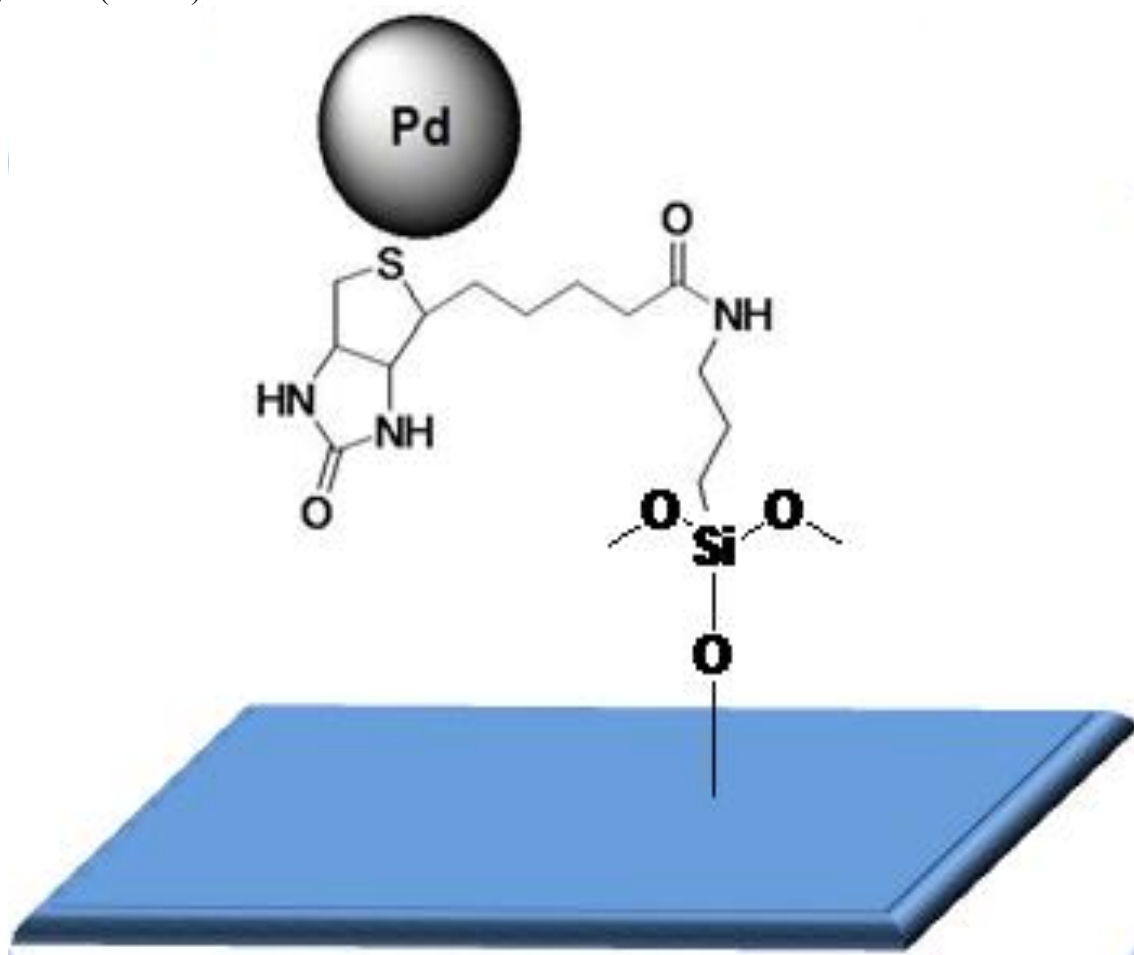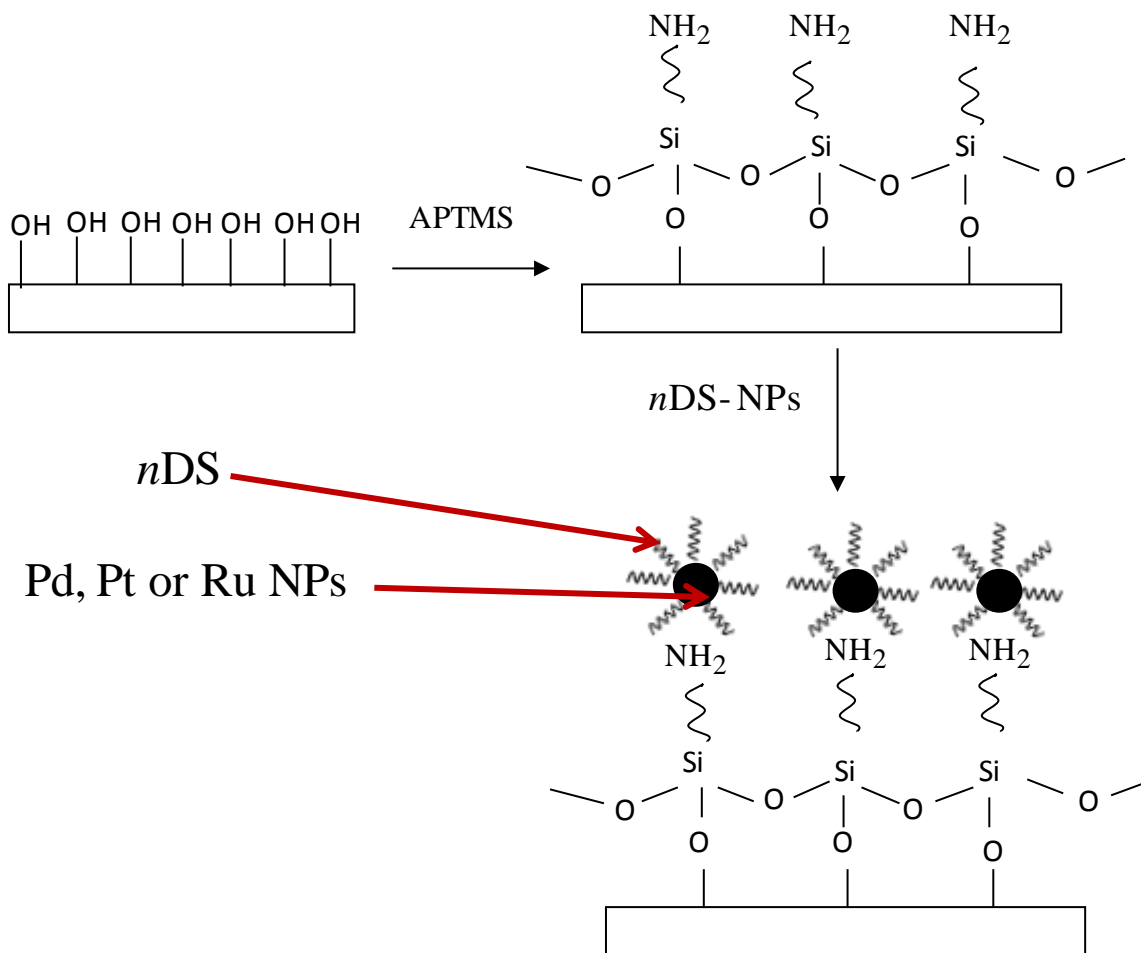
Figure 3.4. Scheme for immobilization of *n*DS-Pd, Pt and Ru NPs on substrates. The surfaces were oxygen plasma-treated to deposit hydroxyl groups, followed by aminosilanization and coordination of NPs with the primary amine groups to complete the immobilization.

3.3.4 Surface characterization: FT-IR

Reflective aluminum wafers (24×11 cm) were modified following the same procedure described above, due to their similar surface chemistry to glass. For substrates with immobilized biotinylated Pd NPs and APTMS-Pd NPs, FT-IR spectra were acquired by a Magna–Nicolet IR-560 spectrometer (Waltham, MA) after each step of the surface modification process on aluminum to determine the surface functionalities.

3.3.5 Surface characterization: XPS

A Perkin Elmer Phi 5600 ESCA (Waltham, MA) system with a magnesium KBr X-ray source was used for all experiments. Samples were analyzed at pressures between 10^{-9} and 10^{-8} torr with a passing energy of 29.35 eV and a take-off angle of 45°. The spot size was roughly 250 μm^2. Atomic concentrations were determined by using previously established sensitivity factors. All peaks were referenced to the signature C1s peak for adventitious carbon at 284.6 eV.

3.3.6 *In-situ* immobilization of NPs in sealed microfluidic reactors

We used the two-step protocol described above to develop two methods for *in-situ* immobilization of biotin- and APTMS-Pd NPs in sealed microfluidic reactors. A Harvard Apparatus PHD 22/2000 infusion/withdrawal syringe pump (Holliston, MA) was used to infuse the APTMS solution into the serpentine microfluidic channels at a flow rate of 0.025 mL/min for at least 3 h, followed by one hour of curing at 60°C. The NHS-EDC-biotin-Pd solution was then continuously stirred at 300 RPMas it was either withdrawn from a vial into the channels or infused into the channels from a vial by pumping air into the vial. This step was followed by one hour of curing at 60°C. Similarly, the APTMS-stabilized Pd NPs were introduced into the microfluidic reactor by either infusion or withdrawal, followed by curing. Thus, four different types of microfluidic reactors were prepared and assigned the following names: infused biotinylated Pd, withdrawn biotinylated Pd, infused APTMS-Pd and withdrawn APTMS-Pd. Solutions of *n*DS-Pd, -Pt and -Ru NPs were introduced into the aminosilanized PDMS microfluidic reactors in infusion mode by a syringe pump at a flow rate of 0.025 mL/min for

74

several hours, followed by curing at 70°C for 1 h in an oven. The resulting microfluidic reactors were labeled nDS-Pd, nDS-Pt and nDS-Ru.

3.3.7 General procedure for homogeneous hydrogenation of 6-Bromo-1-hexene in a batch system using colloidal NPs

A round bottom flask containing 6-bromo-1-hexene (0.05 mL, 0.37 mmol) and colloidal noble metal NPs (0.5 mmoL, 3 mmol) in ethanol (for biotinylated and APTMS-Pd NPs) or methanol (for nDS-Pd, -Pt and -Ru NPs) was subjected to a vacuum for a few seconds, then immediately connected to a rubber bladder containing H_2 at 1 atm. The solution was stirred at room temperature for 12 h, after which the rubber bladder was disconnected from the flask. An aliquot of the reaction mixture was taken and centrifuged to separate the Pd NPs from the solution. We observed that the Pd NPs remained as solids at the bottom of the centrifuge tube. An aliquot of the supernatant was analyzed by gas chromatography (GC, Agilent 6890N, Santa Clara, CA) to determine the degree of conversion.

3.3.8 Hydrogenation of 6-bromo-1-hexene in microfluidic reactors with immobilized NPs

To assess the catalytic activity of biotinylated and APTMS-Pd NPs, reactant mixtures with 6-bromo-1-hexene concentrations of 10 mM and 50 mM in anhydrous methanol were infused into the four microfluidic reactors and into a blank microfluidic reactor by a syringe pump at a flow rate of 0.1 mL/h and 0.56 mL/min, respectively [29, 30]. Hydrogen was introduced into the reaction mixture through the other arm of the Y-shaped entrance to the microfluidic reactor through a gas tight syringe. After each reaction cycle, the microfluidic reactor system was rinsed with anhydrous methanol and dried with hydrogen to clean out any reaction residue. Products

were collected in vials at the outlet of the channels and analyzed using an Agilent 6890N gas chromatograph (Santa Clara, CA).

Hydrogenation of 6-bromo-1-hexene was conducted in microfluidic reactors with immobilized nDS-Pd, -Pt and -Ru NPs. The microfluidic reactors were pretreated by flowing hydrogen at 100°C for 1 h through the system before initiating reactions, to activate catalyst surfaces. The pre-treatment procedure partially removed the stabilizing ligands and activated the catalyst surfaces. All reactions were conducted at room temperature (25°C) and hydrogen pressure of 1 atm. Reactant solutions of 1, 5, and 10 mM were introduced independently into the microfluidic reactors through the Y-shaped inlet using a mass flow controller (Bronkhorst F-201CV-020-AGD-20-V, Ruurlo, Nederland) and a syringe pump (Harvard apparatus PHD 2200, Holliston, MA). The gas and liquid flow rates were adjusted to produce an annular flow pattern in which the gas travelled in the center and the liquid along the channel walls. After a stable flow pattern was obtained (based on visual inspection), the reaction product was collected continuously for 10 min in a single vial at the outlet. At the end of each run, the entire product was diluted 100 times prior to analysis by a gas chromatograph (Agilent 6890 with a flame ionization detector, and a DB1dimethylsiloxane column, 0.250 mm I.D., 1.00 μm film thickness and 30 m in length). Each microfluidic reactor was rinsed with methanol between runs, and purged with hydrogen for 15 min. Replicate runs were conducted under similar reaction conditions in at least two different microfluidic reactors with identical immobilization schemes.

3.3.9 Assessment of catalyst loading in microfluidic reactors and metallic content of product streams using ICP-AES

After the *in-situ* catalyst immobilization process, the microfluidic reactors were cut into small pieces and immersed in a known volume of aqua regia solution (3 volumes of concentrated hydrochloric acid and 1 volume of concentrated nitric acid) overnight to digest the immobilized NPs. The resulting solution was diluted with deionized water to 4% aqua regia, and an aliquot of the sample was analyzed by ICP-AES (Vista Pro, Varian, Cary, NC) to determine the metallic content of the microfluidic reactors, and enable the calculation of the TOF. The reaction mixture was collected after GC analysis, followed by solvent evaporation under nitrogen flow, and re-digestion by aqua regia. The digested sample was analyzed by ICP-AES to determine the metal content. Standard solutions of each metal element at different concentrations were prepared and measured to obtain corresponding standard curves (concentrations vs. elemental peak area) for further analysis.

3.3.10 Post reaction characterization of microfluidic reactors with immobilized NPs by SEM and EDS

To observe the particle morphology before and after immobilization process, blank PDMS and glass slides and the ones with immobilized metal NPs were characterized by SEM (JEOL JSM-7500F, Tokyo, Japan) equipped an energy dispersive X-ray spectrometer (Oxford Instrument, UK). All samples were coated with a thin layer of osmium to introduce electron conductivity. All SEM images were taken at an acceleration voltage of 15 kV, an emission current of 20 µA and a working distance of 4.5 mm. All EDS spectra were collected at an accelerated voltage of 15 kV, an emission current of 20 µA and a working distance of 8 mm. All characterization was carried out in a vacuum lower than 9.6×10^{-5} Pa.

3.4 Results and discussions

3.4.1 Characterizations of modified reactor surfaces

The FT-IR spectra (Figure 3.5) of APTMS and APTMS-Pd show a peak at 1577cm^{-1} representing the N-H scissoring bending vibration [38, 39]. The two strong absorption peaks at 1145 and 1055 cm^{-1} are from the Si-O-Si asymmetric vibration [38, 39]. The FT-IR spectrum of biotinylated Pd shows a strong peak at 1682 cm^{-1} (amide I) and a weaker peak at 1561 cm^{-1} (amide II) that represent amide bond formation [38, 39]. The peak at 1757 cm^{-1} indicates that a small number of carboxyl groups still remains after the immobilization reaction [38, 39].

XPS was used to obtain the atomic concentrations of characteristic elements after surface modification. Table 3.1 shows the concentrations of surface atoms on glass and PDMS surfaces that were blank, aminosilanized and immobilized with biotinylated or APTMS-Pd NPs, respectively. Compared to the blank surfaces, the sharp increase in carbon and nitrogen content is an indication that ATPMS was attached successfully, as each APTMS molecule contains a three-carbon chain and a primary amine group. The sharp decrease in oxygen and silicon indicates that the glass surfaces had been covered. The characteristic element of biotinylated Pd was shown on both surfaces after immobilization. The atomic concentrations of elements on glass and PDMS surfaces following attachment of APTMS-Pd confirmed successful immobilization of Pd NPs on both glass and PDMS surfaces. However, we do not necessarily draw the conclusion that biotin-Pd loading was higher than APTMS-Pd based on the respective Pd atomic concentrations. The reason is that XPS characterization is a function of the area on the substrate selected for observation. Thus the data obtained are representative of the entire surface

only when the substrate is evenly coated. Two types of Pd were observed on the surface: Pd zero (binding energy of 335.59 eV) from the Pd NPs and Pd oxide (binding energy of 338.08 eV) from surface oxidation in the air (Figure 3.6 (a)).

XPS results also confirmed successful catalyst immobilization on both glass and PDMS surfaces for nDS-stabilized Pd, -Pt and -Ru NPs (Table 3.2). Compared to the data acquired on blank surfaces, we observed sharp increases in C and N on the aminosilanized surfaces, along with decreases in Si and O. The "loss" in the surface concentrations of Si and O is due to coverage of the glass and PDMS surfaces following aminosilanization. The characteristic metal elements from the NPs were detected by XPS on all surfaces with immobilized catalysts, with atomic concentrations ranging from 0.1% to 1.0%. The XPS peaks of the noble metals (Figure 3.6 (b)-(d)) provided evidence that the majority existed in elemental form. However, since the samples were exposed to air during characterization, it was difficult to avoid oxidation of the metals, which resulted in Pd(II), Pt(VI), Ru(IV) and Ru(VI) on the reactor surfaces [17]. Thus, it was necessary to pre-reduce each of the catalysts prior to running the hydrogenation reactions.
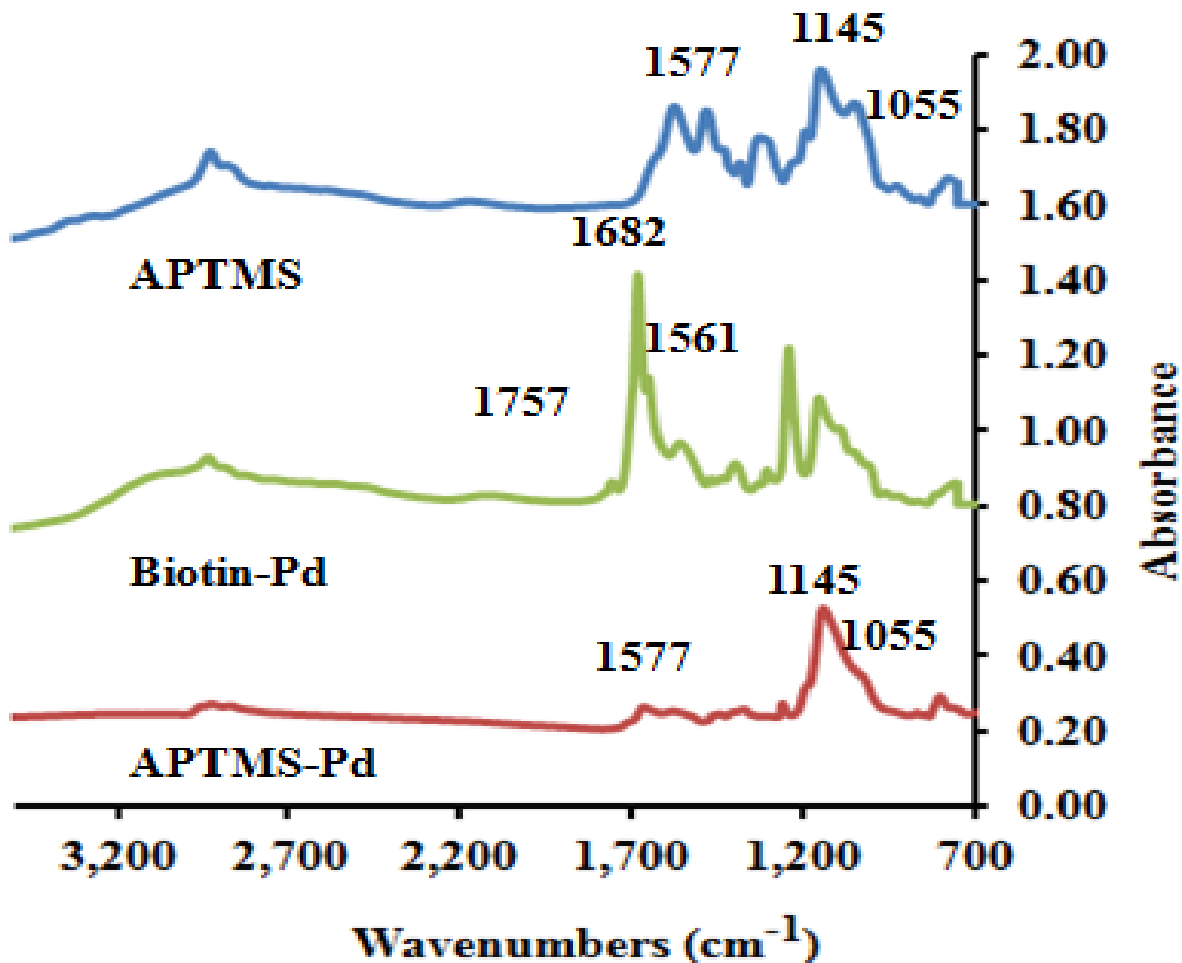
Figure 3.5. FT-IR spectra of APTMS, APTMS-Pd NPs and biotinylated Pd NPs on aluminum surfaces. Y axis: absorbance; X-axis: wave number, from 3,200 to 700 cm^{-1} (left to right). Top: APTMS; center: biotin-Pd; bottom: APTMS-Pd. The peak at 1577 cm^{-1} represents the N-H scissoring bending vibration. The two strong absorption peaks at 1145 and 1055 cm^{-1} are from the Si-O-Si asymmetric vibration. The biotinylated Pd shows a strong peak at 1682 cm^{-1} (amide I) and a weaker peak at 1561 cm^{-1} (amide II) that represent amide bond formation. The peak at 1757 cm^{-1} indicates that a small number of carboxyl groups still remained after the immobilization step.

Table 3.1. Atomic concentrations (%) of different elements on PDMS and glass surfaces after each step of the immobilization process. For biotinylated Pd NPs, step 1: blank surfaces; step 2: aminosilanization; step 3: immersion in biotinylated Pd NP solutions. For APTMS-Pd NPs, step 1: blank surfaces; step 2: immersion in APTMS-Pd NP solutions.

Elements	Atomic Concentrations on Glass, %				Atomic Concentrations on PDMS, %			
	Blank	Aminosila-nization	Biotin-Pd	APTMS-Pd	Blank	Aminosila-nization	Biotin-Pd	APTMS-Pd
C	22.7	53.0	57.5	54.4	45.7	45.8	48.0	47.8
N	1.0	10.6	14.5	5.0	N/A	6.0	6.6	1.9
O	50.7	24.0	23.1	24.3	28.4	29.0	25.7	28.3
Si	24.0	12.0	13.9	16.2	25.9	19.0	17.0	21.9
S	N/A	N/A	1.1	N/A	N/A	N/A	N/A	N/A
Cl	N/A	0.4	0.4	N/A	N/A	0.2	1.6	N/A
Na	0.9	N/A	N/A	N/A	N/A	N/A	N/A	N/A
Ca	0.7	N/A	N/A	N/A	N/A	N/A	N/A	N/A
Pd	N/A	N/A	1.0	0.1	N/A	N/A	1.1	0.1

Table 3.2. XPS characterization of the atomic concentrations of different elements on glass and PDMS surfaces following immobilization of the NPs (nDS-Pd, Pt, and Ru NPs).

Elements	Atomic Concentrations on Glass, %					Atomic Concentrations on PDMS, %				
	Blank	Aminosila-nization	nDS-Ru	nDS-Pd	nDS-Pt	Blank	Aminosila-nization	nDS-Ru	nDS-Pd	nDS-Pt
C	22.7	53.0	55.5	54.2	57.3	45.7	45.8	47.0	47.7	46.2
N	1.0	10.6	6.2	5.0	8.7	N/A	6.0	1.7	1.9	1.8
O	50.7	24.0	24.0	24.3	23.7	28.4	29.0	30.0	28.3	32.0
Si	25.6	12.0	13.9	16.2	9.9	25.9	19.0	20.0	21.9	18.9
S	N/A	N/A	0.1	0.2	0.3	N/A	N/A	0.2	0.05	0.1
Ru	N/A	N/A	0.3	N/A	N/A	N/A	N/A	0.1	N/A	N/A
Pd	N/A	N/A	N/A	0.1	N/A	N/A	N/A	N/A	0.1	N/A
Pt	N/A	N/A	N/A	N/A	0.1	N/A	N/A	N/A	N/A	1.0
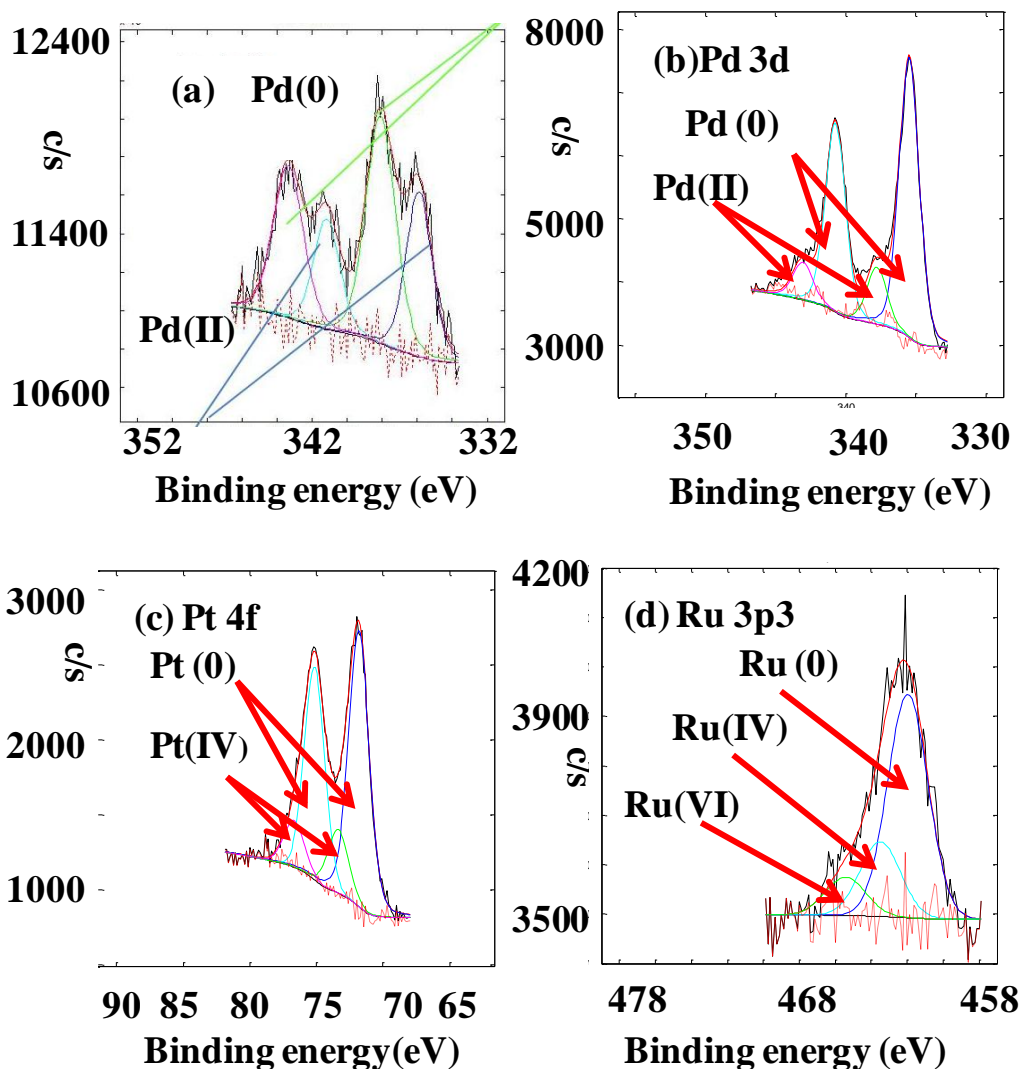
Figure 3.6. XPS spectra of (a) biotinylated or APTMS-Pd NPs, showing two forms of Pd on the surfaces, Pd(0) and Pd(II). Pd(0) is from Pd NPs while Pd(II) is due to surface oxidation in the air; (b) *n*DS-Pd; (c) *n*DS-Pt; and (d) *n*DS-Ru. While most of the metals are in elemental form, exposure of the samples to air during characterization resulted in some oxidation, leading to formation of Pd(II), Pt(VI), Ru(IV) and Ru(VI).

3.4.2 Analysis of liquid hold-up in annular gas-liquid flow in microfluidic reactors

In hydrogenations conducted in the PDMS microfluidic reactors, we adjusted the gas and

liquid flow rates to cause the gas to travel in the center of the channels and the liquid reactant

along the walls. To maintain the annular flow pattern, we used liquid flow rates ranging from 0.1

to 0.2 mL/h and a fixed gas flow rate of 0.8 mL/min, each carefully controlled by a syringe pump

and hydrogen mass controller, respectively. Gas-liquid annular flow in pipes has been well

characterized in the literature, both theoretically and experimentally [40-43].

The Lockhart-Martinelli-Chisholm correlation is a well-established model that describes the

frictional pressure gradient of two-phase gas-liquid flow in pipes. This model is suitable for

laminar flow in microfluidic channels because it incorporates the interfacial shear force function

between the two phases. Rebrov and colleagues have recently used this model to accurately

calculate liquid hold-up and liquid residence times in capillary microreactors for the selective

hydrogenation of phenylacetylene [41-44]. The salient features of the system used by Rebrov and

colleagues are similar to ours. These features include, specifically, the channel dimensions, range

of liquid and gas flow rates, flow patterns, reaction types, and reaction conditions (Table 3.3).

As a result of these similarities, we used the simplified equations derived from the Lockhart-

Martinelli-Chisholm correlation to calculate the liquid hold-up and liquid residence times in our

microreactor systems. The calculations were modified by using the hydraulic diameters of the

rectangular microfluidic channels. The simplified equation is given by

$$\phi_L^2 = 1 + \frac{C}{\chi} + \frac{1}{\chi^2} \qquad\qquad \text{(Equation 3.1)}$$

where ϕ_L and χ are the Lockhart-Martinelli parameters, and C has a numerical value of 5 for

laminar flow.

The parameter ϕ_L is calculated by:

$$\phi_L = 1 + \frac{A_G}{A_L} \qquad\qquad \text{(Equation 3.2)}$$

where A_G and A_L are the cross-sectional capillary areas occupied by the gas and liquid,

respectively.

The second parameter, χ, is calculated by:

$$\chi = \frac{1-x}{x}\sqrt{\frac{\rho_G}{\rho_L}}$$

(Equation 3.3)

where x is the ratio of the mass flow rate of the gas to the total mass flow rate, and is calculated

by:

$$x = \frac{\rho_G v_G}{\rho_L v_L + \rho_G v_G}$$

(Equation 3.4)

with ρ and v the densities and volumetric flow rates of the gas and liquid, respectively.

The liquid hold-up fraction (ε) and the liquid residence time in the capillary (τ) can be

calculated, respectively, by:

$$\varepsilon = \frac{1}{\phi_L}$$

(Equation 3.5)

and

$$\tau = \frac{V\varepsilon}{v_L}$$

(Equation 3.6)

where V is the volume of the capillary.

The results are summarized in Table 3.4. The calculated liquid residence time was used for

the evaluation of turnover frequencies (TOF) for the hydrogenation of 6-bromo-1-hexene in the

PDMS microfluidic reactors in later sections.

Table 3.3. Comparison of features of Rebrov's and our microreactor systems.

	Rebrov's microreactor system	PDMS microreactor system
Characteristic dimensions (mm)	0.25 (I.D.)	0.50 (width)
Liquid flow rate (mL/h)	0.06-0.60	0.10-0.20
Gas flow rate (mL/min)	0.25-0.55	0.80
Flow pattern	Annular	Annular
Liquid Substrates (concentrations and solvents)	Phenylacetylene 10 vol.% in Methanol	6-Bromo-1-hexene 1.0-10 mM in Methanol
Reaction temperature($^\circ$C)	30-50	25
Reaction pressure (atm)	1.0	1.0

Table 3.4. Liquid residence times (min) in PDMS microreactors at different liquid flow rates.

PDMS microfluidic reactor	
v_L(mL/h)	**Residence time (min)**
0.1	1.2
0.2	1.0

3.4.3 Solution phase hydrogenation

The reaction is shown in Scheme 3.1 below. Soluble colloidal NPs present unique opportunities for homogeneous catalysis because of better activity and selectivity. We evaluated the hydrogenation of 6-bromo-1-hexene catalyzed by all the NPs synthesized by thermal decomposition. Analysis of an aliquot of the reaction mixture obtained after 45 min showed the formation of 1-bromohexane as the major product (90%), along with unreacted 6-bromo-1-hexene (10%) for all Pd NPs (biotin-, APTMS-, and *n*DS), while only 18% and 7% conversions were observed for *n*DS-Pt and Ru NPs. After 3 h, 1-bromohexane was the sole product for all Pd NPs.

Scheme 3.1. Hydrogenation of 6-bromo-1-hexene to 1-bromohexane.
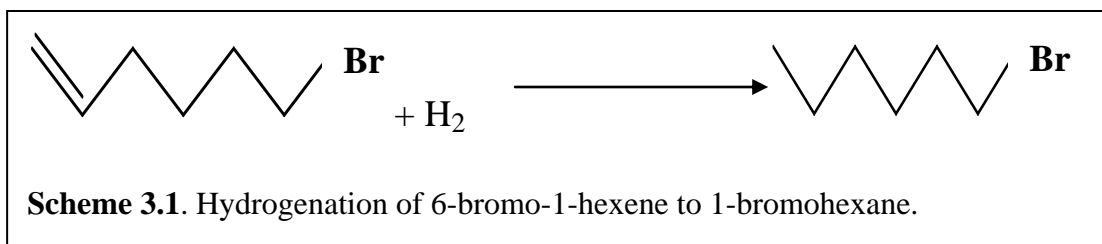
3.4.4 Hydrogenation in microfluidic reactors with biotinylated Pd and APTMS-Pd NPs and assessment of conversion and catalyst recyclability

The average reaction time was approximately 18 min, which was the time it took to exhaust 10 mL of hydrogen from a 10 mL Hamilton gas-tight syringe. The actual residence time was 1.0 min, based on the flow rates used. The flow rates of the liquid and gas were controlled to ensure an annular flow pattern in which the liquid travelled along the walls of the channels, with the gas in the center to maximize liquid-catalyst-gas interaction [29, 30]. There was no 1-bromohexane detected in the reaction products from the microfluidic reactors containing no catalysts, indicating that the reaction is catalytic. In comparison, all the hydrogenation reactions in

87

microfluidic reactors with immobilized Pd NPs, whether stabilized by biotin or APTMS, produced 1-bromohexane at various levels of conversion. In each case, the selectivity of the reaction was 100%, with a carbon balance of about 95%.

We investigated the effects of a) substrate concentrations and b) how the Pd NPs were introduced into the microfluidic reactors on reaction conversions. Figures 3.7 (a) and (b) show the conversion of 6-bromo-1-hexene at reactant concentrations of 10 and 50 mM in microfluidic reactors with immobilized Pd NPs, as a function of catalyst recycle. Conversions of at least 60% were achieved for the first runs in each microfluidic reactor, confirming successful immobilization of the NPs. Complete conversions were repeatedly observed in both biotinylated Pd withdrawal and infusion microfluidic reactors at a substrate concentration of 10 mM, suggesting a robust catalyst layer on the surface during catalyst recycling. At a reactant concentration of 50 mM, conversions in the infusion microfluidic reactors were 30% higher than in the withdrawal reactors for each type of Pd NPs, which is an indication that higher catalyst loadings were achieved by infusion than by withdrawal. However, a significant decrease in conversion was observed after the first cycle of catalyst reuse in both biotinylated Pd infusion/withdrawal microfluidic reactors at a substrate concentration of 50 mM. APTMS-Pd infused microfluidic reactors also showed a higher conversion than the withdrawal ones, again suggesting the infusion method was a more efficient way for catalyst immobilization. At both substrate concentrations, at least 30% decreases in conversion were observed in APTMS-Pd infusion and withdrawal microfluidic reactors.

88
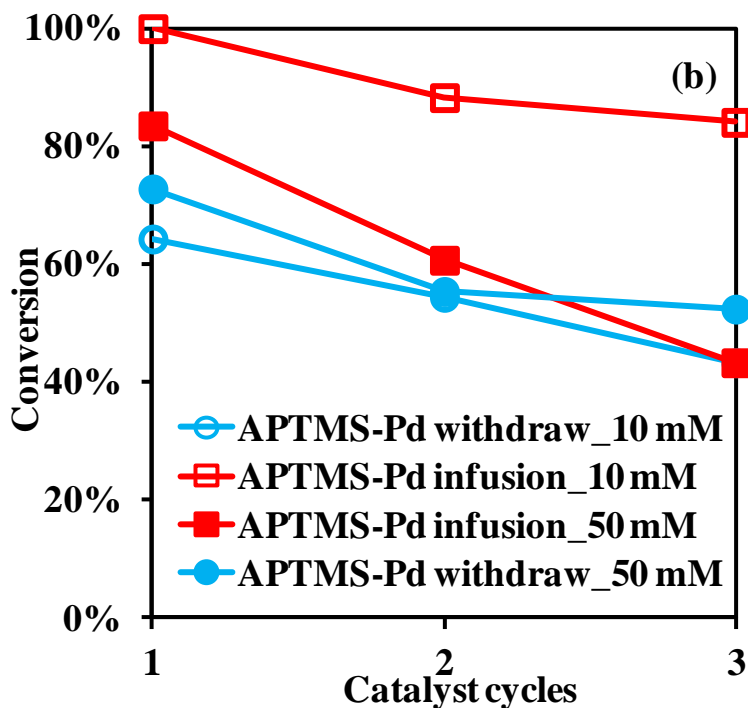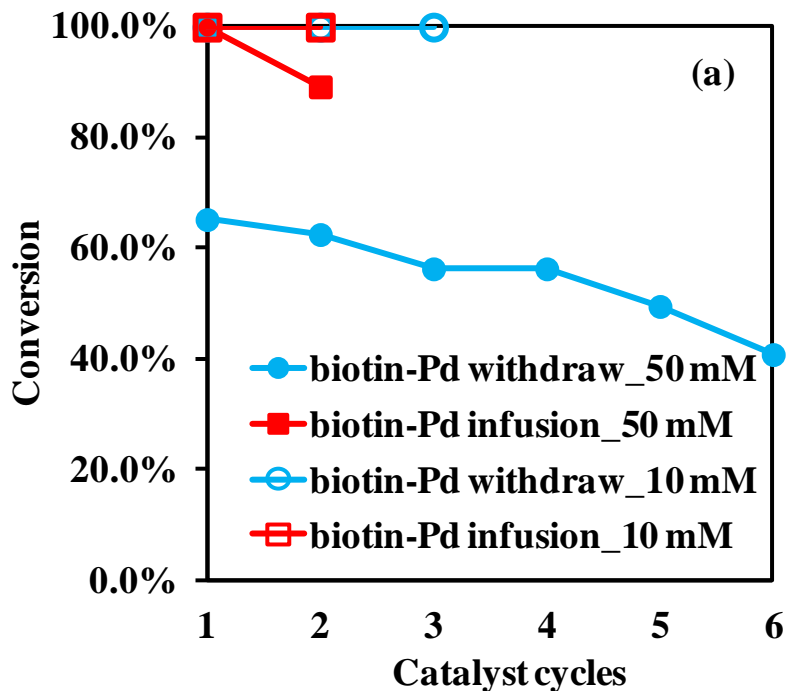
Figure 3.7. Conversion of 6-bromo-1-hexene (at a substrate concentration of 50 and 10 mM) in microfluidic reactors with immobilized Pd NPs by infusion or withdrawal methods over repeated cycles of catalyst use. (a) Biotinylated Pd NPs; (b) APTMS-Pd NPs. The solid lines are for the purpose of guiding the eye; they do not represent model fits of the data.

3.4.5 Hydrogenation in microfluidic reactors with *n*DS NPs: assessment of conversion and catalyst recyclability

All reactions attained 100% selectivity and various degrees of conversion, again confirming the effectiveness of the immobilization scheme for *n*DS-stabilized NPs. Control experiments in blank reactors produced no reactions. Over 96% of carbon balance was achieved in each reaction.

The microfluidic reactor system served as a convenient tool to screen different nanocatalysts with the same stabilizing ligand. At a substrate concentration of 1 mM, both Pd and Pt converted over 90% of the substrate to the desired product (1-bromo-hexane) upon first use of the catalysts, approximately 2.5 times higher than Ru (Figure 3.8). These results are in agreement with previous reports that Pd and Pt are more effective in reducing carbon-carbon double bonds [45]. Though Ru is better known for reducing carbonyl bonds than carbon-carbon double (olefenic) bonds, we still observed a first time conversion of 38%.

We assessed the effects of substrate concentration on the overall conversion for each of the three catalysts. The conversion levels for Pd and Pt dropped steadily from low to high substrate concentration (Figure 3.9), which may be an indication of the physical limits on catalyst performance during the very short residence time (1.0 min) over which these one-pass reactions were conducted in the microfluidic reactor. By contrast, the conversion achieved with Ru increased significantly at the highest substrate concentration over the nearly identical levels observed at the two lower concentrations. One could speculate that this is an indication that Ru has a higher performance saturation ceiling for conversion of the substrate than either Pd or Pt, even though its overall conversion is lower. It is also possible that the rate of reaction is a much stronger function of concentration for Ru than for the other catalysts. For example, the total

amount of substrate converted (estimated simply as the product of reactant concentration and percent conversion) increased from low to high substrate concentrations for all three catalysts, but much more significantly for Ru. Overall, the catalyst effectiveness for this reaction may be characterized as Pd ≈ Pt > Ru, in agreement with other reports in the published literature [17, 45-48].

The effect of substrate flow rates on conversion was assessed by keeping the gas flow rate constant at 2.4 mL/min and doubling the liquid flow rate to 0.2 mL/h, using Pt at a substrate concentration of 10 mM as an example. The desired annular flow pattern was still observed, with H_2 in the center of the channel and the liquid reactant along the walls. However, as would be expected, the liquid film thickness along the channels increased. A decrease in substrate conversion at the higher liquid flow rate was observed (Figure 3.10), which was attributed to the shorter residence time in the channel.

We investigated catalyst reactivity upon recycling at all three substrate concentrations, with each catalyst reused a minimum of three times. Pd achieved a complete conversion over three consecutive runs at a substrate concentration at 1 mM (Figure 3.11(a)). However, the conversion decreased significantly by the third recycle at substrate concentrations of 5 and 10 mM, more likely a result of the short residence times than catalyst inactivation. Pt activity remained relatively stable at a substrate concentration of 5 mM, although conversions decreased after the first run at the other two substrate concentrations (Figure 3.11(b)). Ru was recycled three times without significant loss in activity at substrate concentrations of 1 and 5 mM, but the conversion level dropped by about 50% after the first run at the substrate concentration of 10 mM (Figure 3.11(c)).
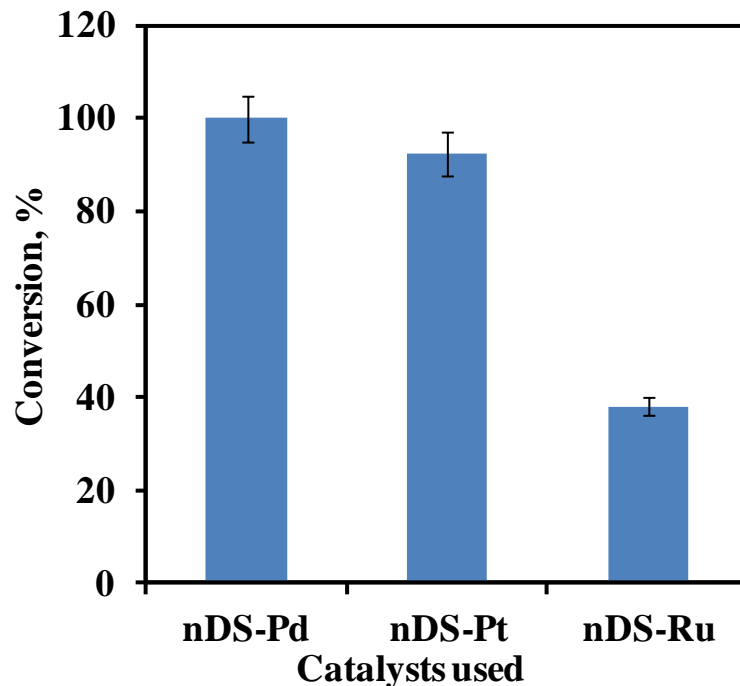
Figure 3.8. Conversion of 6-bromo-1-hexene to 1-bromohexane upon first use of Pd, Pt and Ru catalysts, respectively, at a substrate concentration of 1 mM. All reactions were conducted in PDMS microfluidic reactors at room temperature and hydrogen pressure of 1 atm. The gas flow rate was set at 2.4 mL/min by a mass controller and the liquid flow rate at 0.1 mL/h by a syringe pump. Each reaction lasted 10 min (with actual residence times of 1.0 min). The reaction products were collected over the entire duration of each experiment, and analyzed by GC.
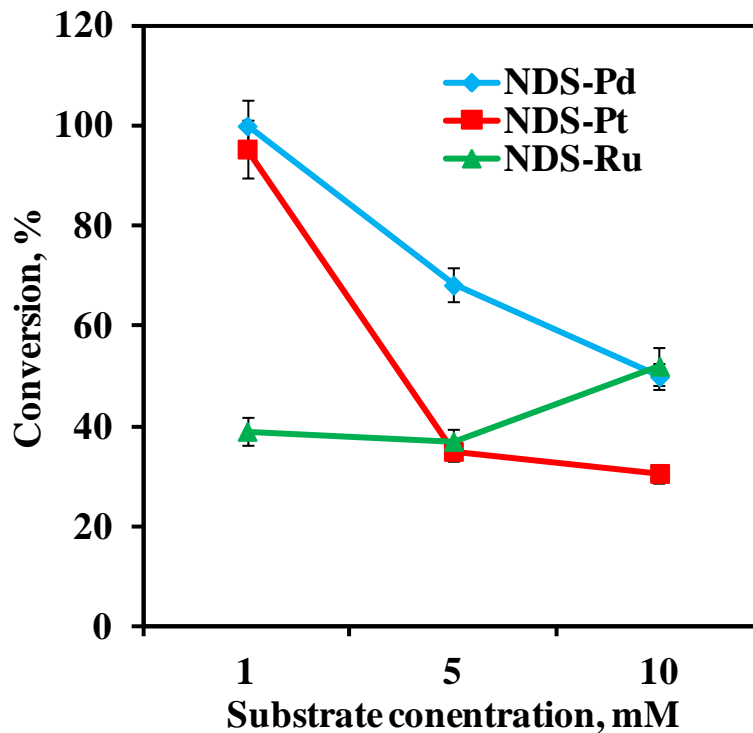
Figure 3.9. Effect of substrate concentration on the conversion of 6-bromo-1-hexene upon first use of Pd, Pt and Ru nanocatalysts, respectively, at substrate concentrations of 1, 5 and 10 mM. The reaction conditions are the same as described in Fig. 3.8. The solid lines are for the purpose of guiding the eye; they do not represent model fits of the data.
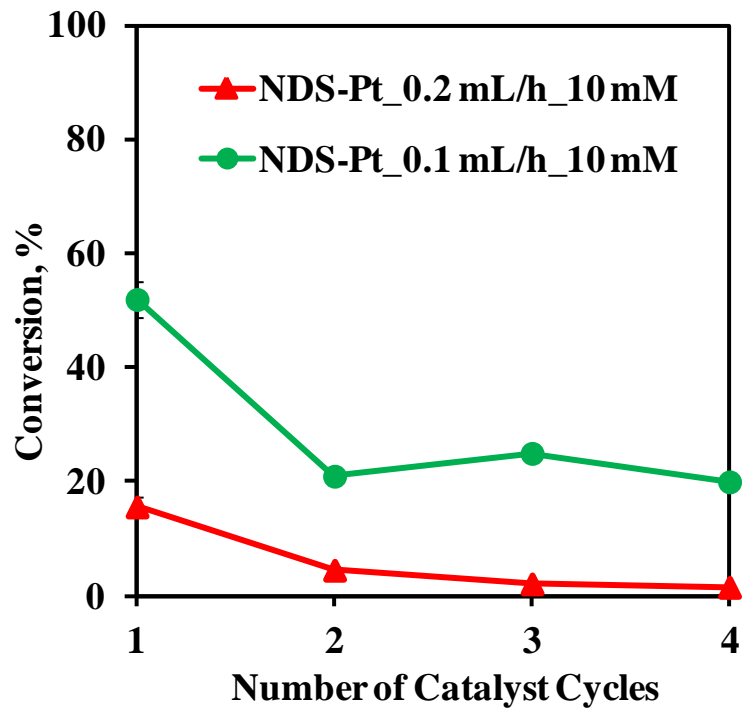
Figure 3.10. Assessment of the effect of liquid flow rates on the conversion of 6-bromo-1-hexene catalyzed by Pt at a substrate concentration of 10 mM. The reaction conditions are the same as described in Fig. 3.8, except that two liquid flow rates were used: 0.1 mL/h and 0.2 mL/h. Pt was recycled 4 times at each liquid flow rate. The solid lines are for the purpose of guiding the eye; they do not represent model fits of the data.
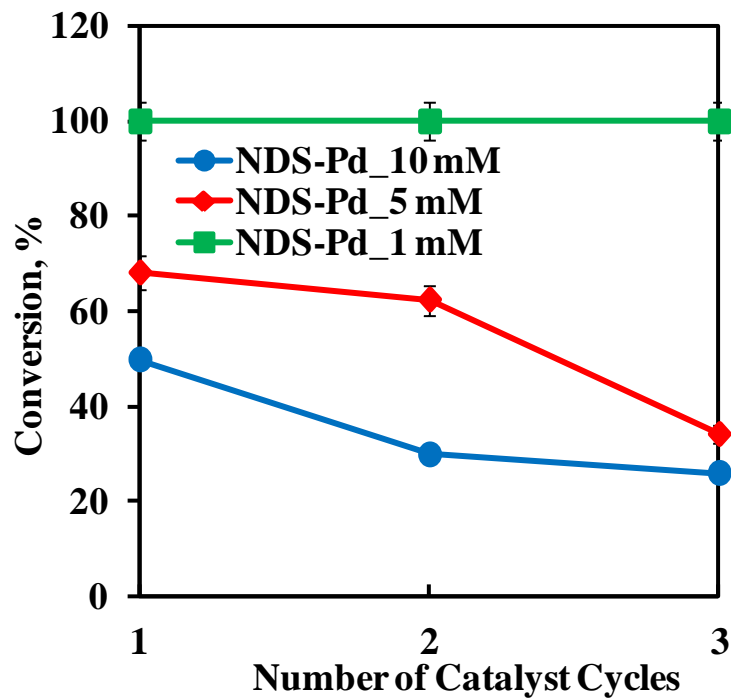
Figure 3.11. Conversion of 6-bromo-1-hexene as a function of the number of catalyst recycles at substrate concentrations of 1, 5 and 10 mM. Reaction (a) was catalyzed by Pd, (b) by Pt, and (c) by Ru. All reactions were conducted at room temperature and hydrogen pressure of 1 atm. The liquid and gas flow rates were 0.1 mL/h and 2.4 mL/min, respectively. The solid lines are for the purpose of guiding the eye; they do not represent model fits of the data.

Figure 3.11 (cont'd)
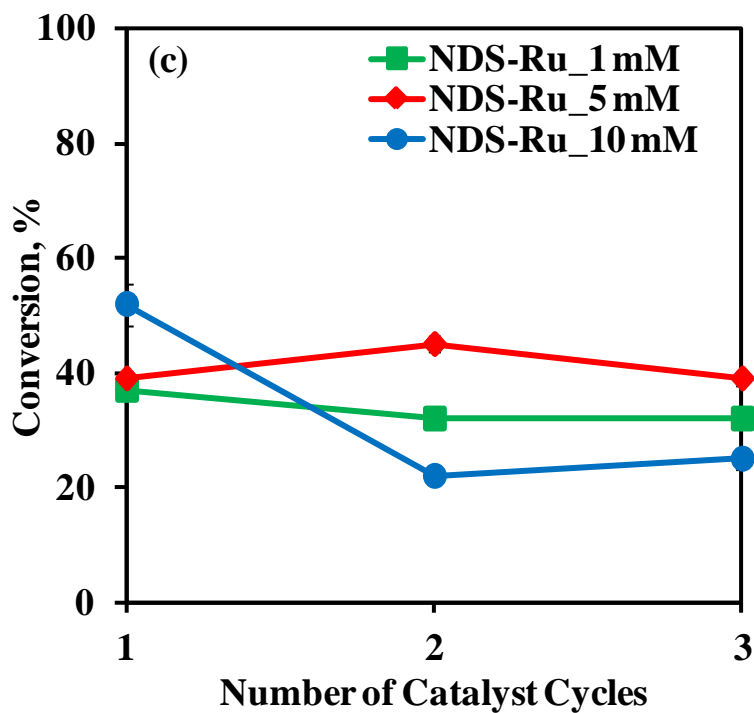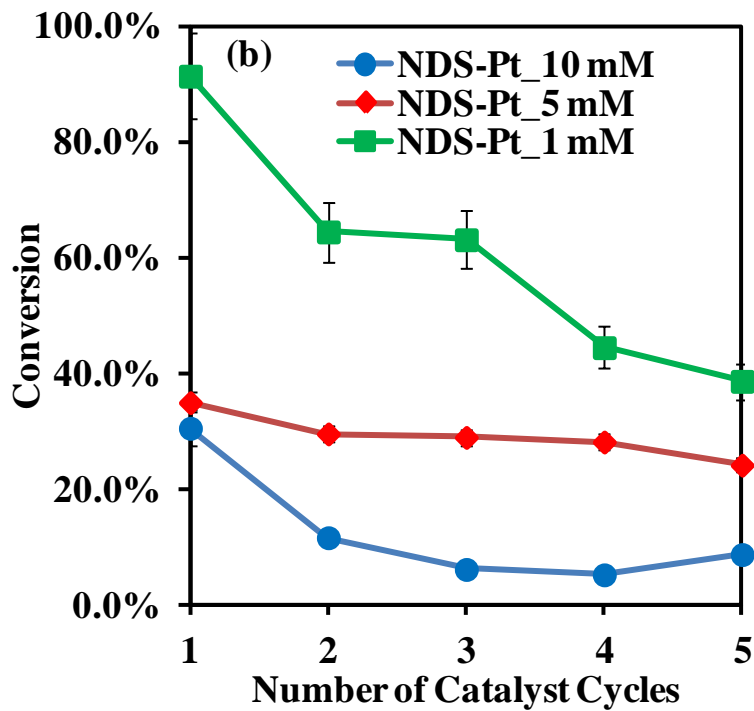
3.4.6 TOF calculations based on concentration of surface atoms and comparison with batch reactor systems

In spite of the difficulty of making accurate measurement of surface active sites, the nanocatalysts we used had well-defined crystal structures with essentially spherical shapes. Therefore, one could calculate the fraction of surface metal atoms based on the metal crystal structures and sizes, by assuming that all surface atoms serve as active sites in the reactions [49]. While not perfect, this approximation provides a realistic picture of catalyst performance. TOF values based on surface atoms were calculated by Equation 3.7, expressed as the number of substrate molecules converted (in moles) per active catalytic site (in moles) per unit time (in seconds):

$$TOF = \frac{(Number\ of\ molecules\ reacted)}{(Number\ of\ sites) \times (residence\ time)} \qquad \text{(Equation 3.7)}$$

Equations 3.8 and 3.9 provide estimates of the fraction of surface metal atoms [50]:

$$fraction\ of\ surface\ atoms\ (hcp) = \frac{\left(\dfrac{Surface\ area\ of\ one\ NP}{Surface\ area\ of\ one\ atom}\right)}{\dfrac{Volume\ of\ one\ NP}{\left(\dfrac{Volume\ of\ one\ atom}{Packing\ factor}\right)}}$$

$$= \frac{(4\pi R^2)/(\dfrac{3\sqrt{3}}{2}r^2)}{(\dfrac{4\pi R^3}{3})/(\dfrac{4\pi r^3}{3}/0.74)} = 6.54\frac{r}{R} \quad (Equation\ 3.8)$$

$$fraction\ of\ surface\ atoms\ (fcc) = \frac{\left(\dfrac{Surface\ area\ of\ one\ NP}{Surface\ area\ of\ one\ atom}\right)}{\dfrac{Volume\ of\ one\ NP}{\left(\dfrac{Volume\ of\ one\ atom}{Packing\ factor}\right)}}$$

$$= \frac{(4\pi R^2)/(4r^2)}{(\frac{4\pi R^3}{3})/(\frac{4\pi r^3}{3}/0.74)} = 4.25\frac{r}{R}\quad (Equation\ 3.9)$$

where R is the radius of metal NPs determined from HRTEM characterization; r is the radius of the metal atoms (Pd: 0.139 nm; Pt: 0.136 nm; Ru: 0.134 nm); α is the packing factor, taken as 0.74 for closed-packed *face-centered-cubic* (Pd and Pt) and *hexagonal-close-packing* (Ru) crystal structures.

The TOF values for the thio-ether stabilized NPs for the first catalyst cycle were three orders of magnitude higher than those in the batch reactors (Table 3.5). Since temperature and hydrogen pressure are identical in the two reactor systems, this result is attributed to the fact that the microfluidic reactor is an essentially steady state system (constant reactant concentration with time), while the flask is transient (reactant concentration continuously changing with time). So we do not mean to imply that the reaction proceeds in an identical fashion in the two systems. Rather, this TOF comparison is used only to provide an indication that the microfluidic reactor is a much more efficient system for catalyst evaluation, in terms of both materials and time. In essence, the much higher TOF value provides validation that the high surface area to volume ratios afforded by the combination of nanocatalysts and microfluidics promotes much better access to catalytic sites. Coupled with the much shorter residence times required for complete reactions, the system has great potential for high throughput screening of catalysts.

Table 3.5. TOF values based on estimated fraction of surface atoms for different catalysts for the hydrogenation of 6-bromo-1-hexene (1 mM) in PDMS microfluidic reactors.

Catalysts	TOF (h^{-1})	Batch TOF (h^{-1})
*n*DS-Pd	55±6.1	0.75
*n*DS-Pt	56±7.2	0.17
*n*DS-Ru	16±3.4	0.05
Biotin-Pd	59±5.0	0.78
APTMS-Pd	38±4.2	0.71

3.4.7 Investigation of catalyst deactivation

We noticed sharp decreases in TOF values after the first catalyst cycle. There are two possible explanations for this observation. The first is metal leaching during the reactions. We measured the trace metal content by ICP-AES (detection limit of 80 ppb) in the reaction mixture, but did not observe any metals in the product mixtures. However, we could not completely rule out the possibility of metal leaching because the catalyst loading (~10^{-8} mol) measured in the microfluidic reactors was already at the lower end of the detection limit. Therefore, even if 50% of the metals were lost during the reaction, we would not be able to measure the amount accurately under the current experimental conditions. If significant quantities of metals leached into the reaction mixture, the reaction could essentially be considered homogeneous. We would then observe increased catalyst activity during the second catalyst cycle and very little reaction afterwards. However, we observed a continuous decrease in catalyst activity over several catalyst cycles in our system. Therefore, we conclude that no significant catalyst leaching occurred during the reactions.

The second possible explanation for the observed decreases in catalyst activity is particle aggregation. We used SEM to characterize the glass and PDMS surfaces and NP morphology

99

before and after particle immobilization, along with EDS to determine the elemental composition on surfaces (Figures 3.12 to 3.20). The EDS elemental analysis and line scans again confirmed the successful immobilization of Pd, Pt, and Ru NPs on glass and PDMS surfaces. However, we also observed that some NPs aggregated to micron-size chunks on the surfaces. It was observed that the immobilized particles tended to stay on the side walls of the microfluidic reactors, leaving the glass channel bottom largely uncovered. This uneven particle deposition would make reaction modeling difficult, and thus should be given critical attention. Based on this SEM observation, it would not be accurate to assume monolayer deposition of NPs on the microfluidic channel surfaces.

Particle aggregation could be due to a number of factors. During the first step of particle immobilization, namely aminosilanization by APTMS in anhydrous methanol, complete removal of the methanol was not possible. As a result, the APTMS molecules may have interacted with the hydroxyl groups at the reactor surface, as well as with the hydroxyl groups in the remaining methanol. This may have prevented the even formation and uniform coverage of aminosilane films on the reactor surfaces, which would lead to an uneven distribution of immobilized NPs.

We also used methanol to re-dissolve the NPs because of its compatibility with PDMS. We subsequently observed partial particle aggregation caused by the reduced solubility of thio-ether ligands in the polar solvent. Even though methanol is compatible with the PDMS microfluidic reactors and suitable for the model reaction, it is not a good solvent for nDS [24]. No aggregation of biotin-Pd in methanol was observed, so the aggregation most possibly occurred after immobilization, probably due to change of environment and evaporation of solvent.

Particle aggregation is a major cause of loss of surface atoms and available active sites. For example, in the worst case scenario when several small Ru NPs fuse into a large particle, we

could compare the surface atom fractions. Assuming two spherical Ru particles of 1µm and 3.5 nm in diameter with atoms hexagonally close-packed, the fraction of surface atoms in the smaller particle is approximately 286 times that of the larger particle (as calculated by Equation 3.9).

In reality, we observed that the Ru NPs aggregated into chunky masses of irregular shapes (Figure 3.20(b)). Inevitably, the aggregates preserved some level of porosity, which means the actual loss in the fraction of surface atoms can be much lower than the estimation above. Given the difficulty of estimating the porosity of the aggregates and the lack of 3-D image information, we could not quantify the exact percentage of atoms lost from particle surfaces. However, the estimation based on assumed spherical particles gives some idea of how great the loss in fractional surface atoms could be. In summary, particle aggregation may have played a significant role in decreasing catalyst activity. On the positive side, the reduced surface area resulting from aggregated NPs would mean that the TOF values were actually underestimated for the experiments in the microfluidic reactor. This, in a sense, provides further evidence of the high efficiency at which the system operates.
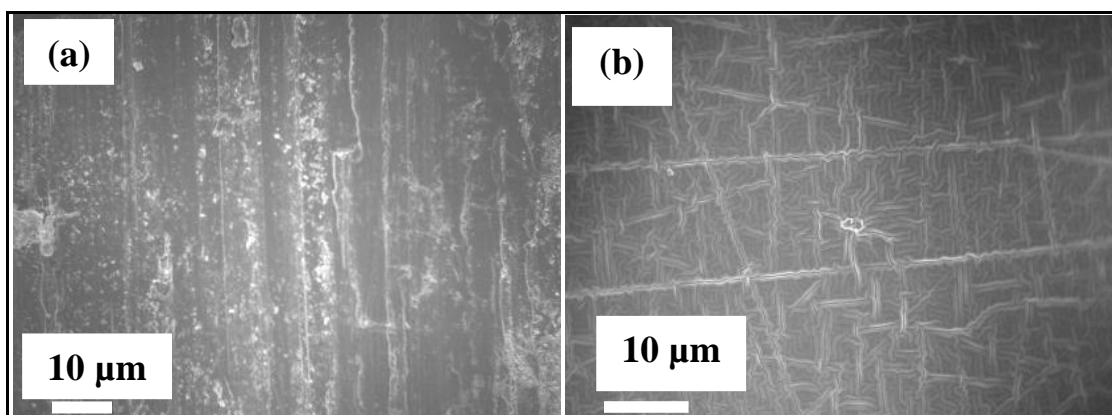
Figure 3.12. SEM images of (a) blank glass at a magnification of 1,200; (b) blank PDMS at a magnification of 1,800.
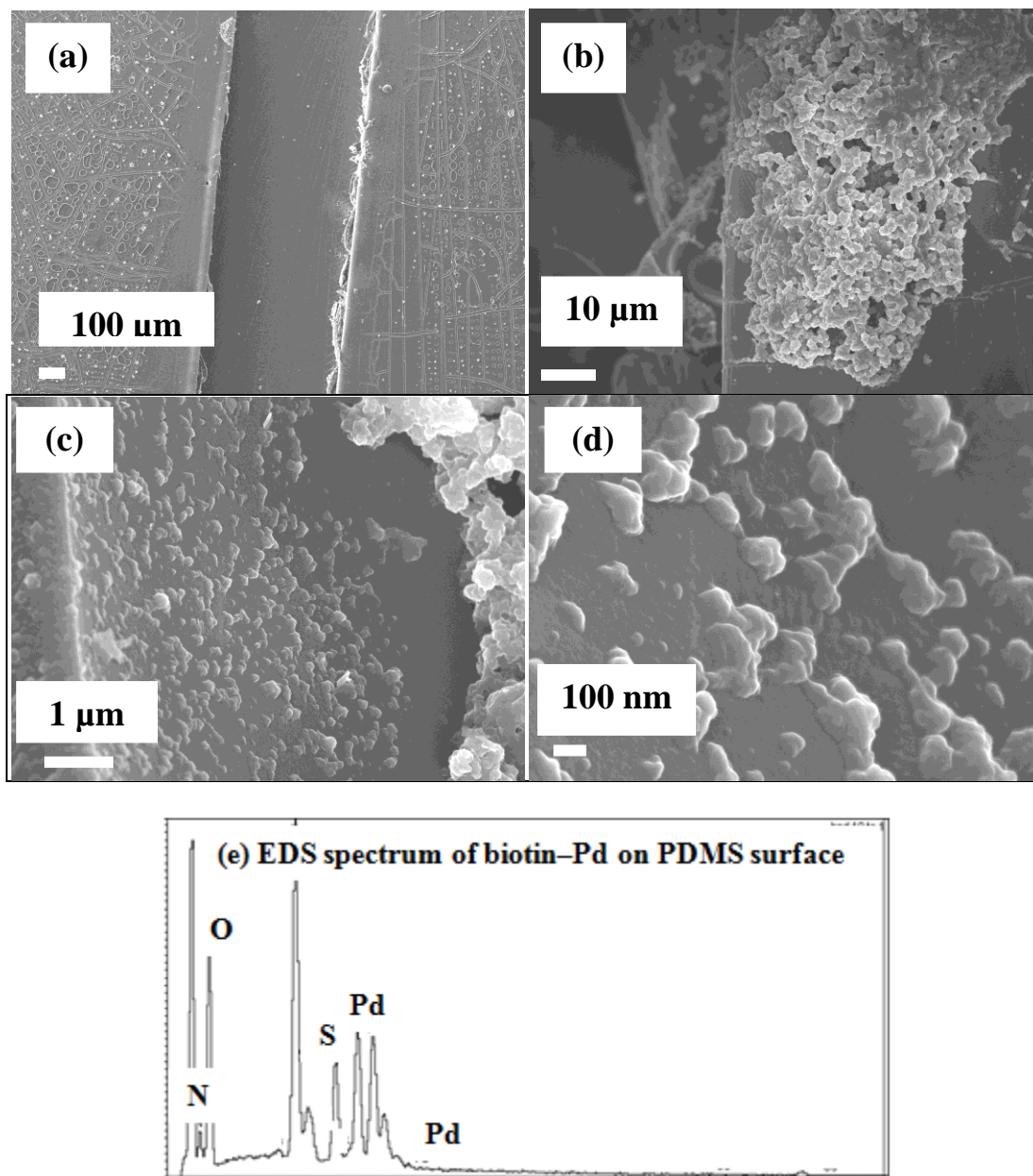
Figure 3.13. SEM images of biotinylated Pd modified PDMS microfluidic channels at different magnifications: (a) 60; (b) 1,300; (c) 16,000; (d) 75,000; (e) EDS spectrum of PDMS surface with immobilized biotin-Pd NPs, confirming its successful immobilization.
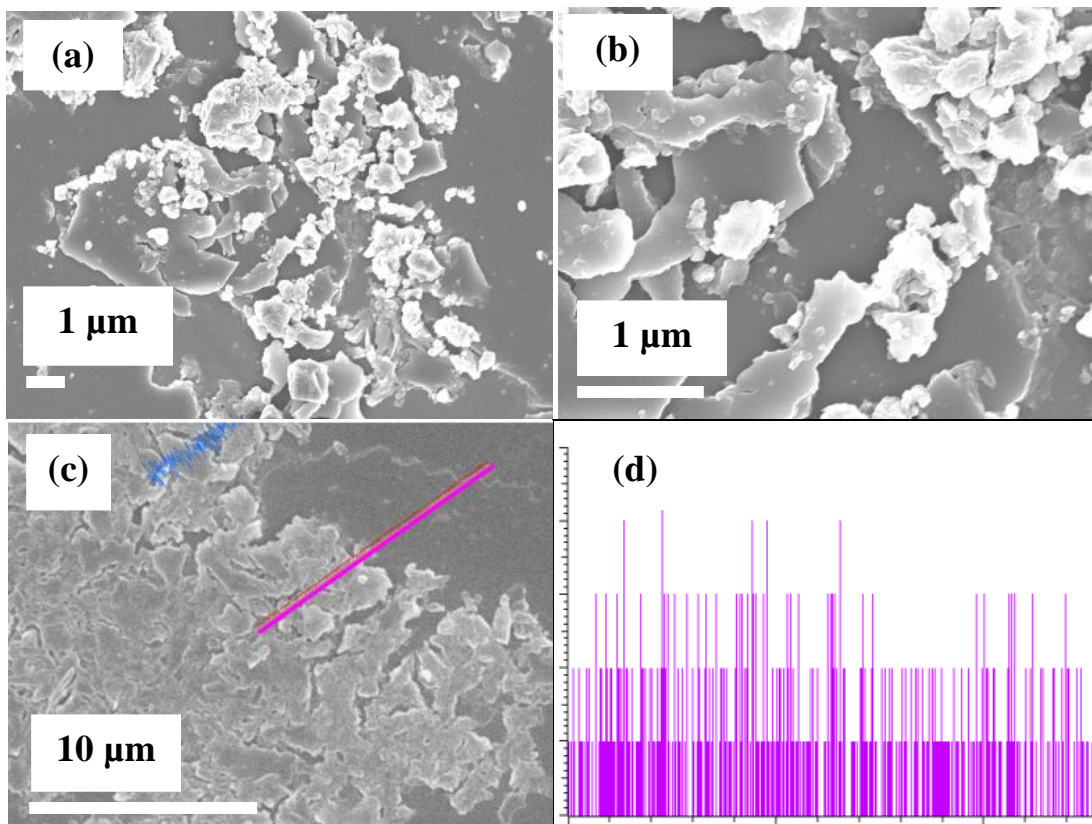
Figure 3.14. SEM images of glass surface with immobilized biotinylated Pd NPs at different magnifications: (a) 9,000; (b) 27,000; (c) 5,500 with an elemental line scan (pink line); (d) enlarged line scan spectrum of Pd, Y-axis: signal strength, X-axis: distance of the line (µM) from left to right.
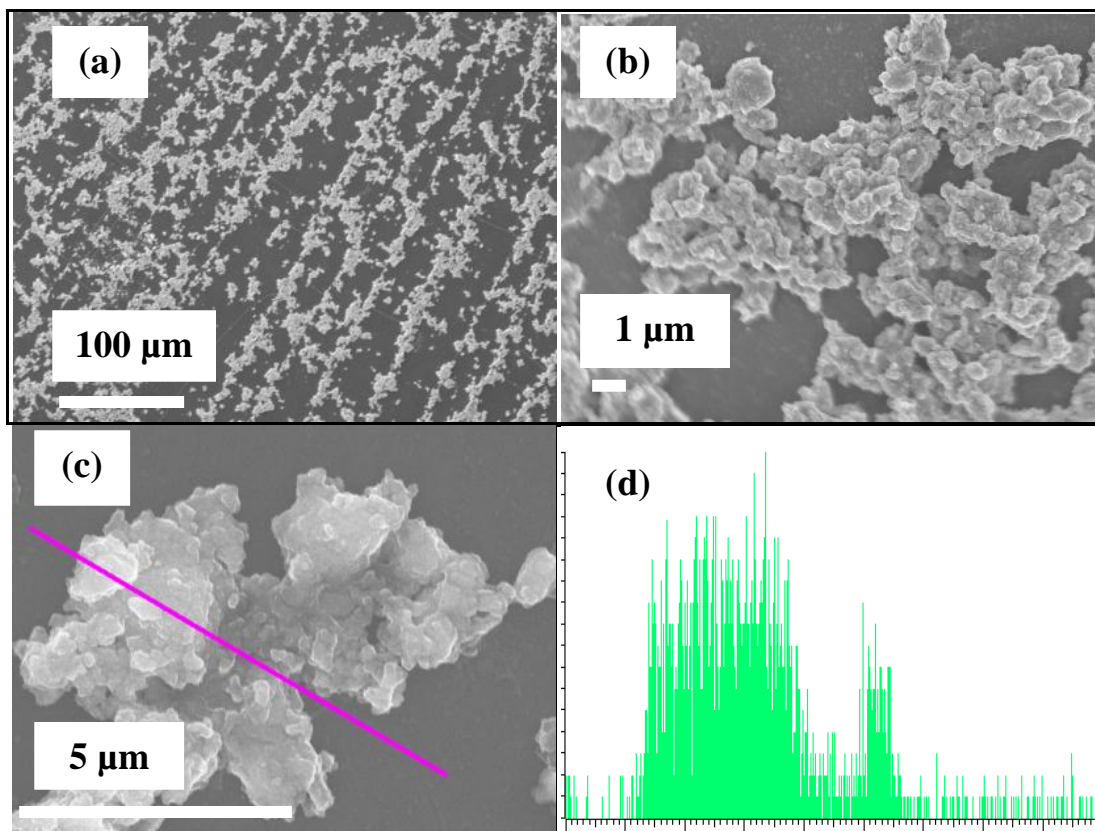
Figure 3.15. SEM images of PDMS surface with immobilized APTMS-Pd NPs at different magnifications: (a) 270; (b) 7,000; (c) 12,000 with an elemental line scan (pink line); (d) enlarged line scan spectrum of Pd, Y-axis: signal strength, X-axis: distance (µm) of the line from left to right.
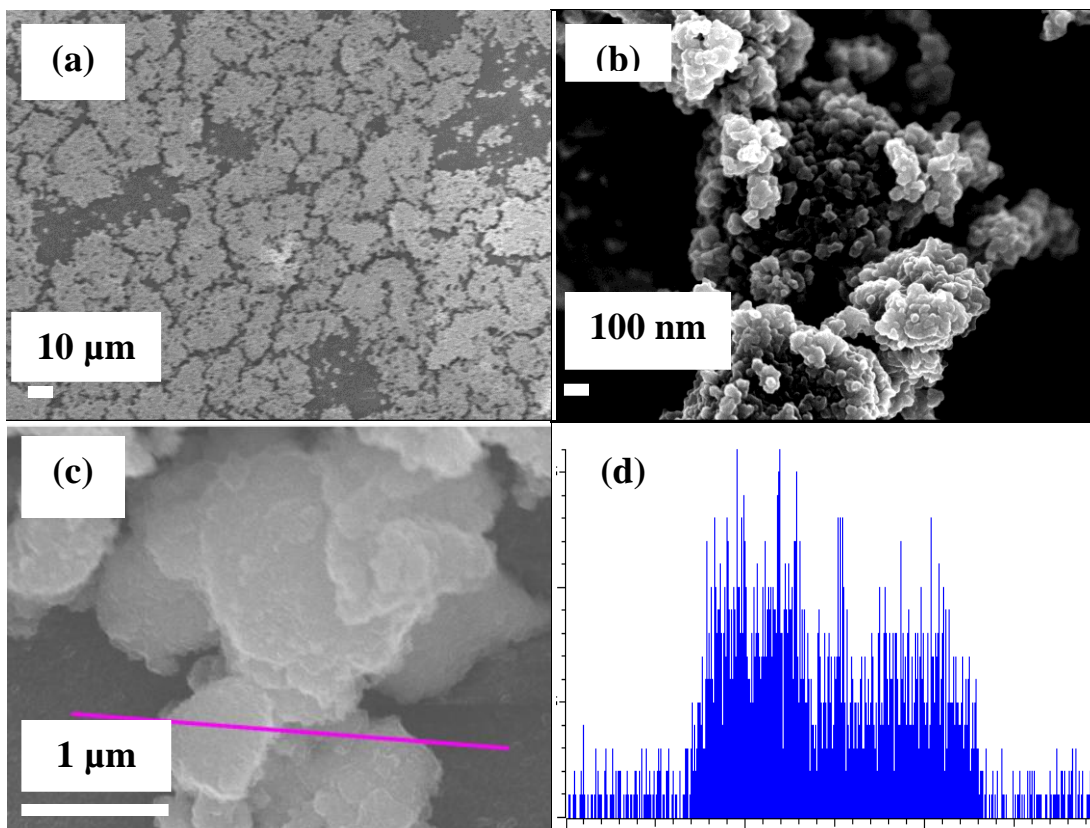
Figure 3.16. SEM images of glass surface with immobilized APTMS-Pd NPs at different magnifications: (a) 500; (b) 50,000; (c) 33,000 with an elemental line scan (pink line); (d) enlarged line scan spectrum of Pd, Y-axis: signal strength, X-axis: distance (μm) of the line from left to right.
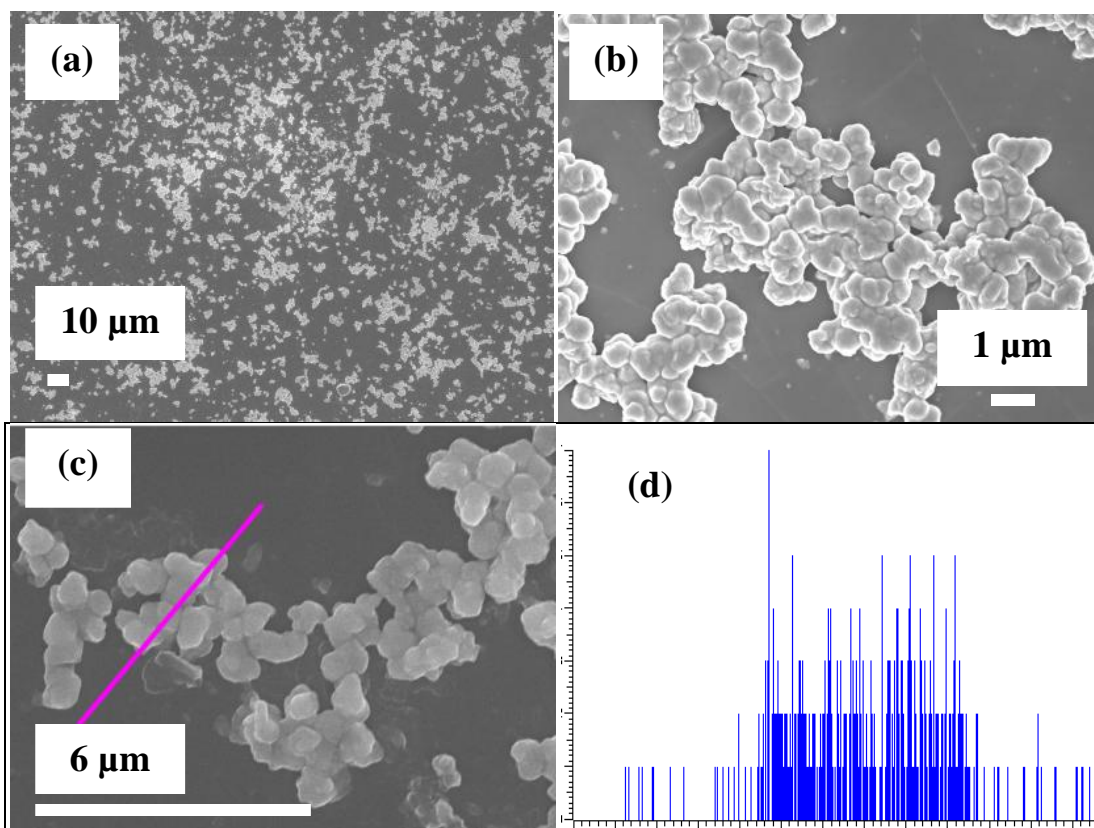
Figure 3.17. SEM images of PDMS surface with immobilized *n*DS-Pt NPs at different magnifications: (a) 500; (b) 10,000; (c) 10,000 with an elemental line scan (pink line); (d) enlarged line scan spectrum of Pt, Y-axis: signal strength, X-axis: distance (µm) of the line from left to right.
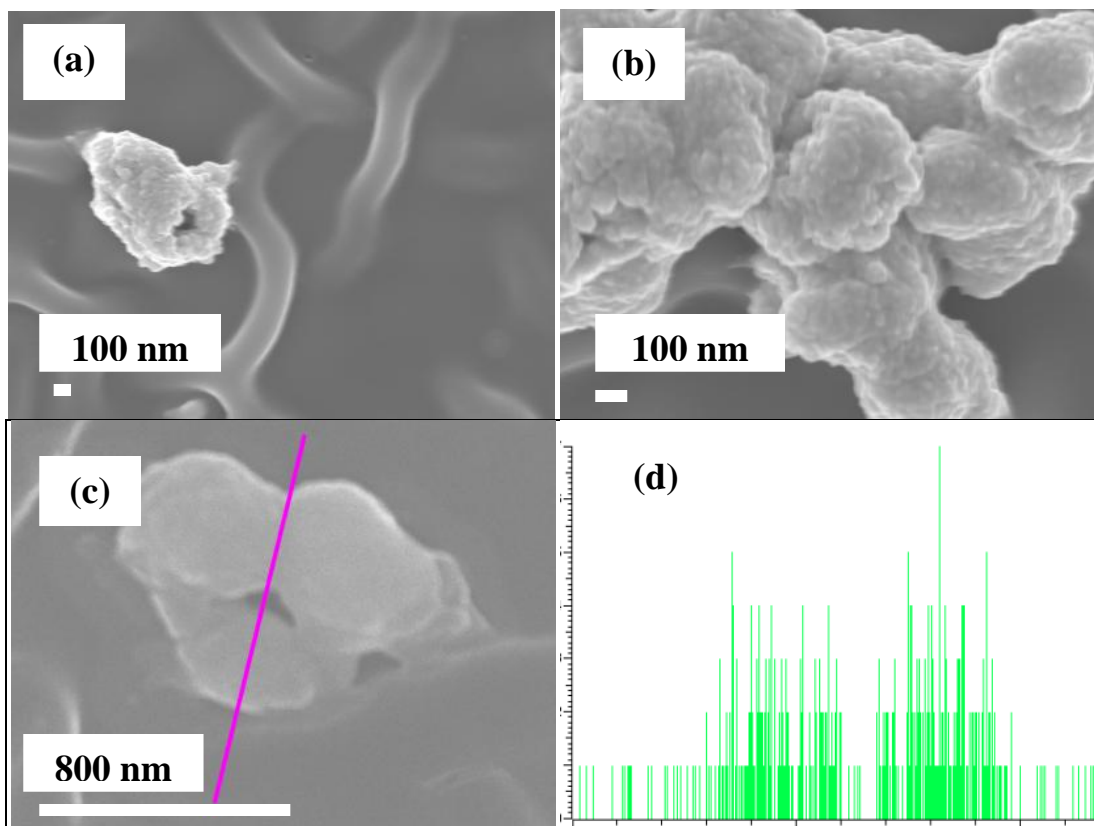
Figure 3.18. SEM images of glass surface with immobilized *n*DS-Pt NPs at different magnifications: (a) 35,000; (b) 70,000; (c) 70,000 with an elemental line scan (pink line); (d) enlarged line scan spectrum of Pt, Y-axis: signal strength, X-axis: distance (μm) of the line from left to right.

.
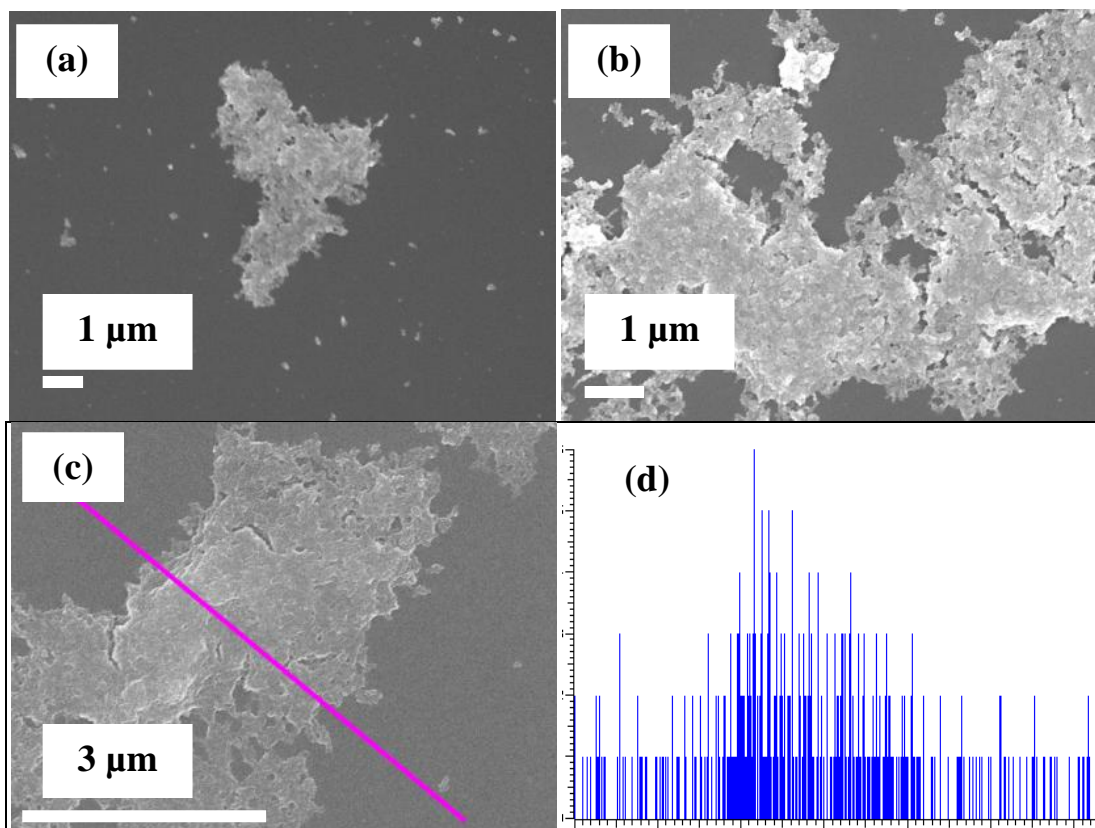
Figure 3.19. SEM images of *n*DS-Ru NPs immobilized on glass surface at different magnifications: (a) 8,500; (b) 13,000; (c) 18,000 with elemental line scan (pink line); (d) enlarged line scan spectrum of Ru, Y-axis: signal strength; X-axis: distance (μm) of the line from left to right.
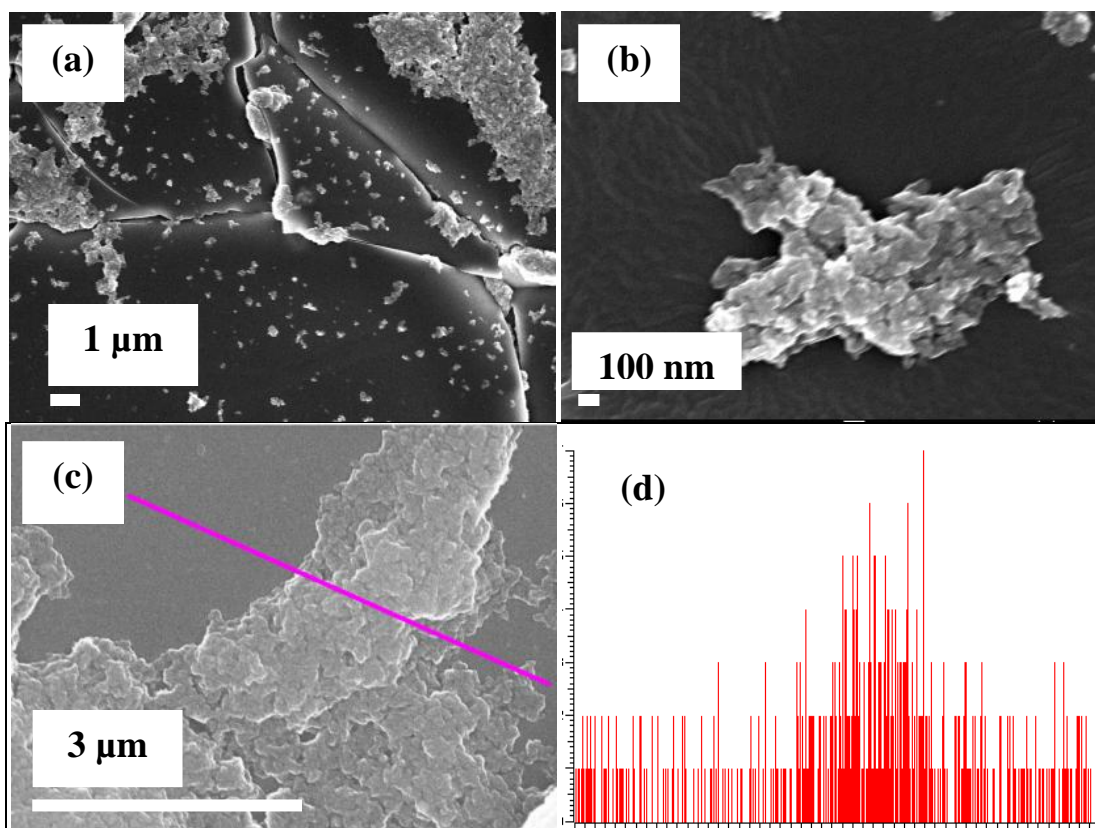
Figure 3.20. SEM images of *n*DS-Ru NPs immobilized on PDMS surface at different magnifications: (a) 6,000; (b) 45,000; (c) 18,000 with elemental line scan (pink line); (d) enlarged line scan spectrum of Ru, Y-axis: signal strength; X-axis: distance (μm) of the line from left to right.

3.5 Conclusions

We have designed and fabricated a PDMS microfluidic reactor by soft lithography. The small dimensions of the reactor have greatly enhanced mass transfer, enabled precise flow control and a much shorter reaction times. The catalytic NPs were robustly immobilized *in-situ* on surfaces of the microfluidic reactors by a simple and reproducible method, and the degree of attachment was confirmed by a number of physical and chemical characterizations. The effectiveness of immobilization was evaluated by hydrogenation of 6-bromo-1-hexene at room temperature and at a hydrogen pressure of 1 atm. High selectivities and reaction conversions ranging from 30 to 100% were achieved in a very short reaction time in the system. Higher

reaction conversions were reached at lower substrate concentrations and slower liquid flow rates. The TOF values in the microfluidic reactor were three orders of magnitude higher than those measured in the batch reactor under similar reaction conditions. This has demonstrated that microfluidics and nanoscale catalysts can be integrated to produce a low cost but highly effective reactor system. Such devices can be used to minimize mass transfer limitations during multiphase hydrogenation reactions, and enable reactions to be carried out in a timely manner under mild reaction conditions. The system provides a convenient tool for high throughput evaluation of catalyst performance under a variety of reaction conditions.

REFERENCES

REFERENCES

1.   Kobayashi, J., Y. Mori, and S. Kobayashi, *Multiphase organic synthesis in microchannel reactors.* Chemistry-an Asian Journal, 2006. **1**(1-2): p. 22-35.

2.   Irfan, M., T.N. Glasnov, and C.O. Kappe, *Heterogeneous Catalytic Hydrogenation Reactions in Continuous-Flow Reactors.* Chemsuschem, 2011. **4**(3): p. 300-316.

3.   Bonnemann, H. and R.M. Richards, *Nanoscopic metal particles - Synthetic methods and potential applications.* European Journal of Inorganic Chemistry, 2001(10): p. 2455-2480.

4.   Raimondi, F., et al., *Nanoparticles in energy technology: Examples from electrochemistry and catalysis.* Angewandte Chemie-International Edition, 2005. **44**(15): p. 2190-2209.

5.   Thomas, J.M., et al., *High-performance nanocatalysts for single-step hydrogenations.* Accounts of Chemical Research, 2003. **36**(1): p. 20-30.

6.   Ganesan, M., R.G. Freemantle, and S.O. Obare, *Monodisperse thioether-stabilized palladium nanoparticles: Synthesis, characterization, and reactivity.* Chemistry of Materials, 2007. **19**(14): p. 3464-3471.

7.   Jahnisch, K., et al., *Chemistry in microstructured reactors.* Angewandte Chemie-International Edition, 2004. **43**(4): p. 406-446.

8.   Fletcher, P.D.I., et al., *Micro reactors: principles and applications in organic synthesis.* Tetrahedron, 2002. **58**(24): p. 4735-4757.

9.   Fukuyama, T., et al., *Adventures in inner space: Microflow systems for practical organic synthesis.* Synlett, 2008(2): p. 151-163.

10.   Jas, G. and A. Kirschning, *Continuous Flow Techniques in Organic Synthesis.* Chem. Eur. J., 2003. **9**: p. 5708-5723.

11.   Mason, B.P., et al., *Greener approaches to organic synthesis using microreactor technology.* Chemical Reviews, 2007. **107**(6): p. 2300-2318.

12.   Watts, P. and S.J. Haswell, *The application of micro reactors for organic synthesis.* Chemical Society Reviews, 2005. **34**(3): p. 235-246.

13.   Kiwi-Minsker, L. and A. Renken, *Microstructured reactors for catalytic reactions.* Catalysis Today, 2005. **110**(1-2): p. 2-14.

14.   Klemm, E., et al., *Microstructured reactors in heterogeneous catalysis.* Chemical Engineering & Technology, 2007. **30**(12): p. 1615-1621.

15.   Xia, Y.N. and G.M. Whitesides, *Soft lithography.* Angewandte Chemie-International Edition, 1998. **37**(5): p. 551-575.

16.   Castellana, E.T., et al., *Direct writing of metal nanoparticle films inside sealed microfluidic channels.* Analytical Chemistry, 2006. **78**(1): p. 107-112.

17.   Zawadzki, M. and J. Okal, *Synthesis and structure characterization of Ru nanoparticles stabilized by PVP or gamma-Al2O3.* Materials Research Bulletin, 2008. **43**(11): p. 3111-3121.

18.   McCreedy, T., *Rapid prototyping of glass and PDMS microstructures for micro total analytical systems and micro chemical reactors by microfabrication in the general laboratory.* Analytica Chimica Acta, 2001. **427**(1): p. 39-43.

19.   McDonald, J.C. and G.M. Whitesides, *Poly(dimethylsiloxane) as a material for fabricating microfluidic devices.* Accounts of Chemical Research, 2002. **35**(7): p. 491-499.

20.   Whitesides, G.M. and A.D. Stroock, *Flexible methods for microfluidics.* Physics Today, 2001. **54**(6): p. 42-48.

21.   Lin, R., et al., *In-situ immobilization of palladium nanoparticles in microfluidic reactors and assessment of their catalytic reactivity.* Nanotechnology, 2010: p. 325605.

22.   Iles, A., et al., *A Simple technique for microfluidic heterogeneous catalytic hydrogenation reactor fabrication.* Catalysis Letters, 2007. **114**(1-2): p. 71-74.

23.   McCreedy, T., *Fabrication techniques and materials commonly used for the production of microreactors and micro total analytical systems.* Trac-Trends in Analytical Chemistry, 2000. **19**(6): p. 396-401.

24.   Lee, J.N., C. Park, and G.M. Whitesides, *Solvent compatibility of poly(dimethylsiloxane)-based microfluidic devices.* Analytical Chemistry, 2003. **75**(23): p. 6544-6554.

25.   Losey, M.W., M.A. Schmidt, and K.F. Jensen, *Microfabricated multiphase packed-bed reactors: Characterization of mass transfer and reactions.* Industrial & Engineering Chemistry Research, 2001. **40**(12): p. 2555-2562.

26.   Besser, R.S., X. Ouyang, and H. Surangalikar, *Hydrocarbon hydrogenation and dehydrogenation reactions in microfabricated catalytic reactors.* Chemical Engineering Science, 2003. **58**(1): p. 19-26.

27.   Nassar, R., et al., *Modeling of cyclohexene hydrogenation and dehydrogenation reactions in a continuous-flow microreactor.* Catalysis Today, 2007. **120**(1): p. 121-124.

28.   Abdallah, R., et al., *Gas-liquid and gas-liquid-solid catalysis in a mesh microreactor.* Chemical Communications, 2004(4): p. 372-373.

29.   Kobayashi, J., Y. Mori, and S. Kobayashi, *Hydrogenation reactions using scCO(2) as a solvent in microchannel reactors.* Chemical Communications, 2005(20): p. 2567-2568.

30.   Kobayashi, J., et al., *A microfluidic device for conducting gas-liquid-solid hydrogenation reactions.* Science, 2004. **304**(5675): p. 1305-1308.

31.   Trapp, O., et al., *High-throughput kinetic study of hydrogenation over palladium nanoparticles: Combination of reaction and analysis.* Chemistry-a European Journal, 2008. **14**(15): p. 4657-4666.

32.   Trapp, O., et al., *High-throughput screening of catalysts by combining reaction and analysis.* Angewandte Chemie-International Edition, 2007. **46**(38): p. 7307-7310.

33.   Duffy, D.C., et al., *Rapid prototyping of microfluidic systems in poly(dimethylsiloxane).* Analytical Chemistry, 1998. **70**(23): p. 4974-4984.

34.   McDonald, J.C., et al., *Fabrication of microfluidic systems in poly(dimethylsiloxane).* Electrophoresis, 2000. **21**(1): p. 27-40.

35.   Kong, D.Y., et al., *Biofunctionalization of CeF3 : Tb3+ nanoparticles.* Nanotechnology, 2007. **18**(7).

36.   Nidumolu, B.G., et al., *Functionalization of gold and glass surfaces with magnetic nanoparticles using biomolecular interactions.* Biotechnology Progress, 2006. **22**(1): p. 91-95.

37.   Ye, L., R. Pelton, and M.A. Brook, *Biotinylation of TiO2 nanoparticles and their conjugation with streptavidin.* Langmuir, 2007. **23**(10): p. 5630-5637.

38.   Liu, Z. and M.D. Amiridis, *Quantitative FT-IRRAS spectroscopic studies of the interaction of avidin with biotin on functionalized quartz surfaces.* Journal of Physical Chemistry B, 2005. **109**(35): p. 16866-16872.

39.   Silverstein, R.M., G.C. Bassler, and T.C. Morrill, eds. *Spectrometric Identification of Organic Compounds*. 1991, NewYork:John Wiley& Sons, INC.

40.   Chisholm, D., *A theoretical basis for the Lockhart-Martinelli correlation for two-phase flow.* International Journal of Heat and Mass Transfer, 1967. **10**(12): p. 1767-1778.

41.   Rebrov, E.V., et al., *Selective Hydrogenation of 2-Methyl-3-butyne-2-ol in a Wall-Coated Capillary Microreactor with a Pd(25)Zn(75)/TiO(2) Catalyst.* Organic Process Research & Development, 2009. **13**(5): p. 991-998.

42.   Rebrov, E.V., et al., *Gold supported on mesoporous titania thin films for application in microstructured reactors in low-temperature water-gas shift reaction.* Catalysis Today, 2008. **138**(3-4): p. 210-215.

43.   Rebrov, E.V., et al., *Capillary microreactors wall-coated with mesoporous titania thin film catalyst supports.* Lab on a Chip, 2009. **9**(4): p. 503-506.

44.   Rebrov, E.V., et al., *Thin catalytic coatings on microreactor walls A way to make industrial processes more efficient.* Chimica Oggi-Chemistry Today, 2009. **27**(4): p. 4-7.

45.   Ruta, M., N. Semagina, and L. Kiwi-Minsker, *Monodispersed Pd nanoparticles for acetylene selective hydrogenation: Particle size and support effects.* Journal of Physical Chemistry C, 2008. **112**(35): p. 13635-13641.

46.   Liu, R.X., et al., *Selective hydrogenation of citral catalyzed with palladium nanoparticles in CO2-in-water emulsion.* Green Chemistry, 2009. **11**(7): p. 979-985.

47.   Mekasuwandumrong, O., et al., *Preparation of Nano-Pd/SiO2 by One-Step Flame Spray Pyrolysis and its Hydrogenation Activities: Comparison to the Conventional Impregnation Method.* Industrial & Engineering Chemistry Research, 2009. **48**(6): p. 2819-2825.

48.   Weerachawanasak, P., et al., *Effect of strong metal-support interaction on the catalytic performance of Pd/TiO2 in the liquid-phase semi hydrogenation of phenylacetylene.* Journal of Catalysis, 2009. **262**(2): p. 199-205.

49.   Boudart, M., *Turnover rates in heterogeneous catalysis.* Chem. Rev. , 1995. **95**: p. 661-666.

50.   Conway, J.H., N.J.A. Sloan, and E. Bannai, *Sphere packings, lattices, and groups.* Springer, 1999: p. Section 6.3.

CHAPTER 4 CATALYTIC ACTIVITY ASSESSMENT OF NOBLE METALLIC AND

BIMETALLIC NANOPARTICLES IN THICK WALL GLASS CAPILLARY

MICROREACTORS

4.1 Abstract

The *in-situ* immobilization method described in Chapter 3 was extended to PVP-stabilized Pd, Ru and PdRu alloy NPs in PDMS microfluidic reactors. XPS characterization confirmed that the loading of the PVP-stabilized nanocatalysts on the microreactor surfaces was higher than that of *n*DS-stabilized NPs. However, due to the incomplete removal of the capping agent, the PDMS microfluidic reactors with immobilized PVP-stabilized NPs did not show any reactivity for hydrogenation of 6-bromo-1-hexene, pyruvic acid, or lactic acid. Improvement in the system was therefore necessary.

Although the PDMS microfluidic reactor system allows simple and convenient high throughput assessments of noble metallic catalysts and greatly improves catalyst efficiency, a number of issues needed to be addressed. Due to the swelling of the PDMS microfluidic reactor upon exposure to organic solvents, metal NPs had to be re-dispersed in other less compatible solvents. Unfortunately, the stabilizing ligands had limited solubility in the new solvents, causing particle aggregation and catalyst deactivation. In addition, the PDMS microfluidic system has low tolerance for heat and pressure, making catalyst pre-reduction impossible. For these reasons, a thick wall glass capillary system with high heat and chemical tolerance was used to improve catalyst performance. Both carbon-carbon double bond reduction reactions and selective hydrogenation of trans-cinnamaldehyde (CAL) were used to evaluate catalyst activity, selectivity and reusability under different reaction conditions. Parameters assessed included reaction temperatures, substrate concentrations, and liquid flow rates. The glass capillary reactor systems achieved the goals of higher catalyst stability and steady and continuous production of the desired intermediates.

4.2 Introduction

The catalytic hydrogenation of CAL using noble metallic catalysts has wide application in the fine chemicals and pharmaceutical industries. The hydrogenation products, cinnamyl alcohol (COL) and hydrocinnamyl alcohol (HCOL), are important ingredients in the perfume, cosmetics and food industries, while hydrocinnamaldehyde (HCAL) was found in recent years to be a useful intermediate in the synthesis of HIV drugs [1]. The ability to selectively produce any of the three products (HCAL, COL, HCOL) by the choice of different catalysts of distinct structures would be a desirable achievement. In addition, a systematic study of the effects of reaction parameters on catalyst behavior is critical in performance enhancement and process optimization. The information generated would also be helpful in reactor design.

Several attempts have been reported to use wall-coated capillary microreactor systems to study the performance of metal catalysts for α, β-unsaturated aldehyde and ketone hydrogenations [2-9]. The capillary microreactor systems were well-characterized, and coated catalytic thin-film around the walls proved to be efficient. Pd catalysts were shown to exhibit excellent activity and selectivity towards HCAL and even HCOL, while Ru catalysts demonstrated moderate activity and selectivity towards HCAL and COL [10]. The potential for synergetic effects of Pd-Ru alloy bimetallic NPs on this reaction are also of great interest. A glass capillary reactor system was built to incorporate well-defined colloidal noble metallic and bimetallic catalysts to study how the overall catalyst performance in such a continuous flow system depends on various parameters.

In this chapter, we report the systematic improvement resulting from combining nanocatalysts and microfluidics to enhance reaction stability and efficiency of multiphase hydrogenations. We used a thick wall glass capillary reactor to attain greater mechanical

strength, higher temperature tolerance and better chemical compatibility to address the particle aggregation issues discussed in the previous chapter. The noble metallic and bimetallic NPs stabilized either by thio-ether or PVP were immobilized on the capillary surfaces for high throughput assessment of intrinsic catalytic activity. The simple and robust immobilization protocol was based on our previously reported scheme [11]. Due to better chemical resistance, it was not necessary to re-dissolve nDS-stabilized NPs in methanol. Instead, nanoparticles could be kept in their original toluene solvent, thus preventing particle agglomeration. In addition, the capillary system enabled high temperature catalyst activation, thus promoting catalyst recycling and regeneration.

4.3 Experimental

4.3.1 Materials

Trans-cinnamaldehyde (99%), pyruvic acid (≥97%) and anhydrous methanol (99.8%) were purchased from Sigma-Aldrich (St. Louis, MO). Cinnamyl alcohol (98%), hydrocinnamaldehyde (95%) and 3-phenyl-1-propanol (99%) were purchased from Alfa Aesar (Ward Hill, MA). Isopropyl alcohol (ACS grade) was obtained from Macron Chemicals (Charlotte, NC). High purity hydrogen gas tank (99.999995%) was obtained from Airgas Great Lakes (Lansing, MI).

4.3.2 Set-up of capillary reactor system

The thick wall glass capillary (0.508 +/- 0.0254 mm I.D. × 6.4 +/- 0.460 mm O.D. × 30.084 cm length, Friedrich & Dimmock Inc., Millville, NJ,) was first placed inside two pieces of aluminum coats (Michigan State University Mechanical Machine Shop, East Lansing, MI) and clamped together. The glass capillary was connected to a PTFE tubing (0.5 mm I.D. × 1.5875 mm O.D., VICI Valco Instruments Co. Inc., Houston, TX) for sample introduction and collection by Swagelok zero-dead-volume stainless fittings (0.5 mm I.D. × 6.4 mm O.D., H. E. Lennon,

Farmington Hills, MI). A heavy insulated heating tape with a digital temperature controller (BriskHeat, Columbus, OH) was wrapped tightly around the two pieces of aluminum coats. The reaction temperature was controlled by the digital controller and a thermal couple inserted underneath the heating tape. Another temperature controller was used to measure the temperature of the exterior wall of the glass capillary. The typical temperature difference between the aluminum coat and the capillary was about 10°C, and remained stable throughout each reaction process.

One end of the glass capillary was connected to the Y-inlet PDMS microfluidic channel described in Chapter 3. The gas and liquid were first mixed in the PDMS channels and then transported into the glass capillary. The other end of the glass capillary was connected to a glass vial for sample collection. The collecting vial was immersed in ice water to ensure minimal sample evaporation. The liquid reactant flow rate was controlled by a syringe pump (PHD 22/2000, Harvard Apparatus, Holliston, MA), while the gas flow rate was controlled by a Bronkhorst hydrogen mass flow controller (F-201CV-020-AGD-20-V, Ruurlo, Nederland). The set-up is shown in Figure 4.1.
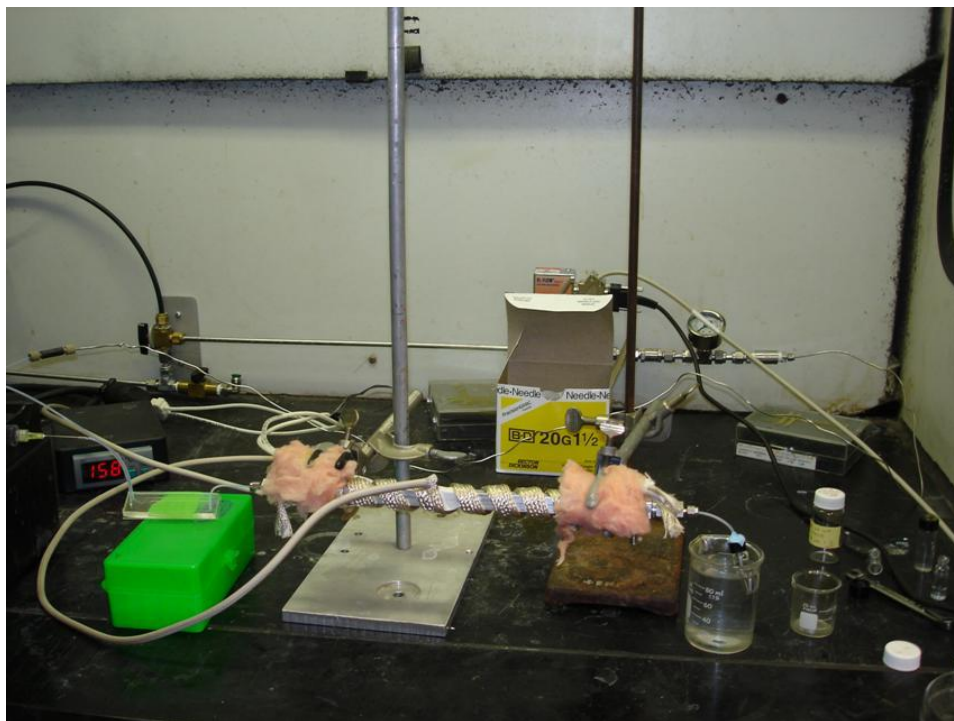
Figure 4.1. Set-up of the glass capillary reactor system. The heavy wall capillary was placed inside an aluminum coat around which the heating tape was wrapped. The heating tape was connected to a digital temperature controller to monitor the temperature.

4.3.3 *In-situ* immobilization of noble metallic and bimetallic NPs in the capillary system

The glass capillaries were first thoroughly cleaned with hexane, acetone, isopropanol, ethanol, methanol, and DI water, and dried with pure nitrogen. A mixture of HCl, hydrogen peroxide (H_2O_2) and DI water (1:1:5 in volume ratio) was introduced into the capillary and allowed to remain for 15 min, followed by rinsing with DI water for 5 min and drying with pure nitrogen. This step introduced a rich layer of hydroxyl groups on the glass surface. The surfaces were coated with primary amine groups by aminosilanization. Five percent (5%, v/v) of the APTMS solution in anhydrous methanol was kept in the capillary for 30 min, followed by rinsing with methanol, drying with nitrogen and curing in the oven at 120°C for 2 h. *n*DS-stabilized (Pd and Ru) and PVP-stabilized NPs (Pd, Ru and PdRu alloy) dissolved in toluene and

methanol, respectively, were immobilized *in situ* inside the aminosilanized capillary walls by allowing the solutions to sit in the capped capillary overnight at room temperature. The solution was evaporated by flowing nitrogen and the dry capillaries cured in an oven at 70°C for 2 h (Figure 4.2). The capillaries with different types of NPs were labeled as follows: *n*DS-Ru_CAP, *n*DS-Pd_CAP, PVP-Pd_CAP, PVP-PdRu_CAP, PVP-Ru1_CAP, PVP-Ru2_CAP, and PVP-Ru3_CAP. PVP-stabilized Ru NPs of different sizes (see Table 4.1) were immobilized in the three PVP-Ru capillaries. A similar immobilization procedure was carried out on glass slides (1 × 1 cm) for the purpose of XPS characterization.
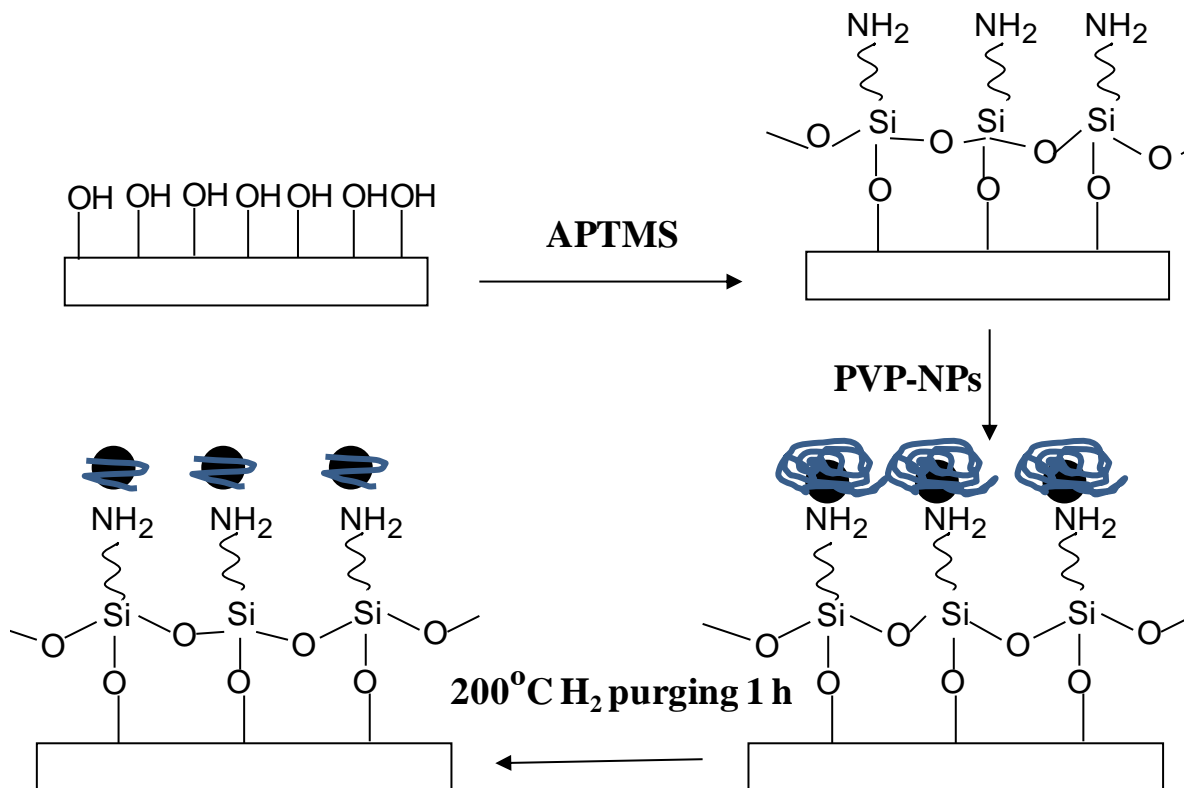
Figure 4.2. Immobilization scheme for PVP-stabilized NPs inside heavy wall glass capillary reactors. PVP-stabilized NPs were attached to the aminosilanized glass surfaces, and the stabilizers were partially removed after hydrogen reduction at $200^{\circ}C$ for 1 h, allowing substrate access to the surface atoms.

4.3.4 Determination of catalyst loading in capillary reactors and reaction mixtures

The glass capillary was cut into 5-mm pieces and immersed in 2 mL of aqua regia (3 volumes of HCl and 1 volume of concentrated nitric acid) for 1 h to completely dissolve the metal inside the capillary. All reaction mixtures and rinsing solutions were collected, evaporated and dissolved in aqua regia solutions. The aqua regia solution was later diluted with DI water to 5% solution and analyzed by ICP-AES. Standard curves of Pd and Ru elements were constructed by measuring the concentrations of five standard samples ranging from 0.08 ppm to 50 ppm.

124

4.3.5 Homogeneous hydrogenation in PDMS microfluidic reactors

In a typical homogeneous hydrogenation reaction, colloidal NPs were suspended in the substrate solution (20 mM) with a catalyst to substrate molar ratio of 100 to 1. The light brown mixture was then introduced into the PDMS microfluidic reactor system along with high purity hydrogen, and the reacting medium was collected over specific time intervals. The samples were then diluted 20 times and analyzed by GC.

4.3.6 Heterogeneous hydrogenation in PDMS and capillary microreactors

The details of heterogeneous hydrogenation in PDMS microfluidic reactors were described in Chapter 3. For a typical heterogeneous hydrogenation in the capillary microreactor, the system was first saturated with high purity hydrogen at a flow rate of 8.0 mL/min at 200°C for 1 h to activate the catalysts. To ensure sufficient surface wetting, the capillary was rinsed with a reaction solvent under hydrogen atmosphere at the same temperature for another 0.5 h, with a liquid flow rate of 0.1 mL/h and a gas flow rate of 2.4 mL/min. The liquid and gas were mixed in blank Y-shaped PDMS microfluidic channels connected to the capillary. After catalyst pre-treatment, the liquid substrate at various target concentrations was introduced into the capillary at controlled flow rates and mixed with high purity hydrogen at the target temperature. Once the system temperature and observed flow pattern were stable, reaction products were collected over specific time intervals into a vial immersed in ice water at the outlet of the capillary.

Hydrogenation of 6-bromo-1-hexene (substrate concentration 10 mM in anhydrous methanol) was conducted at room temperature and 1 atm. hydrogen pressure. Hydrogenation of CAL (at substrate concentrations of 5 to 20 mM in IPA) was conducted at temperatures between 65 and 150°C and 1 atm. hydrogen pressure (Scheme 4.1). Control experiments were conducted

in blank capillary microreactors under similar reaction conditions. Between each reaction, the capillary was regenerated by purging with hydrogen and rinsing with a solvent. The rinsing solvent was collected and analyzed by ICP-AES to determine if any catalyst leaching had occurred.
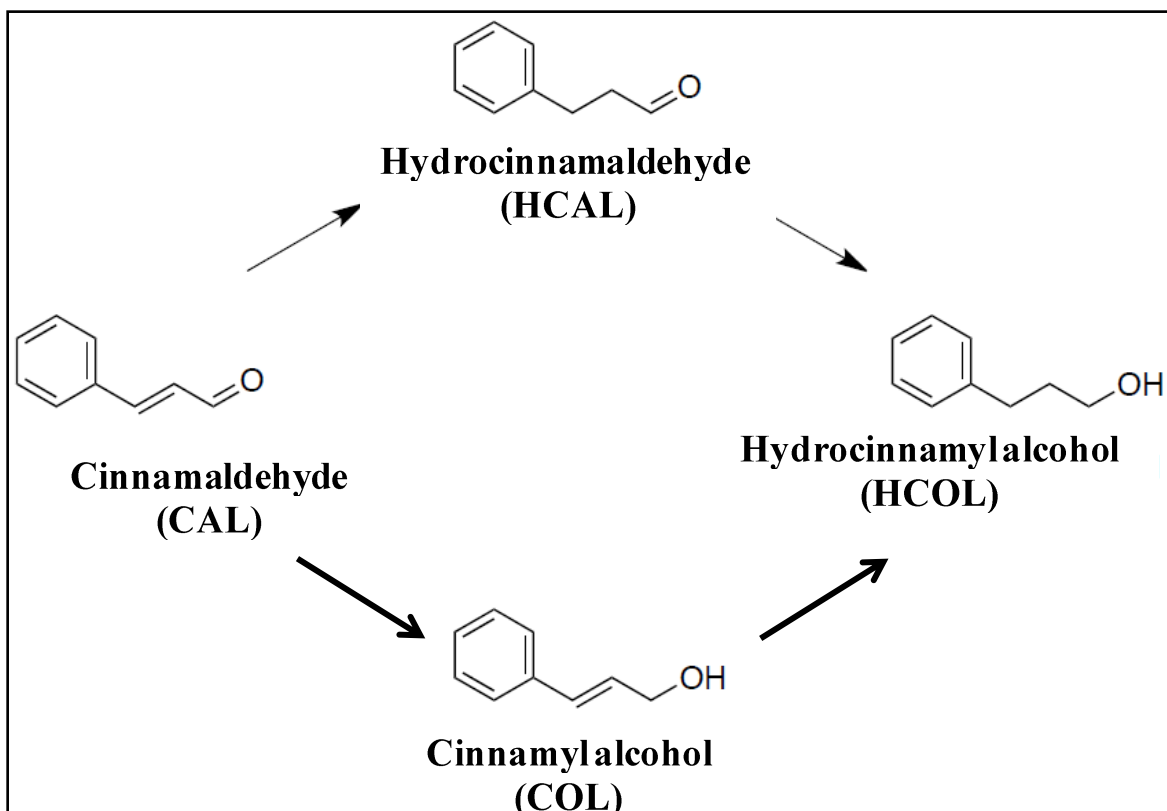
Scheme 4.1. Reaction scheme for hydrogenation of CAL: C=C reduction leads to HCAL, C=O reduction leads to COL; HCOL is produced when both bonds are reduced.

4.3.7 GC analysis of reaction products

The samples were diluted with the same solvents used in the reactions, and analyzed by a GC (Bruker 450, Bruker Daltonics, Fremont, CA) equipped with FID and an auto sampler. The GC column was coated with a highly inert non-polar 100% dimethylpolysiloxane phase (column

dimension 15 m length $\times$ 0.25 mm I.D. $\times$ 0.25 µm film thickness, VF-1ms, Varian Inc., Lake

Forest, CA). .   For analysis of allyl bromide compounds, the oven was kept at 40°C for 2 min,

and ramped to 200°C at a rate of 10°C/min. For analysis of CAL and its hydrogenation

products, the oven was kept at 90°C for 2 min, ramped to 200°C at a rate of 15°C/min and held

at 200°C for 1.7 min. The detector temperature was 250°C and the injection temperature was

280°C. The multi-point standard calibration curves shown in Figure 4.3 were used to compute

conversions, product compositions and total material balances.
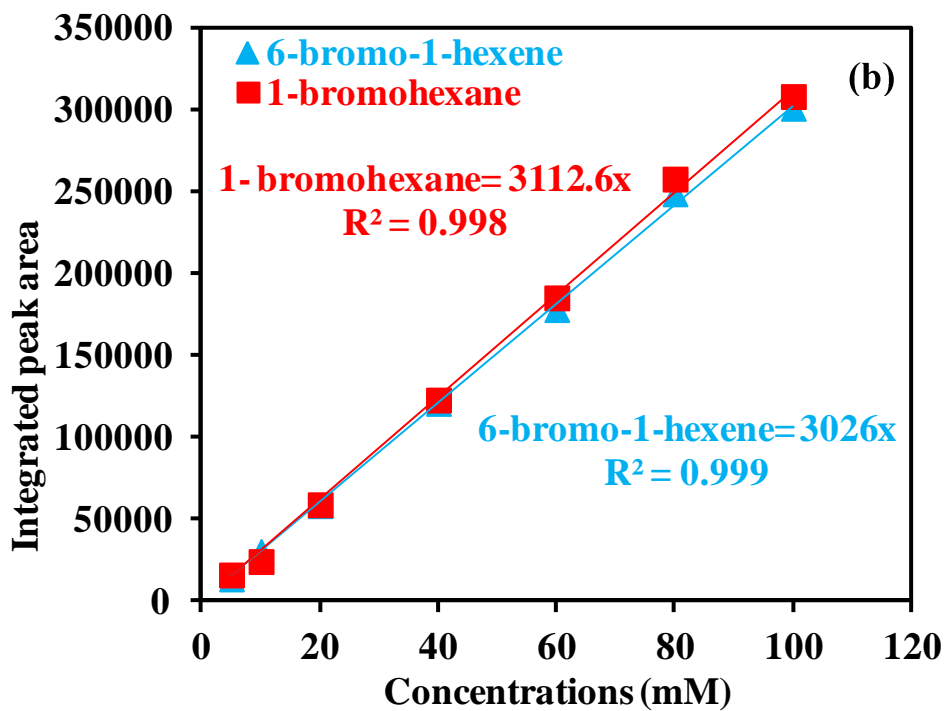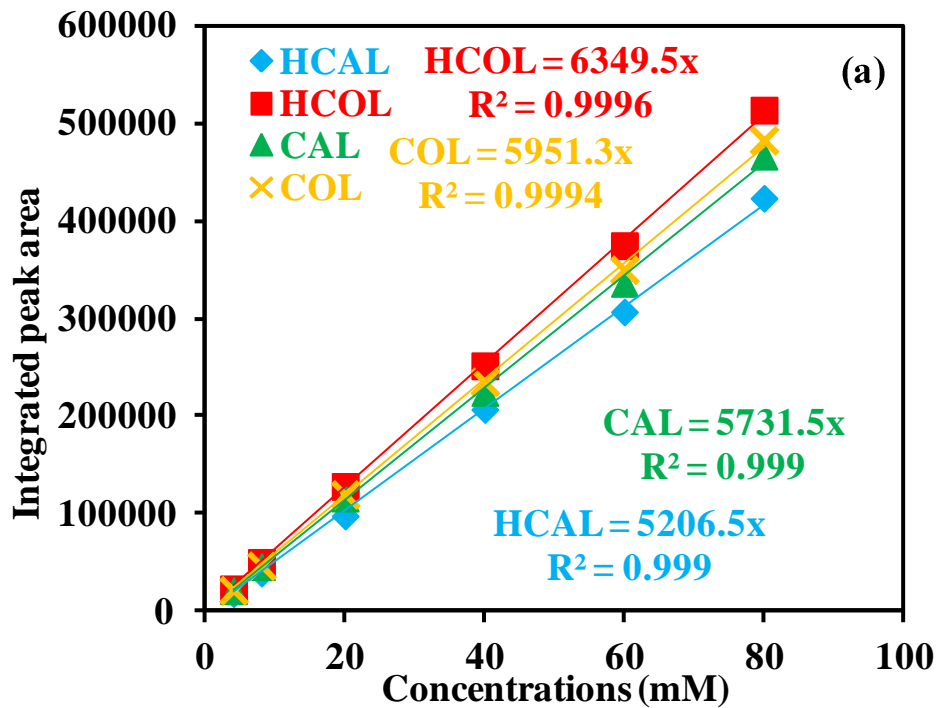
Figure 4.3. GC Calibration curves for (a) CAL, HCAL, COL and HCOL; (b) 6-bromo-1-hexene and 1-bromohexane.

128

4.3.8 Thermogravimetric/differential analysis of *n*DS-Ru NPs

This analysis was carried out on a thermogravimetric analyzer (TGA/DSC, Mettler-Toledo Inc., Columbus, OH). Its purpose was to characterize the transformation of the catalysts during the heating treatments. In a typical analysis, about 70 mg of the dried NP sample was placed in an alumina sample holder, and heated from room temperature to 700°C at a rate of 10°C/min, under a nitrogen atmosphere.

4.4 Results and discussions

4.4.1 Catalyst immobilization on glass capillary walls

XPS results confirmed successful immobilization of the PVP-stabilized NPs on the glass surfaces (Table 4.1). The atomic concentrations of immobilized NPs on the surfaces were the averages of three replicate measurements. Compared to the data acquired on blank surfaces, we observed sharp increases in C and N on the aminosilanized surfaces, along with decreases in Si and O. The increased C and N contents are due to the molecular structure of APTMS with a 3-carbon arm and a primary amine group at the end. The PVP stabilizer surrounding the NPs also contributed to the increase in carbon content on the surface. The "loss" in the surface concentrations of Si and O is due to coverage of the glass surfaces following aminosilanization. The characteristic metal elements from the NPs were detected by XPS on all surfaces with immobilized catalysts, with atomic concentrations ranging from 0.3% to 4.6%. The Pd-Ru colloidal alloyed NPs consisted of 50% Pd and 50% Ru, as measured by ICP-AES. After their deposition on the glass surface, the average atomic concentrations of the bimetallic NPs measured by XPS were 3.0% Pd and 2.4% Ru, matching relatively well to their original elemental composition. The discrepancy could be explained by the randomness of XPS

129

measurements and possibly to imperfect distribution of the two metals. Since the samples were

exposed to air during characterization, it was difficult to avoid oxidation of the metals, which

resulted in Pd(II), Ru(IV) and Ru(VI) on the glass surfaces [12]. Thus, it was necessary to pre-

reduce each of the catalysts prior to running the hydrogenation reactions.

Table 4.1. Atomic concentrations (%) of different elements on blank and modified glass surfaces.

Elements	Atomic Concentrations on Glass, %						
	Blank	Aminosil anization	PVP-Pd (14.1±2.1 nm)	PVP-Ru1 (3.5±0.5 nm)	PVP-Ru2 (27±24 nm)	PVP-Ru3 (121±21 nm)	PVP-PdRu
C	22.7	53.0	45.3±6.5	51.9±4.5	46.1±1.7	47.7±4.2	78.2±12.1
N	1.0	10.6	7.5±1.0	5.9±0.2	5.5±0.8	3.5±1.3	0.8±0.1
O	50.7	24.0	31.3±5.0	26.7±2.0	34.5±0.7	31.5±2.7	14.6±1.4
Si	25.6	12.0	10.7±2.3	9.0±1.0	10.9±1.1	17.1±5.8	0.6±0.1
Ru	N/A	N/A	N/A	4.6±0.4	3.0±0.3	0.3±0.1	2.4±0.3
Pd	N/A	N/A	2.3±0.5	N/A	N/A	N/A	3.0±0.6
Na	0.0	0.0	1.8±0.7	2.5±0.0	0.0	0.0	0.0
Cl	0.0	0.0	1.1±0.4	0.0	0.0	0.0	0.24±0.05

4.4.2 Catalytic assessment of PVP-stabilized NPs in a PDMS microfluidic reactor

Hydrogenation of 6-bromo-1-hexene was conducted in PDMS microfluidic channels with

immobilized PVP-stabilized Pd and Ru NPs. Less than 1% of the substrate was converted to

product, suggesting no catalyst activity. Hydrogenation of pyruvic acid in PDMS microfluidic

reactors with immobilized PVP-stabilized Ru NPs did not yield any lactic acid either. The lack of

activity can be attributed to incomplete removal of the stabilizer used to synthesize the

nanocatalysts, as demonstrated by a companion study in our laboratory [13].

We observed a conversion of 60% where PVP-stabilized Pd NPs were used in a 1 to 100

molar ratio in the homogeneous reaction to hydrogenate 6-bromo-1-hexene (Figure 4.4). After

the system stabilized (0.5 h), the conversions remained relatively unchanged for another 0.75 h.

We believe this increase in conversion was due to the high solubility of PVP in anhydrous

methanol. The linear polymer chains were able to extend into the solvent (rather than being

tightly wrapped around the metal NPs) and allow substrate access to catalytic sites.
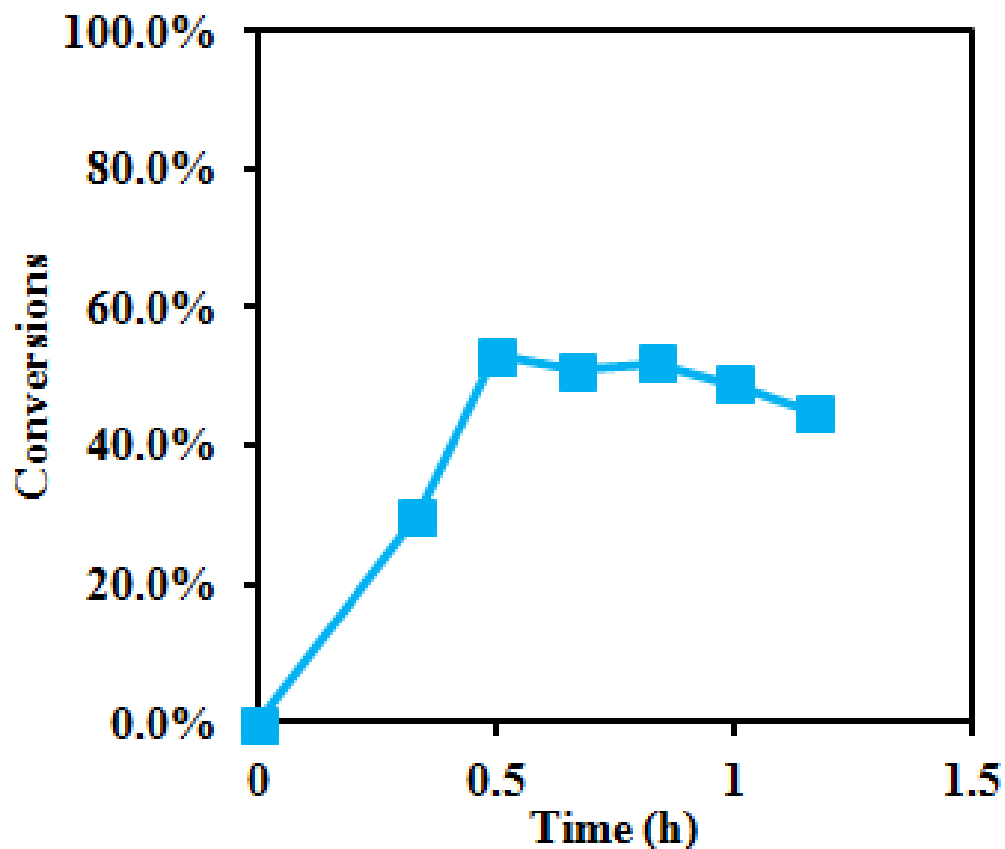
Figure 4.4. Conversion of 6-bromo-1-hexene versus time (h) in PDMS microfluidic reactors
using PVP-stabilized Pd NPs. The reaction was conducted at room temperature and 1 atm.
hydrogen pressure, with a liquid flow rate of 0.025 mL/min and a gas flow rate of 2.4 mL/min.
The substrate concentration was 20 mM, and the catalyst loading was 0.02 mM in anhydrous
methanol. The lines connecting the points are for directing the eyes; they are not model fits.

4.4.3 Assessment of the phase of the reaction medium in the capillary microreactor

4.4.3.1 Description of experimental set-up

We conducted the hydrogenation of CAL in capillary microreactors with immobilized nanocatalysts, under 1 atm hydrogen pressure and reaction temperatures ranging from 65°C to 150°C. We only detected reaction products at reaction temperatures of 105°C and above. This observation is in agreement with previous reports that, at low hydrogen pressure, high reaction temperatures are required to facilitate the reduction of CAL [14, 15]. Since the boiling point of the reaction solvent IPA (82.5°C) is lower than the reaction temperatures in our reactor system, it is necessary to ascertain whether the reaction occurred in the liquid or vapor phase.

In a typical reaction, the capillary was placed in two pieces of aluminum coats. A heating tape with constant power density was tightly wrapped around the aluminum coat (Figure 4.5; insulation around aluminum coats not shown). We read the temperature of the heating tape from the digital temperature controller connected to the tape. The exterior wall temperature of the capillary was monitored by a thermocouple tightly pressed between the internal wall of the aluminum coat and the exterior wall of the glass capillary. We read the exterior wall temperature of the glass capillary from the temperature monitor. After 2 h of pre-heating the empty glass capillary, the exterior wall temperature of the capillary reached the pre-set value with little fluctuation and remained relatively constant afterwards.

The pre-set hydrogen gas to liquid substrate flow rate ratio is designed to produce annular flow pattern, as shown in the flow maps in literature [16]. Before the liquid substrate and hydrogen entered the capillary, we observed fully-developed annular flow pattern in the Y-shaped PDMS micro mixer. Based on the Lockhart-Martinelli-Chisholm correlation for gas-

liquid two-phase flow in the tubes [17], the liquid hold-up in the glass capillary at room temperature was calculated as 5.8% of the total capillary volume at liquid and gas flow rates of 0.1 mL/h and 2.4 mL/min, respectively (similar calculation procedure was detailed in Chapter 3 section 3.4.2). The calculated liquid film thickness was 0.0074 mm. Given the extremely small amount of liquid reactant (at 25°C) entering the capillary, the reactant mixture would be quickly heated up to the pre-set temperature.
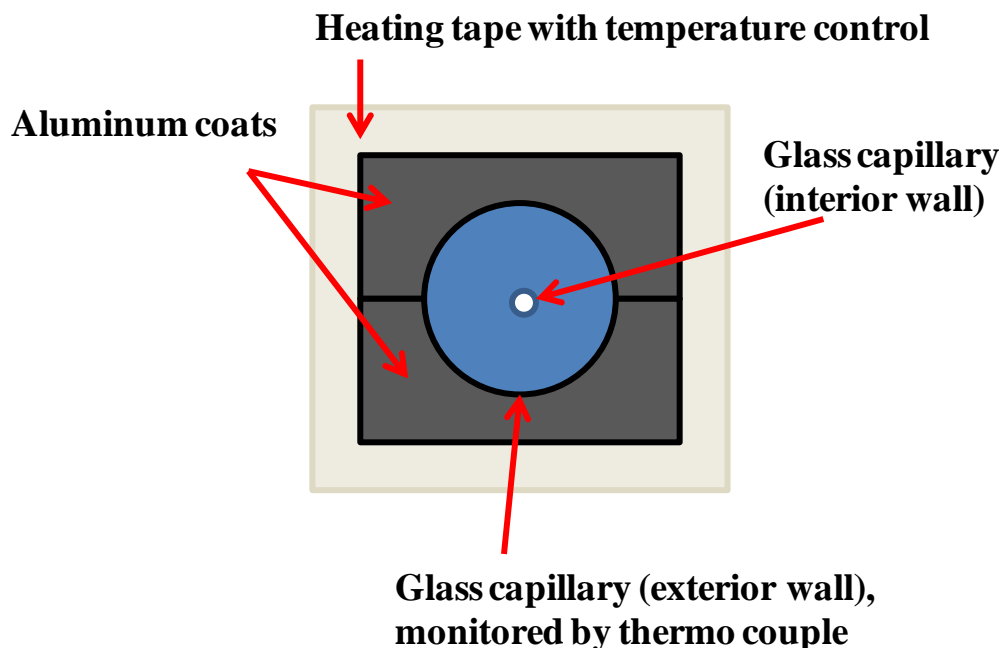
Figure 4.5. Schematic diagram of the capillary microreactor set-up (cross-sectional view). The glass capillary was placed inside two pieces of aluminum coats, and the heating tape was wrapped around the aluminum coats. The temperatures of the heating tape and exterior wall of the glass capillary were monitored by temperature controllers.

4.4.3.2 Review of two-phase flow boiling in micro-channels

In macro-scale flows, one can take an infinitesimal volume of the fluid and monitor its fluid dynamics and heat transfer by the classical governing equations [18]. Combined with proper boundary conditions, the flow velocity and temperature profiles can be constructed and the phase of the fluid at different locations of the tube can be determined. Given the significant dimensional effects on friction factors and heat transfer coefficients in micro-channels, modeling heat transfer has remained a great challenge and received considerable interests in recent years [2, 19-23]. It was reported that macro-scale analysis and methods work reasonably well in single-phase flows in micro-channels [18, 19, 22, 23]. However, several case studies have illustrated the risk of extrapolating macro-scale two-phase flow methods, including flow maps, flow boiling heat transfer methods and two-phase pressure drop models, to micro-channels below 3 mm diameter [2, 20, 21, 24-26].

Experimental studies on boiling in micro-channels have produced conflicting results in relationships among heat transfer coefficients, heat flux and mass velocity [2, 16, 19-28]. The conflicting trends compared to macro-scale flow boiling appear to result from surface effects and different heat transfer mechanisms characteristic to micro-channel boiling [19, 29]. A number of empirical prediction methods for boiling in micro-channels were developed to give various correlations of heat transfer coefficients [30-34]. Essentially the empirical micro-scale prediction methods are modifications of macro-scale flow boiling methods, which consider nuclear boiling the primary heat transfer mechanism [18]. This is not true for annular two-phase flow in micro-channels, where convective evaporation across the liquid film dominates [18]. In addition, concerns remain for the combination of stable and unstable boiling results in empirical studies [18].

134

Jacobi and Thome [35] proposed a theoretically based prediction slug flow boiling model for micro-channels, which fit the experimental data well. Their most recent-developed three zone heat transfer model demonstrated that the thin film evaporation was the primary heat transfer mechanism [36, 37]. Some of the major assumptions for the models include homogeneous and stable slug flow, uniform and constant heat flux and very thin and smooth liquid film [36, 37]. Another theoretically based model with reasonable success for water and a number of organic solvents was the steady state, one dimensional boiling two phase flow in triangular micro-channel [38]. It was assumed that the flow was laminar and steady, the heat flux uniform and the vapor velocity much higher than the liquid velocity [38]. This model also validated that the vapor pressure drop was negligible in the process [38]. It was found that the dry-out length (the length where the liquid completely evaporates) increased with hydraulic diameter and decreased with increased heat flux [38].

Our goal is to test the hypothesis that the liquid reactant is quickly evaporated in the heated capillary. For more comprehensive models, the readers are referred to the previously published doctoral dissertations [39, 40]. Our approach is to first estimate the heating lengths with either pure IPA or pure hydrogen in the capillary. The heating length values calculated for the two-phase flow should fall in the range of pure substances. Based on the experimental set-up, the following assumptions are valid: a) the fully-developed two-phase laminar flow is stable and steady; b) all elements of the fluid stream have the same thermal history in travelling along the capillary; c) the IPA stream undergoes an isothermal phase transition; d) the overall heat-transfer coefficient is constant; e) the external heat flux provided by the heating tape is uniform and constant at steady state; d) heat losses are negligible; and e) the physical properties of the solvent IPA is used in the calculations due to a diluted substrate concentration. As a result, the fluid flow

135

temperature only changes axially and the temperature profile is independent of time. All the

parameters in Equations 4.1 to 4.19 in Sections 4.4.3.3 and 4.4.3.4 are listed in Table 4.2.

4.4.3.3 Assessment of pure reactant phase change in capillary microreactor

To obtain the internal wall temperature profile (T_{in}) as a function of capillary length with

pure hydrogen or pure IPA, we have the following heat balance equations, where the amount of

heat for the fluid flow temperature increase (Q_1) is provided by the amount of heat transferred

from the heating tape around the capillary surface(Q_2):

$$Q_1 = m \times C_p \times (T_{out} - T_{in}) \qquad \text{(Equation 4.1)}$$

$$Q_2 = U \times SA \times \frac{(T_{out} - T_{in})}{\ln(T_{ex} - T_{in})/(T_{ex} - T_{out})} \qquad \text{(Equation 4.2)}$$

Based on the assumption that the temperature at the external wall of the capillary is constant

at 150°C, The overall heat transfer coefficient (U) for heat transfer from the external wall of the

capillary to the fluid can be determined by Equation 4.3 [18]:

$$U = \frac{1}{[\frac{1}{h_i} + \frac{R_{iw}}{k} \times \ln\left(\frac{R_{ow}}{R_{iw}}\right)]} \qquad \text{(Equation 4.3)}$$

Where U = the overall heat transfer coefficient (W/m^{2}K);

k = the thermal conductivity of the glass capillary (W/mK);

h_i = the individual convection heat transfer coefficient for each fluid (W/m^{2}K);

R_{iw} = the inner diameter of the tube (m).

At external wall temperature of 150°C, hydrogen has travelled 1.1 cm (less than 4% of the total capillary length) to reach 150°C, as observed from the internal wall temperature profile (Figure 4.6a). For the calculations of IPA temperature profile, we divided the process into three stages: (I) liquid IPA from room temperature to boiling point; (II) isothermal phase transition of IPA at boiling point; (III) vapor IPA from boiling point to external wall temperature. It only takes 0.05 cm for the liquid IPA to reach boiling point and complete phase transition to vapor (Figure 4.6b). The IPA vapor then travels 0.34 cm to reach external wall temperature of 150°C (Figure 4.6c). The total evaporation length for pure IPA is about 0.39 cm which is less than 1.4% of the total capillary length. The mixture evaporation length should be between 0.39 and 1.1 cm.
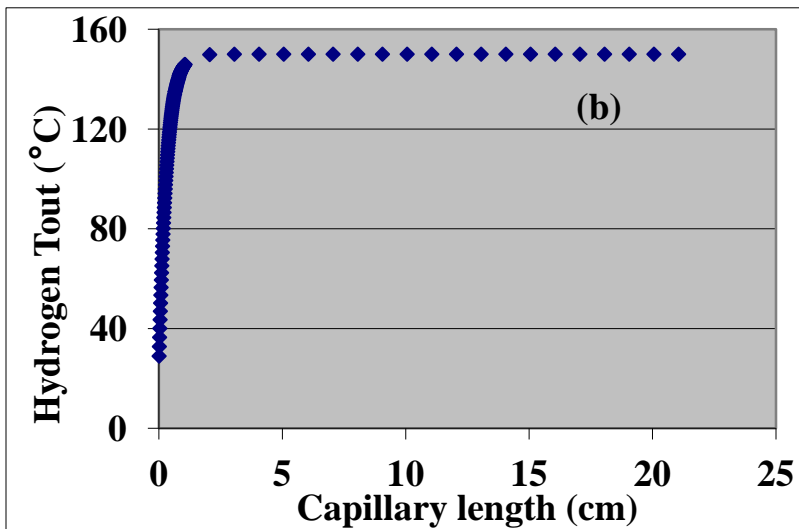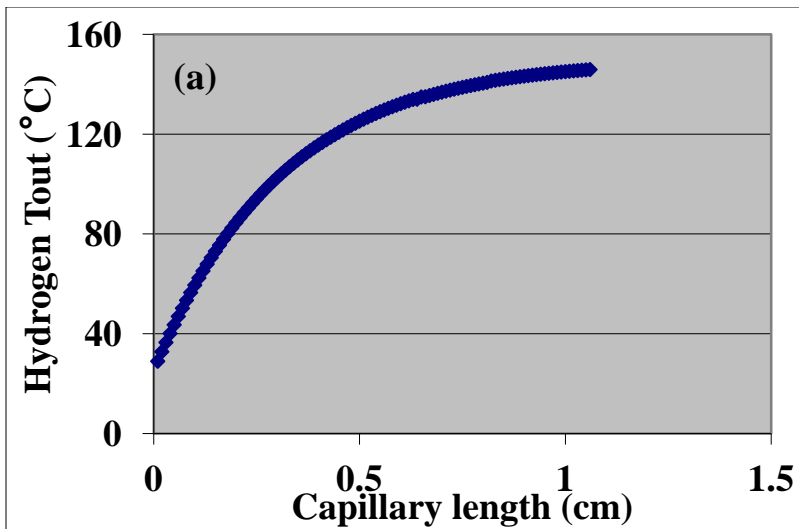
Figure 4.6. Internal wall temperature profiles of a) and b) pure hydrogen; c) liquid IPA stages I and II; and d) overall IPA (all three stages).

Figure 4.6 (cont'd)
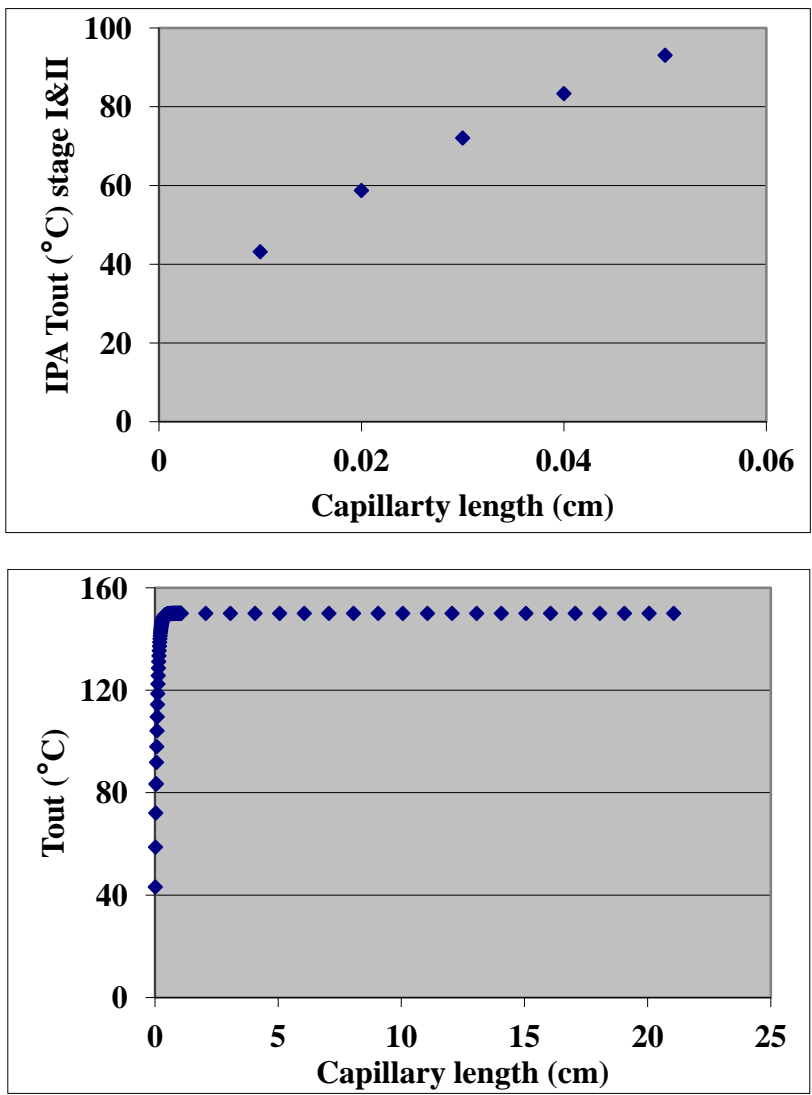
4.4.3.4 Assessment of mixed reactant phase change in capillary microreactor

We first consider the radial heat conduction through the glass wall from the exterior to the interior when there is no flow in the capillary, to estimate the amount of heat required for the interior wall temperature to reach the pre-set exterior wall temperature. This is given by the Fourier equation governing heat conduction equation through a tube in the radial direction (Equation 4.4a) [41]:

$$\frac{Q}{2\pi L} = -k\frac{dT}{dr}$$
(Equation 4.4a)

Equation 4.4a may be integrated to Equation 4.4b, considering the boundary conditions:

$$Q = \frac{k2\pi L(T_{ex}-T_{out})}{ln(R_{ow}/R_{iw})}$$
(Equation 4.4b)

The driving force is the temperature difference between the exterior (T_{ex}) and interior walls (T_{out}). As the interior wall temperature increases, the temperature difference grows smaller, thus less heat is required. The calculated heat consumption value with the largest temperature difference (between room temperature and the highest reaction temperature 150°C) is smaller than the heating power of the heating tape (105 W). We observed a slight temperature fluctuation ($\pm 1^{\circ}$C) at the exterior wall measured by the thermal couple. As a result, we expect a certain degree of temperature fluctuation at the interior wall as well. This slight temperature fluctuation ensured a small temperature difference between the exterior and interior walls, providing a small but consistent driving force for the heat conduction [42].

When the liquid and hydrogen gas flow through the heated capillary, the heating flux can be calculated by Equation 4.5:

$$Q = k2\pi UA(T_{ex} - T_{out})$$
(Equation 4.5)

The overall heat transfer coefficient (U) can be calculated by Equation 4.3. When the liquid substrate and hydrogen gas enter the heated capillary at room temperature and eventually reached the exterior wall temperature, within this period of time they have gone through three stages [24-26]. At stage I, the liquid substrate and hydrogen gas are heated from room temperature to the boiling point of IPA. If we consider a differential axial distance (dz) in the

140

capillary, at any given moment, the amount of heat transferred through the glass wall in the radial direction would be instantaneously transferred to the very thin liquid film in contact with the interior wall for it to reach the boiling point of IPA. The steady-state heat transfer under this stage could be expressed by Equation 4.6. $(R_{iw} - R_g)$ is the liquid film thickness calculated in section 4.4.3.1, which equals to 0.0074 mm.

$$\rho_g \pi R_{iw}^2 dz C_{pg} dT + \rho_l 2\pi(R_{iw} - R_g) R_{iw} dz C_{pl} dT = 2\pi R_{iw} U(T_{ex} - T)dt \qquad \text{(Equation 4.6)}$$

The left-hand-side term represents the amount of heat (unit: J) the liquid substrate and hydrogen need for their temperature increase (dT) when it travels distance dz; while the right-hand-side term represents the amount of heat (unit: J) transferred from the exterior wall in this time frame dt. During stage I, the liquid substrate has covered distance dz in the time frame of dt with a linear velocity v_z, which gives Equation 4.7:

$$\rho_g \pi R_g^2 \frac{dz}{dt} C_{pg} dT + \rho_l 2\pi(R_{iw} - R_g) R_{iw} \frac{dz}{dt} C_{pl} dT = 2\pi R_{iw} U(T_{ex} - T)$$

(Equation 4.7)

Substitute Equation 4.7 into Equation 4.6 and rearrange, we obtain Equations 4.8 and 4.9:

$$[\rho_g \pi R_g^2 \frac{dz}{dt} C_{pg} v_{zg} + \rho_l 2\pi(R_{iw} - R_g) R_{iw} v_{zl} C_{pl}]dT = 2\pi R_{iw} U(T_{ex} - T) \qquad \text{(Equation 4.8)}$$

$$\frac{dT}{(T_{ex}-T)} = 2\pi R_{iw} U(T_{ex} - T)dz \bullet \frac{1}{[\rho_g \pi R_g^2 \frac{dz}{dt} C_{pg} v_{zg} + \rho_l 2\pi(R_{iw}-R_g) R_{iw} v_{zl} C_{pl}]}$$

(Equation 4.9)

Integrate Equation 4.9, we obtain Equation 4.10 as follows:

$$-\ln(T_{ex} - T) = C +$$

$$2\pi R_{iw} U(T_{ex} - T) \bullet \frac{1}{(\rho_g \pi R_g^2 \frac{dz}{dt} C_{pg} v_{zg} + \rho_l 2\pi (R_{iw} - R_g) R_{iw} v_{zl} C_{pl})}$$

(Equation 4.10)

At the entrance of the capillary ($z = 0$), the entering temperature is room temperature; at the

end of stage I ($z = z_1$), the liquid substrate and hydrogen gas temperatures are the same as the

boiling point of IPA ($T = T_{bp}$). Considering these boundary conditions, we obtain integration

constant C and solve for z_1 (Equations 4.11 and 4.12):

$$C = -\ln(T_{ex} - T_{in}) \qquad \text{(Equation 4.11)}$$

$$z_1 = \frac{\ln\left(\frac{T_{ex} - T_{in}}{T_{ex} - T_{bp}}\right)}{2\pi R_{iw} U_i} \bullet [\rho_g \pi R_g^2 \frac{dz}{dt} C_{pg} v_{zg} + \rho_l 2\pi (R_{iw} - R_g) R_{iw} v_{zl} C_{pl}]$$

(Equation 4.12)

At stage II, the liquid substrate undergoes phase change at a constant temperature T_{bp}. It

changes from liquid to vapor. At any given moment, the amount of heat of vaporization for the

substrate (left-side-term in Equation 4.13) is provided by the heat transferred from the exterior

wall (right-side-term in Equation 4.13). Under steady state, the substrate travels a distance Δz in

a time frame of Δt with a linear velocity of v_z (Equation 4.14):

$$\rho_l 2\pi (R_{iw} - R_g) R_{iw} \Delta z \bullet \Delta H_V = 2\pi R_{iw} U(T_{ex} - T)\Delta z \bullet \Delta t$$

(Equation 4.13)

$$v_z = \frac{\Delta z}{\Delta t} \qquad \text{(Equation 4.14)}$$

Substitute Equation 4.14 into Equation 4.13, we obtain Equation 4.15:

$$\rho_l 2\pi(R_{iw} - R_g)R_{iw}\Delta H_V v_{zl} = 2\pi R_{iw}U(T_{ex} - T)\Delta z \qquad \text{(Equation 4.15)}$$

The total distance (z_2) the substrate has travelled during phase change stage II is given by

Equation 4.16:

$$z_2 = \Delta z = \rho_l 2\pi(R_{iw} - R_g)R_{iw}\Delta H_V v_z / 2\pi R_{iw}U(T_{ex} - T) \quad \text{(Equation 4.16)}$$

At stage III, the vapor substrate temperature continues to rise and eventually reaches the

exterior wall temperature. And so does the hydrogen gas. Considering the observed slight

temperature fluctuation observed during the experiment at the exterior wall, here we set the inner

wall temperature to be 1 K lower than the exterior wall temperature at the end of stage III. At the

beginning of stage III, the substrate temperature is the boiling point of IPA. At any given

moment under steady state, considering a differential distance dz, the amount of heat the vapor

substrate and hydrogen gas need for temperature increase (left-hand-term in Equation 4.17)

equals to the amount of heat transferred from the exterior wall temperature in the time frame dt

(right-hand-side term in Equation 4.17). Similar to the model in stage I, the ratio of dz and dt is

the linear velocity of the substrate. Considering the above conditions, we derive Equations 4.17

and 4.18, and the integration of Equation 4.19 gives the distance (z_3) the substrate has travelled

in stage III to finally reach the exterior wall temperature. The vapor heat capacity used in

Equations 4.17 to 4.19 is the average heat capacity of vapor IPA and hydrogen gas.

$$\rho \pi R_{iw}^2 dz \bullet \overline{C_{pV}} \bullet dT = 2\pi R_{iw}U(T_{ex} - T)\text{dz} \bullet dt \qquad \text{(Equation 4.17)}$$

$$\rho \pi R_{iw}^2 dz \bullet \overline{C_{pV}} \bullet dT = 2\pi R_{iw}U(T_{ex} - T)\text{dz} \qquad \text{(Equation 4.18)}$$

$$z_3 = \frac{\ln\frac{(T_{bp} - T_{ex})}{(T_{iw} - T_{ex})}}{\frac{2\pi R_{iw}U_i}{\overline{C_{pV}}\rho \pi \overline{v_z} R_{iw}^2}} \qquad \text{(Equation 4.19)}$$

Table 4.2. Parameters used in Equations 4.1 to 4.19.

Parameters in Equations 4.1-4.19	Symbols	Values	Units
Thermal conductivity of glass	k	1.14	$W \cdot m^{-1} \cdot K^{-1}$
Length of the glass capillary	L	30.4	cm
Surface area of the glass capillary	SA	611.2	cm^2
Outer radius of the glass capillary	R_{ow}	3.2	cm
Inner radius of the glass capillary	R_{iw}	0. 25	cm
Heat capacity for liquid IPA	C_{pl}	2.7	$J \cdot g^{-1} \cdot K^{-1}$
Heat capacity for vapor IPA	C_{pv}	1.5	$J \cdot g^{-1} \cdot K^{-1}$
Heat of vaporization for IPA	ΔH_V	44	$kJ \cdot mol^{-1}$
Heat capacity of hydrogen	C_{pg}	14.3	$J \cdot g^{-1} \cdot K^{-1}$
Linear velocity of substrate in the z direction	v_z	-	$cm \cdot s^{-1}$
Mass flow rate of hydrogen	m_g	0.000204	g/min
Mass flow rate of reactant	m_l	0.00131	g/min
Convection heat transfer coefficient at the fluid flow interface [18]	h_i (H_2)	10.7	$W/m^2 K$
	h_i (liquid IPA)	50.1	
	h_i (vapor IPA)	34.6	

The results of all calculations are summarized in Table 4.3. The total distance the liquid substrate travelled to reach the vapor phase at a pre-set exterior wall temperature is less than 2% of the total length of the capillary. Therefore, the reaction is a vapor-phase reaction. The inter-phase mass transfer resistances between liquid and gas does not apply in the case of vapor phase reactions [43]. Considering the phase change, the substrate residence time in the capillary is calculated in two parts: one as liquid with liquid volumetric flow rate and the other as vapor. While mixed with hydrogen in one phase, the substrate travels with the hydrogen volumetric flow rate in the capillary. The residence time for the substrate was in the order of seconds, again confirming the high efficiency of the microreactor system.

Table 4.3. System parameters and summary of calculation results. The distance the liquid substrate travels to reach the exterior wall temperature is the sum of z_1, z_2 and z_3. z_1: distance liquid substrate and hydrogen travel in the capillary to reach the boiling point of IPA. z_2: distance the liquid travels until it is completely vaporized at its boiling point. z_3: distance the vapor containing substrate and hydrogen travel to reach the exterior wall temperature of the capillary.

Exterior wall temperature ($^\circ$C)	150	125	105
Distance liquid has travelled to reach external wall temperature (mm)	0.42	0.38	0.34
Phase of the reactants	Vapor	Vapor	Vapor
Substrate residence time (s)	4.2	4.0	3.8

4.4.4 Catalytic assessment of *n*Ds-stabilized NPs in a glass capillary microreactor

4.4.4.1 Hydrogenation of 6-bromo-1-hexene

In Chapter 3, the major cause for catalyst deactivation was considered to be the decreased solubility of thio-ether stabilized NPs in solvents compatible with PDMS. This was not an issue in the glass capillary microreactors because of their excellent chemical tolerance. *n*DS-stabilized NPs dissolved in toluene were successfully immobilized on the glass surfaces without apparent particle agglomeration based on SEM observation. Hydrogenation of 6-bromo-1-hexene was first conducted in a glass capillary with immobilized *n*DS-stabilized Pd NPs (Figure 4.7). Hydrogen purging at room temperature did not completely remove the stabilizing agent around the metal NPs, thus leading to catalyst deactivation. The catalysts were partially regenerated by hydrogen reduction at a higher temperature (70°C); however, the activity still dropped after 0.75 h. We attributed this to the sulfur elements in the residual stabilizing ligands left on the surface of the NPs. Sulfur has been known to poison noble metallic catalysts because of its strong adsorption of hydrogen and substrate, preventing them from reacting with each other on the metal surface [44]. We also noticed that when the ratio of gas flow rate to liquid flow rate decreased, the conversion decreased due to the resulting shorter liquid residence times in the capillary reactor system.
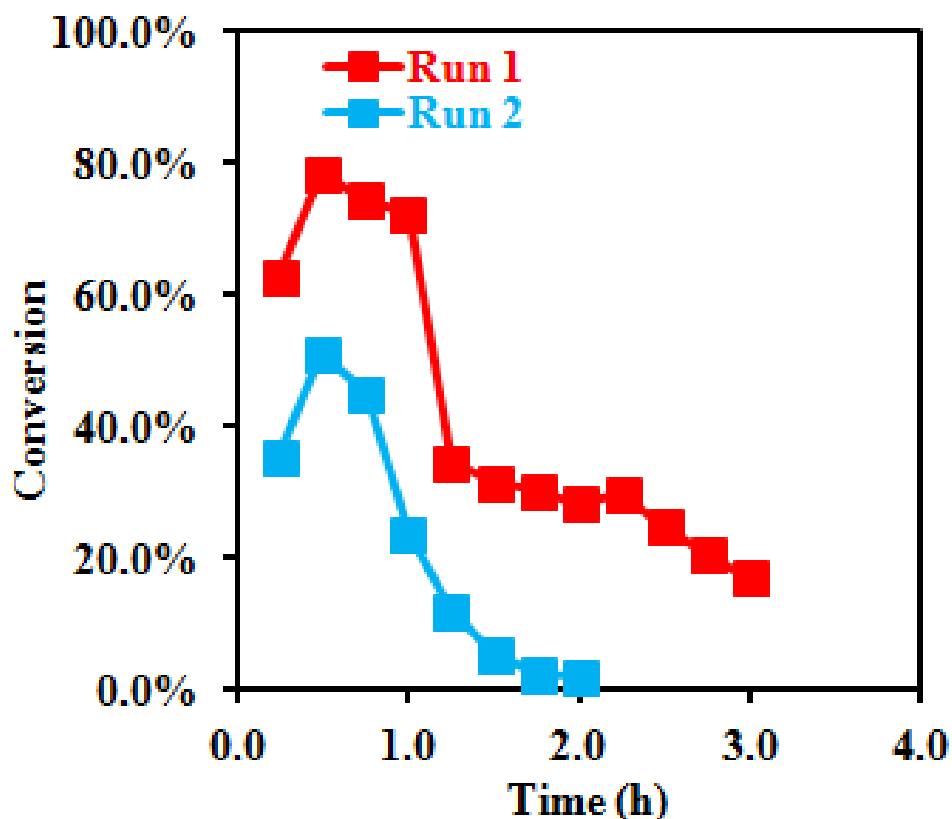
Figure 4.7. Conversion of 6-bromo-1-hexene versus time (h) in two separate runs in a glass capillary reactor with immobilized *n*DS-stabilized Pd NPs. The glass capillary was treated with high purity hydrogen flow at room temperature for 0.5 h. The substrate concentration was 10 mM. For Run 1, the liquid and gas flow rates were 0.1 mL/h 2.4 mL/h, respectively. For Run 2, the liquid and gas flow flow rates were 0.3 mL/h 3.2 mL/min, respectively. High purity hydrogen was flown through the glass capillary at 70°C for 1 h between the two runs.

4.4.4.2 Hydrogenation of CAL in the glass capillary microreactor

We investigated the catalytic properties of *n*DS-stabilized Ru NPs in the glass capillary system using hydrogenation of CAL. CAL can be partially reduced to either HCAL or COL, and fully reduced to HCOL. We studied the effects of pre-treatment conditions, substrate concentrations, substrate flow rates and reaction temperatures on catalyst performance by plotting the concentration profiles of substrate and products as a function of reaction time. We

conducted controlled experiments in a blank glass capillary under similar reaction conditions, and found that less than 1% of CAL was converted, suggesting this reaction is catalytic.

In the study of catalyst pre-treatment conditions, we used a glass capillary with immobilized nDS-Ru NPs without hydrogen purging, and observed approximately 10% of substrate conversion. This was an indication that the catalytic sites were blocked by the stabilizing ligands. When nDS-Ru NPs inside the capillary microreactor were pre-reduced by high purity hydrogen at 200°C, we noticed a significant substrate conversion, indicating efficient removal of the stabilizing ligands [17]. As a result, hydrogen purging at 200°C was adopted as a standard pre-treatment for all subsequent experiments.

The concentration profiles of substrate and products showed that the reaction reached a stable conversion within 0.25 h, maintained the catalyst activity for at least 4 h and achieved a carbon balance between 86 and 95% (Figures 4.8). The nDS-stabilized Ru NPs were regenerated after the first 4-h reaction cycle by hydrogen purging at 200°C, and re-used immediately afterwards. The catalysts remained fully active for another 2.5 h, and eventually lost the activity by the end of the second reaction cycle (Figure 4.9). Thus catalyst life was greatly improved compared to the PDMS microfluidic reactor systems, demonstrating the efficiency of the glass capillary microreactor. However, based on the thermogravimetric studies, sulfur elements in the stabilizing ligands could not be completely removed at temperatures lower than 550°C (Figure 4.10). Thus the remaining sulfur atoms may have poisoned the Ru NPs and caused loss of catalytic activity.

Table 4.4 summarizes the average substrate conversions (%) and product compositions (%) under different reaction conditions at steady state. The uncertainties are from the standard deviation of the averaged values once the reaction reached steady state. Higher reaction temperatures, lower substrate concentrations and substrate flow rates resulted in higher CAL conversions. HCAL was the primary product (> 65% of the total products) in all cases. The production of HCOL decreased from 19% to 2% with the decrease in temperature, possibly due to the slower reduction of intermediates HCAL and COL. COL production increased from 3% to 21% with decreasing temperatures, in agreement with what was observed in the batch reactor system. The reason for this was the less favorable adsorption of C=O bonds on the surfaces of small Ru NPs at high temperature and low hydrogen pressure, as well as the preferred adsorption of C=C bonds at the same time [45]. The HCOL production was significantly reduced at higher substrate flow rates, possibly due to insufficient residence times.

150
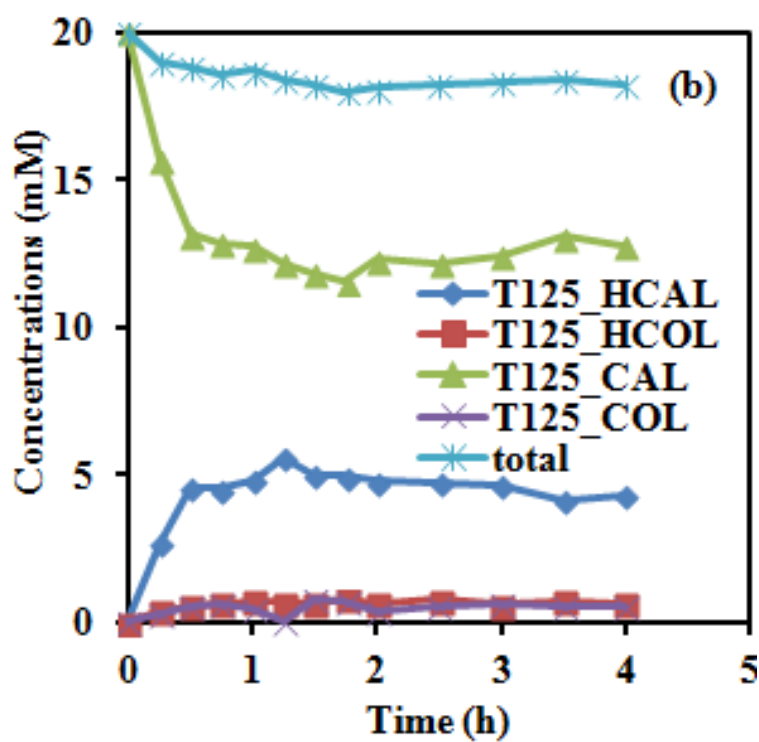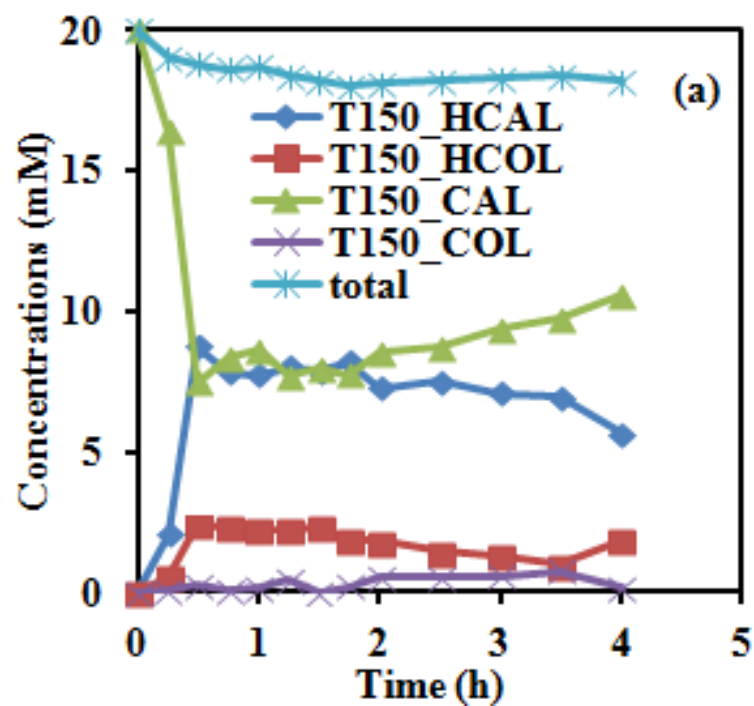
Figure 4.8. Concentration profiles (mM) as a function of time (h) for hydrogenation of CAL under different reaction conditions (all reactions were conducted at a hydrogen pressure of 1

Figure 4.8 (cont'd)

atm and hydrogen flow rate of 2.4 mL/min). (a) T = 150°C; (b) T = 125°C; (c) T = 105°C (reactionsin (a)-(c) were conducted at a substrate concentration of 20 mM and substrate flow rate of 0.1 mL/h); (d) substrate concentration of 10 mM; (e) substrate concentration of 5 mM (reactions in (d)-(e) were conducted at T = 150°C and substrate flow rate of 0.1 mL/h); (f) substrate flow rate of 0.3 mL/h (reactions in (f) were conducted at T = 150°C and substrate concentration of 20 mM).
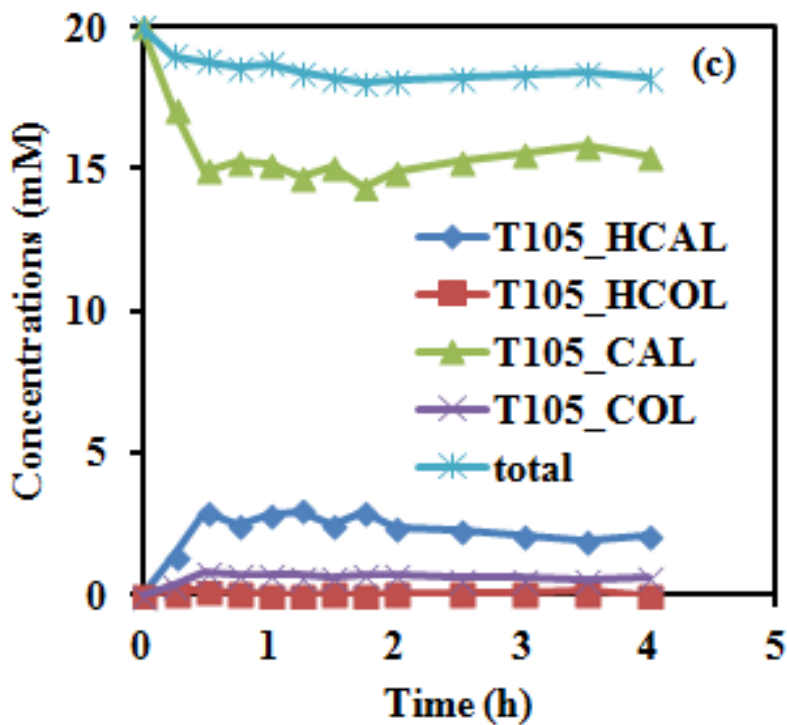
Figure 4.8 (cont'd)
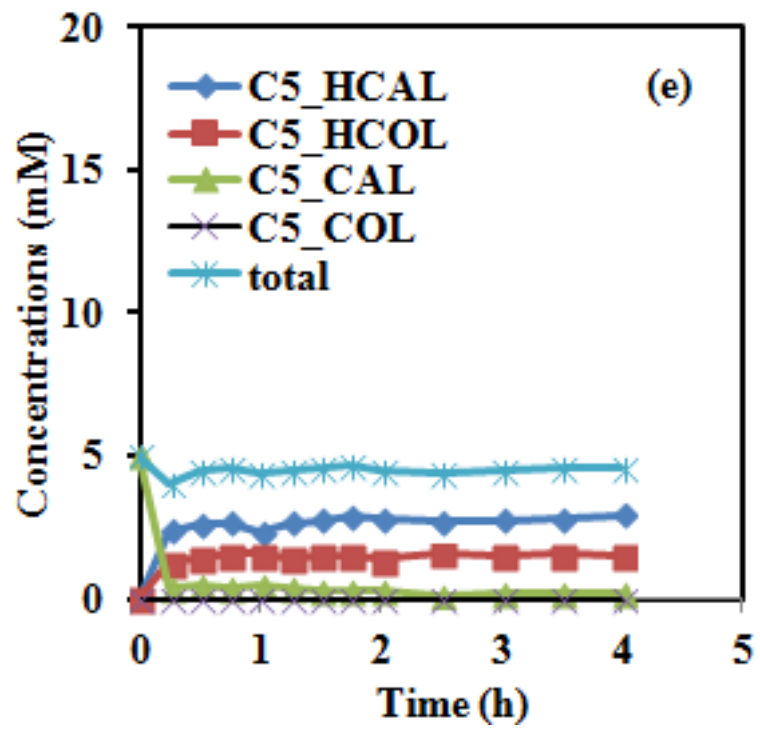
Figure 4.8 (cont'd)

Figure 4.9. Concentration profiles (mM) as a function of time (h) for hydrogenation of CAL over two catalyst cycles (both reactions were conducted at a temperature of $150^{\circ}C$, hydrogen pressure of 1 atm, substrate concentration of 10 mM, substrate flow rate of 0.1 mL/h and hydrogen flow rate at 2.4 mL/min).The reactor system was purged with pure hydrogen at $200^{\circ}C$ for 1.5 h between cycles.
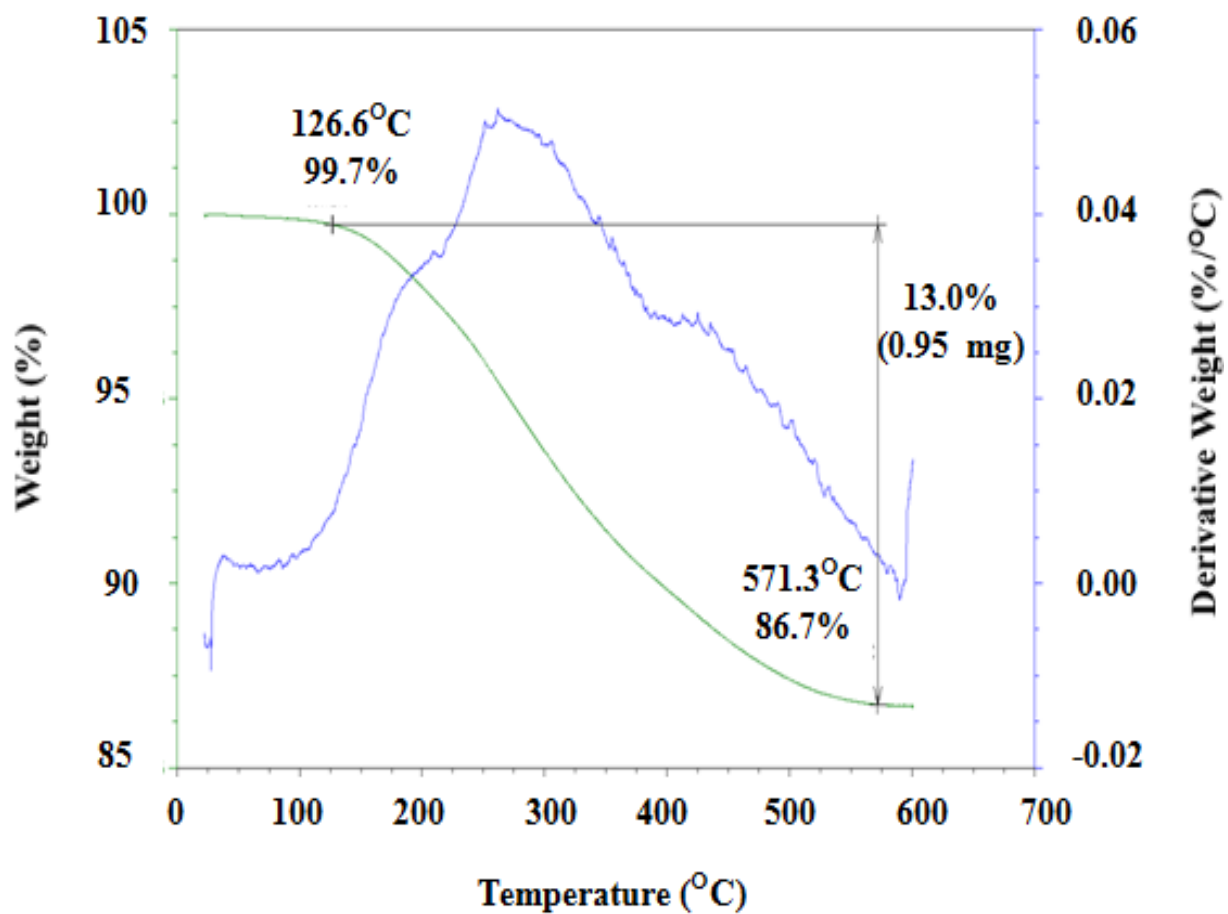
Figure 4.10. Thermogravimetric/differential thermal analysis of *n*DS-Ru NPs. Complete removal of stabilizing ligand from Ru NPs requires the temperature to be higher than 550°C.

Table 4.4. Average substrate conversions (%) and product compositions (%) for CAL hydrogenation with immobilized *n*DS-Ru NPs in glass capillary microreactors under different reaction conditions.

Reaction conditions		Substrate (CAL) conversion (%)	Product composition (%)		
			HCAL	COL	HCOL
T($^\circ$C)	**150**	56.9±4.7	77.2±2.0	3.5±2.8	19.3±4.1
	125	37.7±2.6	80.0±3.4	8.7±3.3	11.3±1.1
	105	24.3±2.1	77.2±2.2	21.1±1.3	1.8±1.4
C (mM)	**20**	56.9±4.7	77.2±2.0	3.5±2.8	19.3±4.1
	10	93.5±3.2	64.9±6.6	8.6±2.4	26.5±8.7
	5	93.8±2.4	64.2±1.9	0.0	35.8±1.9
V$_S$(mL/h)	**0.1**	56.9±4.7	77.2±2.0	3.5±2.8	19.3±4.1
	0.3	17.4±1.8	92.3±3.0	5.8±2.7	1.9±0.8

4.4.5 Catalytic assessment of PVP-stabilized NPs in a glass capillary microreactor

4.4.5.1 PVP-stabilized Pd NPs

The capillary reactor with immobilized PVP-Pd NPs was run under different reaction conditions, including initial substrate concentrations, liquid flow rates and reaction temperatures. Catalyst stability was evaluated first. Two 4-h consecutive reactions (substrate concentration 10 mM) were conducted. After the first 4 h, the surface of the capillary was dried with nitrogen and the reaction residue was rinsed off with IPA, followed with regeneration by hydrogen purging at 200°C for 1 h. By 0.25 h, the concentrations of the substrate and products became stable and remained so afterwards. The total carbon balance of the mixture closed to at 90% or above. We did not observe any catalyst deactivation for the second run, indicating stable catalyst performance under the reaction conditions (Figure 4.11).
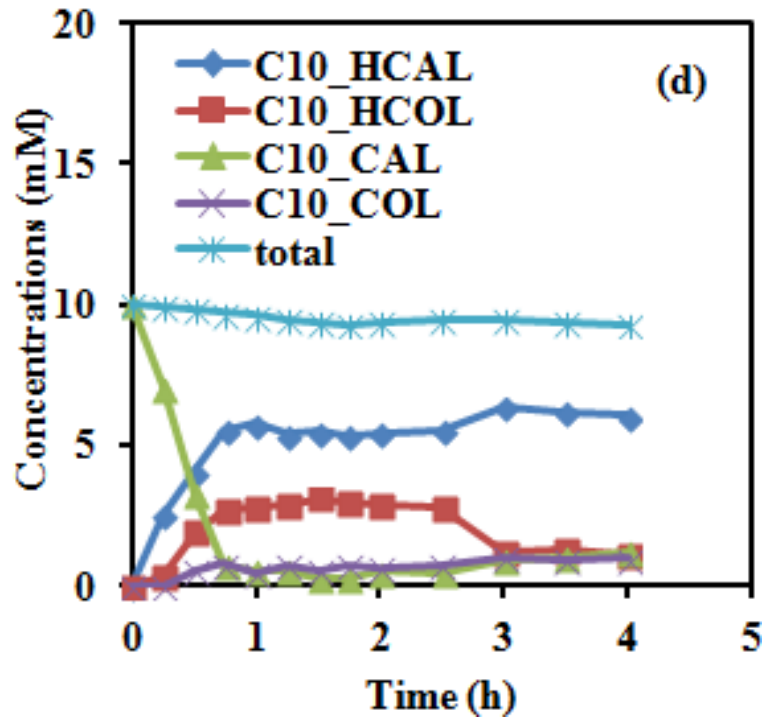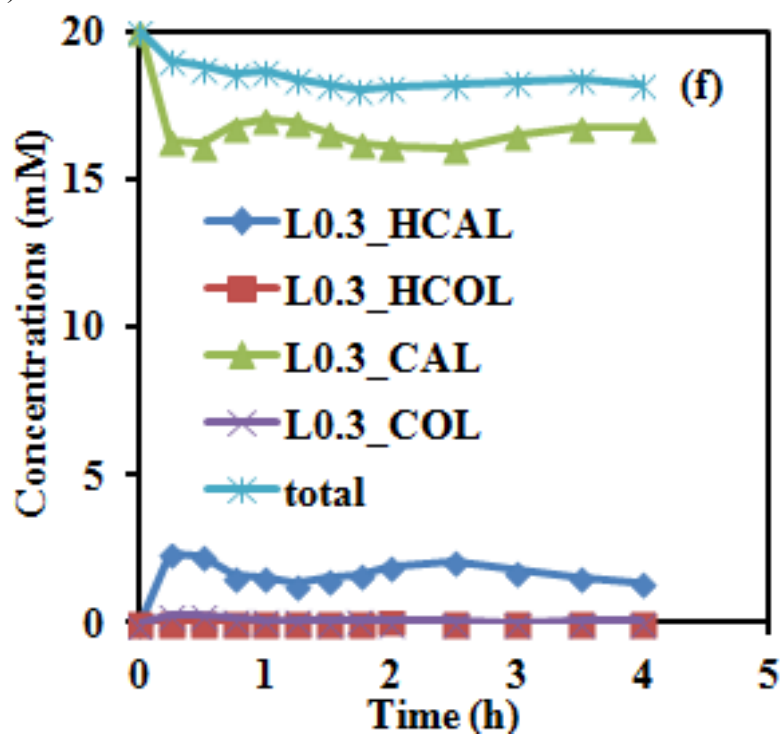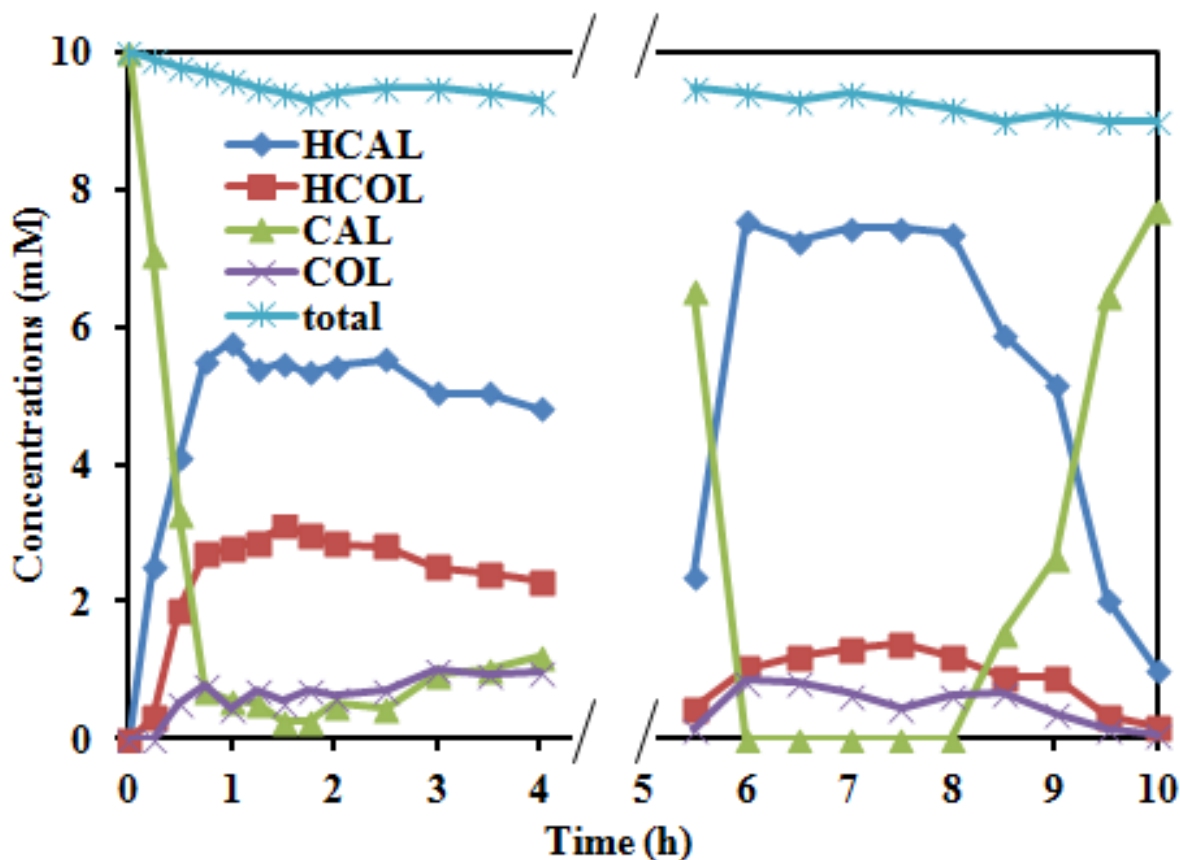
157

Figure 4.11. Concentration profiles (mM) as a function of time (h) for hydrogenation of CAL over two catalyst cycles for PVP-stabilized Pd NPs (both reactions were conducted at temperature of 150°C , hydrogen pressure of 1 atm, substrate concentration of 10 mM, substrate flow rate of 0.1 mL/h and hydrogen flow rate of 2.4 mL/min).The reactor system was purged with pure hydrogen at 200°C for 1 h between cycles.

We conducted the hydrogenation at different reaction temperatures, and observed that all reactions reached steady state by 0.25 h under the given reaction conditions, with carbon balances closing between 89% and 95% (Figure 4.12). The carbon balance was closer to 100% at lower reaction temperatures, possibly due to less sample evaporation. The substrate conversion decreased with decreases in reaction temperature, which was consistent with information in the published literature for CAL hydrogenation [46]. HCAL and HCOL were the major products.

158

COL was not observed in the reaction mixture due to the preferential reduction of C=C bonds by Pd. Increased reaction temperature facilitated complete reduction, resulting in higher HCOL production. Substrate flow rates played a major role on conversions. The substrate conversions dropped from 99% at 0.1 mL/h to 5% at 0.5 mL/h, due to the shortened residence time [47]. There was a slight increase in HCAL but slight decrease in HCOL composition with increased substrate flow rate. Faster substrate flow rate resulted in shorter residence time, thus the partially-reduced HCAL did not have insufficient contact with the catalyst to be further reduced to HCOL. . Substrate concentration had little effect on conversion and product composition. The average substrate conversions and product compositions under different reaction conditions are summarized in Table 4.5.

To further investigate the preference for C=C double bond or C=O double bond reduction by Pd NPs, we carried out hydrogenation of HCAL and COL under similar reaction conditions. The concentration profiles (Figure 4.13) showed that an average of 4% of HCAL was converted to HCOL, while 94% of COL was converted to HCOL and HCAL. The product composition in COL hydrogenation was 91% of the fully-reduced product HCOL and 9% of its isomer HCAL, suggesting the preferred reduction of C=C double bonds by Pd NPs.
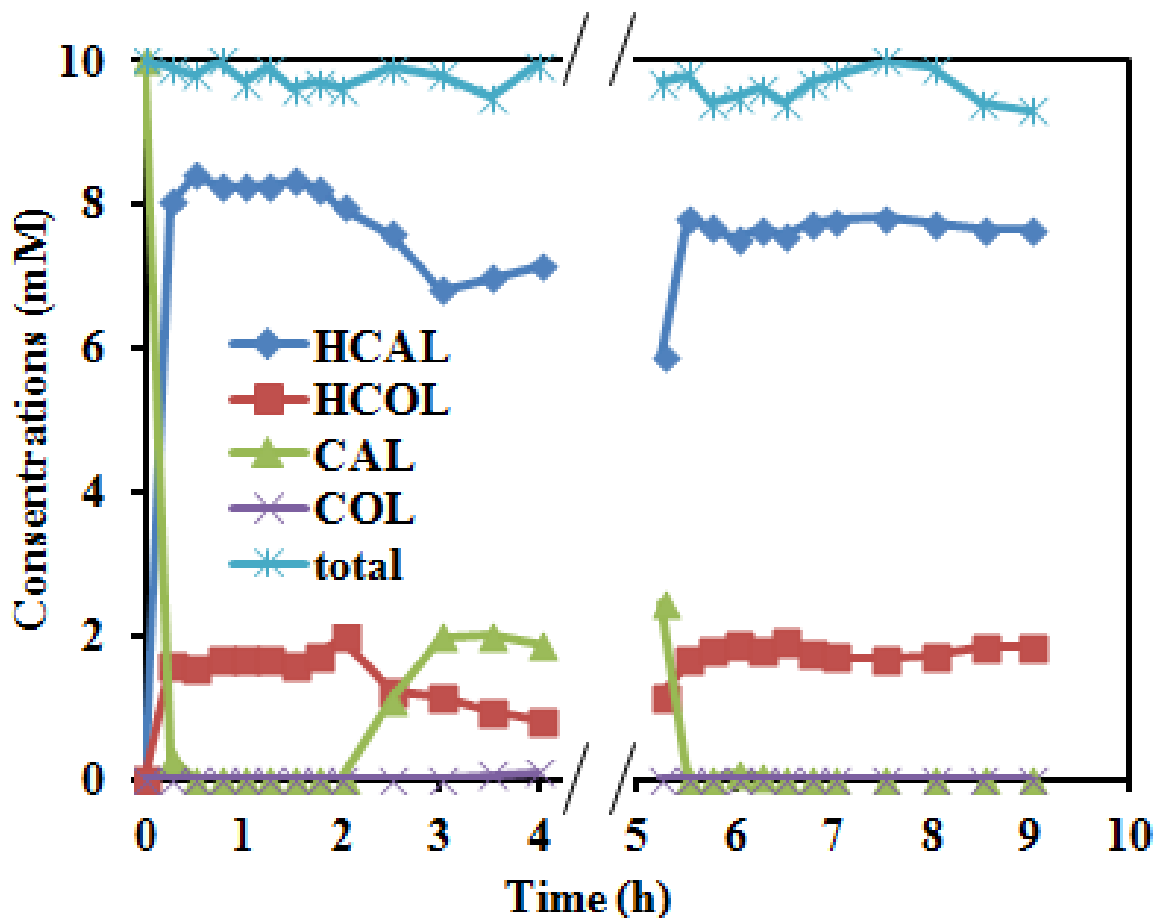
Figure 4.12. Concentration profiles (mM) as a function of time (h) for hydrogenation of CAL catalyzed by PVP-stabilized Pd NPs under different reaction conditions (all reactions were

Figure 4.12 (cont'd)

conducted at hydrogen pressure of 1 atm and hydrogen flow rate of 2.4 mL/min). (a) T = 150°C; (b) T = 125°C; (c) T = 105°C (reactions in (a)-(c) were conducted at a substrate concentration of 20 mM and substrate flow rate of 0.1 mL/h); (e) substrate flow rate = 0.3 mL/h; (d) substrate flow rate = 0.5 mL/h (reactions in (d)-(e) were conducted at T = 150°C and substrate concentration of 20 mM); (f) substrate concentration of 10 mM (reactions in (f) were conducted at T = 150°C and substrate flow rate of 0.1 mL/h).
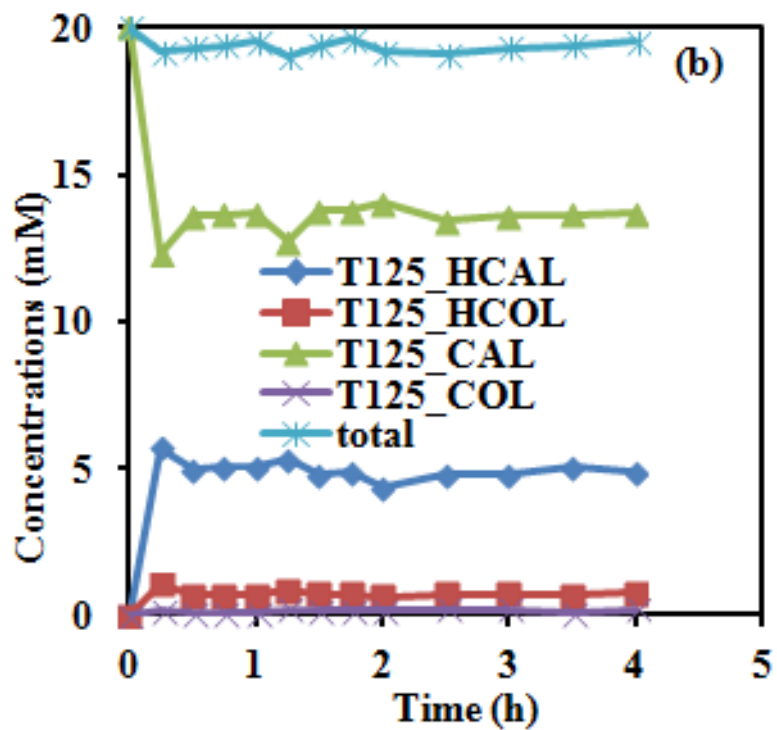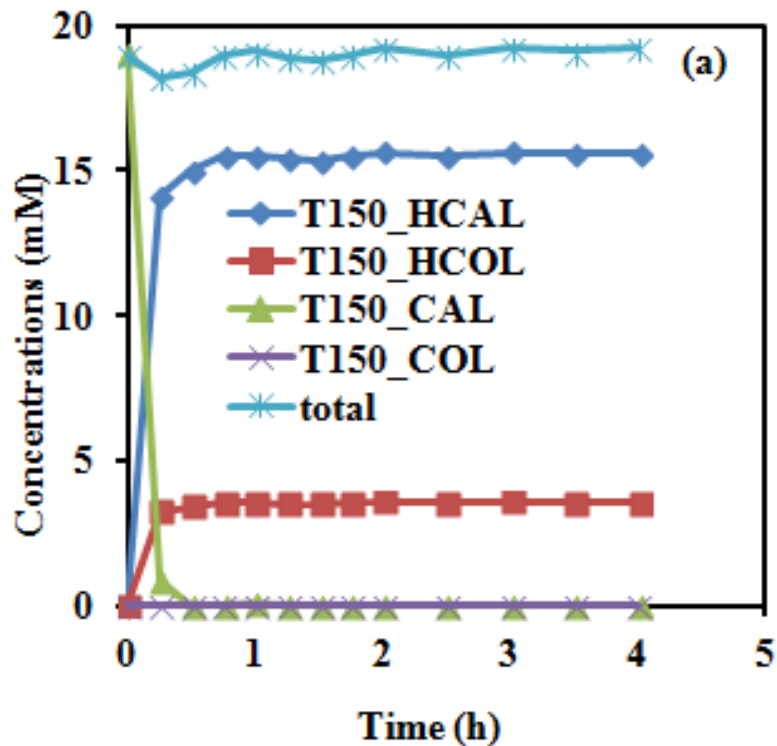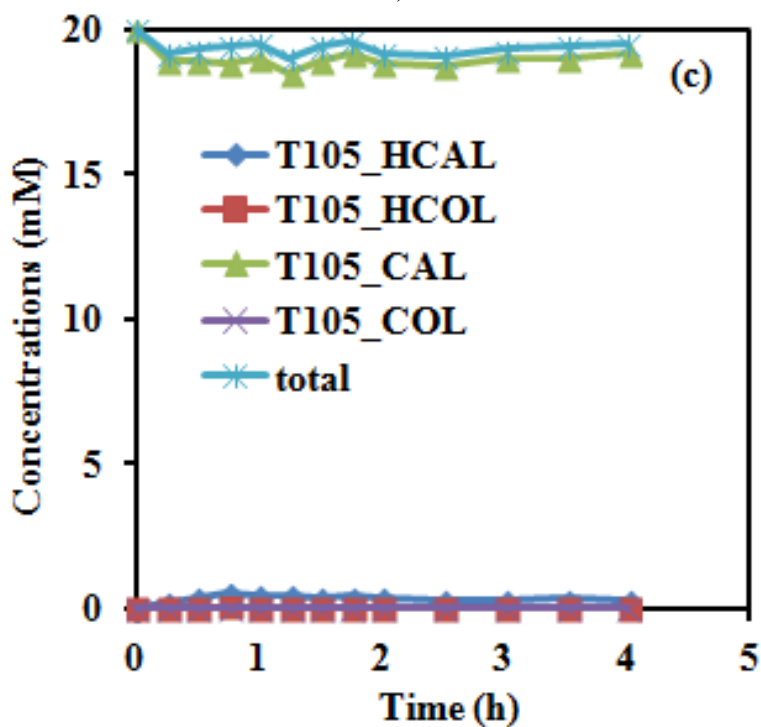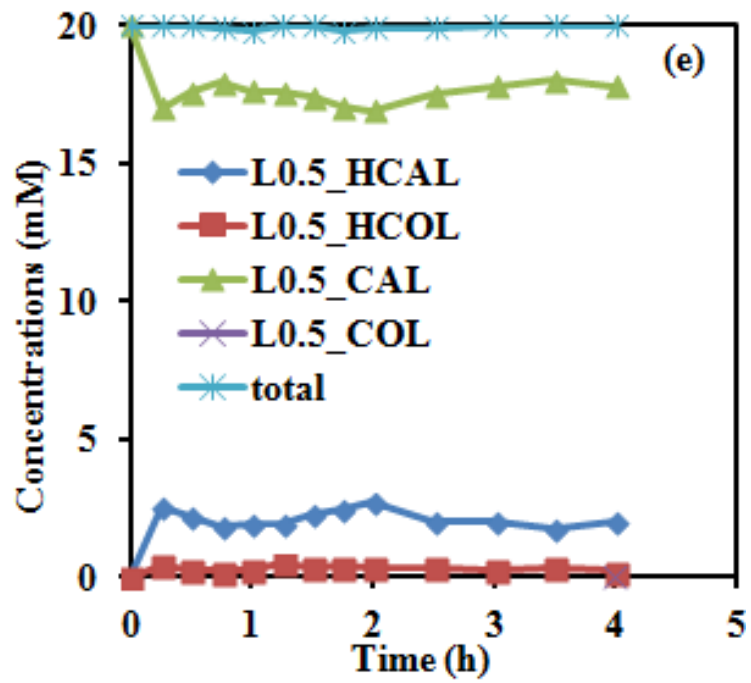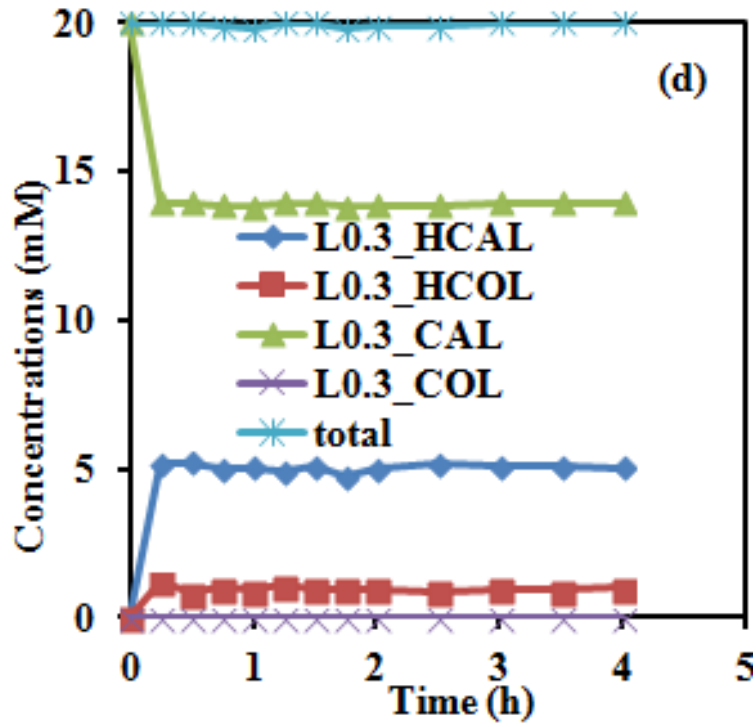
Figure 4.12 (cont'd)

Figure 4.12 (cont'd)
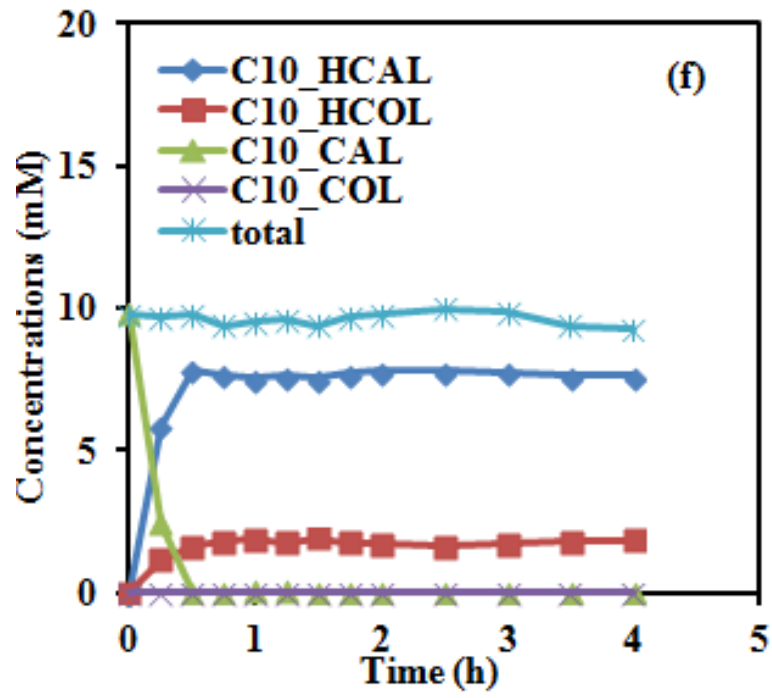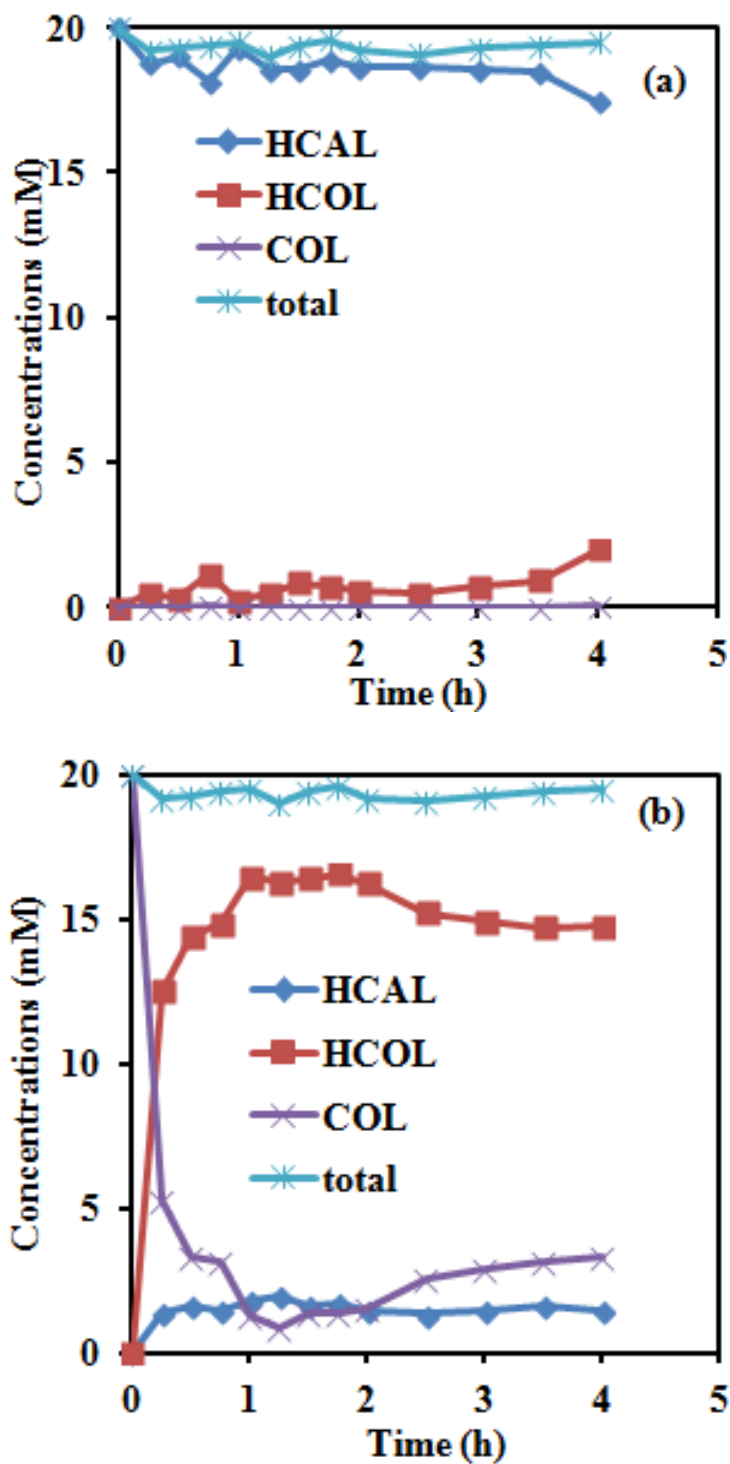
Figure 4.13. Concentration profiles (mM) as a function of time (h) for hydrogenation of HCAL (a) and COL (b) catalyzed by PVP-stabilized Pd NPs (all reactions were conducted at hydrogen pressure of 1 atm, hydrogen flow rate at 2.4 mL/min, T = 150°C, substrate concentration of 20 mM and substrate flow rate of 0.1 mL/h).

Table 4.5. Average substrate conversions (%) and product compositions (%) for CAL hydrogenation with immobilized PVP-Pd NPs in glass capillary microreactors under different reaction conditions.

Reaction conditions		Substrate (CAL) conversion (%)	Product composition (%)		
			HCAL	COL	HCOL
T($^\circ$C)	**150**	99.9±0.1	81.4±0.8	N/A	18.6±0.7
	125	29.7±1.4	85.2±1.6	N/A	12.5±0.5
	105	2.1±0.4	95.1±4.8	N/A	4.9±4.8
V_s (mL/h)	**0.1**	99.9±0.1	81.4±0.8	N/A	18.6±0.7
	0.3	30.3±0.2	83.9±1.3	N/A	16.1±1.3
	0.5	11.9±1.6	87.7±3.2	N/A	12.3±3.3
C(mM)	**20**	99.9±0.1	81.4±0.8	N/A	18.6±0.7
	10	99.9±0.1	81.2±0.9	N/A	18.8±0.9

4.4.5.2 Assessment of PVP-Ru NPs of different sizes

To investigate the effects of particle size on catalytic activity, we prepared three capillary reactors containing different particle sizes of PVP-Ru NPs. We assessed the catalyst performance at different reaction temperatures, substrate flow rates and substrate concentrations (Figures 4.14 and 4.15). Reactions reached steady state within 0.25 h and the carbon balances closed out between 86% and 97%. The average substrate conversions and product compositions are summarized in Table 4.6. Similar to previous observations, higher reaction temperatures and slower substrate flow rates enhanced conversions, while substrate concentration had little effect. For all Ru NPs, COL production was enhanced at lower reaction temperature.

For PVP-Ru1 NPs, faster flow rates resulted in higher production of partially-reduced product HCAL, with the production of COL and HCOL negligible. For PVP-Ru2 NPs, there was 6% increase of COL production at the higher flow rate, but the HCOL production was about the same (8.3 to 8.8%) at different substrate flow rates. Hydrogenation of intermediates HCAL and

165

COL by PVP-Ru1 and Ru2 NPs showed similar conversions of 8 to 10% towards HCOL, demonstrating the distinct lack of selectivity of Ru NPs for either C=C or C=O bond reduction under high temperature and low pressure (Figure 4.16). We thus attributed the 6% difference in COL or HCAL production for PVP-Ru2 at different substrate flow rates to the mutual transformation between these two intermediates, rather than the difference in residence times.

We compared the catalyst performance of the three types of Ru NPs under the same reaction conditions (T of 150°C, substrate concentration of 20 mM, substrate flow rate of 0.1 mL/h). The conversion was 1% for PVP-Ru3, much lower than the other two catalysts. PVP-Ru2 showed moderate reactivity and a higher conversion towards COL, compared to PVP-Ru1. This could be explained by the more favorable adsorption of C=O bonds with less steric hindrance on larger Ru particle surfaces [46]. HCAL was the major product when the reaction was catalyzed by PVP-Ru1. The COL composition increased significantly as the particle size increased.

Table 4.6. Average substrate conversions (%) and product compositions (%) for CAL hydrogenation with immobilized PVP-Ru NPs of various sizes in glass capillary microreactors under different reaction conditions.

Catalysts	Reaction conditions		Substrate (CAL) conversion (%)	Product composition (%)		
				HCAL	COL	HCOL
PVP-Ru1	**T(°C)**	**150**	74.0±1.5	84.8±1.4	1.9±0.7	13.3±1.9
		125	38.9±4.8	68.8±2.1	21.4±2.6	9.8±1.3
		105	16.3±1.0	44.5±2.0	55.3±2.1	0.2±0.4
	Vs (mL/h)	**0.1**	74.0±1.5	84.8±1.4	1.9±0.7	13.3±1.9
		0.3	11.0±0.2	99.7±0.6	N/A	0.3±0.6
	C(mM)	**20**	74.0±1.5	84.8±1.4	1.9±0.7	13.3±1.9
		10	95.5±3.4	76.6±4.4	N/A	23.4±4.7
PVP-Ru2	**T(°C)**	**150**	32.0±2.5	73.7±5.4	18.1±4.5	8.3±1.7
		125	16.8±6.4	65.0±3.6	25.9±3.3	9.0±2.2
		105	9.6±1.5	56.0±2.6	41.6±2.8	23.6±1.1
	Vs (mL/h)	**0.1**	32.0±2.5	73.7±5.4	18.1±4.5	8.3±1.7
		0.3	1.1±0.3	66.7±2.1	24.5±1.4	8.8±1.2
	C(mM)	**20**	32.0±2.5	73.7±5.4	18.1±4.5	8.3±1.7
		10	44.7±2.7	66.7±2.1	15.5±1.2	17.8±2.1
PVP-Ru3	**T(°C)**	**150**	1.0±0.1	43.1±2.8	56.9±2.5	N/A
	Vs (mL/h)	**0.1**				
	C(mM)	**20**				
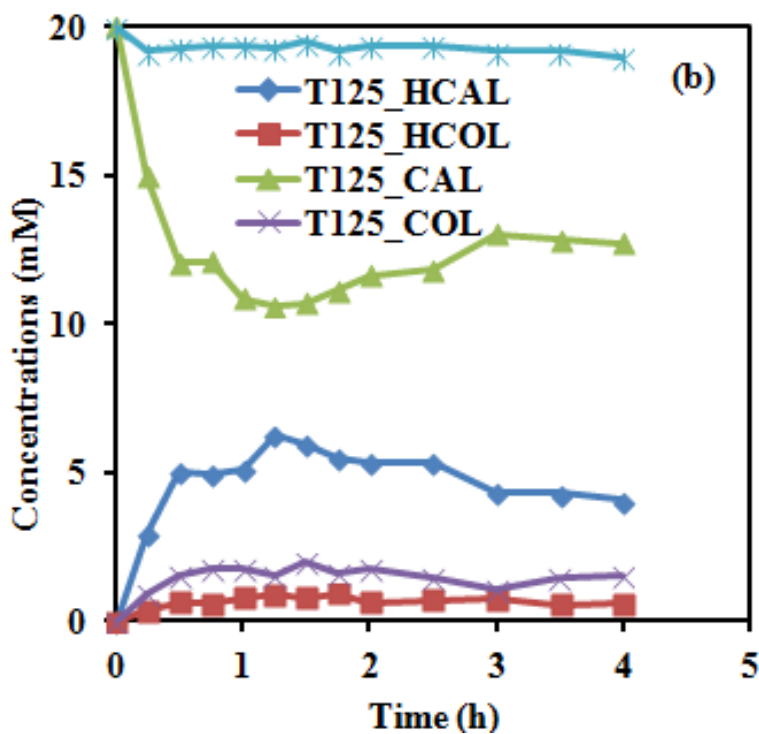
Figure 4.14. Concentration profiles (mM) as a function of time (h) for hydrogenation of CAL catalyzed by PVP-Ru1 under different reaction conditions (all reactions were conducted at

168

Figure 4.14 (cont'd)

hydrogen pressure of 1 atm and hydrogen flow rate of 2.4 mL/min). (a) T = 150°C; (b) T = 125°C; (c) T = 105°C (reactions in (a)-(c) were conducted at substrate concentration of 20 mM and substrate flow rate of 0.1 mL/h); (d) substrate flow rate = 0.3 mL/h (reactions in (d) were conducted at T = 150°C and substrate concentration of 20 mM); (e) substrate concentration = 10 mM (reactions in (e) were conducted at T = 150°C and substrate flow rate of 0.1 mL/h).

Figure 4.14 (cont'd)

170

Figure 4.15. Concentration profiles (mM) as a function of time (h) for hydrogenation of CAL catalyzed by PVP-Ru2 under different reaction conditions (all reactions were conducted at hydrogen pressure of 1 atm and hydrogen flow rate of 2.4 mL/min). (a) T = 150°C; (b) T = 125°C; (c) T = 105°C (reactions in (a)-(c) were conducted at substrate concentration of 20 mM and substrate flow rate of 0.1 mL/h); (d) substrate flow rate = 0.3 mL/h (reactions in (d) were conducted at substrate concentration of 20 mM and temperature of 150°C.

Figure 4.15 (cont'd)

Figure 4.15 (cont'd)

Figure 4.15 (cont'd)

Figure 4.16. Concentration profiles (mM) as a function of time (h) for hydrogenation of intermediates catalyzed by PVP-Ru1: (a) HCAL; (b) COL (all reactions were conducted at

175

Figure 4.16 (cont'd)
hydrogen pressure of 1 atm, hydrogen flow rate of 2.4 mL/min, T = 150°C, substrate concentration of 20 mM and substrate flow rate of 0.1 mL/h).

4.4.5.3. Assessment of PVP-stabilized Pd-Ru alloy NPs

To investigate the effects of composition on catalytic activity, we deposited PVP-PdRu alloys in the capillary reactors. We assessed catalyst performance at different reaction temperatures, substrate flow rates and substrate concentrations (Figures 4.17). Reactions reached steady state within 0.25 h and the carbon balances closed out between 87% and 98%. Similar to the single metallic Pd or Ru NPs, higher reaction temperatures and slower substrate flow rates enhanced substrate conversions, while substrate concentration had little effect for Pd-Ru bimetallic NPs. However, in addition to HCAL, HCOL comprised18-30% of the product composition, with COL production negligible (Table 4.6). Hydrogenation of intermediate HCAL by PVP-PdRu alloyed NPs showed 7% conversion towards HCOL, with over 90% of COL to either HCAL and HCOL, demonstrating the ease of reduction of C=C bonds in the presence of Pd (Figure 4.18).

Under the same reaction conditions, C=C reduction was favored in the presence of Pd and for smaller Ru NPs, resulting in HCAL being the primary product. HCOL production increased for the bimetallic NPs compared to monometallic NPs, which was consistent with the results obtained in the batch system. The synergy between Pd and Ru changed the typical crystal structures of pure Pd and Ru NPs, thus facilitating the conversion of the intermediates to the fully-reduced product [48]. Unsaturated alcohol production was hindered by Pd and PdRu NPs because more than 90% was readily reduced to HCOL and the rest was transformed to the more stable unsaturated aldehyde molecules.
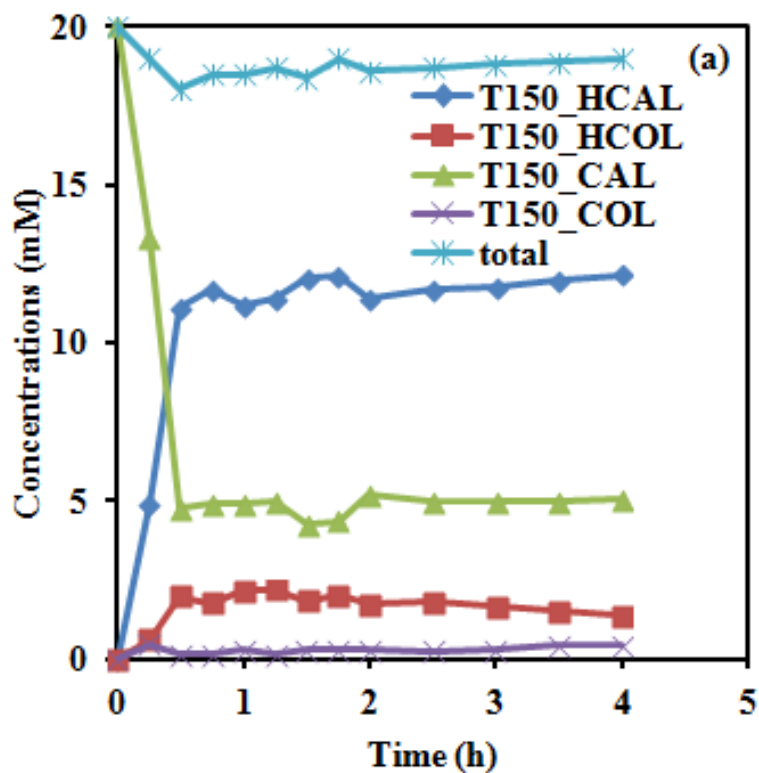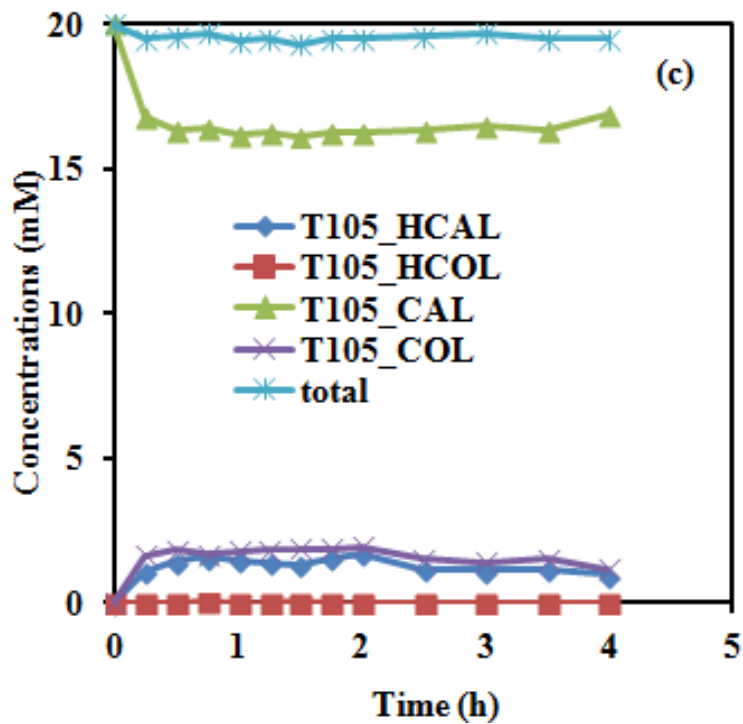
176
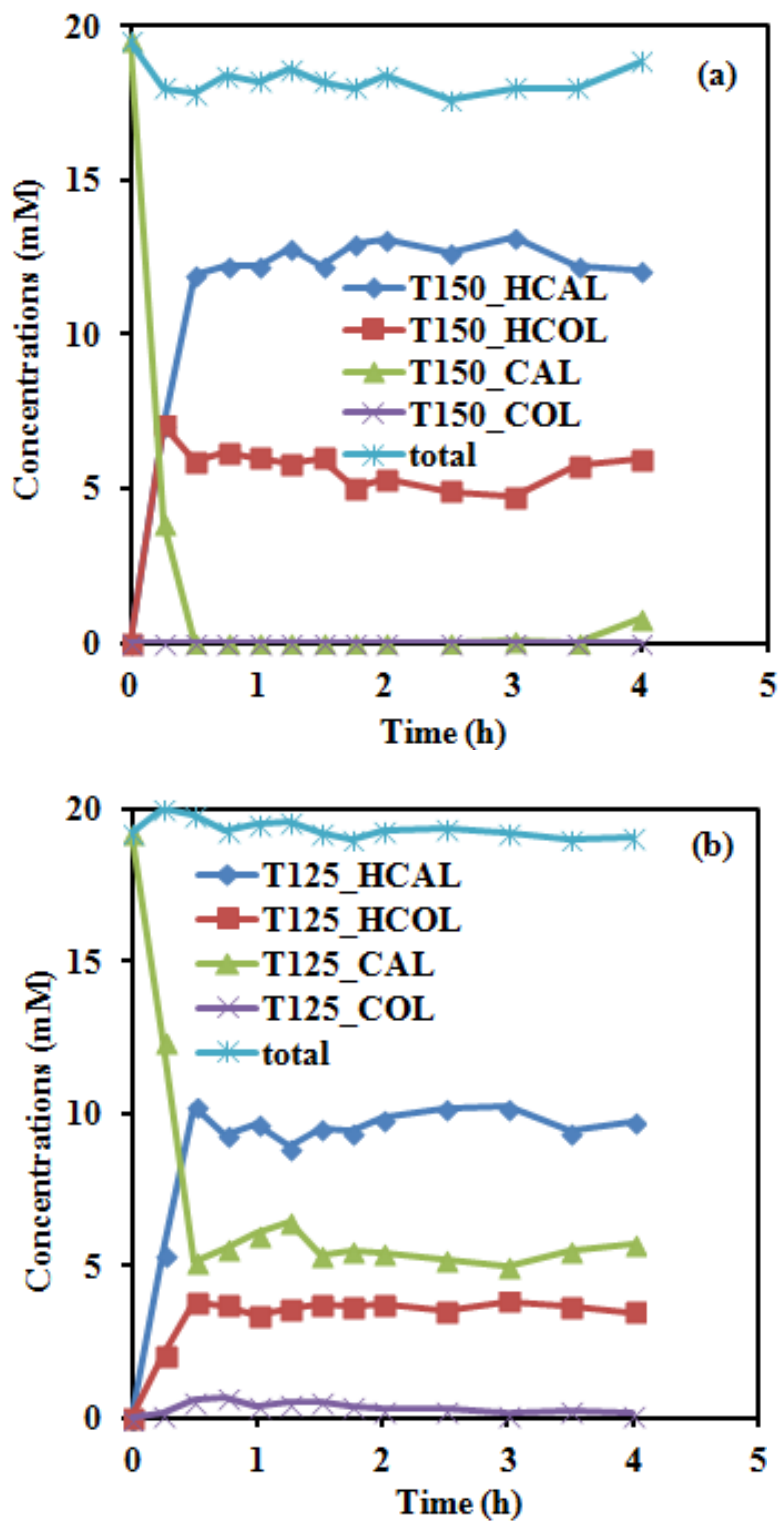
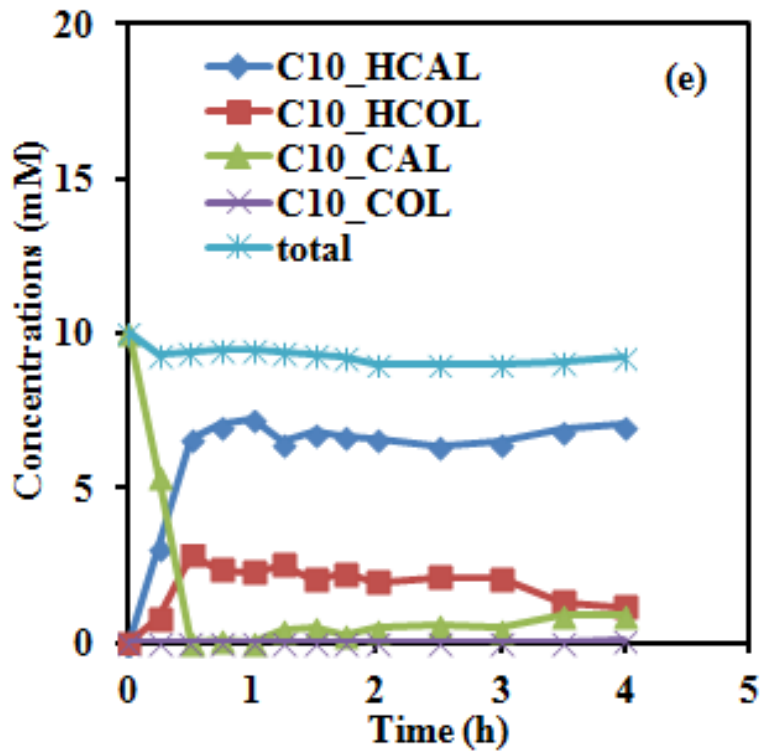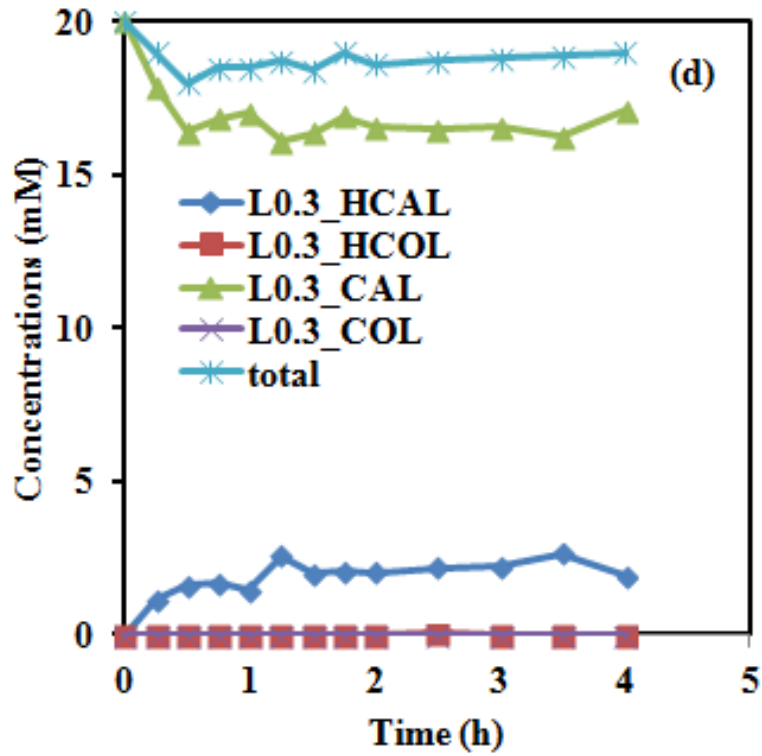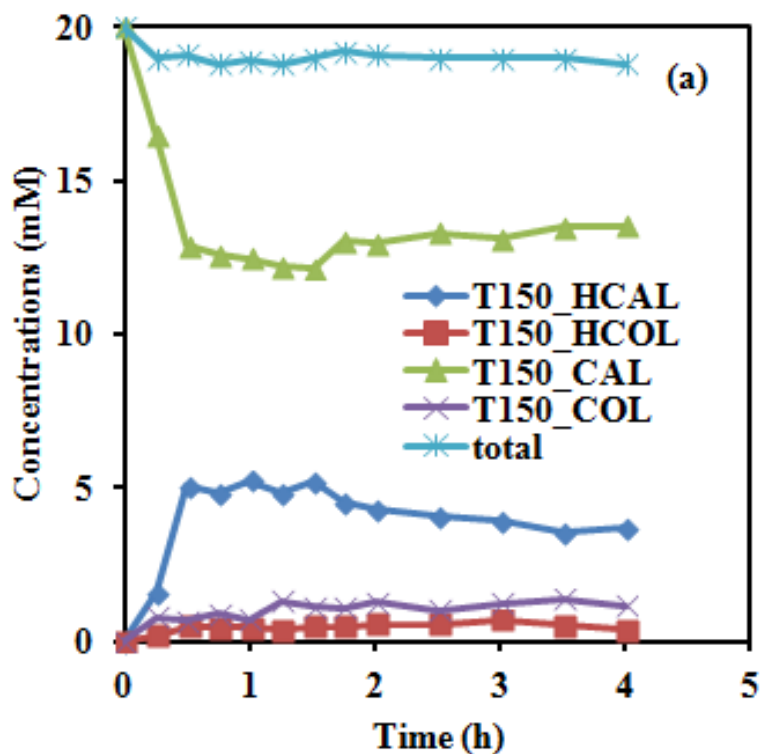**Figure 4.17.** Concentration profiles (mM) as a function of time (h) for hydrogenation of CAL catalyzed by PVP-Pd-Ru under different reaction conditions (all reactions were conducted at

Figure 4.17 (cont'd)

a hydrogen pressure of 1 atm and hydrogen flow rate of 2.4 mL/min). (a) T = 150°C; (b) T = 125°C; (c) T = 105°C (reactions in (a)-(c) were conducted at a substrate concentration of 20 mM and substrate flow rate of 0.1 mL/h); (d) substrate flow rate = 0.3 mL/h (reactions in (d) were conducted at a substrate concentration of 20 mM and reaction temperature of 150°C).
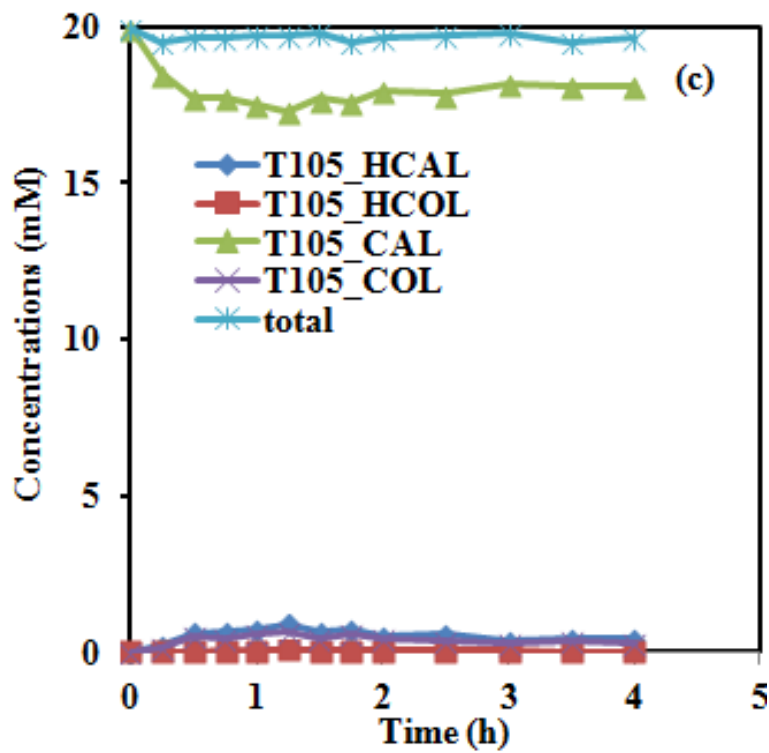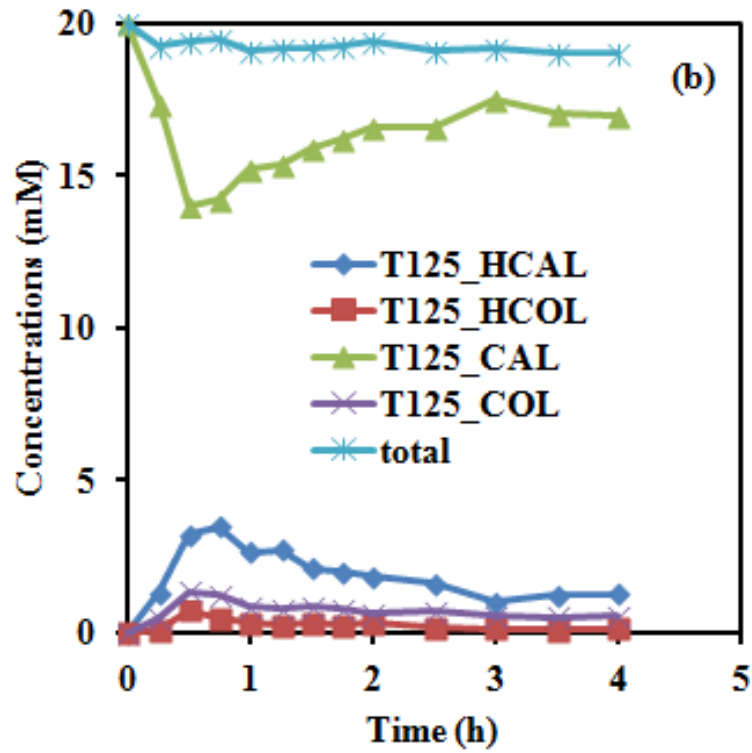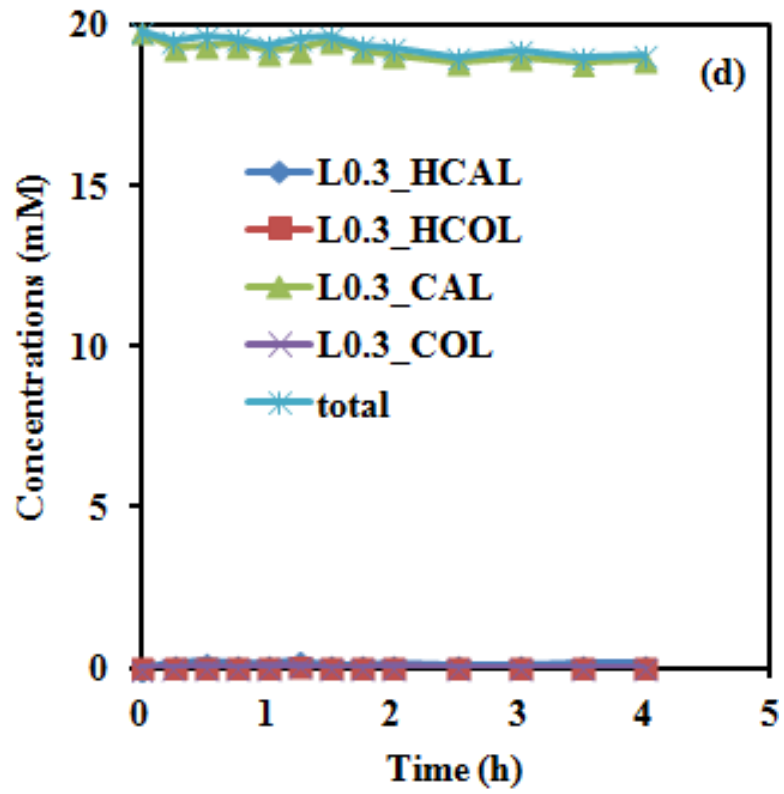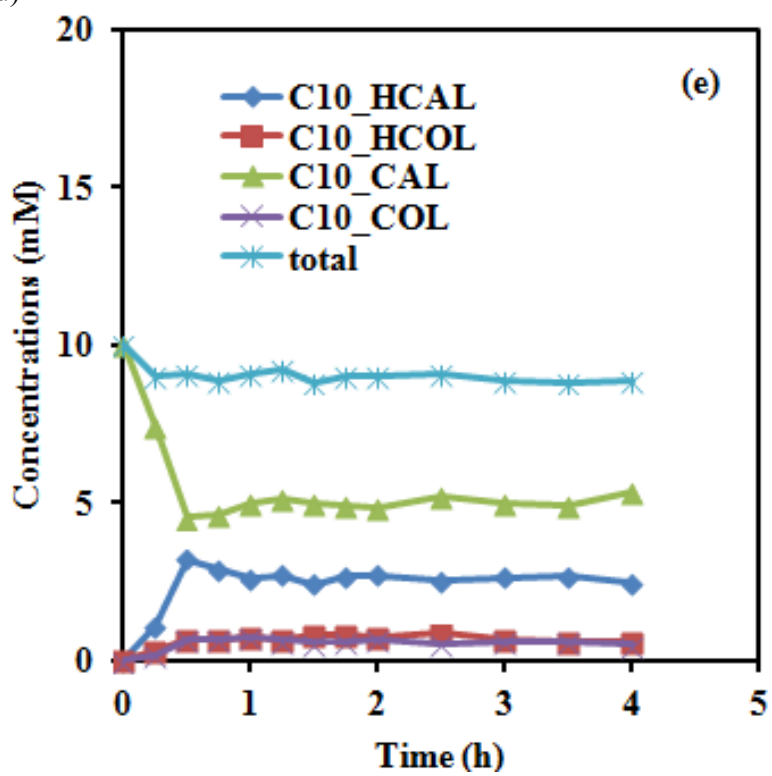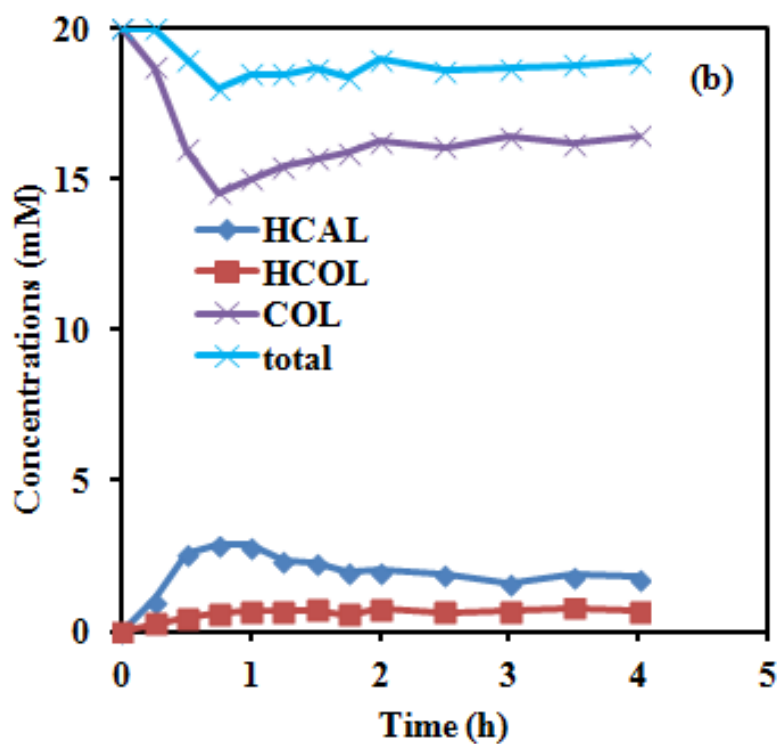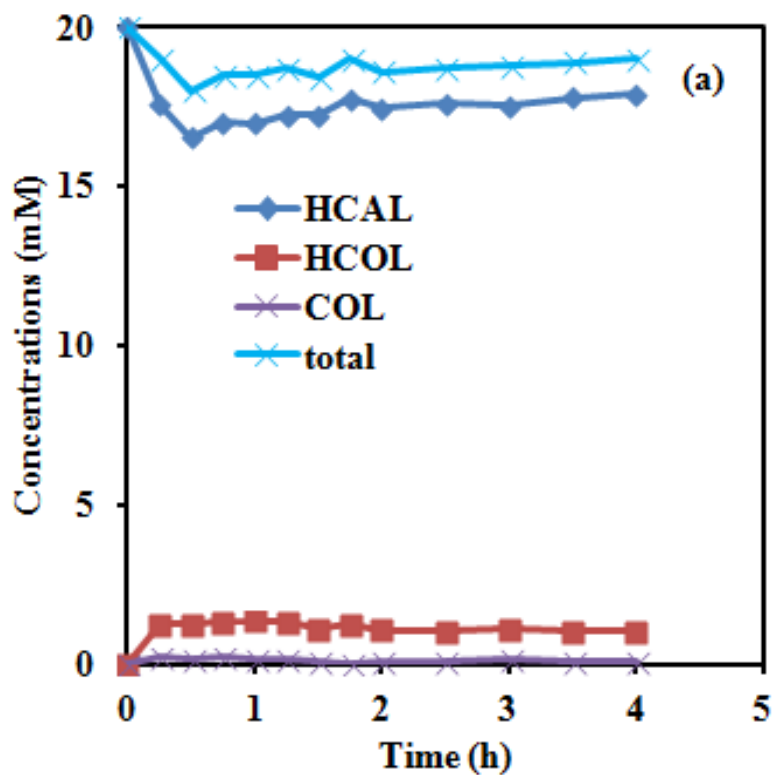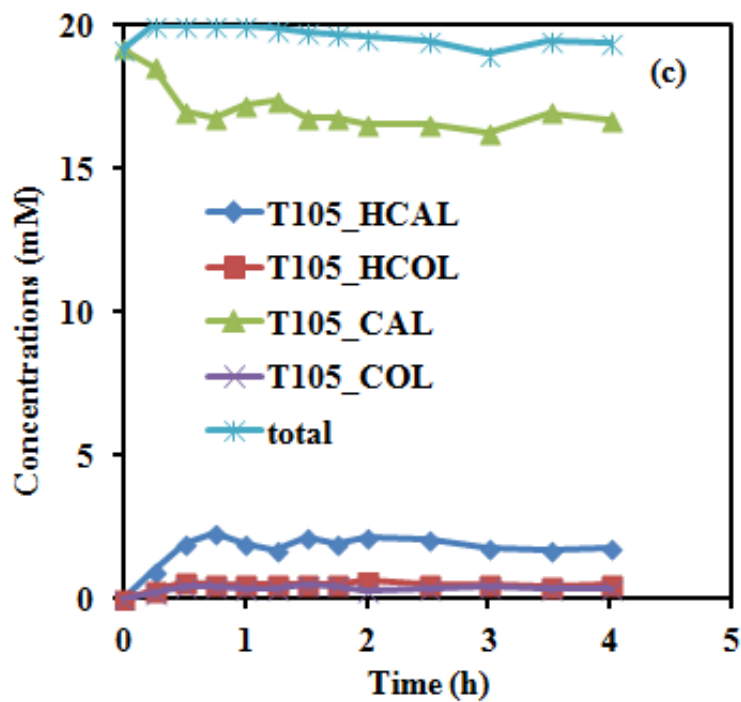
Figure 4.17 (cont'd)
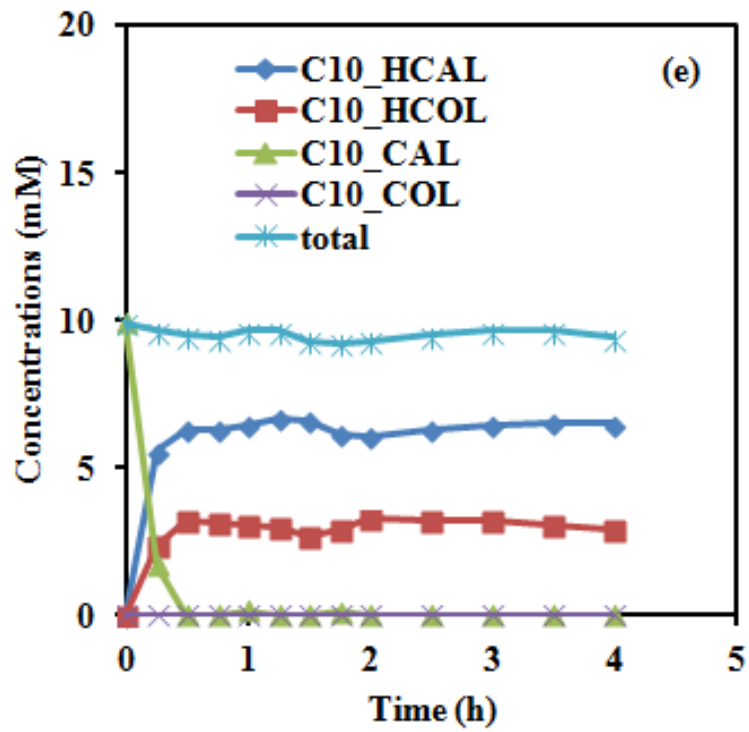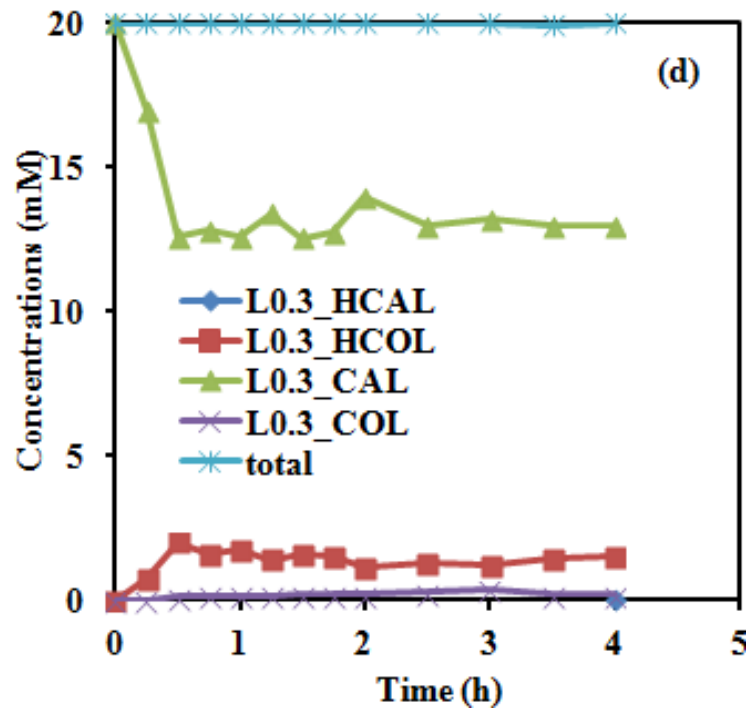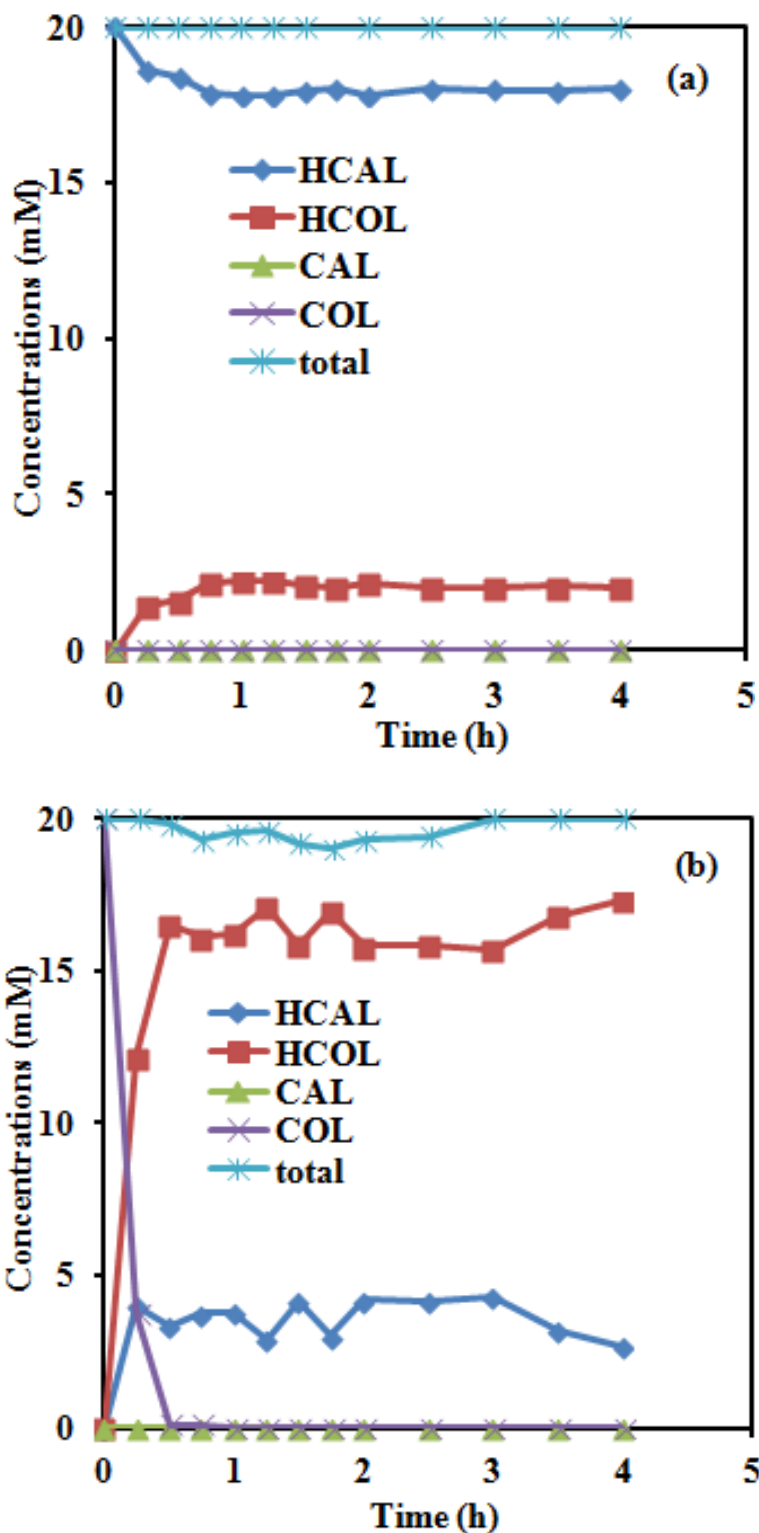
Figure 4.18. Concentration profiles (mM) as a function of time (h) for hydrogenation of intermediates catalyzed by PVP-PdRu: (a) HCAL; (b) COL (all reactions were conducted at

Figure 4.18 (cont'd)

a hydrogen pressure of 1 atm, hydrogen flow rate of 2.4 mL/min, T = 150°C, substrate concentration of 20 mM and substrate flow rate of 0.1 mL/h).

Table 4.7. Average substrate conversions (%) and product compositions (%) for CAL hydrogenation with immobilized bimetallic alloy PVP-PdRu NPs in glass capillary microreactors under different reaction conditions.

Reaction conditions		Substrate (CAL) conversion (%)	Product composition (%)		
			HCAL	COL	HCOL
T(°C)	150	99.6±1.2	69.0±2.5	N/A	31.0±2.5
	125	71.3±2.1	70.6±1.7	2.8±1.3	26.5±0.9
	105	14.5±1.1	67.9±2.4	13.5±2.2	18.6±1.7
V_s (mL/h)	0.1	99.6±1.2	69.0±2.5	N/A	31.0±2.5
	0.3	35.0±2.1	75.4±1.7	3.1±1.1	21.6±2.5
C(mM)	20	99.6±1.2	69.0±2.5	N/A	31.0±2.5
	10	99.7±0.6	67.6±1.7	N/A	32.4±1.7

4.4.5.4 Calculations of TOF values for PVP-stabilized catalysts

Table 4.8 summarizes the TOF values based on the fraction of surface atoms available for CAL hydrogenation in the glass capillary microreactors. The immobilization procedure in the glass capillary was adopted from those in previous reports where PVP-stabilized NPs were anchored to silanized silica supports [49, 50]. Instead of silanized silica supports, we grafted the PVP-stabilized NPs on silanized glass capillary interior wall surfaces. The metal atoms coordinated to the aminosilanized films while the surrounding PVP stabilizers were partially removed during the pre-reduction procedure. The high TOF values for PVP-stabilized NPs were the result of the vapor-phase reaction and the very short residence times. We did not observe any

particle aggregation in the glass capillary microreactor systems. Thus, catalyst stability and recyclability were greatly improved, compared to reactions in the PDMS microfluidic reactors.

We observed that TOF values decreased as the average Ru particle sizes increased. This was attributed to the decrease in the fraction of surface metal atoms. The high standard deviation in the TOF values for Ru2 is due to its bimodal distribution of particle sizes. In spite of the identical pre-reduction procedures, the quantities of surface atoms reduced in different-sized Ru catalysts varied. The uneven reduction level led to disproportionate changes in surface catalytic sites and TOF values for different Ru particle sizes. Since our catalyst loading was extremely low, it was practically impossible to quantify the proportions of reduced metal atoms on the reactor surfaces, and thus obtain the exact number of catalytic sites. However, the estimated TOF values based on the concentration of surface atoms, while not as accurate as they could be, still provide realistic catalyst performance that can be correlated to particle size and composition. Pd-Ru alloyed NPs have intermediate TOF values between those for monometallic Pd and Ru nanocatalysts. This was attributed to the synergy effects of the two different elements [13-15].

Table 4.8. TOF values based on estimated fraction of surface atoms for different catalysts used for the hydrogenation of cinnamaldehyde (20 mM) in glass capillary microreactors. The average diameter of Ru1, Ru2 and Ru3 are 3.5, 27 and 121 nm, respectively.

Catalysts	TOF($\times 10^{-3}$ h^{-1})
PVP-Pd (14.7 nm)	7.3±0.7
PVP-Ru1 (3.5 nm)	0.6±0.05
PVP-Ru2 (27 nm)	0.4±0.1
PVP-Ru3 (121 nm)	0.3±0.03
PVP-PdRu (14.1 nm)	4.6±0.4

4.4.5.5 Apparent activation energy of PVP-stabilized catalysts

We estimated the apparent activation energies (E_A) for CAL hydrogenation by Arrhenius plots of the natural logarithm of TOF versus reciprocal absolute temperature (Figures 4.19). The TOF values used for the Arrhenius plots were based on the amount of metal NPs in the capillary microreactor systems. In each capillary microreactor with immobilized metal nanoparticles, the catalyst loading was controlled over a narrow range (between 0.99 and 1.02×10^{-9} mol). We could not base TOF values on surface active sites for two reasons. First, due to the sparse distribution and low loading of metal nanocatalysts on the capillary microreactor surfaces, it was not practical to measure the metal dispersion by common surface techniques such as BET physisorption or hydrogen chemisorption. Second, even if metal dispersion data were available, not every surface metal atom serves as an active site, as documented in recent computational and experimental reports [51, 52].

We found that the apparent activation energies of the catalysts were independent of particle size and composition, under the reaction conditions used in the continuous flow microreactor systems. The apparent activation energies in the capillary microreactor agreed well (within 15%) with those calculated in the batch reactor system, further supporting the reliability of the microreactor system.
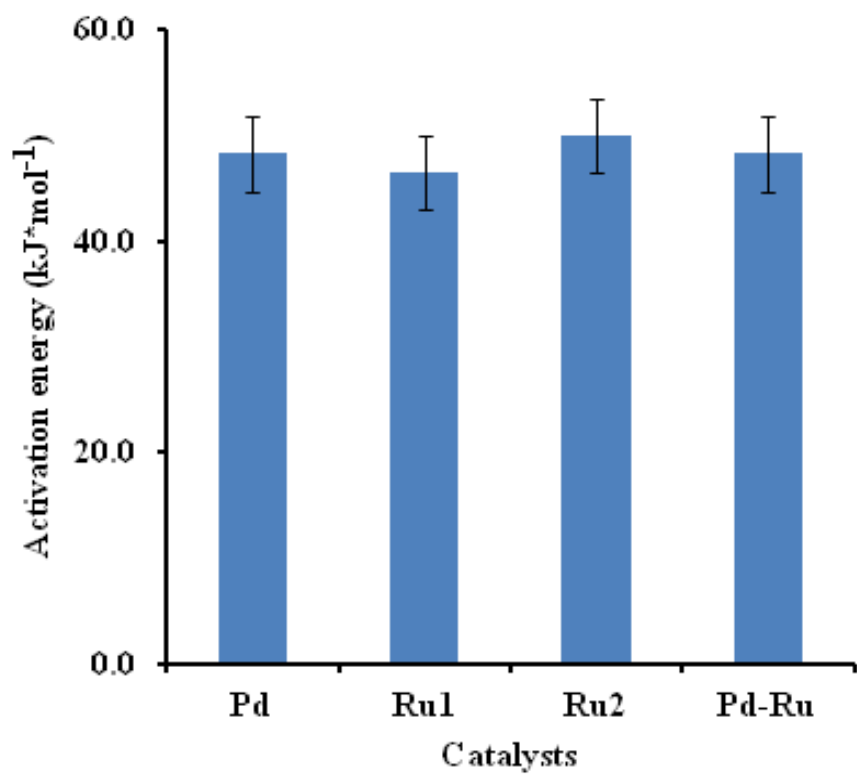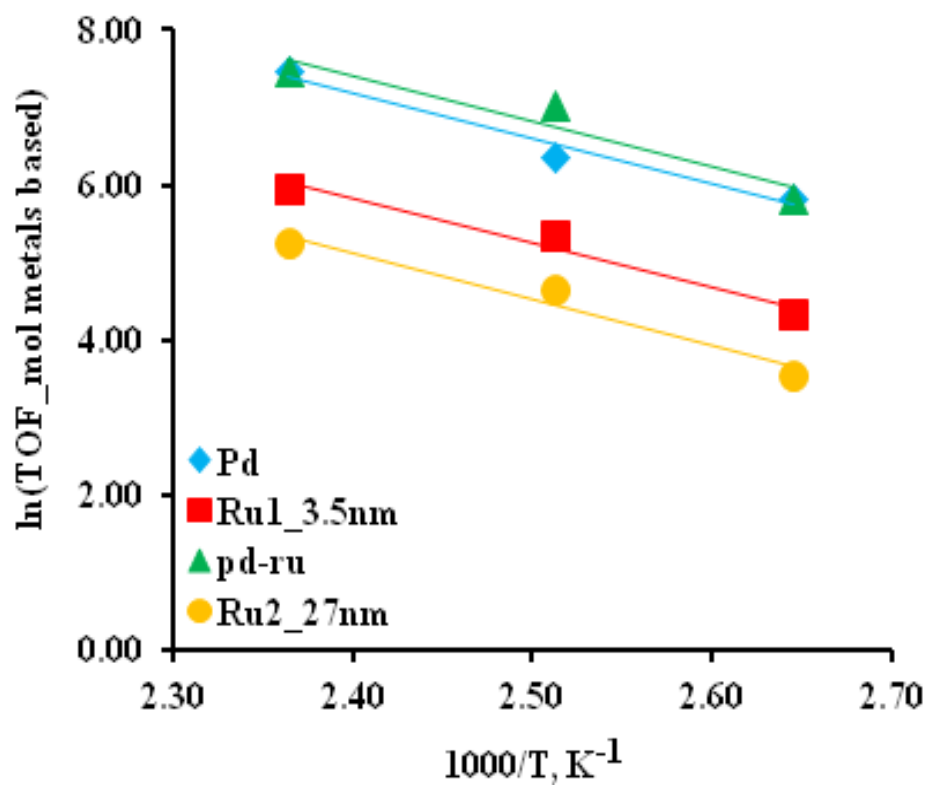
Figure 4.19. Arrhenius plots for cinnamaldehyde hydrogenation over PVP-stabilized metallic

Figure 4.19 (cont'd)

and bimetallic NPs (above), and apparent activation energies obtained by linear regression of the Arrhenius plots (below). All the reactions were conducted under conditions of 0.99 to 1.02×10^{-9} mol of metal loading in the glass capillaries, 20 mM solution of CAL in IPA, and hydrogen pressure of 1 atm. The reaction temperatures ranged from 378 K to 423 K for each catalyst. Linear regression of the data for each catalyst gives the Arrhenius intercept $\ln(TOF_0)$ and $-E_A/R$ in the Arrhenius equation: $\ln(TOF) = \ln(TOF_0) - E_A/RT$.

4.5 Conclusions

We have integrated catalytic NPs with microfluidics, and developed a reliable protocol for immobilization of nanocatalysts in glass capillary microreactors. The immobilization procedure is reproducible and robust, and promotes catalyst recovery and reuse with improved stability compared to PDMS microfluidic reactors. We have demonstrated that the system can be used to efficiently evaluate intrinsic catalytic activity for selective hydrogenation of α, ß-unsaturated aldehydes under different reaction conditions, and to assess kinetic parameters such as catalyst turnover frequencies and apparent activation energies. This continuous system also has enabled stable production of desired intermediate products compared to batch reactors. The integration of well-defined nanocatalysts and microfluidics provides an excellent platform with great potential for high throughput screening of catalysts and for mechanistic studies of reaction kinetics.

REFERENCES

REFERENCES

1. Besson, M. and P. Gallezot, *Deactivation of metal catalysts in liquid phase organic reactions.* Catalysis Today, 2003. **81**: p. 547-559.

2. Cheng, L., et al., *New Prediction Methods for CO2 Evaporation inside Tubes: Part I - A Two-Phase Flow Pattern Map and a Flow Pattern Based Phenomenological Model for Two-Phase Flow Frictional Pressure Drops.* International Journal of Heat Mass Transfer, 2008. **51**: p. 111-124.

3. Muraza, O., et al., *Selectivity control in hydrogenation reactions by nanoconfinement of polymetallic nanoparticles in mesoporous thin films.* Applied Catalysis a-General, 2009. **368**(1-2): p. 87-96.

4. Protasova, L.N., et al., *A kinetic study of the liquid-phase hydrogenation of citral on Au/TiO(2) and Pt-Sn/TiO(2) thin films in capillary microreactors.* Applied Catalysis a-General, 2011. **399**(1-2): p. 12-21.

5. Rebrov, E.V., et al., *Gold supported on mesoporous titania thin films for application in microstructured reactors in low-temperature water-gas shift reaction.* Catalysis Today, 2008. **138**(3-4): p. 210-215.

6. Rebrov, E.V., et al., *Capillary microreactors wall-coated with mesoporous titania thin film catalyst supports.* Lab on a Chip, 2009. **9**(4): p. 503-506.

7. Rebrov, E.V., et al., *Thin catalytic coatings on microreactor walls A way to make industrial processes more efficient.* Chimica Oggi-Chemistry Today, 2009. **27**(4): p. 4-7.

8. Rebrov, E.V., et al., *Design of a thick-walled screen for flow equalization in microstructured reactors.* Journal of Micromechanics and Microengineering, 2007. **17**(3): p. 633-641.

9. Rebrov, E.V., et al., *Selective Hydrogenation of 2-Methyl-3-butyne-2-ol in a Wall-Coated Capillary Microreactor with a Pd(25)Zn(75)/TiO(2) Catalyst.* Organic Process Research & Development, 2009. **13**(5): p. 991-998.

10. Ide, M.S., et al., *Mechanistic Insights on the Hydrogenation of alpha,beta-Unsaturated Ketones and Aldehydes to Unsaturated Alcohols over Metal Catalysts.* Acs Catalysis, 2012. **2**(4): p. 671-683.

11. Lin, R., et al., *In-situ immobilization of palladium nanoparticles in microfluidic reactors and assessment of their catalytic reactivity.* Nanotechnology, 2010: p. 325605.

12. Zawadzki, M. and J. Okal, *Synthesis and structure characterization of Ru nanoparticles stabilized by PVP or gamma-Al2O3.* Materials Research Bulletin, 2008. **43**(11): p. 3111-3121.

13. Ma, X., *Ruthenium-based Model Catalysts for Liquid Phase Hydrogenation of Bio-derived Organic Acids and Aldehydes*, in *Department of Chemical Engineering & Materials Science*. 2013, Michigan State University: East Lansing.

14. Neri, G., et al., *Kinetic analysis of cinnamaldehyde hydrogenation over alumina-supported ruthenium catalysts.* Industrial & Engineering Chemistry Research, 1997. **36**(9): p. 3554-3562.

15. Nuithitikul, K. and J.M. Winterbottom, *The hydrogenation of cinnamaldehyde by supported aqueous phase (SAP) catalyst of RhCl(TPPTS)(3): Selectivity, kinetic and mass transfer aspects.* Chemical Engineering Science, 2006. **61**(18): p. 5944-5953.

16. Wang, Y., et al., *Two-phase flow and heat transfer in micro-channels and their applications in micro-system cooling.* Heat and Mass Transfer in Porous Media, Advanced Structured Materials ed. J.M.P.Q. Delgado. Vol. 13. 2012: Springer-Verlag Berlin Heidelberg 47-82.

17. Chisholm, D., *A theoretical basis for the Lockhart-Martinelli correlation for two-phase flow.* International Journal of Heat and Mass Transfer, 1967. **10**(12): p. 1767-1778.

18. Thome, J.R., *Wolverine Engineering Data Book III*. 2006: Wolverine Tube, Inc. .

19. Mehendale, S.S. and A.M. Jacobi, *Evaporative Heat Transfer in mesoscale Heat Exchangers.* ASHRAE Trans. , 2000. **106**: p. 446-452.

20. Ribatski, G., L. Wojtan, and J.R. Thome, *An Analysis of Experimental Data and Prediction Methods for Flow Boiling Heat Transfer and Two-Phase Frictional Pressue*

Drop in Micro-Scale Channels. Experimental Thermal and Fluid Science, 2006. **31**: p. 1-19.

21.   Cheng, L., G. Ribatski, and J.R. Thome, *New Prediction Methods for CO2 Evaporation inside Tubes: Part II - An Updated General Flow Boiling Heat Transfer Model Based on Flow Patterns.* International Journal of Heat Mass Transfer, 2008. **51**: p. 125-135.

22.   Kandlikar, S.G. and S. Garimella, *Heat Transfer and Fluid Flow in Minichannels and Microchannels*. 2005: Elsevier Science, USA.

23.   Cheng, P. and H. Wu, *Mesoscale and Microscale Phase-Change Heat Transfer*. Advances in Heat Transfer Vol. 39. 2006: Elsevier. 461-563.

24.   Cao, B. and L. Luo, *Modeling of Gas Liquid Taylor Flow in Capillaries by Using a Two Fluid Model.* Industrial & Engineering Chemistry Research, 2012. **51**: p. 13054-13061.

25.   Leung, S.S.Y., et al., *Effect of Flow Characteristics on Taylor Flow Heat Transfer.* Industrial & Engineering Chemistry Research, 2011. **51**: p. 2010-2020.

26.   Gupta, R., D.F. Fletcher, and B.S. Haynes, *CFD modelling of flow and heat transfer in the Taylor flow regime.* Chemical Engineering Science, 2010. **65**: p. 2094-2107.

27.   Gunther, A. and K.F. Jensen, *Multiphase microfluidics: from flow characteristics to chemical and materials synthesis.* Lab on a Chip, 2006. **6**(12): p. 1487-1503.

28.   Kandlikar, S.G. *Two-Phase Flow Patterns, Pressure Drop and Heat Transfer during Boiling in Minichannel and Microchannel Flow Passages of Compact Heat Exchangers*. in *Compact Heat Exchangers and Enhancement Technology for the Process Industries - 2001*. 2001. Begell House, NY.

29.   Kandlikar, S.G. and W.J. Grande, *Evolution of Microchannel Flow Passages - Thermohydraulic Performance and Fabrication Technology.* Heat Transfer Engineering, 2003. **24**: p. 3-17.

30.   Pribyl, D.J., A. Bar-Cohen, and A.E. Bergles. *An Investigation of Critical Heat Flux and Two-Phase Flow Regimes for Upward Steam and Water Flow*. in *5th International Conference in Boiling Heat Transfer*. 2003. Jamaica.

31.   Bowers, M.B. and I. Mudawar, *High Flux Boiling in Low Flow Rate, Low Pressure Drop Minichannel and Micro-channel Heat Sinks.* International Journal of Heat Mass Transfer, 1994. **37**: p. 321-332.

32.   Qu, I. and W. Mudawar, *Measurement and Correlation of Critical Heat Flux in Two-Phase Micro-Channel Heat Sinks.* International Journal of Heat Mass Transfer, 2004. **47**: p. 2045-2059.

33.   Zhang, W., et al., *Correlation for Critical Heat Flux for Flow Boiling of Water in Mini-Channels.* International Journal of Heat Mass Transfer, 2006. **49**: p. 1058-1072.

34.   Wojtan, L., R. Revellin, and J.R. Thome, *Investigation of Critical Heat Flux in Single, Uniformly Heated Microchannels.* Experimental Thermal and Fluid Science, 2007. **30**: p. 765-774.

35.   Jacobi, A.M. and J.R. Thome, *Heat Transfer Model for Evaporation of Elongated Bubble Flows in Microchannels.* Journal of Heat Transfer, 2002. **124**: p. 1131-1136.

36.   Thome, J.R., V. Dupont, and A.M. Jacobi, *Heat Transfer Model for Evaporation in Microchannels, Part I: Presentation of the Model.* International Journal of Heat Mass Transfer, 2004. **47**: p. 3375-3385.

37.   Dupont, V., J.R. Thome, and A.M. Jacobi, *Heat Transfer Model for Evaporation in Microchannels, Part II: Compartison with the Database.* International Journal of Heat Mass Transfer, 2004. **47**: p. 3387-3401.

38.   Peles, Y.P. and S. Haber, *A Steady State, One Dimensional, Model for Boiling Two Phase Flow in Triangular Micro-Channel.* International Journal of Multiphase Flow, 2000. **26**: p. 1095-1115.

39.   Wattelet, J.P., *Heat Transfer Flow Regimes of Refrigerants in a Horizontal-Tube Evaporator*, in *Mechanical Engineering*. 1994, University of Illinois at Urbana-Champaign: Urbana, IL, USA. p. 241.

40.   Dhavaleswarapu, H.K., *Microscale Transport in Evaporating Thin Liquid Films*. 2010, Purdue University: Weat Lafayette, IN USA. p. 193.

41.   Dunn, D.J., *Free Study Heat Transfer Tutorial 1-Conduction* 2012, www.freestudy.co.uk.

42.   Dunn, D.J., *Free Study of Heat Transfer Tutorial 2-Convection and Radiation*. 2012, www.freestudy.co.uk.

43.   Beskok, A., *Gas flows in the transition and free molecular flow regimes*. Microfluidics Based Microsystems: Fundamentals and Applications., ed. S. Kakac. 2010: Springer Science.

44.   Lahr, D.G. and B.H. Shanks, *Effect of sulfur and temperature on ruthenium-catalyzed glycerol hydrogenolysis to glycols.* Journal of Catalysis, 2005. **232**(2): p. 386-394.

45.   de Loos, S.R.A., et al., *Heterogeneous catalysis in a microchannel using a layer of carbon nanofibers on the channel wall.* Chemical Engineering Journal, 2012. **179**: p. 242-252.

46.   Wu, D., et al., *Mixed-phase PdRu bimetallic structures with high activity and stability for formic acid electrooxidation.* Physcal Chemistry Chemical Physics, 2012. **14**: p. 8051-8057.

47.   Hornung, C.H., et al., *A Palladium Wall Coated Microcapillary Reactor for Use in Continuous Flow Transfer Hydrogenation.* Advanced Synthesis & Catalysis, 2010. **352**(10): p. 1736-1745.

48.   Teddy, J., et al., *Influence of particles alloying on the performances of Pt-Ru/CNT catalysts for selective hydrogenation.* Journal of Catalysis, 2011. **278**(1): p. 59-70.

49.   Brayner, R., G. Viau, and F. Bozon-Verduraz, *Liquid-phase hydrogenation of hexadienes on metallic colloidal nanoparticles immobilized on support via coordination capture by bifunctional organic molecules.* Journal of Molecular Catalysis A: Chemical, 2002. **182-183**: p. 227-238.

50.   Zhou, X., et al., *Ru nanoparticles stabilized by poly(N-vinyl-2-pyrrolidone) grafted onto silica: Very active and stable catalysts for hydrogenation of aromatics.* Journal of Molecular Catalysis A: Chemical, 2009. **306**: p. 143-148.

51.   Pazmino, J.H., et al., *Metallic Pt as active sites for the Water-Gas Shift reaction on alkali-promoted supported catalysts.* Journal of Catalysis, 2012. **286**: p. 279-286.

52.   Shekhar, M., et al., *Counting Au Catalytic Sites for the Water-Gas Shift Reaction.* Journal of Catalysis, 2012. **293**: p. 94-102.

CHAPTER 5

CONCLUSIONS AND RECOMMENDATIONS FOR FUTURE RESEARCH

5.1 Major conclusions

The goal of this work was to develop efficient nanocatalysts and a novel reactor platform for catalytic multiphase hydrogenation, which plays a significant role in the conversion of biorenewables to chemicals and fuels. The approach we chose was the strategic integration of nanotechnology, colloid science and microfluidics for heterogeneous catalysis. To do this, well-defined nanocatalysts with high surface-area-to-volume ratios were robustly immobilized on the surfaces of the microfluidic reactors, and their intrinsic catalyst activity was assessed in the system under negligible mass transfer limitations. The separation of catalyst synthesis, characterization and immobilization allows for better control of particle morphology and structure, more accurate performance assessment and more predicable structure-performance correlations.

We synthesized and characterized colloidal noble metallic NPs with well-defined morphology. The particle size, shape and composition were carefully controlled by finely tuning such synthesis parameters as reaction temperature, reaction time, precursor type, stabilizer type, and precursor to stabilizer ratio. Thermal decomposition and polyol reduction provided convenient, simple and reproducible synthesis procedures. The well-characterized colloidal metallic NPs provided a good platform for quantitative investigation of catalyst activity.

In addition to the rational design of nanocatalysts, we also developed a microfluidic platform to achieve fast catalyst screening and assessment with enhanced mass transfer. The first-generation PDMS microfluidic reactor contained robustly-immobilized NPs synthesized by thermal decomposition, and was used for the facile hydrogenation of C=C bonds, with complete reactions in a residence time of 1 min. The system was very efficient, enabling measured TOF values that were at least two orders of magnitude higher than those measured in a glass flask

under identical reaction conditions. There was a problem with particle aggregation in the PDMS microfluidic reactor system, which was a major cause of catalyst deactivation. In addition, because of the low heat tolerance of PDMS, it was difficult to remove the capping PVP stabilizer by calcination after the NPs were immobilized in the microfluidic reactors.

To address this issue, we built a second-generation microreactor using thick wall glass capillaries with similar surface chemistry, but higher heat tolerance and better chemical compatibility to evaluate the catalyst performance of the catalytic NPs. Catalyst recyclability was greatly improved for thio-ether stabilized NPs in the glass capillary microreactor system, compared to the PDMS microreactors. In addition, PVP-stabilized Pd, Ru and PdRu NPs were robustly immobilized on the walls of the capillary microreactor without noticeable particle aggregation. The hydrogenation of CAL was achieved over very short residence times in the capillary microreactor. Catalyst stability was greatly improved under harsher reaction conditions, and catalysts could be easily regenerated. Compared to the batch system in which a mixture of HCAL, HCOL and COL were produced as a function of time, the catalysts in the capillary microreactor system produced one dominant product (HCAL) steadily and continuously, thus reducing the potential need for product separation.

In summary, the combination of well-defined nanocatalysts and microfluidics significantly enhanced the diffusion of hydrogen to catalytic sites, thus eliminating mass transfer limitations and enabling evaluation of the intrinsic catalytic activity. The system provides a convenient platform for high throughput screening of catalysts, and for conducting mechanistic studies of reaction kinetics.

5.2 Suggested directions for future research

Although microreactors have been shown to be suitable for the optimization of many organic reactions, their applications are still somewhat limited. The robust, reliable and efficient immobilization of solid catalysts in microreactors still remains a major challenge and the limiting step to the wide application of microreactors. Recent reports of mesoporous support layers embedded with metal nanocatalysts coated on microreactor walls portray great potential to expand the use of microreactors in industry [1]. Progress in experimental and computational gas-liquid flow dynamics in micro-channels will also facilitate development of intrinsic kinetic models and reaction mechanisms in microreactors [2-4]. Catalytic microreactors have great promise for the development of chemical processes. It is foreseeable that well-defined, well-characterized and well-controlled catalytic microreactors will soon provide the reliability and reusability necessary to promote green chemistry. They can then be used not only as a platform for fundamental probing of reaction mechanisms and catalyst assessment, but also as a source of intrinsic data that enable development of practical mini pilot plants in the chemical industry to promote process scale-up and optimization.

Significant research work is currently being devoted to nanocatalysis. It is often not practical to synthesize large quantities of materials for characterization as well as assessment in traditional batch reactor systems. Microreactors can therefore play a bigger role in studies of nanocatalysis. In addition, the precise flow and control of mixing in the small confined space of microreactors may provide a novel tool to synthesize metal nanoparticles continuously [5]. Finally, *in-situ* characterization of heterogeneous nanocatalysts in the liquid phase inside the microreactors will provide critical data on how catalysts perform in real time, thus improving the rational design of catalysts for target chemical reactions.

REFERENCES

REFERENCES

1. Muraza, O., et al., *Mesoporous silica films as catalyst support for microstructured reactors: Preparation and characterization.* Chemical Engineering Journal, 2008. **135**(Supplement 1): p. S99-S103.

2. Nagy, K.D. and K.F. Jensen, *Catalytic processes in small scale flow reactors Status and opportunities.* Chimica Oggi-Chemistry Today, 2011. **29**(4): p. 18-21.

3. McMullen, J.P. and K.F. Jensen, *Rapid Determination of Reaction Kinetics with an Automated Microfluidic System.* Organic Process Research & Development, 2011. **15**(2): p. 398-407.

4. Henriksen, T.R., et al., *Highly sensitive silicon microreactor for catalyst testing.* Review of Scientific Instruments, 2009. **80**(12).

5. Abou-Hassan, A., O. Sandre, and V. Cabuil, *Inorganic Chemistry in Microreactors.* Angewandte Chemie-International Edition, 2010. **49**: p. 6268-6286.